RÉPUBLIQUE FRANÇAISE
Liberté Égalité Fraternité

Université de Toulouse

Doctorat de l'Université de Toulouse

délivré en co-tutelle avec Université de Salerne

Dynamique d'écoulements en interaction avec des structures movibles et des surfaces libres

Thèse présentée et soutenue, le 26 juin 2026 par

Théo MOUYEN

École doctorale
MEGEP - Mécanique, Energétique, Génie civil, Procédés

Spécialité
Dynamique des fluides

Unité de recherche
IMFT - Institut de Mécanique des Fluides de Toulouse

Thèse dirigée par
David FABRE et Flavio GIANNETTI

Composition du jury
M. Ardeshir HANIFI, Rapporteur, KTH Royal Institute of Technology
M. Franco AUTERI, Rapporteur, Politecnico di Milano
Mme Patricia ERN, Examinatrice, CNRS Université de Toulouse
M. Michel FOURNIE, Examinateur, Université de Toulouse Institut de Mathématiques de Toulouse
M. Edouard BOUJO, Examinateur, Ecole Polytechnique de Lausanne
M. Olivier MARQUET, Examinateur, Onera
M. David FABRE, Directeur de thèse, Université de Toulouse
M. Flavio GIANNETTI, Co-directeur de thèse, Università degli Studi di Salerno

"Let everything happen to you: beauty and terror.
Just keep going. No feeling is final."

— Rainer Maria Rilke

Abstract

In this thesis, we study the flow dynamics involving moving structures and free-surfaces.

A linear and non-linear Arbitrary Lagrangian Eulerian framework are developed and validated for multiple spring-mounted bodies. The derived formulations are then applied to a set of configurations including the two-cylinder tandem and side-by-side configurations as well as the multiple in-line cylinders.

We then propose a low computational-cost impedance-based criterion to predict the instability thresholds. The criterion is found to be in perfect agreement with the classical linear stability analysis and is used to detect instability thresholds in the parameter space. The effects of mass, damping and spacing between the bodies are investigated.

Finally, a linear Arbitrary Lagrangian Eulerian framework is developed for the interaction of a spring-mounted body with a deformable free-surface. We explore the impact of free-surfaces on the wake and vortex-induced vibrations of the body, for different immersion heights.

Keywords: vortex shedding, linear stability analysis, flow–structure interactions, impedance-based stability criterion, free-surface

Paper and conferences:

- Mouyen, T. et al. (2026) 'Stability prediction of vortex-induced vibrations of multiple freely oscillating bodies', *Journal of Fluid Mechanics*, 1032, p. A70. DOI: 10.1017/jfm.2026.11365.
- ERCOFTAC Symposium "Multiphysics critical flow dynamics involving moving/ deformable structures with design applications" 7-9 June 2023, ENSEEIHT, Toulouse, France
- 15th ERCOFTAC SIG 33 Workshop "Progress in Flow Instability, Transition and Control" Alghero, Italy, June 28-30, 2023
- 1st European Fluid Dynamics Conference (EFDC1) RWTH Aachen University, Aachen, Germany, 16-20 September, 2024

Contents

Part I

Introduction

Chapter 1

Introduction and Literature Review

1.1 General introduction and context

The Anangu people are Aboriginal Australians originating from the desert regions of central Australia. Their culture and way of life in this harsh environment extend back more than 40,000 years. Knowledge about their environment, as well as their mythological stories, has traditionally been transmitted orally through what is known as the Dreaming. In this worldview, the sandstone monolith Uluru holds a central cultural and spiritual significance. Rainfall in this region is infrequent and water resources are scarce (figure 1.1). However, over long periods of time, rainfall has eroded crevasses and formed waterholes within the rock, allowing water to be retained. As a result, Uluru became an important source of water for the Aboriginal people and gradually took on a prominent place in their myths and legends.

Humans have long recognized the ubiquity of fluids in nature and the profound influence they exert on their environment. From the erosion of landscapes to the transport of sediments and nutrients, fluid motion shapes many natural systems. Over time, these observations motivated the scientific study of fluid mechanics, which seeks to understand and predict the behavior of liquids and gases in motion. One of the most emblematic examples of fluid–structure interaction is the flow past a bluff body. When a fluid flows around a circular cylinder, the structure of the wake is governed by the

Figure 1.1: The Uluru sandstone monolith during a rare rainfall event, with water cascading along erosion-carved channels in the rock. “Wet Uluru” by Greg Schechter, CC BY 2.0.

competition between inertial and viscous forces. This balance is commonly quantified by the Reynolds number, which, when large enough, leads to the periodic shedding of vortices in what is known as the von Kármán vortex street. While the von Kármán vortex street is often introduced as a purely hydrodynamic instability, the periodic shedding of vortices also generates fluctuating forces on the body that produces them. When the structure is able to move or deform, these unsteady aerodynamic forces may interact with its dynamics and lead to sustained oscillations. This coupling between the fluid flow and the structural response forms the basis of what is broadly referred to as fluid–structure interactions (FSI).

Fluid-structure interactions have been of great interest to many fields of engineering. They are generally classified either as vortex-induced vibrations (VIV) or wake-induced vibrations (WIV) when a body is in the wake of another. The collapse of the Tacoma Narrows bridge in 1940 is an obvious example of the impact a fluid can have on a deformable/oscillating structure. Many applications involving such objects require a deep knowledge to prevent such oscillations, in order to avoid damage. Griffin & Ramberg (1982) reviewed studies on the VIV of marine risers and listed means to suppress such oscillations. The potential oscillations of bridges components are still being investigated; as in the work of Chen *et al.* (2020), on the WIV of suspender cables.

The design of oscillating/deformable structures that are conceived to increase the efficiency of some engenireeng systems is another example of recent research. Aurégan *et al.* (2024) have for instance shown that an underwater propeller with an appropriate flexible material can maintain a high efficiency in off-design conditions. Another notable recent development is the morphing aircraft with the idea of compliant wings adapting their

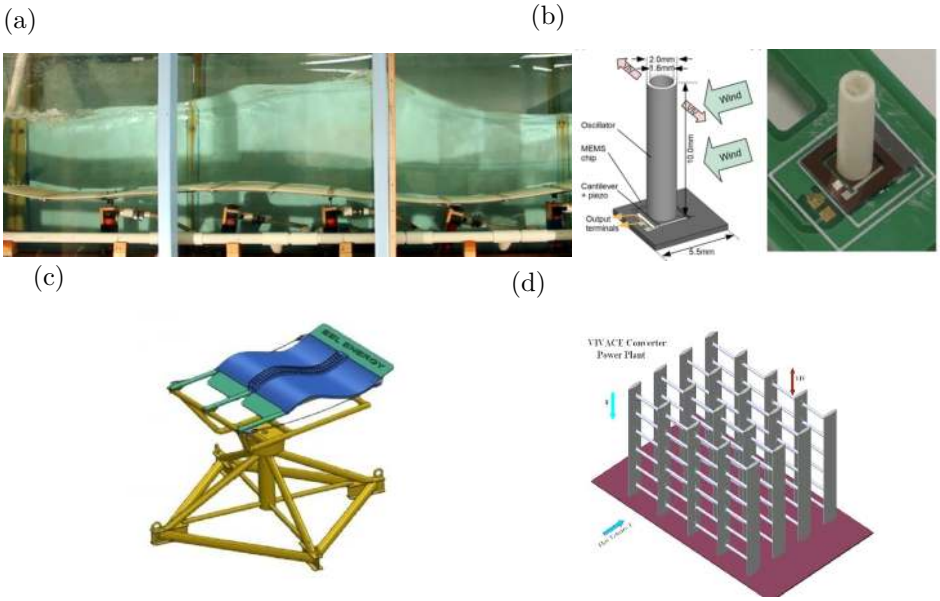

Figure 1.2: (a) Wave Carpet concept from the TAFLab in Berkeley University, reproduced from Lehmann *et al.* (2013). (b) MEMS device based on vortex-induced vibrations, reproduced from Lee *et al.* (2019). (c) Energy harvesting concept from Eel Energy, reproduced from Träsch (2019). (d) VIVACE energy harvester, reproduced from Bernitsas *et al.* (2008).

shape depending on in-flight conditions (Barbarino *et al.*, 2011).

Another major recent interest is to optimise the motion of rigid bodies or the deformation of flexible structures in order to harvest energy from the wind, waves or marine currents (see the review by Bernitsas, 2016). Some striking examples include the Wave Carpet project developed by Alam (2012) that aims to extract energy from waves using a deformable carpet (see figure 1.2(a)). Eel Energy proposed a similar concept to extract energy from marin currents (see figure 1.2(c)) The VIVACE concept from Bernitsas *et al.* (2008) proposes to convert kinetic energy from marine currents to electricity using vortex-induced vibrations of multiple oscillating cylinders (see figure 1.2(d)). Energy harvesting strategies also find applications in microfluidics: for instance, Lee *et al.* (2019) proposed a MEMS energy harvester based on the oscillation of a cylinder mounted on a piezoelectric chip (see figure 1.2(b)). In this context, at low Reynolds numbers, they found that the efficiency of the device was greater

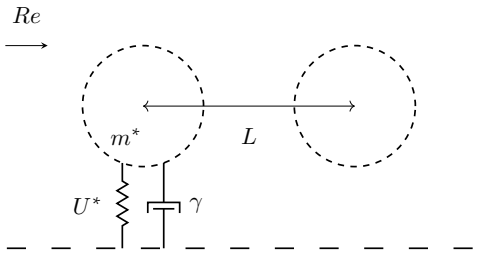

Figure 1.3: Spring mounted cylinders with reduced mass, reduced velocity and damping parameter: m^*, U^* and γ. For systems composed of multiple bodies, the distance between bodies L is defined as the distance centre to centre. See section 2.1 for a more detailed schematic and explenation of the problem's parameters.

when placed in a dense field of oscillating cylinders.

1.2 Vortex-induced vibrations of a single spring-mounted body

For a simple spring-mounted system (figure 1.3), the dynamics are governed by three non-dimensional parameters: the reduced velocity U^*, the reduced mass m^*, and the damping coefficient γ, which respectively compare flow speed to natural frequency, structural to fluid masses, and energy dissipation. The reader is directed to section 2.1 for a detailed definition of these parameters.

One of the first studies on vortex-induced vibrations of a single oscillating cylinder was that of Bishop & Hassan (1964). Since then, an extensive amount of publications have investigated this phenomenon and the reader can refer to the reviews of Bearman (1984); Parkinson (1989); Williamson *et al.* (2004); Sarpkaya (2004); Williamson & Govardhan (2008)

Heavy focus was put on the lock-in phenomenon (Williamson *et al.*, 2004) (figure 1.4). It is defined as a synchronisation between the frequency associated with transverse oscillations of the rigid body and the one of the vortex shedding in the wake of the cylinder. Outside of the lock-in regime, however, the frequency tends to the vortex shedding frequency of a fixed cylinder. Navrose

& Mittal (2016) found that the lock-in phenomenon induces high amplitude vibrations of the cylinder. It has also been shown that a decrease in the mass ratio leads to a wider synchronisation regime.

Note that most studies with a single cylinder considered a single degree of freedom (1DOF) corresponding to transverse motion. According to Zhou *et al.* (1999); Williamson *et al.* (2004), in-line motion, if structurally allowed (two-degree of freedom i.e. 2DOF), does not change much the dynamics, and mostly turns the transverse oscillation into a figure-eight trajectory where the stream-wise motion is induced by a nonlinear effect. On the other hand, pure in-line oscillations seem not to have been observed for a single cylinder. Such motion would be linked to symmetric vortex shedding which is likely not observed.

Experiments as well as numerical simulations were used early on to study the oscillations of a spring-mounted body, while global linear stability analysis (LSA) was first used by Cossu & Morino (2000) (1DOF). Two unstable eigenmodes were found: the "nearly structural" and "von Kármán" modes. The first mode's frequency tends in the small reduced mass limit to the one of the spring mounted system while the latter's is that of the purely fluid system. At low Reynolds number, the threshold for instability was found to be linked to the "nearly structural" mode, while the von Kármán mode was stable.Mittal & Singh (2005) then employed LSA for the 2DOF spring-mounted cylinder and found self-excited oscillations above Re = 21.7 for a spring-mounted cylinder of reduced mass m^* = 4.73.

Other authors have proposed theoretical models. De Langre (2006) proposed a linear wake oscillator model and showed that coupled-mode flutter is responsible for large oscillations in the lock-in regime. The model captures relatively well the frequency evolution and amplification of the body's motion in the regime, even if it does not provide amplitudes of motion. The shift of the lock-in regime with increasing reduced mass is also well predicted by the model.

Confinement of a body can drastically influence its motion. A new confined-induced vibration instability (CIV) was identified by Semin *et al.* (2012) for a confined cylinder at Re = 20. That threshold is well below that of classical vortex-induced vibrations. A simple Van der Pol model was found to describe the onset of the CIV instability.

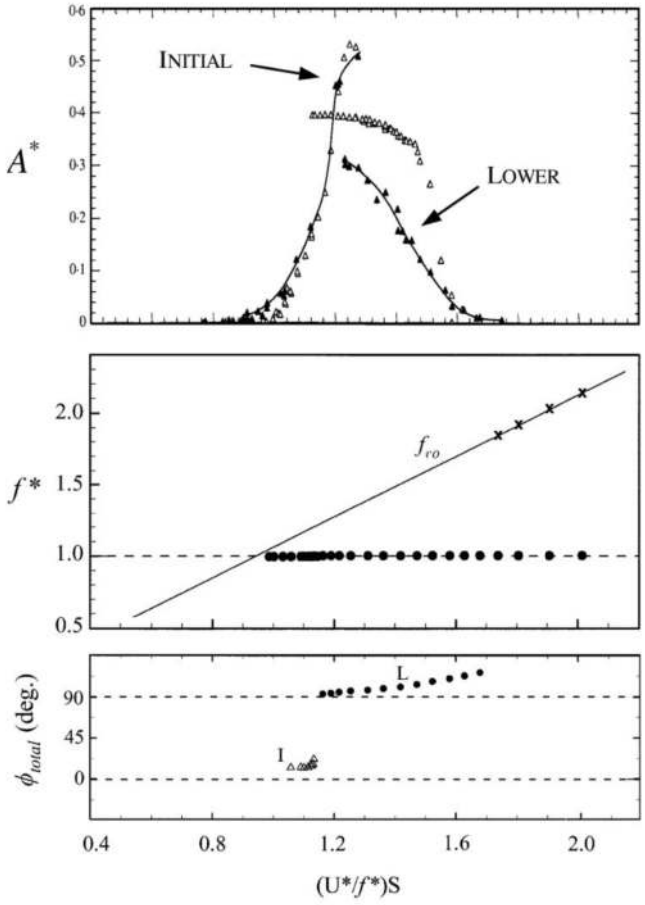

Figure 1.4: Typical response of a spring-mounted cylinder ($m^* \approx 250$ and $Re \approx 10^4$), reproduced from Williamson *et al.* (2004): from top to bottom, amplitudes of motion, frequency and phase of the transverse force. An "initial" and "lower" branch are observed in the amplitude response, with a hysteretic transition between them. Concerning the frequency, the lock-in regime is characterised by a synchronisation of the frequencies with the natural frequency. Finally, it was also observed that the jump in the amplitude corresponds to a jump in the phase of the forces relative to the motion.

Recently, some studies focused on shapes different from the canonical cylinder. Notably, vortex shedding suppression can occur naturally as was shown by Hanke *et al.* (2010) who found that the unique geometry of seal vibrissae could reduce significantly VIV. The cactus-like cylinder was found to vibrate at reduced amplitudes but with an onset of VIV at lower reduced velocities (Wu *et al.*, 2024). In the turbulent regime, porous coating on a cylinder was found to reduce VIV by Chen & Wu (2024). Focus was also given to the VIV of square cylidners (Li *et al.*, 2019).

Vortex-induced vibrations of a single canonical cylinder are still of recent interest. Notable recent results include the characterisation of vortex-induced vibrations from imposed rotation of the body (Bourguet, 2025).

1.3 Vortex-induced vibrations of multiple bodies

Research on the vortex-induced vibrations of multiple bodies first emerged in aeronautical engineering, where it was associated with the oscillations of twin wing-support struts (Biermann & Herrnstein Jr, 1934). It subsequently spread to hydronautical applications and later to civil engineering with problems such as wind-excited in-line chimneys (Vickery, 1981) and marine structures like offshore platforms.

As the multi-body systems are inherently more complex, authors first focused on multiple fixed bodies.

1.3.1 Two fixed bodies

Price (1976) experimentally investigated the evolution of force coefficients of two bluff bodies with respect to free-stream turbulence and surface roughness for $Re = [2.98 \times 10^4, 7.14 \times 10^4]$. Zdravkovich & Pridden (1977) experimentally observed, when varying the spacing, discontinuous changes in the flow patterns for the tandem, side-by-side and staggered arrangements at $Re = [2.5 \times 10^4 - 1.2 \times 10^5]$.

Many experimental studies then followed, a notable one being that of Zdravkovich (1987), that produced a very thorough classification of the flow patterns for the tandem, side-by-side and staggered arrangements at low Reynolds numbers (see figure 1.5). First, concerning the tandem arrangement, they found three notable behaviours depending on the spacing.

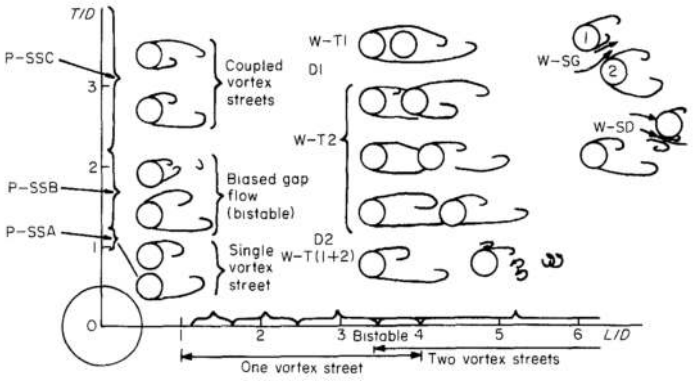

Figure 1.5: Classification of the flow patterns for tandem, side-by-side and staggered configurations, reproduced from Zdravkovich (1987).

For $1 < L < 1.8$, the two cylinders behave as a single bluff body and the boundary layer of the first body does not reattach to the second one, therefore producing the vortex street. For $1.8 < L < 3.8$, the shear layer of the front body reattaches to the rear one and a vortex street is formed in the wake of the rear body. Then, increasing further the spacing to $L > 3.8$, a vortex street is formed in the wake of both bodies. Secondly, when the bodies are placed in side-by-side arrangement, three different regimes appear. For $1 < T/D < 1.2$, the bodies shed vortices as a single bluff body. For $1.2 < T/D < 2.2$, two wakes are formed behind the bodies and a bistable jet-like flow goes through the gap. For $2.2 < T/D < 5$, both wakes are equal in size and are mirrored along the gap axis.

Experimental studies continued, notably with the extensive investigation on the staggered configuration by Sumner *et al.* (2000). Nine distinct flow patterns were identified for staggered cylinders in the regime $Re = 850 - 1900$, controlled by the gap ratio and inclination angle. The flow exhibits mechanisms such as shear-layer reattachment, induced separation, vortex pairing, synchronisation, and vortex impingement, with small changes in inclination sometimes producing different regimes. Vortex shedding from the upstream cylinder occurs in most configurations and interacts strongly with the gap flow, even for small spacings. This shedding typically occurs at a higher frequency than the downstream wake. The commonly observed dual shedding frequencies originate from the individual shear layers. They

found that the outer shear layer of the downstream cylinder produces low-frequency Kármán vortices, while the inner shear layer synchronises with the higher-frequency shedding from the upstream cylinder. Flow-pattern boundaries were proposed to predict the flow regime and help interpret force measurements and vibration susceptibility. The extensive review by Sumner (2010) sums up the experimental studies that took place since that of Price (1976).

The first numerical study on the tandem and side-by-side arrangements was that of Meneghini *et al.* (2001). They performed direct numerical simulations for $Re = 200$, $1.5 < L < 4$ for the tandem configuration and $1.5 < T/D < 4$ for the side-by-side configuration. First, for the tandem configuration, they found similar results to the experimental ones. Secondly, for the side-by-side arrangement, they confirmed experimental results and uncovered a "flopping" mechanism where the wake is alternately deflected towards one of the bodies. A series of numerical studies then followed and the reader is referred to the review of Zhou & Alam (2016).

1.3.2 Multiple fixed bodies

Some early experimental work on the heat exchange around four in-line cylinders was motivated by search for high performance heat exchangers (Aiba & Yamazaki (1976)). Later, Igarashi (1986) classified the flow patterns of that configuration into five distinct categories based on the behavior of the shear layers, which vary according to the spacing and Reynolds numbers. A critical reattachment Reynolds number was also identified as well as the emergence of a hysteresis.

Hetz *et al.* (1991) extended previous findings to five in-line cylinders. They found that multiple shedding mechanisms may coexist notably gap shedding between cylinder gaps and bluff-body shedding behind the last cylinder. Gap shedding is found to dominate for all tested spacings in flows with subcritical Reynolds number. The shedding patterns and their interaction are characterised (figure 1.6(a)) and are linked to known flow regimes.

Some studies focused on four cylinders positioned in a square configuration. Sayers (1988) investigated the lift and drag coefficients on single cylinders within such a group subjected to cross-flow. Significant fluctuations with orientation and spacing were found with the force coefficients repeating every

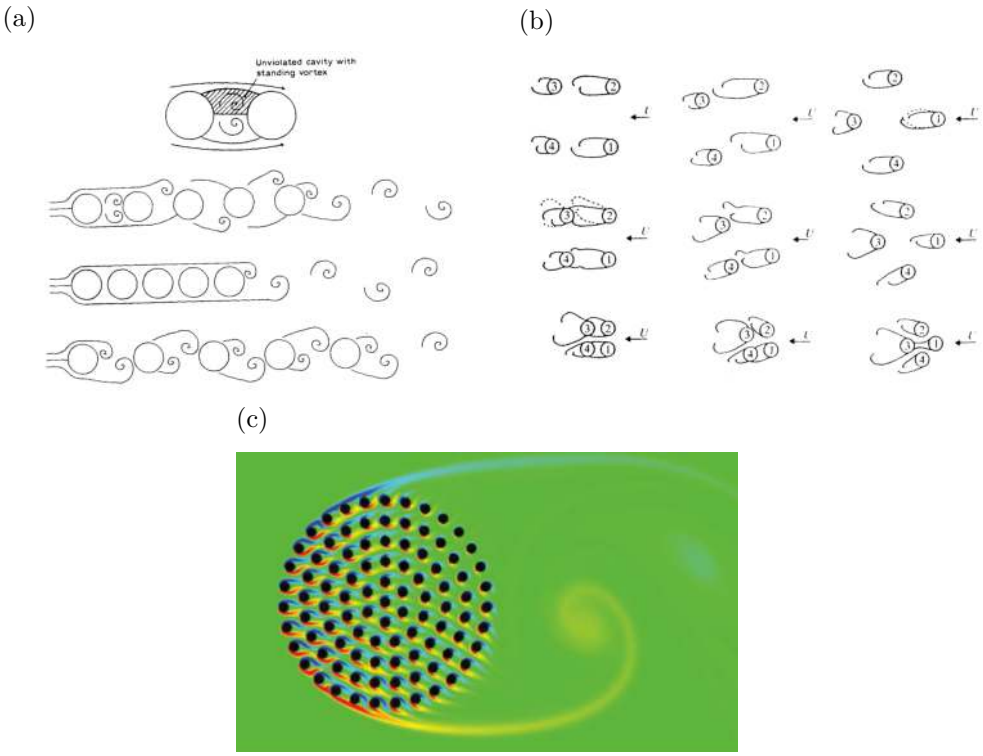

Figure 1.6: (a) Classification of the flow patterns for $N = 5$ in-line cylinders, reproduced from Hetz *et al.* (1991). (b) Classification of the flow patterns for $N = 4$ cylinders in square patterns, reproduced from Lam & Lo (1992). (c) Flow visualisation for $N = 95$ cylinders, reproduced from Nicolle & Eames (2011).

90°. Lam & Lo (1992) extended that work for a wider range of parameters and for Re = 2100. They classified the flow patterns (see figure 1.6(b)): at large spacing, cylinders behave like isolated ones but reducing spacing causes complex wake interactions, including suppression of vortex shedding and bistable wake states. Later, Han *et al.* (2013) investigated that configuration numerically for Re = 200 and showed different flow patterns depending on the spacing.

Igarashi (1993) investigated the flow around three in-line cylinders of different diameters to reproduce an H-II rocket geometry. Alam *et al.* (2018) later numerically investigated the three-body in-line configuration for circular cylinders of the same diameter. They found that the flow at Re = 200 was more sensitive to variations in the distance between the first and second cylinder rather than the second and third. In fact, the presence of a third body has little impact on the dynamics for long spacings, as was also confirmed by Hosseini *et al.* (2021). On the other hand, Hosseini *et al.* (2021) identified a region of shorter spacings where the placement of a third body suppresses the vortex shedding in the gap between the two upstream bodies. For the in-line configuration, Harimi & Saghafian (2012) showed for different spacings that the variation of heat transfer from the third body is not correlated to the variation in the rest of the system.

Liang *et al.* (2009) numerically investigated the effect of spacing on six in-line cylinders for Re = 100. They found that increasing the spacing renders the flow more asymetric. The force coefficients on the last three bodies are maximised for some intermediate spacings where the vortex shedding is synchronised with the spacing.

Zhao *et al.* (2015) numerically investigated the flow around 36 cylinders in square configuration for various spacings at Re = 100 while Nicolle & Eames (2011) investigated the flow around a circular array of 1 to 133 cylinders at Re = 2100. For low fractions, Nicolle & Eames (2011) found that bodies behave like isolated ones. For moderate fractions, a stabilised wake forms behind the array while for high fractions, the array starts behaving like solid body and vortex street is shed in the wake (figure 1.6(c)). On the other hand, Hosseini *et al.* (2020) investigated the flow in a 2 to 100 in-line cylinders array at Re = 200 for various spacings. For small arrays, they found that the flow in the gap could be steady, fluctuating or vortex shedding for short, medium and large spacings respectively. In larger arrays however, these regimes occur

in geometric series. Building on this, He *et al.* (2026) showed that three-dimensional effects cannot be neglected and significantly alter the flow past a line of cylinders at $Re \gtrsim 175$. This leads to marked differences with 2D simulations.

Another approach to investigate the flow around arrays of in-line bodies is to assume spatial periodicity as was done by Kevlahan (2007) with Floquet theory.

1.3.3 Two spring-mounted bodies

A number of configurations involving multiple freely oscillating bodies have been explored. Authors have first focused on wake-induced vibrations (WIV). King & Johns (1976) first explored WIV of flexible cylinders (2DOF) in tandem traversing a free-surface, either rigidly connected or not, for spacings of $L = [1.25–7]$, where D is the diameter of the cylinders and L is the non-dimensional distance between the centres, at Reynolds numbers $Re = [10^3 - 2 \times 10^4]$ They observed that the vortex shedding "from upstream cylinder generally reinforces that from the downstream cylinder". Also, both transverse oscillations and in-line oscillations are observed, but the latter where only reported at much larger values of the Reynolds number. Bokaian & Geoola (1984) focused on the transverse WIV (1DOF) of the rear body by fixing the front one. In the interval $Re = [2900, 5900]$, they found that the vortex shedding behind the front cylinder is suppressed for spacings of $L \leq 2$. Tatsuno *et al.* (1985) experimentally investigated the tandem arrangement with the front body fixed and the rear body oscillating (1DOF), at low Reynolds numbers. They found a synchronisation region of the rear body's motion with the vortex shedding, which shrinks when the cylinders are brought further apart from each other.

Later studies also explored in detail the WIV of a rear oscillating body in the 2DOF (Brika & Laneville, 1999) and 1DOF configurations (Assi *et al.*, 2006, 2010). Fontaine *et al.* (2006) showed that riser pipes at small spacing may become unstable due to VIV and WIV and proposed a model for in-line vibrations based on correlation formulas. Assi *et al.* (2010) found that for large spacing between bodies, the amplitude of the rear body is decreased and resembles a VIV amplitude. Later, Assi *et al.* (2013) (1DOF) developed the concept of wake stiffness in the galloping of cylinders placed in tandem. The steady lift across the wake is defined as a restoring force towards the center line, acting as a fluid dynamic spring. The Strouhal number associated with

the wake stiffness was found to be constant with the Reynolds number.

Mittal & Kumar (2001) numerically studied the tandem and staggered configurations with 2DOF for low Reynolds number (Re = 100) in the wake interference regime (L = 5.5). For this large spacing the front body behaves like an isolated cylinder with trajectories resembling an eight shape. Soft lock-in was observed and the vortex-shedding frequency of the bodies is detuned from the natural frequency. The rear body displays trajectories in a shape of an eight or a tilted ovoid whether it is placed in tandem or in staggered configuration. Papaioannou *et al.* (2008) used an Arbitrary Lagrangian-Eulerian (ALE) method to further explore the effect of spacing on the 2DOF tandem. For Re = 160 and reduced mass m^* = 10, they explored spacings (L = $[2.5, 3.5, 5.0]$) corresponding to different flow regimes in the fixed tandem case (Zdravkovich, 1987). Small values of the spacing lead to stronger oscillations of the upstream cylinder over a wider reduced velocity range and shifts the response curves to higher reduced velocities.

Borazjani & Sotiropoulos (2009) directly simulated a tandem of cylinders with 1DOF for a low reduced mass, L = 1.5 and Re = 200. For low values of the reduced velocity, they found that the oscillation amplitudes are small and therefore outside of the lock-in region. The front cylinder exhibits larger oscillation amplitudes than the rear one (see figure 1.7). The effect of an increase of the reduced velocity is to bring the cylinders' oscillations out of phase, thus increasing their amplitudes of motion. At a critical reduced velocity, the cylinders continue to oscillate out of phase but the rear cylinder's amplitude becomes greater than that of the front one. In particular, the authors found a wider lock-in region than for an isolated cylinder. Besides, a structure that would be outside of the lock-in region can be brought into it by placing it in a tandem with a similar structure.

Kim *et al.* (2009*b*) experimentally studied the VIV of the tandem configuration with 1DOF transverse to the fluid flow for several spacings (L = 1.1 – 4.2) at Re = 4365 – 74200. Five distinct regimes were identified. Regime I ($1.1 < L < 1.2$) features negligible vibrations due to minimal fluctuating lift forces, while Regime II ($1.2 < L < 1.6$) exhibits strong vibrations, particularly in the upstream cylinder, for higher reduced velocities. Regime III ($1.6 < L < 3.0$) shows significant vibrations of both bodies, with the upstream cylinder's response being influenced by the downstream cylinder. In Regime IV ($3.0 < L < 3.7$), vibrations are again

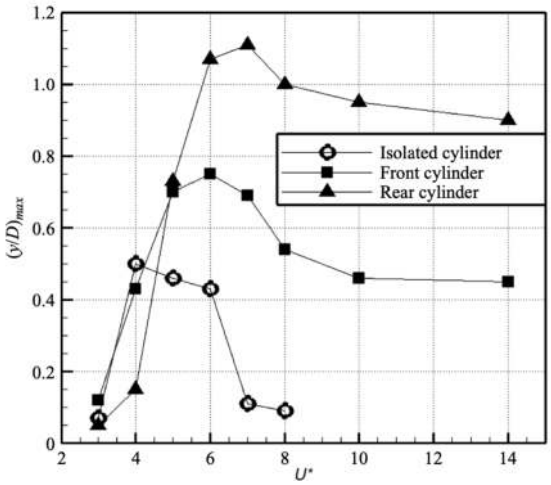

Figure 1.7: Typical amplitude response for the tandem configuration, reproduced from Borazjani & Sotiropoulos (2009).

minimal; the downstream cylinder stabilises the wake. Finally, Regime V ($L > 3.7$) displays higher vibrations in the downstream cylinder, attributed to periodic Kármán vortex shedding. In a subsequent study, Kim *et al.* (2009*a*) used tripping wire to suppress vortex-induced vibrations. They found that placing the wires at an optimal position effectively suppressed vibrations in flow regimes I–IV by altering the shear layer behaviour and preventing vortex formation.

Prasanth & Mittal (2009*b*,*a*) numerically examined the free vibrations of two cylinders in the staggered and tandem configurations with 2DOF at $Re = 100$ for $m^* = 10$, $L = 5.5$ and compared the dynamic responses to that of a single cylinder. In the staggered configuration, the upstream cylinder behaves similarly to a single cylinder but with slightly higher oscillation amplitudes, while the downstream cylinder exhibits significantly larger transverse oscillations. Lock-in occurs over a range wider than for a single cylinder, with shared vortex shedding frequencies. The downstream cylinder in the staggered case displays both eight-shape and orbital motions, influenced by complex vortex interactions and asymmetrical flow patterns. For the tandem configuration, the upstream cylinder shows early lock-in and significant influence from the downstream cylinder, despite having a qualitatively similar transverse response to an isolated one. The downstream

cylinder experiences much larger oscillations that are twice that of a single cylinder in the laminar regime. Its behaviour mimics high Reynolds number responses, including the presence of an upper branch in the vibration response. Both cylinders undergo synchronisation, with frequency and phase shifts tied to vortex shedding and lift forces. Phase differences and hysteresis effects are observed, and the flow regime is divided into different regions based on flow-structure interactions.

Mysa *et al.* (2016) explored the WIV of a cylinder (1DOF) in tandem with a fixed front one, at Re = 200 and L = 5. Due to the wake interaction, the rear body's oscillation frequency is locked to the upstream shedding and varies linearly with reduced velocity. Phase differences between the forces and motion play a major role in the amplitude response. The interaction of the wake of the first body with the second one changes the position of the stagnation points and the pressure distribution. Eventually, this leads to stronger vibrations in the post-lock-in regime. Bao *et al.* (2011) also considered a tandem where the front body was fixed and focused on the influence of angle of attack of the cross-flow on the array.

Griffith *et al.* (2017) investigated the dynamic response of staggered cylinders at Re = 200 with 1DOF, for a fixed stream-wise spacing (L = 1.5). They found that gap flow, which reverses direction as the cylinders oscillate, plays a critical role. A regime map was developed, categorising major vortex shedding modes and temporal behaviours. Unlike a single cylinder, matched natural and shedding frequencies do not produce synchronised oscillations; instead, quasi-periodic and chaotic responses emerge. For rigid cylinders, three base modes were observed: no gap flow, gap pair dominated, and wake pair dominated—shifting with cross-stream offset. Near the gap/wake pair transition, more complex flow states appear. When cylinders are free to oscillate, low reduced velocities yield minimal motion and rear-cylinder vortex shedding. At intermediate velocities, out-of-phase oscillations enlarge the gap and produce an irregular vortex street. At higher velocities, the rear cylinder chases the front, with joint vortex shedding. As the spacing increases, vortex pairs dominate and the system approaches single-cylinder behaviour.

Huera-Huarte & Gharib (2011) conducted an experimental study of VIV and WIV of a tandem of flexible cylinders (2DOF) in the wake interference regime. They found that both flexible cylinders in a tandem arrangement exhibit classical VIV near lock-in reduced velocities, regardless of the gap

distance. At higher reduced velocities, their dynamic responses diverge depending on the spacing between the bodies. The upstream cylinder shows stronger VIV for smaller gaps, while the downstream cylinder may experience WIV at larger gaps, due to the presence of vortex shedding in the gap region.

Zhang *et al.* (2024*a*) investigated fluid-induced vibrations (1DOF) of two square cylinders in tandem through simulations and reduced-order modelling. Multiple vibration branches, such as VIV, biased oscillation, and galloping, are identified depending on reduced velocity and spacing ratio and their link to wake and structural modes is analysed.

Yao & Jaiman (2019) used linear stability analysis (LSA) for the exploration of the WIV of circular and square cylinders in tandem arrangement (1DOF). They focused on low Reynolds number and reduced mass, and fixed the front body. Increasing the spacing between the bodies, they found a decrease in the critical Reynolds number as well as the critical reduced velocity for the onset of WIV. Tirri *et al.* (2023) and Zhang *et al.* (2024*b*) also conducted LSA at low Reynolds number for the tandem configuration with 1DOF over a very limited range of structural parameters. They both found two leading unstable eigenmodes, one being associated with the classical vortex shedding behaviour in the wake of a tandem of fixed bodies and the other being of structural nature since they don't have a counterpart in the case of fixed bodies.

Note that, in most of the cited bibliography, configurations in which the cylinder are allowed to move in two directions (2DOF) essentially lead to the same dynamics as those in which the cylinder are only allowed to vibrate transversely (1DOF), driven by the transverse force due to antisymmetric vortex shedding. Pure in-line oscillation, which would be linked to symmetric vortex shedding, has not been reported, with the notable exception of King & Johns (1976). However, such behaviour was only observed for $Re > 10^3$, away from the range considered here. Likewise, no known study seems to have reported coupling with the third degree of freedom corresponding to rotational motion of the cylinder. Such motion would be linked to a torque, which is not expected to be significant for a cylinder, as it would be exerted by viscous stress only and not pressure, unlike for more elongated bodies where this kind of motion, known as flutter, is an important subject of research (Chai *et al.*, 2021).

1.3.4 Multiple spring-mounted bodies

Authors also explored configurations with more bodies and outlined the complexity of such systems. Paidoussis (1981, 1983) reviewed early experimental work on the vibrations of arrays of cylinders. Later, Pettigrew & Taylor (2003) reviewed tube vibrations in heat exchangers and proposed guidelines to prevent failure.

Xu *et al.* (2009) numerically investigated vortex-induced vibrations of four cylinders in a square configuration (2DOF) at low Reynolds number. They showed that the upstream cylinders experienced stronger forces and larger transverse oscillations while the downstream cylinders are more influenced by wake interactions. As the spacing increases, wake patterns become more complex with in-phase and anti-phase vortex shedding. Zhao & Cheng (2012) explored a similar configuration with a spacing ratio of $L = 3$ and found that the lock-in range in terms of reduced velocity is broadened for that arrangement. Ghasemi & Kevlahan (2017) focused on the role of the Reynolds number in the vibrations for cylinders in square arrangement with $L = 1.5$, rotated or not. They showed that the effect of the Reynolds number depends highly on the configuration. When the array is in-line with the flow direction, the critical reduced velocity for VIV is very sensitive to the Reynolds number. On the other hand, for rotated arrays, the Reynolds number has mainly a destabilising effect.

Behara *et al.* (2023) numerically investigated the VIV (1DOF) of $N = 3$ in-line square cylinders at a low mass ratio ($m^* = 2$) and Reynolds number ($Re = 150$). For an isolated cylinder at this reduced mass, no galloping instability is observed. For $N = 3$, galloping emerges after the vortex-induced vibration (VIV) regime. The instability is first observed on the first body and is attributed to wake interference induced by the presence of the downstream bodies. The spacing between cylinders strongly influences the onset of galloping. For smaller gap ratios, wake interference occurs at lower reduced velocities. Galloping begins immediately after the VIV regime as U^* increases. For larger gaps, the transition is more gradual and is characterised by a continuous decrease in the vibration frequency from the higher-frequency VIV frequency to the lower-frequency of the galloping regime. The VIV response exhibits oscillation amplitudes, associated with the presence of a strong recirculation region that is convected downstream. In contrast, during galloping, this recirculation region is absent and the oscillation amplitude

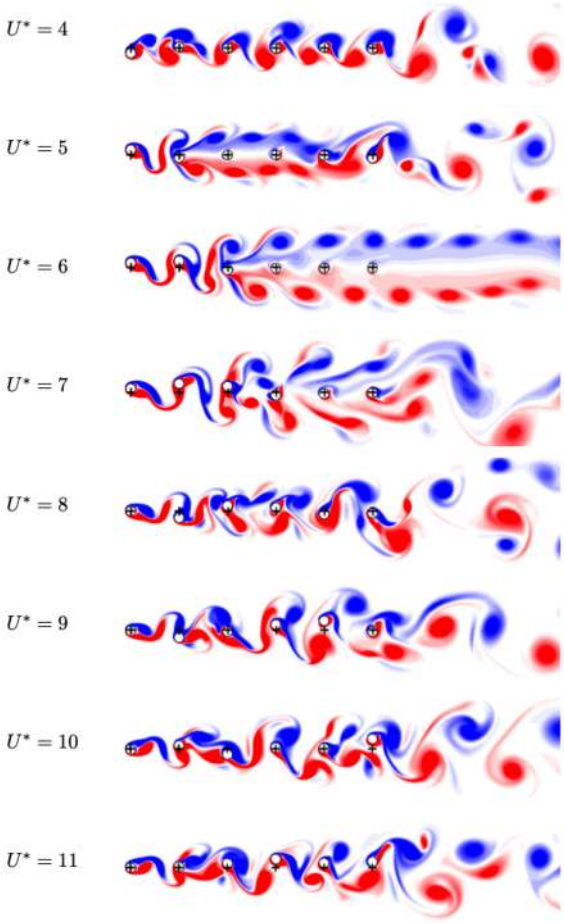

Figure 1.8: Flow past $N = 6$ in-line spring-mounted cylinders, reproduced from Hosseini (2021): $Re = 200$, $L = 5$ and $m^* = 2.546$

increases monotonically with increasing U^*. Overall, wake interference reduces the critical mass ratio required for the onset of galloping. For a spacing ratio $L = 3$, galloping is reported for $U^* > 25$, whereas for $L = 5$ the instability appears only for $U^* > 32$.

In a later study, Behara *et al.* (2024) explored the effect of the angle of inclination ($\alpha = 0°$, $\alpha = 22.5°$ and $\alpha = 45°$) on the same configuration. The inclination of the cylinders significantly modified the wake interactions and led to multiple response regimes, particularly for the downstream bodies, which experienced more complex dynamics due to the influence of vortices shed by the upstream cylinder. At non-zero inclination angles, the upstream cylinder exhibited three distinct response regimes, while the downstream cylinders displayed four, including a lock-in regime characterised by rapid amplitude growth. The vortex shedding patterns also depended on the inclination angle, highlighting the strong coupling between wake dynamics and structural response.

The tandem of three in-line cylinders oscillating transversely (1DOF) for $Re = 100$, $L = [1.2 - 5.0]$ and $m^* = 2$ was investigated by Chen *et al.* (2018). For small spacings, a wake-induced galloping regime appears where vibration amplitudes increase monotonically with reduced velocity. synchronised between the vortex shedding and the bodies motion is observed. For larger spacing, galloping disappears. The upstream cylinder behaves similarly to an isolated one and the downstream cylinders still experience large oscillations due to strong wake interaction. Zhu *et al.* (2024) did a similar study for $Re = 150$ and $L = [2 - 6]$.

Hosseini *et al.* (2022) did a first exploration of more than three in-line bodies and explored the VIV of $N = 2$ to $N = 6$ spring-mounted cylinders for $Re = 200$, $m^* = 2.546$ and $L = [1.5, 3, 5]$ (figure 1.8).

1.4 Vortex-induced vibrations near a deformable free-surface

As previously mentioned, there is a growing interest in the application of fluid-structure interactions to the energy harvesting of waves or marine currents. In that context, many systems are thought to operate close to a free-surface. The understanding of the effect of the latter motivated previous

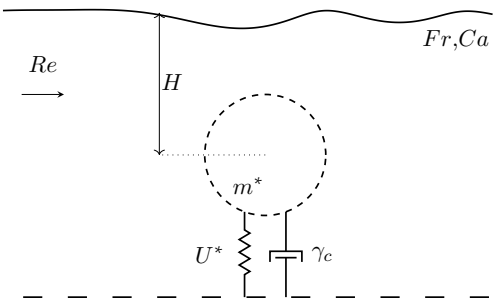

Figure 1.9: Spring mounted cylinder beneath a free-surface. See section 3.1 for a more detailed schematic and explenation of the problem's parameters.

studies in our group (Achour, 2022).

In addition to the Reynolds number, the dynamics of the flow past a cylinder close to a deformable free-surface (figure 1.9) are characterised using several dimensionless numbers. The Froude number $Fr = \frac{U_\infty}{\sqrt{gD}}$ compares inertial forces to gravitational forces, g being the gravity. Surface tension effects are described through several related parameters. The Weber number $We = \frac{\rho U_\infty^2 D}{\gamma}$ compares inertial forces to capillary forces (γ being here the surface tension), while the Bond number $Bo = \frac{\rho g D^2}{\gamma}$ compares gravitational forces to capillary forces. The Capillary number $Ca = \frac{\mu U_\infty}{\gamma}$ measures the relative importance of viscous stresses with respect to surface tension. These dimensionless numbers are linked through the relations $Bo = \frac{We}{Fr^2}$ and $We = ReCa$. In addition to these parameters, the relative immersion of the cylinder H (centre of the body to the surface) plays a key role in the problem.

1.4.1 Fixed cylinder near a free-surface

The behaviour of the wake of a confined cylinder is extensively different than that of a cylinder in an unbounded domain. The experimental work of Bearman & Zdravkovich (1978) and later of Lei *et al.* (1999) showed that, for a cylinder placed less than $0.2 - 0.3D$ above a plane boundary, the vortex shedding in the wake was suppressed.

Concerning a cylinder confined beneath a deformable free-surface distinct wake patterns were observed by Sheridan *et al.* (1997). For the Reynolds

numbers investigated ($5990 < Re < 9120$) and depending on the Froude number and submersion depth, a jet-like flow is formed between the free-surface and the cylinder that can either attach to the cylinder or to the free-surface (see figure 1.10(a)). This behaviour was confirmed at lower Reynolds numbers by subsequent numerical studies (Zhao *et al.*, 2022*a*; Patel *et al.*, 2025). For some selected parameters, the deformation of the free-surface is metastable and the flow can switch between two states in a hysteretic manner (Sheridan *et al.*, 1995).

Reichl *et al.* (2005) used volume-of-fluid simulations to investigate the flow around a cylinder close to a free-surface at $Re = 180$ and for gap ratios $H = [0.6 - 5.5]$. For low Froude numbers they found that the flow behaved similarly to a configuration with no-slip wall. For moderate Froude numbers $Fr = [0.3 - 0.4]$, transitions lead to a sharp interface or even wave breaking. They also found that the local Froude number around the gap could be greater than unity. Also, surface vorticity was shown to affect the wake and potentially suppress the absolute instability. For large Froude numbers, the authors also observed the metastable states experimentally seen by Sheridan *et al.* (1995), despite a consequent Reynolds difference. They proposed that the switching observed was controlled by a feedback loop. Finally, the authors found that vortex shedding was suppressed for very small gap ratios.

Zhao *et al.* (2022*a*) numerically investigated (URANS) the 2D flow past a circular cylinder positioned beneath a free-surface for $Re = 4.96 \times 10^4$. They scanned the parameter space varying the Froude number ($Fr = [0.2 - 0.8]$) and gap ratio ($H = [0.15 - 2.5]$), revealing distinct flow regimes including jet flow, one-sided vortex shedding, free-surface modulated Kármán vortex shedding, and classical Kármán vortex shedding. The interactions of three shear layers between the cylinder and free-surface are shown to control wake transitions and surface wave patterns. The authors noted the presence of a recirculation zone near the free-surface due to the blockage of the body. Additionally, the presence of the free-surface causes a consistent downward thrusts that intensifies as the cylinder nears the surface.

Zhao *et al.* (2024) used 3D direct numerical simulations to investigate the dynamics of two cylinders placed in tandem configuration below a free-surface at $Re = 180$. They explored cylinder spacings of $L = [1.5 - 4]$, submersion depths of $H = [0.7 - 2.5]$ and Froude numbers in the range $Fr = [0.2 - 0.8]$. For small submersion depths, they recover the jet like feature in the wake of

the upstream cylinder. As the spacing between the two bodies increases, this jet-like flow can either impinge the downstream body, flow between the gap or start oscillating in the vicinity of the free-surface. A wide variety of wake patterns was observed. Notably, at intermediate spacing between the bodies, the wake resembles that of the staggered configuration due to the jet-like flow in the gap. The authors showed that the three-dimensionality of the wake increased with the Froude number. As observed in other studies high Froude number can increase the effect of the free-surface for bigger immersion depths.

Patel *et al.* (2025), on the other hand, performed direct numerical simulations at low Reynolds number (Re = 150). The Weber number was fixed to 1000 and they explored the parameters, Bo = [100 – 5000] and H = [1 – 2.5]. Three distinct regimes were found (see figure 1.10(b)). First, interfacial waves occur for the lower range of Bond number investigated and their perturbation grows due to the suction effect from the alternating vortex shedding. If the submersion is reduced, the waves break and gas bubble are entrained (see figure 1.10(c)). Secondly, for intermediate values of Bond, and for all submersion depth explored, gas bubbles are being entrained. Note that in this regime the authors also observed vortex shedding suppression depending on the choice of parameters. Finally, for high value of the immersion depth and high values of the Bond number, reduced deformation of the free-surface is observed. An increase of the lift force when decreasing H was observed.

Sun *et al.* (2025) did direct simulations for We = 1000, Fr = 1 and H = 1 and varied the Reynlods number in the range Re = 400 – 2000. At low Reynolds numbers ($Re \approx 400$), a gap jet stabilises the wake and suppresses vortex shedding. Beyond $Re \approx 500$ the system becomes unsteady and periodic shedding reappears with increasing frequency as the Reynolds increases. For higher values of Reynolds, surface rupture (wake breakup) generates entrained bubbles.

Most studies used direct numerical simulations or experiments. The only study reporting the use of linear stability analysis for such problems was that of González-Gutierrez *et al.* (2019). They explored relatively high Froude numbers (Fr = [0.5 – 4]) for the immersion depths $H = [1.05, 1.5, 2.5]$. In order to obtain a stationary solution at high Froude numbers, the authors had to use a damping frequency method. Instabilities linked to the deformation of the free-surface were found.

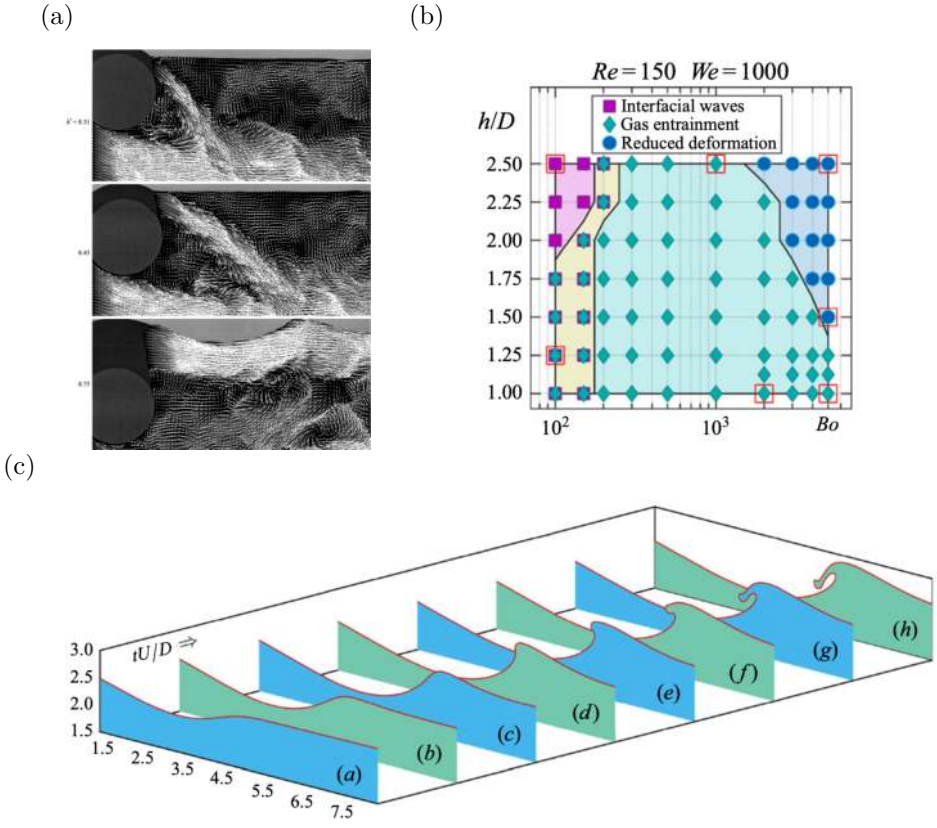

Figure 1.10: (a) Instantaneous velocity fields for different immersion depths, reproduced from Sheridan *et al.* (1997). (b) Regime map and (c) gas entrainement mechanism, reproduced from Patel *et al.* (2025).

1.4.2 Spring-mounted cylinder near a free-surface

A few studies focused on the vortex-induced vibrations of a cylinder close to a free-surface. Chung (2016) numerically investigated the 2DOF spring-mounted cylinder close to a free-surface for $Re = 100$. The authors found that proximity to the free-surface strengthens and suppresses the VIV for low and high Froude numbers respectively, both in term of the maximum amplitude and width of the lock-in regime. It was also found that in-line oscillations could not be neglected. The mean lift was found to be negative and to increase with strong confinements. In the parameter space explored, the wake was found to be dominated by alternate vortex shedding though additional free-surface-induced vortices could appear at higher Froude numbers.

Kinaci *et al.* (2022) experimentally investigated the 1DOF configuration for various mass ratios, damping parameters and immersion depths for $18000 < Re < 72000$. The authors also noticed a stabilising effect of the free-surface on the VIV. Both the range of synchronisation and the amplitudes if motion decreased when the cylinder was brought closer to the free-surface. In terms of energy harvesting, they found a decrease of harnessed power in the vicinity of the surface.

1.5 Review on methodology for fluid-structure interaction problems

1.5.1 Numerical methods

For the specific case of vortex-induced vibrations, the use of direct numerical simulations was first employed by Blackburn & Karniadakis (1993) to compute the flow arround a single spring-mounted cylinder. Then, the first numerical study to employ DNS for a more than one body was that of Meneghini *et al.* (2001) for the in-line tandem configuration.

To compute the deformation of a surface, one can either use conforming or non-conforming mehtods. Non-conforming methods propose to evaluate the fluid problem on a computational grid which does not conform with that of the solid (or other fluid), therefore requiring to interpolate the quantities on the boundary. The first numerical method proposed for solving FSI problems was the Immersed Boundary Method (IBM) by Peskin (1977), applied to the

problem of moving valves in the human heart. Other similar approaches were developed with the example of the level-set method or the volume of fluids (VOF) method used computation of free-surface flows. Note that research on numerical methods for free-surface problems is still ongoing (Colagrossi *et al.*, 2019).

Non-conforming methods, while efficient computationally, might lack in precision when it comes to the calculation of the variables on the boundary. More specifically, for the case of vortex-induced vibrations and free falling objects, the immersed boundary method was shown to yield incorrect results when the added-mass effect is not properly taken into account (Suzuki & Inamuro, 2011).

This, in part, motivated the development of conforming methods where all quantities are evaluated on the same computational grid and an exact description of the interface is provided. The Arbitrary Lagrangian Eulerian (ALE) is one of these methods and the reader is oriented to section 2.2.1 for more details.

1.5.2 Stability analysis

Experiments and direct numerical simulations are costly and limit the number of parameters that can be explored. One approach to avoid this issue is to use stability analysis. It consists in the linearisation of the Navier-Stokes equations which allows the calculation of a steady state as well as modal perturbations around that state. One therefore trades the resolution of a non-linear system with an eigenvalue problem easier to solve. One can then produce stability maps in the parameter space. This method was first employed for a spring-mounted body by Cossu & Morino (2000) and then applied to a tandem of spring-mounted bodies by Tirri *et al.* (2023).

In the stability community (Sipp & Lebedev, 2007), and more specifically in our team (for instance Sabino *et al.*, 2020; Sierra-Ausin *et al.*, 2022*b*), the finite element software FreeFem++ (Hecht, 2012) has been a popular tool for such studies. In the last decade, the open-source toolbox StabFem (Fabre *et al.*, 2018) has been developed in our team as a convenient interface to FreeFem++ designed to perform parametric stability analyses. This toolbox has been used in this thesis and some sample results are published on the website of the project (`https://stabfem.gitlab.io/StabFem/`).

1.5.3 Generalised aerodynamic forces

Even employing classical stability analysis can be tedious considering the extensive number of parameters in the multi-body systems for instance. Another strategy for analysing fluid-structure interactions has been to project the fluid forces onto the structural degrees of freedom and treat the problem as a harmonically forced structural oscillator, using generalised aerodynamic forces (GAF) to represent the fluid loading. The idea of exploiting the unsteady forces exerted on the body in a prescribed oscillating motion to predict instability was pursued in Sabino *et al.* (2020). The forces were computed through exact resolution of the linearized Navier-Stokes equations allowing to define a mechanical impedance as the ratio between the lift force and the velocity of the cylinders. This allowed to treat the problem by exploiting an analogy with electric systems (Conciauro & Puglisi, 1981) for which an impedance of negative real part is a necessary condition for instability. Note that a similar concept of impedance can be applied to acoustic systems, as was done by Fabre *et al.* (2019) for an oscillating flow through a thin circular aperture. It was then applied for the stability prediction of the flow through a circular aperture in a thick plate (see Fabre *et al.*, 2020; Sierra-Ausin *et al.*, 2022*b*)

1.6 Vortex-induced vibrations for energy harvesting

As shortly mentioned in the beginning of this introduction, energy harvesting applications can be divided into two approaches: micro devices based on piezoelectric coupling and marine applications.

Soti *et al.* (2017) numerically investigated the energy harvesting from VIV of a spring-mounted cylinder for $Re = 150$. They compared a constant damping with an electromagnetic system. Fixing the reduced velocity to match the lock-in regime, they found that both systems produced the same average power output. The increase in mass ratio little increased the power output but widened the synchronisation region. It was also found that increasing the Reynolds number increases the power output.

Extending these results, Zhao *et al.* (2022*b*) did experiments on a rotating spring-mounted cylinder. They showed that the damping and rotation strongly modified the vibration response and therefore the energy harvesting potential. They found that rotation could enhance vibration amplitudes within a limited

parameter range. Overall, they suggested that a continuously rotating cylinder might not be the optimal configuration for efficient energy harvesting. On the other hand, Zhao *et al.* (2025) found that a spring-mounted cylinder with mechanically coupled rotation could enhance energy harvesting.

The concept of energy harvesting from VIV coupled to piezoelectric was investigated by Mehmood *et al.* (2013). Numerically solving the fully coupled fluid-structure-electrical system across different flow regimes, they showed that the electrical resistance influences the VIV response. They also found that the maximum power output did not correspond to the largest oscillations.

Alternative systems have been proposed, drawing inspiration from galloping vibrations observed in tandem configurations (Sun *et al.*, 2019; Kim *et al.*, 2022).

Lee *et al.* (2019) also investigated the efficiency of a VIV energy harvesting MEMS device (see figure 1.2(b)), both experimentally and numerically. They found an increase in power output when the energy harvester was placed within a formation of cylinders, compared to it being isolated. This way they found they could double the maximum power time-averaged power output but however highlighted the limited parameter space that was explored.

Others have come up with concepts to extract energy from waves (see figure 1.2(a)) and marine currents. The reader is directed towards the comprehensive reviews of Rashki *et al.* (2025); Bernitsas (2016); Rostami & Armandei (2017).

1.7 Objective of the thesis and outline

The first objective of this thesis is to develop efficient numerical methods based on the ALE formulation in order to solve FSI problems of spring-mounted bodies possibly interacting with a deformable free-surface. The second main objective is to explore physical configurations that are lacking in the litterature, mainly the exploring the transitions at low Reynolds number. This thesis is split into three parts including the present introduction.

In the second part, methodologies for solving FSI problems are presented. In Chapter 2, we present three methodologies for solving FSI problems of multiple spring-mounted bodies. First we describe a discrete-ALE non-linear formulation for direct-numerical simulations. Then a linear problem is derived based on the discrete-ALE ansatz, allowing for classical linear stability analysis. Thirdly, we propose an impedance-based method to efficiently predict instability thresholds. In Chapter 3, we derive a linear ALE formulation for solving the motion of a spring-mounted body below a deformable free-surface.

Then, in the third part, we present results produced with the developed methods. In Chapter 4, we present results for two spring-mounted bodies. We first show results of the DNS simulations, eigenvalue problems as well as impedance-based detections for the tandem configuration. Then we present results from the impedance-based method and eigenvalue problem for the side-by-side configuration. In Chapter 5, we present results for multiple in-line bodies, from the three methodologies presented. Finally in Chapter 6, we present linear results of a spring-mounted body beneath a free-surface.

Part II

Methods

Chapter 2

Methods for multiple oscillating cylinders

2.1 General equations

Let us consider N spring-mounted bodies immersed in an incompressible fluid. The actual (deformable) fluid domain is denoted $\tilde{\Omega}(t)$ and its interface with the cylinders, $\tilde{\Gamma}_i(t)$. The non-dimensional parameters governing the flow in this configuration are the Reynolds number $Re = \frac{U_\infty D}{\nu}$ and the spacing ratio L/D; where ν is the kinematic viscosity, ρ the density, U_∞ the incoming velocity, D the diameter and L the spacing between the cylinders.

The fluid flow is described by the set of unknowns $\{\tilde{\boldsymbol{u}}, \tilde{p}\}$, which are governed by the following set of equations in non-dimensional form

$$\left.\frac{\partial \tilde{\boldsymbol{u}}}{\partial t}\right|_{\tilde{\boldsymbol{x}}} + (\tilde{\nabla}\tilde{\boldsymbol{u}})\tilde{\boldsymbol{u}} - \tilde{\nabla}\cdot\tilde{\boldsymbol{\sigma}}(\tilde{\boldsymbol{u}}, \tilde{p}) = \mathbf{0} \qquad \text{in} \quad \tilde{\Omega}(t), \tag{2.1}$$

$$\tilde{\nabla}\cdot\tilde{\boldsymbol{u}} = 0 \qquad \text{in} \quad \tilde{\Omega}(t), \tag{2.2}$$

with $\tilde{\boldsymbol{\sigma}}(\tilde{\boldsymbol{u}}, \tilde{p}) = -\tilde{p}\mathrm{I} + 2\mu\tilde{\boldsymbol{D}}(\tilde{\boldsymbol{u}})$ the stress tensor with $\tilde{\boldsymbol{D}}(\tilde{\boldsymbol{u}}) = \frac{1}{2}\left(\tilde{\nabla}\tilde{\boldsymbol{u}} + \tilde{\nabla}\tilde{\boldsymbol{u}}^T\right)$. The symbol $(\tilde{\ })$ is used for time-dependent quantities as well as time and spatial derivatives evaluated in the time-dependent domain.

Each body is characterised by the following set of non-dimensional numbers: the mass ratio $m_i^* = \frac{4m_{c_i}}{\pi D^2 \rho_f}$, the reduced velocity $U_i^* = 2\pi U_\infty \sqrt{m_{c_i}/k_i}/D$, and the damping coefficient $\gamma_i = g_i/(2\sqrt{m_{c_i} k_i})$. Where,

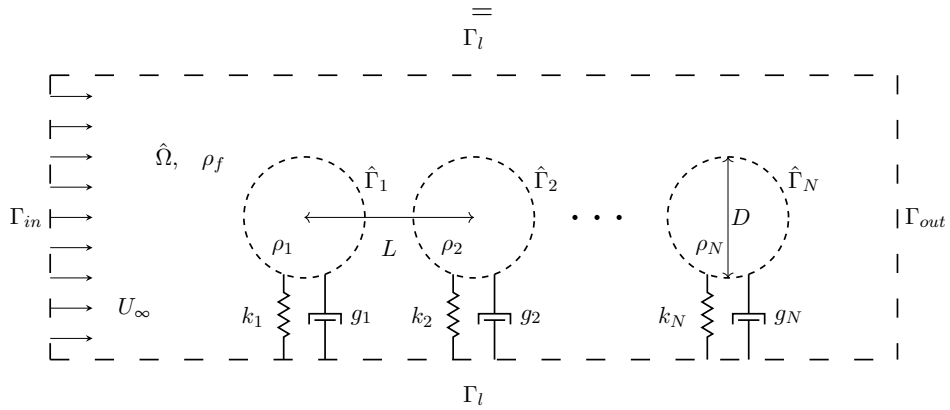

Figure 2.1: Sketch of the domain in the reference configuration: Array of N spring mounted cylinders with densities, spring stiffness and damping parameters: ρ_i, k_i and g_i. The cylinders are immersed in a fluid domain $\hat{\Omega}$ of density ρ_f. The domain is delimited by inlet and outlet boundaries, Γ_{in} and Γ_{out} as well as lateral boundaries Γ_l.

m_{c_i}, k_i and g_i respectively are the mass, spring stiffness and damping parameter of the i-th body.

The set of unknowns $\{Y, \dot{Y}\}$ describing the motion of each body is then prescribed by the following equations in non-dimensional form:

$$\dot{Z}_i + \frac{4\pi\gamma_i}{U_i^*} Z_i + \left(\frac{2\pi}{U_i^*}\right)^2 Y_i = \frac{4F_{y_i}(t)}{\pi m_i^*}, \quad \text{for } i = 1, \ldots, N, \tag{2.3}$$

$$\dot{Y}_i = Z_i \tag{2.4}$$

with $F_{y_i} = \int_{\tilde{\Gamma}_i} \boldsymbol{e}_y \cdot \tilde{\boldsymbol{\sigma}} \cdot \boldsymbol{n} \, d\tilde{\Gamma}_i$ the lift force acting on the i-th body.

Additionally, a few boundary conditions need to be enforced. First the velocity of the bodies needs to match the fluids velocity on the bodies' boundaries:

$$\tilde{\mathbf{u}} = Z_i \mathbf{e}_y \quad \text{on} \quad \tilde{\Gamma}_i(t). \tag{2.5}$$

2.2 Non-linear formulation

2.2.1 ALE formulation

When looking at fluid-structure interaction problems a common approach is to keep the Eulerian frame of reference in the fluid and the Lagrangian one for the solid boundary, linking the two descriptions through a non-conforming computational grid, as is done in immersed boundary or level-set methods. Where these methods are computationally efficient, they lack in precision at the interfaces. The Arbitrary Lagrangian-Eulerian (ALE) method is a hybrid method first introduced by Hughes *et al.* (1981) that is now extensively used for fluid-structure interaction and free-surface problems. As described in the founding paper of Hughes *et al.* (1981), the movement of the interfaces are described in a Lagrangian manner and the deformed physical domain is mapped via a conforming computational grid to a reference domain where the fluid can be described in a Eulerian manner.

Following Pfister *et al.* (2019), we apply the Arbitrary Lagrangian Eulerian (ALE) method to the set of equations previously described. We therefore apply a change of variables that allows the mapping of the actual physical domain $\tilde{\Omega}(t)$ through a fixed reference domain $\hat{\Omega}$. In all of the following, the symbol $(\hat{})$ will denote time-dependent quantities as well as time and spatial derivatives evaluated in the reference domain. That mapping involves an extension field $\hat{\boldsymbol{\xi}}_e$ and can be written as

$$\tilde{\boldsymbol{x}} = \hat{\boldsymbol{x}} + \hat{\boldsymbol{\xi}}_e(\hat{\boldsymbol{x}}, t). \tag{2.6}$$

Applying that change of coordinates to the fluids equations 2.1 and 2.2 yields the ALE formulation of the incompressible Navier-Stokes equation in a stress-free configuration

$$\hat{J}\left(\hat{\boldsymbol{\xi}}_e\right)\frac{\partial \hat{\boldsymbol{u}}}{\partial t} + \left((\hat{\nabla}\hat{\boldsymbol{u}})\hat{\boldsymbol{\Phi}}\left(\hat{\boldsymbol{\xi}}_e\right)\right)\left(\hat{\boldsymbol{u}} - \frac{\partial \hat{\boldsymbol{\xi}}_e}{\partial t}\right) - \hat{\nabla}\cdot\hat{\boldsymbol{\Sigma}}\left(\hat{\boldsymbol{u}}, \hat{p}, \hat{\boldsymbol{\xi}}_e\right) = \boldsymbol{0} \quad \text{in} \quad \hat{\Omega}, \tag{2.7}$$

$$-\hat{\nabla}\cdot\left(\hat{\boldsymbol{\Phi}}\left(\hat{\boldsymbol{\xi}}_e\right)\hat{\boldsymbol{u}}\right) = 0 \quad \text{in} \quad \hat{\Omega}. \tag{2.8}$$

$\hat{\nabla}$ is the gradient in the reference coordinates. $\hat{\boldsymbol{\Phi}}\left(\hat{\boldsymbol{\xi}}_e\right) = \hat{J}\left(\hat{\boldsymbol{\xi}}_e\right)\hat{\boldsymbol{F}}\left(\hat{\boldsymbol{\xi}}_e\right)^{-1}$ denotes the deformation operator introduced by the change of variables, with $\hat{J}\left(\hat{\boldsymbol{\xi}}_e\right) = \det\left(\hat{\boldsymbol{F}}\left(\hat{\boldsymbol{\xi}}_e\right)\right)$ the Jacobian of the deformation gradient $\hat{\boldsymbol{F}}\left(\hat{\boldsymbol{\xi}}_e\right) = \mathrm{I} + \hat{\nabla}\hat{\boldsymbol{\xi}}_e$. The ALE fluid stress tensor expressed in the reference configuration writes as

$$\hat{\boldsymbol{\Sigma}}\left(\hat{\boldsymbol{u}}, \hat{p}, \hat{\boldsymbol{\xi}}_e\right) = \hat{\boldsymbol{\sigma}}\left(\hat{\boldsymbol{u}}, \hat{p}, \hat{\boldsymbol{\xi}}_e\right)\hat{\boldsymbol{\Phi}}\left(\hat{\boldsymbol{\xi}}_e\right)^T, \tag{2.9}$$

where $\hat{\boldsymbol{\sigma}} = -\hat{p}\mathrm{I} + \frac{2}{Re}\hat{\boldsymbol{D}}$, with the viscous dissipation tensor defined as

$$\hat{\boldsymbol{D}}\left(\hat{\boldsymbol{u}}, \hat{\boldsymbol{\xi}}_e\right) = \frac{1}{2}\frac{1}{\hat{J}\left(\hat{\boldsymbol{\xi}}_e\right)}\left((\hat{\nabla}\hat{\boldsymbol{u}})\hat{\boldsymbol{\Phi}}\left(\hat{\boldsymbol{\xi}}_e\right) + \hat{\boldsymbol{\Phi}}\left(\hat{\boldsymbol{\xi}}_e\right)^T(\hat{\nabla}\hat{\boldsymbol{u}})^T\right). \tag{2.10}$$

The extension field's role is to propagate the deformation of the Lagrangian interface to the fluid domain. It requires a governing equation as well as boundary conditions which can be written as

$$\hat{\nabla}\cdot\Sigma_e(\hat{\boldsymbol{\xi}}_e) = \mathbf{0} \quad \text{in} \quad \hat{\Omega}, \tag{2.11}$$

$$\hat{\boldsymbol{\xi}}_e = Y_i\mathbf{e}_y \quad \text{on} \quad \hat{\Gamma}_i, \tag{2.12}$$

Σ_e being an arbitrary elliptic operator.

2.2.2 The discrete-ALE ansatz

The choice of the operator Σ_e has been found to be crucial for the stability of the numerical codes implemented and an "elasticity"-type equation has been chosen in most cases. Equation 2.11 being linear, and the number of cylinders being finite, we can look for a solution of the extension field as a function of the cylinders' vertical displacement

$$\hat{\boldsymbol{\xi}}_e = \sum_{i=1}^{N} Y_i(t)\hat{\boldsymbol{\xi}}_{e_i}, \tag{2.13}$$

where $\hat{\boldsymbol{\xi}}_{e_i}$ is an elementary field associated to the displacement of the i-th cylinder, namely the solution of the elementary problem

$$\begin{cases} \hat{\nabla}\cdot\Sigma_e(\hat{\boldsymbol{\xi}}_{e_i}) = \mathbf{0}, & (2.14)\\ \hat{\boldsymbol{\xi}}_{e_i} = \mathbf{e}_y \quad \text{on} \quad \hat{\Gamma}_i, & (2.15)\\ \hat{\boldsymbol{\xi}}_{e_i} = \mathbf{0} \quad \text{on} \quad \hat{\Gamma}_j \quad \text{for all} \quad i \neq j. & (2.16) \end{cases}$$

We call (2.13) the *discrete-ALE ansatz*. The main advantage of this expression is that it is sufficient to solve N elementary problems once to reconstruct the deformation field for all possible values of Y_i, allowing for a reduction of the computational time required to solve the entire system.

Introducing the change of variable 2.6 and the decomposition 2.13 in the equations of motion 2.3 gives the lift force acting on the i-th

$$F_{y_i} = \int_{\hat{\Gamma}_i}\left(-\hat{p}\mathrm{I} + \frac{1}{Re}\hat{\boldsymbol{D}}(\hat{\boldsymbol{u}}, \hat{\boldsymbol{\xi}}_e)\right)\hat{\boldsymbol{\Phi}}\left(\hat{\boldsymbol{\xi}}_e\right)^T\boldsymbol{n}\cdot\boldsymbol{e}_y\, d\hat{\Gamma}_i. \tag{2.17}$$

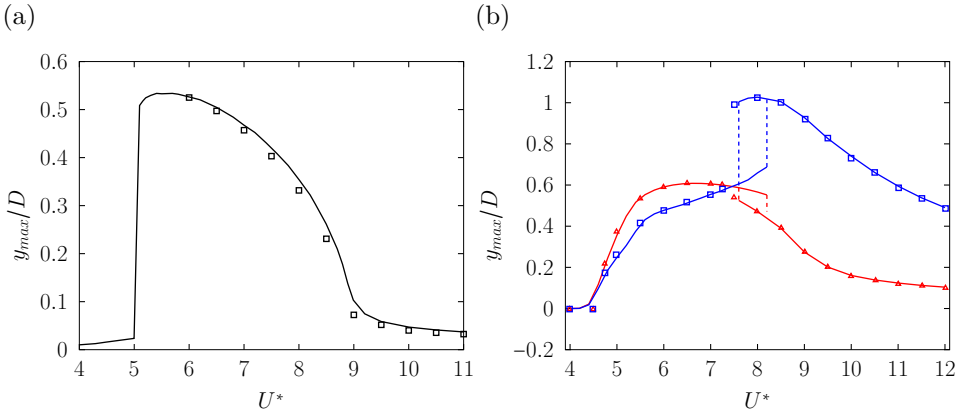

Figure 2.2: Maximum amplitudes of motion against reduced velocity for: (a) a single spring-mounted body at $\{Re = 60,\ m^* = 5\}$ and (b) a tandem of spring-mounted cylinders at $\{L = 3,\ Re = 60,\ m^* = 5\}$. Navrose & Mittal (2016) is represented as — and the present code as ◘. The amplitudes of the front and rear cylinder from Boujo (2021) are respectively presented as ◘ and ◘. Amplitudes of the front and rear cylinder from the present code are shown respectively as — and —.

2.2.3 Numerical implementation

The equations described above are rewritten in variational form, following the formulation described in Pfister *et al.* (2019) for a deformable solid immersed in an incompressible fluid. Since the velocity is prescribed on the cylinder boundary, the boundary terms arising from integration by parts vanish. The temporal discretisation is performed using a Backward Differentiation Formula (BDF) scheme. Given a generic time-dependent quantity f, its time derivative at the current time step is approximated by

$$\frac{\partial f}{\partial t} \approx \frac{\alpha_0(f + \delta f) + \alpha_1 f^p + \alpha_2 f^{pp}}{\Delta t},$$

where f^p and f^{pp} denote the values at the previous and pre-previous time steps, respectively, and δf is the Newton increment. The coefficients are chosen as $[\alpha_0, \alpha_1, \alpha_2] = [3/2, -2, 1/2]$ for the second-order Backward Differentiation Formula (BDF2), and $[\alpha_0, \alpha_1, \alpha_2] = [1, -1, 0]$ for the backward Euler scheme. The equations are spatially discretised and solved with the FreeFem++ open-source software (Hecht, 2012). A Dirichlet boundary condition is imposed at the inflow boundary Γ_{in}: $\tilde{\boldsymbol{u}}_0|_{\Gamma_{in}} = U_\infty \mathbf{e}_x$ with $U_\infty \equiv 1$, and a stress-free

condition is imposed on the lateral and outflow boundaries. Additionally, for the extension field, homogeneous Dirichlet boundary conditions are imposed on all outer boundaries. The domain is 150 diameters in length and 80 diameters in width, and the first cylinder is placed at one third of the domain length in the middle of its width. Adaptive mesh refinement is systematically used. The FreeFem++ codes are implemented in the StabFem open source project, for more information refer to Fabre *et al.* (2018).

2.2.4 Validation

For the validation of our numerical code, we look at two vortex-induced-vibration cases. First we investigate the flow around a single spring-mounted cylinder at $Re = 60$ and $m^* = 5$ as was done by Navrose & Mittal (2016). Secondly, we investigate the flow around a tandem of spring-mounted cylinders at $Re = 60$ and $m^* = 5$ and spaced of $L = 3$ diameters as was done by Boujo (2021) (private communication). Figure 2.2 shows the maximum amplitudes of motion with respect to the reduced velocity. Our code shows very good agreement. Interestingly, depending on the initial conditions used to initialise the simulations, different amplitude branches are obtained (when the reduced velocity is varied by progressively increasing or decreasing its value). These differences indicate the existence of multiple stable solutions. Similar behaviours have been reported for tandem configurations of both stationary (Papaioannou, 2006) and spring mounted (Tirri *et al.*, 2023) cylinders as well as for the vortex-induced vibrations of a single elastically mounted cylinder and are commonly interpreted as evidence of a hysteresis phenomenon arising from nonlinear fluid–structure interaction.

2.3 Linear formulation

2.3.1 Linearised equations in the discrete ALE formalism

Following the usual approach, both the fluid and structural variables are decomposed into a steady component and a small-amplitude perturbation which is searched under a modal form. Namely, for the fluid part of the problem, we start with the expansion

$$\hat{\boldsymbol{q}}_f(\hat{\boldsymbol{x}}, t) = \hat{\boldsymbol{q}}_{f,0}(\hat{\boldsymbol{x}}) + \varepsilon \boldsymbol{q}_f(\hat{\boldsymbol{x}}) e^{-i\omega t} \tag{2.18}$$

were $\hat{\boldsymbol{q}}_{f,0}$ is the so-called *base flow*, corresponding to the steady solution of the Navier-Stokes equations in the reference domain, $\varepsilon \ll 1$, $\boldsymbol{q}_f$ is the fluid part of

the eigenmode, and ω is an a-priori complex eigenvalue.

Similarly, for the structural part of the problem, we parametrize the displacement of the cylinders by

$$Y_i(t) = \varepsilon y_i e^{-i\omega t}; \qquad \dot{Y}_i(t) = \varepsilon z_i e^{-i\omega t} \quad \text{with } z_i = -i\omega y_i. \tag{2.19}$$

The eigenmode of the fluid-structure problem is thus defined as $\boldsymbol{q} = \left(\boldsymbol{q}_f, y_1, ..., y_N, z_1, ..., z_N\right)$, where $\boldsymbol{q}_f = (\boldsymbol{u}, p)$ denotes its "fluid" part and $[y_1, ..., y_N, z_1, .., z_N]$ its "solid part".

The base flow $\hat{\boldsymbol{q}}_{f,0}$ for all cases is calculated keeping the structures fixed at their initial position. Two examples of base flows calculated for $N = 2$ bodies with $L = 1.5$ and $L = 10$ at $Re = 23.512$ are shown in figure 2.3. The stream-wise velocities are also reported, as well as the vorticity calculated as $\Xi = \partial_x U_y - \partial_y U_x$. At $Re = 23.512$, the flow around a fixed isolated cylinder is linearly stable and the length of the reverse flow region was found to be $S/D = 1.150$ by Negi *et al.* (2020). For a tandem of cylinders separated by $L = 1.5$, the downstream cylinder is located in the recirculation region of the upstream one. For $L = 10$, the length of the recirculation bubble behind the front cylinder is $S/D = 1.134$.

Substituting the ansatz eq. (2.18) into eqs. (2.1) to (2.3) and (2.5), applying the discrete-ALE ansatz 2.13 and writing the equations in the steady deformed configuration (see Pfister *et al.*, 2019, for more details) leads to the following formulations

$$\begin{aligned}
-i\omega\Bigg(\underbrace{\boldsymbol{u}}_{\boldsymbol{B}_{ff}\mathbf{q}_f} + \sum_{i=1}^{N} y_i \underbrace{\left(-\hat{\boldsymbol{\xi}}_{e_i}\cdot\hat{\nabla}\hat{\boldsymbol{u}}_0\right)}_{\boldsymbol{B}_{ui}\mathbf{q}_f}\Bigg) &= \underbrace{-\left(\boldsymbol{u}\cdot\hat{\nabla}\hat{\boldsymbol{u}}_0 + \hat{\boldsymbol{u}}_0\cdot\hat{\nabla}\boldsymbol{u}\right) + 2\mu\hat{\nabla}\cdot\tilde{\boldsymbol{D}}(\boldsymbol{u})}_{\boldsymbol{A}_{uu}\mathbf{q}_f}\ \underbrace{-\hat{\nabla}p}_{\boldsymbol{A}_{up}\mathbf{q}_f} \\
&+ \sum_{i=1}^{N}\underbrace{\left[-\hat{\boldsymbol{u}}_0\cdot\left(\left(\hat{\nabla}\hat{\boldsymbol{u}}_0\right)\left((\hat{\nabla}\cdot\hat{\boldsymbol{\xi}}_{e_i})\mathrm{I} - \hat{\nabla}\hat{\boldsymbol{\xi}}_{e_i}\right)\right) - \hat{\nabla}\cdot\left[\hat{p}_0\mathrm{I}\left((\hat{\nabla}\cdot\hat{\boldsymbol{\xi}}_{e_i})\mathrm{I} - \hat{\nabla}\hat{\boldsymbol{\xi}}_{e_i}\right)^T\right]\right]}_{\boldsymbol{A}_{ui}^{(1)}y_i} y_i \\
&+ \sum_{i=1}^{N}\underbrace{\left[-\mu\hat{\nabla}\cdot\left(\left(\hat{\nabla}\hat{\boldsymbol{u}}_0\right)\left(\hat{\nabla}\hat{\boldsymbol{\xi}}_{e_i}\right) + \left(\hat{\nabla}\hat{\boldsymbol{\xi}}_{e_i}\right)^T\left(\hat{\nabla}\hat{\boldsymbol{u}}_0\right)^T\right) - 2\mu\hat{\nabla}\cdot\left(\tilde{\boldsymbol{D}}(\hat{\boldsymbol{u}}_0)\left((\hat{\nabla}\cdot\hat{\boldsymbol{\xi}}_{e_i})\mathrm{I} - \hat{\nabla}\hat{\boldsymbol{\xi}}_{e_i}\right)^T\right)\right]}_{\boldsymbol{A}_{ui}^{(2)}y_i} y_i,
\end{aligned} \tag{2.20}$$

$$0 = \underbrace{\hat{\nabla}\cdot\boldsymbol{u}}_{\boldsymbol{A}_{pu}\mathbf{q}_f} + \sum_{i=1}^{N}\underbrace{\hat{\nabla}\cdot\left(\left(\hat{\nabla}\cdot\hat{\boldsymbol{\xi}}_{e_i}\mathrm{I} - \hat{\nabla}\hat{\boldsymbol{\xi}}_{e_i}\right)\hat{\boldsymbol{u}}_0\right)}_{\boldsymbol{A}_{pi}y_i} y_i\,. \tag{2.21}$$

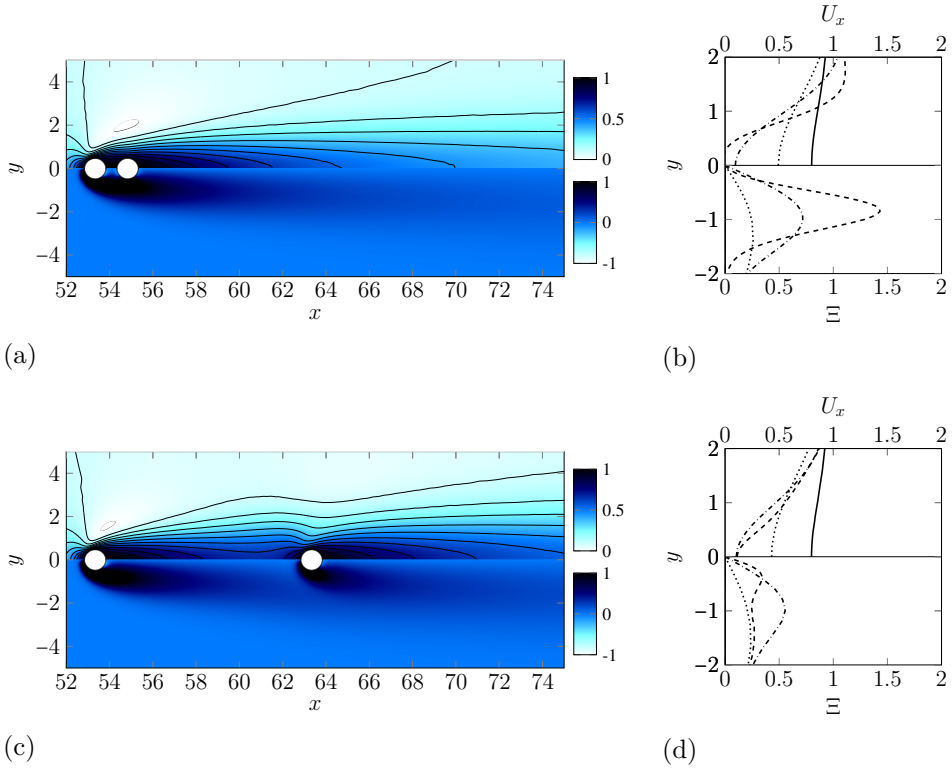

Figure 2.3: (a) Baseflow for $L = 1.5$ and $Re = 23.512$. Lower part: vorticity Ξ. Upper part: axial velocity U_x and streamlines. (b) Profiles of the stream-wise velocity (upper) and vorticity (lower) at $x = x_1 - 3D/2$ (——), $x = x_2 - 3D/4$ (- - -), $x = x_2 + 2D$ (-·-·) and $x = x_2 + 10D$ (·····), with x_1 and x_2 the x-coordinates of the center of the front and rear cylinder. (c) and (d): same for $L = 10$.

The boundary conditions on the objects surface are

$$\begin{cases} \boldsymbol{u}\cdot\boldsymbol{e}_y = z_i & \text{on} \quad \hat{\Gamma}_i, \qquad (2.22) \\ \boldsymbol{u}\cdot\boldsymbol{e}_y = 0 & \text{on} \quad \hat{\Gamma}_{j,i\neq j}. \quad (2.23) \end{cases}$$

They are symbolically noted as $-i\omega\sum \boldsymbol{B}^*_{fi}y_i + \boldsymbol{A}^*_{ff}\boldsymbol{q}_f = 0$, where $\boldsymbol{B}^*_{fi}$ and $\boldsymbol{A}^*_{ff}$ are restriction operators extracting the degrees of freedom localized along the boundaries of the cylinders.

The linearization of eqs. (2.7) and (2.8) thus introduces the operators $\boldsymbol{A}_{ff} = \boldsymbol{A}_{uu} + \boldsymbol{A}_{up} + \boldsymbol{A}_{pu} + \boldsymbol{A}^*_{ff}$ and $\boldsymbol{B}_{ff}$ that are purely driven by fluid variables, and the operators $\boldsymbol{A}_{fi} = \boldsymbol{A}^{(1)}_{ui} + \boldsymbol{A}^{(2)}_{ui} + \boldsymbol{A}_{pi}$ and $\boldsymbol{B}_{fi} = \boldsymbol{B}_{ui} + \boldsymbol{B}^*_{fi}$ that arise from the interaction of fluid and ALE variables. In this way, eqs. (2.7) and (2.8) can be symbolically written with the previously defined operators as

$$-i\omega\left(\boldsymbol{B}_{ff}\boldsymbol{q}_f + \sum_{i=1}^{N}\boldsymbol{B}_{fi}y_i\right) = \boldsymbol{A}_{ff}\boldsymbol{q}_f + \sum_{i=1}^{N}\boldsymbol{A}_{fi}y_i, \qquad \text{in } \hat{\Omega}_f. \tag{2.24}$$

The lift force F_{y_i} acting on the i-th cylinder was defined previously in primitive coordinates in section 2.1. Using the ALE ansatz and the definition 2.9 of the stress tensor, one is led to an expression of with the form

$$F_{y_i} = \boldsymbol{F}_{if}\boldsymbol{q}_f + \sum_{j=1}^{N}F^*_{ij}y_j \tag{2.25}$$

This expression is composed of two terms. The first is found by integrating on the boundary the stress which is purely linked to the fluid motion:

$$\boldsymbol{F}_{if}\boldsymbol{q}_f = \int_{\hat{\Gamma}_i}\left(-p\boldsymbol{n} + 2\mu\tilde{\boldsymbol{D}}(\boldsymbol{u})\boldsymbol{n}\right)\cdot\boldsymbol{e}_y \; d\hat{\Gamma}_i. \tag{2.26}$$

The second component contains the effect of the deformation of the domain associated to the ALE method, and thanks to the discrete-ALE ansatz, it depends only upon the elementary extension fields $\boldsymbol{\xi}_j$ associated to each of the cylinders

$$\begin{aligned} F^*_{ij} = &\int_{\hat{\Gamma}_i}\left(-\hat{p}_0\mathrm{I} + 2\mu\tilde{\boldsymbol{D}}(\hat{\boldsymbol{u}}_0)\right)\left(\hat{\nabla}\cdot\boldsymbol{\xi}_j\mathrm{I} - \hat{\nabla}\boldsymbol{\xi}_j\right)^T\boldsymbol{n}\cdot\boldsymbol{e}_y \; d\hat{\Gamma}_i \\ &-\int_{\hat{\Gamma}_i}\mu\left((\hat{\nabla}\hat{\boldsymbol{u}}_0)(\hat{\nabla}\boldsymbol{\xi}_j) + (\hat{\nabla}\boldsymbol{\xi}_j)^T(\hat{\nabla}\hat{\boldsymbol{u}}_0)^T\right)\boldsymbol{n}\cdot\boldsymbol{e}_y \; d\hat{\Gamma}_i. \end{aligned} \tag{2.27}$$

Introducing eq. (2.18) in eq. (2.3), we obtain the following system for $i = 1, \dots, N$

$$-i\omega y_i = z_i, \tag{2.28}$$

$$-i\omega z_i = -\frac{4\pi\gamma_i}{U_i^*} z_i - \left(\frac{2\pi}{U_i^*}\right)^2 y_i + \frac{4}{\pi m_i^*}\left(\boldsymbol{F}_{i,f}\boldsymbol{q}_f + \sum_{j=1}^{N} F_{i,j}^* y_j\right) \tag{2.29}$$

Considering the coupled problem formulated in terms of the state-vector $\boldsymbol{q}$ containing both the fluid part $\boldsymbol{q}_f$ and the solid part $[y_1, ...y_N, z_1, .., z_N]$, the equations detailed in the two previous subsections can be written in the following matricial system

$$-i\omega \boldsymbol{B}\boldsymbol{q} = \boldsymbol{A}\boldsymbol{q}, \tag{2.30}$$

with matrices

$$\boldsymbol{B} = \begin{bmatrix} \boldsymbol{B}_{ff} & \boldsymbol{B}_{f1} & \dots & \boldsymbol{B}_{fN} & 0 & \dots & 0 \\ & 1 & & & & & \\ & & \ddots & & & (0) & \\ & & & 1 & & & \\ & & & & 1 & & \\ & (0) & & & & \ddots & \\ & & & & & & 1 \end{bmatrix}, \tag{2.31}$$

and

$$\boldsymbol{A} = \begin{bmatrix} \boldsymbol{A}_{ff} & \boldsymbol{A}_{f1} & \dots & \boldsymbol{A}_{fN} & 0 & \dots & 0 \\ & & & & 1 & & \\ & & (0) & & & \ddots & \\ & & & & & & 1 \\ \frac{4}{\pi m_1^*}\boldsymbol{F}_{1f} & \frac{4}{\pi m_1^*}F_{11}^* - \left(\frac{2\pi}{U_1^*}\right)^2 & & \frac{4}{\pi m_1^*}F_{1N}^* & -\frac{4\pi\gamma_1}{U_1^*} & & \\ \vdots & \vdots & \ddots & \vdots & & \ddots & \\ \frac{4}{\pi m_N^*}\boldsymbol{F}_{Nf} & \frac{4}{\pi m_N^*}F_{N1}^* & & \frac{4}{\pi m_N^*}F_{NN}^* - \left(\frac{2\pi}{U_N^*}\right)^2 & & & -\frac{4\pi\gamma_N}{U_N^*} \end{bmatrix}. \tag{2.32}$$

Note that the formulation of the linear fluid equations obtained here correspond to the steady-deformed configuration from Pfister *et al.* (2019). In this formulation the perturbations are obtained by decomposing the fields from the Lagrangian point of view. Alternatively, one can apply a Eulerian decomposition and will recover the linear stability equations

of Fernández & Le Tallec (2003). The linear stability equations arising from the Eulerian-based approach are relatively simple but second order derivatives arise which renders the numerical implementation more tedious. Secondly, for the Lagrangian-based approach, there exists an alternative way to arrive to the linear stability equations described above. As described in Bonnefis (2019); Sierra-Ausin *et al.* (2022*a*), one can start from the non-linear incompressible Navier-Stokes equations of section 2.1 and linearise those directly by introducing the extension field as $\hat{\boldsymbol{x}} = \tilde{\boldsymbol{x}} + \epsilon\hat{\boldsymbol{\xi}}_e$, with $\varepsilon \ll 1$. Then, the derivation of all the linearised operators will allow one to recover the steady-deformed linearised equations introduced above.

2.3.2 Numerical implementation

The equations are rewritten in a variational formulation (see Pfister *et al.*, 2019, for more details), spatially discretised and solved with the FreeFem++ open-source software (Hecht, 2012). The problem is suplemented with suitable boundary conditions as described section 2.2.3. Following the classical procedure, the base-flow is computed using a Newton method (see Fabre *et al.*, 2018, for more details), and the eigenproblems are solved using a shift-invert method as implemented in the SLEPc library. Mesh adaptation is intensively used to increase the mesh density in regions of strong gradients while decreasing it in other regions. For the linearised problem, we employ the complex mapping method (Sierra *et al.*, 2020) to characterise the stability properties of the problem and to suppress artificial unstable modes arising due to the strongly convective nature of the wake. Monitoring of all computations and post-processing is done thanks to the StabFem interface (Fabre *et al.*, 2018).

2.3.3 Validation

We first solve the matricial system 2.30 for $N = 1$, both for a fixed cylinder and a spring-mounted one. The growth rate and frequency of the leading unstable eigenvalue for a fixed cylinder are shown in figure 2.4(a) and 2.4(b). We recover the critical Reynolds number $Re = 47$ of the vortex-shedding instability and our results are in accordance with Fabre *et al.* (2018). The growth rate and frequency of the leading unstable eigenvalues for a tandem of spring-mounted cylinders are shown for $Re = 60$, $m^* = 5$ and $m^* = 20$ figure 2.4(c,d,e,f). Accordingly to the results of Sabino *et al.* (2020), two leading unstable eigenmodes are found. In a second step, the code was further

validated for a tandem ($N = 2$) spring mounted bodies, yielding results in agreement with Zhang *et al.* (2024*b*) and Tirri *et al.* (2023), as described in section 4.1 of chapter 4.

2.4 Forced problem and impedance criterion

Besides the resolution of the coupled problem as an eigenvalue problem as just described, we will also make use of an alternative method which consists of first considering the *forced problem* in which the motion of the cylinders are imposed to behave harmonically, i.e. $Y_i(t) = y_i e^{-i\omega t}$ with imposed amplitudes y_i and real frequency ω. Transfer functions Z_{ij} relating the force on body i to the opposite of the velocity of body j arise from the resolution of the set of forced problems. Injecting these transfer functions back into the harmonic oscillator equations 2.3 allows for a compact stability criterion. Details about this method as well as its validation can be found in Mouyen, T. et al. (2026) (paper section 4.1).

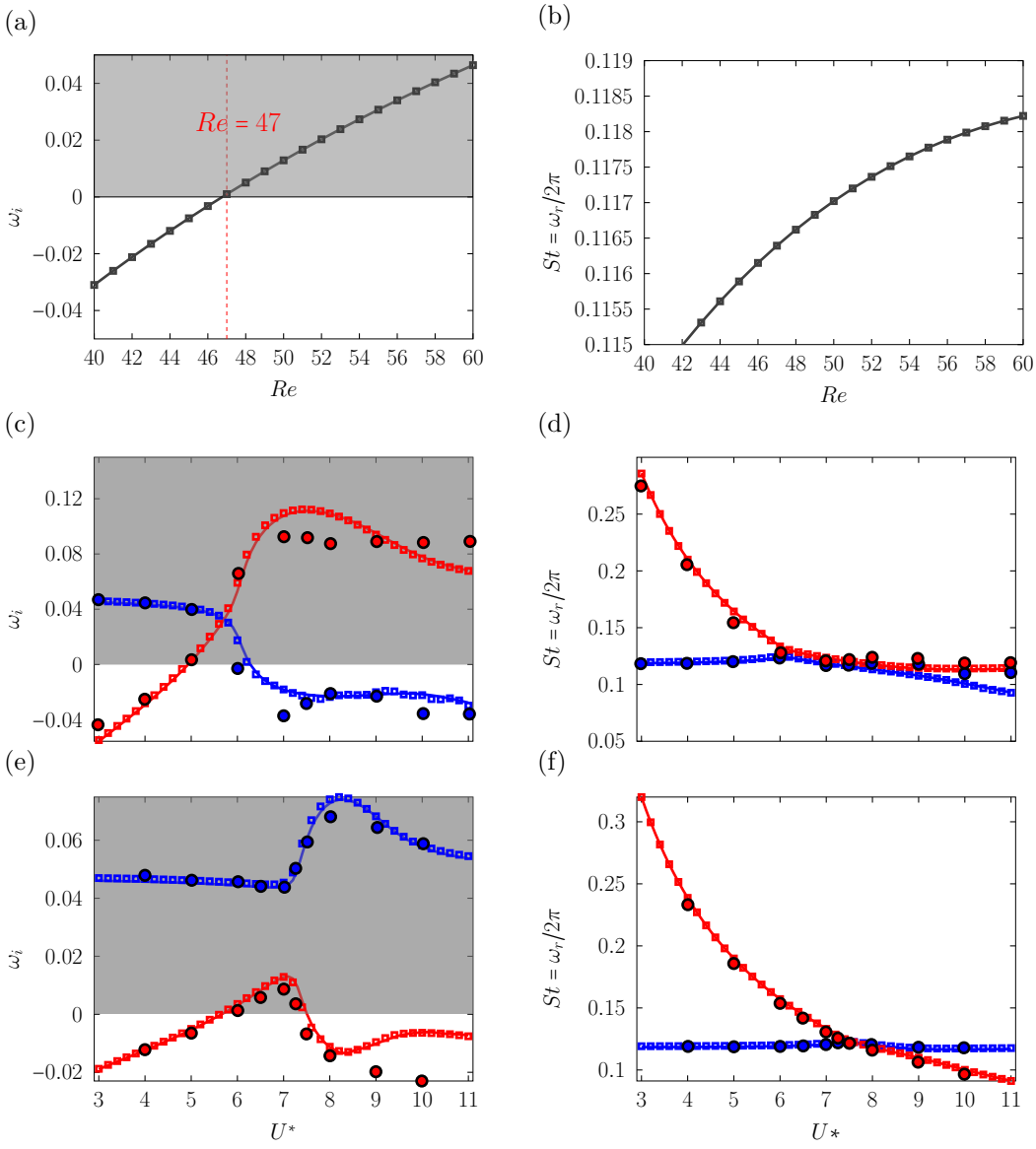

Figure 2.4: Growth rate (a) and Strouhal number (b) of the leading mode in the case of a fixed cylinder. Present results are shown as — and compared to results produced from the code developed by Fabre *et al.* (2018) (□). Real and imaginary parts of the leading eigenvalues with respect to U^* at $Re = 60$ for $m^* = 5$ (c,d) and $m^* = 20$ (e,f). The unstable region is depicted as the grey zone. The eigenvalues of the two leading modes found by the present study are respectively shown by — and —. Results found by Sabino *et al.* (2020) are displayed as □ and □; and results from Tirri *et al.* (2023) are shown as ○ and ○.

Chapter 3

Methods for an oscillating cylinder beneath a free-surface

3.1 General equations

Let us now consider $N = 1$ spring-mounted body immersed in an incompressible fluid, close to a free-surface. The flow is physically parametrized by the kinematic viscosity ν, the density ρ_f, the gravity g, the incoming velocity U_∞, the cylinder's diameter D, and the cylinder's immersion H. The free-surface is parametrized by its surface tension γ and curvature $\tilde{\kappa}$, as well as the normal to its surface $\tilde{\boldsymbol{n}}$. The non-dimensional numbers for this problem are the immersion H/D, the Reynolds number $Re = \frac{U_\infty D}{\nu}$, the Capillary number $Ca = \frac{\mu U_\infty}{\gamma}$ and the Froude number $Fr = \frac{U_\infty}{\sqrt{gD}}$. Note that in the present work the surface tension is neglected.

The fluid flow is described by the set of unknowns $\{\tilde{\boldsymbol{u}}, \tilde{p}\}$, which are governed by equations 2.1 and 2.2 complemented with gravity

$$\left.\frac{\partial \tilde{\boldsymbol{u}}}{\partial t}\right|_{\tilde{\boldsymbol{x}}} + (\tilde{\nabla}\tilde{\boldsymbol{u}})\tilde{\boldsymbol{u}} - \tilde{\nabla}\cdot\tilde{\boldsymbol{\sigma}}(\tilde{\boldsymbol{u}}, \tilde{p}) - \boldsymbol{g} = \boldsymbol{0} \qquad \text{in} \quad \tilde{\Omega}(t), \tag{3.1}$$

$$\tilde{\nabla}\cdot\tilde{\boldsymbol{u}} = 0 \qquad \text{in} \quad \tilde{\Omega}(t). \tag{3.2}$$

The stress tensor and other definitions remain the same as described section

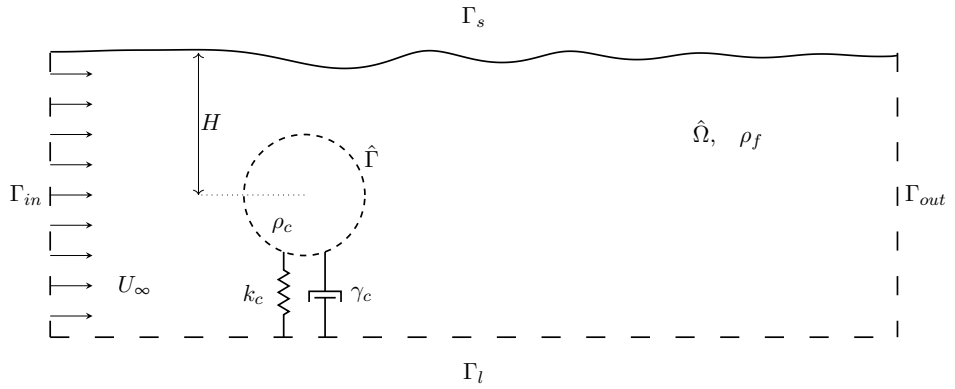

Figure 3.1: Sketch of the domain in the reference configuration: $N = 1$ spring-mounted cylinder with density, spring stiffness and damping parameter: ρ_c, k_c and γ_c. The cylinder is immersed in a fluid domain $\hat{\Omega}$ of density ρ_f. The domain is delimited by inlet and outlet boundaries, Γ_{in} and Γ_{out} as well as lateral boundaries Γ_l.

2.1. Similarly, the motion of the body is prescribed by the equations

$$\dot{Z} + \frac{4\pi\gamma_c}{U^*} Z + \left(\frac{2\pi}{U^*}\right)^2 Y = \frac{4F_y(t)}{\pi m^*}, \tag{3.3}$$

$$\dot{Y} = Z, \tag{3.4}$$

and the velocity of the body needs to match the fluids velocity on the boundary:

$$\tilde{\mathbf{u}} = Z\mathbf{e}_y \quad \text{on} \quad \tilde{\Gamma}(t). \tag{3.5}$$

The density, stiffness and damping parameter respectively are ρ_c, k_c and γ_c and the associated non-dimensional parameters follow the same definitions as in section 2.1.

The free-surface is parametrized by the unknowns $\{\tilde{\kappa}, \tilde{\boldsymbol{\eta}}\}$, where the field $\tilde{\boldsymbol{\eta}}$ is the deformation of the surface. Specific boundary conditions are required to handle the free-surface deformation. First, we assume a kinematic boundary condition to impose that the normal component of the velocity of the interface coincides with that of the fluid velocity

$$\frac{d\tilde{\boldsymbol{x}}}{dt} \cdot \tilde{\boldsymbol{n}} = \tilde{\boldsymbol{u}} \cdot \tilde{\boldsymbol{n}} \quad \text{on} \quad \tilde{\Gamma}_s(t). \tag{3.6}$$

Secondly, we assume a dynamic boundary condition specifying that the jump in normal stress is proportional to the curvature of the surface (Young-Laplace

law)

$$\tilde{\boldsymbol{\sigma}}\left(\tilde{\boldsymbol{u}},\tilde{p}\right)\cdot\tilde{\boldsymbol{n}}=\gamma\tilde{\kappa}\tilde{\boldsymbol{n}}\quad\text{on}\quad\tilde{\Gamma}_s(t). \tag{3.7}$$

Alternatively, one can choose as unknown the normal component of the stress tensor $\tilde{\sigma}_n$ instead of $\tilde{\kappa}$, as was done in Achour (2022).

The problem is supplemented with boundary conditions on the inlet, outlet and lateral (bottom) boundaries. A uniform flow is imposed at the inlet:

$$\tilde{\boldsymbol{u}}=U_{in}\boldsymbol{e}_x\quad\text{on}\quad\tilde{\Gamma}_{in}. \tag{3.8}$$

At the outlet, a no-stress boundary condition is prescribed allowing for the vertical deformation of the free-surface:

$$\tilde{\boldsymbol{\sigma}}\cdot\boldsymbol{n}=0\quad\text{on}\quad\tilde{\Gamma}_{out}. \tag{3.9}$$

On the bottom, a slip boundary condition is imposed.

3.2 Linear formulation

3.2.1 ALE formulation

The Arbitrary Lagrangian Eulerian method is applied to map the physical domain $\tilde{\Omega}(t)$ through a reference domain $\hat{\Omega}$. The equations for the fluid variables are similar to the ones described section 2.2.1

$$\hat{J}\left(\hat{\boldsymbol{\xi}}_e\right)\frac{\partial\hat{\boldsymbol{u}}}{\partial t}+\left((\hat{\nabla}\hat{\boldsymbol{u}})\hat{\boldsymbol{\Phi}}\left(\hat{\boldsymbol{\xi}}_e\right)\right)\left(\hat{\boldsymbol{u}}-\frac{\partial\hat{\boldsymbol{\xi}}_e}{\partial t}\right)-\hat{\nabla}\cdot\hat{\boldsymbol{\Sigma}}\left(\hat{\boldsymbol{u}},\hat{p},\hat{\boldsymbol{\xi}}_e\right)=\boldsymbol{g}\quad\text{in}\quad\hat{\Omega}, \tag{3.10}$$

$$-\hat{\nabla}\cdot\boldsymbol{\Sigma}_e\left(\hat{\boldsymbol{\xi}}_e\right)=\boldsymbol{0}\quad\text{in}\quad\hat{\Omega}, \tag{3.11}$$

$$-\hat{\nabla}\cdot\left(\hat{\boldsymbol{\Phi}}\left(\hat{\boldsymbol{\xi}}_e\right)\hat{\boldsymbol{u}}\right)=0\quad\text{in}\quad\hat{\Omega}. \tag{3.12}$$

In the equation of motion 3.3 of the cylinder, the lift force becomes $F_y=\int_{\hat{\Gamma}}\boldsymbol{e}_y\cdot\hat{\boldsymbol{\Sigma}}\cdot\boldsymbol{n}\,d\hat{\Gamma}$. On the boundary of the moving body, the velocity of the fluid has to match that of the body and the extension field has to match the body's displacement:

$$\hat{\boldsymbol{u}}=Z\boldsymbol{e}_y\quad\text{and}\quad\hat{\boldsymbol{\xi}}_e=Y\boldsymbol{e}_y\quad\text{on}\quad\hat{\Gamma}. \tag{3.13}$$

Note here that the discrete-ALE ansatz cannot be applied, for the degrees of freedom in the problem are not finite due to the free-surface deformation. Therefore, the lift acting on the cylinder is

$$F_y=\int_{\hat{\Gamma}}\left(-\hat{p}\mathrm{I}+\frac{1}{Re}\hat{\boldsymbol{D}}(\hat{\boldsymbol{u}},\hat{\boldsymbol{\xi}}_e)\right)\hat{\boldsymbol{\Phi}}\left(\hat{\boldsymbol{\xi}}_e\right)^T\boldsymbol{n}\cdot\boldsymbol{e}_y\,d\hat{\Gamma}. \tag{3.14}$$

Considering the free-surface, the normal to its boundary in the physical domain can be decomposed in the reference domain as $\tilde{\boldsymbol{n}} = \hat{\boldsymbol{n}} + \frac{\partial \hat{\eta}_n}{\partial \hat{s}}\hat{\boldsymbol{t}} + \hat{\eta}_t \frac{\partial \hat{\boldsymbol{n}}}{\partial \hat{s}}$. Introducing the mapping through the extension field of equation 2.6 in the kinematic boundary conditions equation 3.6 of the free-surface yields

$$\frac{d}{dt}(\hat{\boldsymbol{x}} + \hat{\boldsymbol{\xi}}_e) \cdot (\hat{\boldsymbol{n}} + \frac{\partial \hat{\eta}_n}{\partial \hat{s}}\hat{\boldsymbol{t}} + \hat{\eta}_t \frac{\partial \hat{\boldsymbol{n}}}{\partial \hat{s}}) = \hat{\boldsymbol{u}} \cdot (\hat{\boldsymbol{n}} + \frac{\partial \hat{\eta}_n}{\partial \hat{s}}\hat{\boldsymbol{t}} + \hat{\eta}_t \frac{\partial \hat{\boldsymbol{n}}}{\partial \hat{s}}) \quad \text{on} \quad \hat{\Gamma}_s. \tag{3.15}$$

Similarly, the dynamic boundary condition 3.7 becomes

$$\hat{\boldsymbol{\Sigma}}\left(\hat{\boldsymbol{u}}, \hat{p}, \hat{\boldsymbol{\xi}}_e\right) \cdot (\hat{\boldsymbol{n}} + \frac{\partial \hat{\eta}_n}{\partial \hat{s}}\hat{\boldsymbol{t}} + \hat{\eta}_t \frac{\partial \hat{\boldsymbol{n}}}{\partial \hat{s}}) = \gamma \hat{\kappa} \cdot (\hat{\boldsymbol{n}} + \frac{\partial \hat{\eta}_n}{\partial \hat{s}}\hat{\boldsymbol{t}} + \hat{\eta}_t \frac{\partial \hat{\boldsymbol{n}}}{\partial \hat{s}}) \quad \text{on} \quad \hat{\Gamma}_s. \tag{3.16}$$

Obviously, an additional condition needs to be imposed on the extension field. Mainly, it needs to match the surface displacement on the free-surface boundary $\hat{\Gamma}_s$:

$$\hat{\boldsymbol{\xi}}_e = \hat{\boldsymbol{\eta}} \quad \text{on} \quad \hat{\Gamma}_s. \tag{3.17}$$

3.2.2 Steady state

To obtain the steady state, we seek time-independant solutions $\{\hat{\boldsymbol{u}}_0, \hat{p}_0, \hat{\boldsymbol{\xi}}_{e_0}, \hat{\kappa}_0, \hat{\boldsymbol{\eta}}_0\}$ to the problem described above. The so called base flow $\{\hat{\boldsymbol{u}}_0, \hat{p}_0\}$ as well as the steady state solution of the extension field $\hat{\boldsymbol{\xi}}_{e_0}$ satisfy

$$\left(\hat{\nabla}\hat{\boldsymbol{u}}_0 \hat{\boldsymbol{\Phi}}\left(\hat{\boldsymbol{\xi}}_{e_0}\right)\right)\hat{\boldsymbol{u}}_0 - \hat{\nabla} \cdot \hat{\boldsymbol{\Sigma}}\left(\hat{\boldsymbol{u}}_0, \hat{p}_0, \hat{\boldsymbol{\xi}}_{e_0}\right) = \boldsymbol{0} \quad \text{in} \quad \hat{\Omega}, \tag{3.18}$$

$$-\hat{\nabla} \cdot \hat{\boldsymbol{\Sigma}}_{\mathrm{e}}\left(\hat{\boldsymbol{\xi}}_{e_0}\right) = \boldsymbol{0} \quad \text{in} \quad \hat{\Omega}, \tag{3.19}$$

$$-\hat{\nabla} \cdot \left(\hat{\boldsymbol{\Phi}}\left(\hat{\boldsymbol{\xi}}_{e_0}\right)\hat{\boldsymbol{u}}_0\right) = 0 \quad \text{in} \quad \hat{\Omega}. \tag{3.20}$$

In the steady-state case, the cylinder is considered fixed, and the following boundary conditions are applied

$$\hat{\boldsymbol{u}}_0 = 0 \quad \text{and} \quad \hat{\boldsymbol{\xi}}_{e_0} = 0 \quad \text{on} \quad \hat{\Gamma}. \tag{3.21}$$

The kinematic and dynamic boundary conditions for the steady-state problem are

$$\hat{\boldsymbol{u}}_0 \cdot \hat{\boldsymbol{n}} = 0 \quad \text{on} \quad \hat{\Gamma}_s, \tag{3.22}$$

$$\hat{\boldsymbol{\Sigma}}\left(\hat{\boldsymbol{u}}_0, \hat{p}_0, \hat{\boldsymbol{\xi}}_{e_0}\right) \cdot \hat{\boldsymbol{n}} = \gamma \hat{\kappa}_0 \hat{\boldsymbol{n}} \quad \text{on} \quad \hat{\Gamma}_s, \tag{3.23}$$

and the static deformation of the free-surface matches the steady-state solution of the extension field

$$\hat{\boldsymbol{\xi}}_{e_0} = \hat{\boldsymbol{\eta}}_0 \hat{\boldsymbol{n}} \quad \text{on} \quad \hat{\Gamma}_s. \tag{3.24}$$

3.2.3 Perturbation

We now look for small amplitude perturbations under modal form around the steady state. For the fluid variables $\hat{\boldsymbol{q}}_f = \{\hat{\boldsymbol{u}}, \hat{p}\}$ we apply the expansion $\hat{\boldsymbol{q}}_f(\hat{\boldsymbol{x}}, t) = \hat{\boldsymbol{q}}_{f,0}(\hat{\boldsymbol{x}}) + \varepsilon \boldsymbol{q}_f(\hat{\boldsymbol{x}}) e^{-i\omega t}$ with $\varepsilon \ll 1$, $\hat{\boldsymbol{q}}_{f,0}$ the so called base flow, $\boldsymbol{q}_f$ the perturbation around that base flow and ω the complex eigenvalue. Applying a similar decomposition to all variables of the problem gives

$$\hat{\boldsymbol{u}}(\hat{\boldsymbol{x}}, t) = \hat{\boldsymbol{u}}_0(\hat{\boldsymbol{x}}) + \varepsilon \boldsymbol{u}(\hat{\boldsymbol{x}}) e^{-i\omega t} \tag{3.25}$$

$$\hat{p}(\hat{\boldsymbol{x}}, t) = \hat{p}_0(\hat{\boldsymbol{x}}) + \varepsilon p(\hat{\boldsymbol{x}}) e^{-i\omega t} \tag{3.26}$$

$$\hat{\boldsymbol{\xi}}_e(\hat{\boldsymbol{x}}, t) = \hat{\boldsymbol{\xi}}_{e_0}(\hat{\boldsymbol{x}}) + \varepsilon \boldsymbol{\xi}_e(\hat{\boldsymbol{x}}) e^{-i\omega t} \tag{3.27}$$

$$\hat{\kappa}(\hat{\boldsymbol{x}}, t) = \hat{\kappa}_0(\hat{\boldsymbol{x}}) + \varepsilon \kappa(\hat{\boldsymbol{x}}) e^{-i\omega t} \tag{3.28}$$

$$\hat{\boldsymbol{\eta}}(\hat{\boldsymbol{x}}, t) = \hat{\boldsymbol{\eta}}_0(\hat{\boldsymbol{x}}) + \varepsilon \boldsymbol{\eta}(\hat{\boldsymbol{x}}) e^{-i\omega t} \tag{3.29}$$

$$Y(t) = \varepsilon y e^{-i\omega t} \tag{3.30}$$

$$\dot{Y}(t) = \varepsilon z e^{-i\omega t} \tag{3.31}$$

Introducing this decomposition in the non-linear problem of section 3.2.1 and subtracting the steady-state equations of section 3.2.2 gives a first order linear perturbation problem. In the steady deformed configuration (see Pfister *et al.*, 2019, for more details), the perturbation equations for the fluid variables are

$$\begin{aligned}
&-i\omega \left(\underbrace{\boldsymbol{u}}_{\boldsymbol{B}_{ff}\mathbf{q}_f} + \underbrace{\left(-\boldsymbol{\xi}_e \cdot \hat{\nabla} \hat{\boldsymbol{u}}_0\right)}_{\boldsymbol{B}_{f\xi}\boldsymbol{\xi}_e} \right) = \underbrace{-\left(\boldsymbol{u} \cdot \hat{\nabla} \hat{\boldsymbol{u}}_0 + \hat{\boldsymbol{u}}_0 \cdot \hat{\nabla} \boldsymbol{u}\right) + 2\mu \hat{\nabla} \cdot \boldsymbol{D}(\boldsymbol{u})}_{\boldsymbol{A}_{uu}\mathbf{q}_f} \underbrace{-\hat{\nabla} p}_{\boldsymbol{A}_{up}\mathbf{q}_f} \\
&\underbrace{-\hat{\boldsymbol{u}}_0 \cdot \left(\left(\hat{\nabla} \hat{\boldsymbol{u}}_0\right) \left((\hat{\nabla} \cdot \boldsymbol{\xi}_e)\mathrm{I} - \hat{\nabla} \boldsymbol{\xi}_e\right)\right) - \hat{\nabla} \cdot \left[\hat{p}_0 \mathrm{I} \left((\hat{\nabla} \cdot \boldsymbol{\xi}_e)\mathrm{I} - \hat{\nabla} \boldsymbol{\xi}_e\right)^T\right]}_{\boldsymbol{A}^{(1)}_{u\xi}\boldsymbol{\xi}_e} \\
&\underbrace{-\mu \hat{\nabla} \cdot \left(\left(\hat{\nabla} \hat{\boldsymbol{u}}_0\right) \left(\hat{\nabla} \boldsymbol{\xi}_e\right) + \left(\hat{\nabla} \boldsymbol{\xi}_e\right)^T \left(\hat{\nabla} \hat{\boldsymbol{u}}_0\right)^T \right) - 2\mu \hat{\nabla} \cdot \left(\tilde{\boldsymbol{D}}(\hat{\boldsymbol{u}}_0) \left((\hat{\nabla} \cdot \boldsymbol{\xi}_e)\mathrm{I} - \hat{\nabla} \boldsymbol{\xi}_e\right)^T \right)}_{\boldsymbol{A}^{(2)}_{u\xi}\boldsymbol{\xi}_e},
\end{aligned} \tag{3.32}$$

$$0 = \underbrace{\hat{\nabla} \cdot \boldsymbol{u}}_{\boldsymbol{A}_{pu}\mathbf{q}_f} + \underbrace{\hat{\nabla} \cdot \left(\left(\hat{\nabla} \cdot \boldsymbol{\xi}_e \mathrm{I} - \hat{\nabla} \boldsymbol{\xi}_e\right) \hat{\boldsymbol{u}}_0 \right)}_{\boldsymbol{A}_{p\xi}\boldsymbol{\xi}_e}. \tag{3.33}$$

The linearisation introduces the operators $\boldsymbol{A}_{ff} = \boldsymbol{A}_{uu} + \boldsymbol{A}_{up} + \boldsymbol{A}_{pu}$ and $\boldsymbol{B}_{ff}$ that are purely driven by fluid variables, and the operators $\boldsymbol{A}_{f\xi} = \boldsymbol{A}_{u\xi}^{(1)} + \boldsymbol{A}_{u\xi}^{(2)} + \boldsymbol{A}_{p\xi}$ and $\boldsymbol{B}_{f\xi}$ that arise from the interaction of fluid and ALE variables. The perturbation equation for the extension field is

$$\mathbf{0} = \underbrace{-\hat{\nabla} \cdot \boldsymbol{\Sigma}_e(\boldsymbol{\xi}_e)}_{\boldsymbol{A}_{\xi\xi}\boldsymbol{\xi}_e}. \tag{3.34}$$

For the motion of the spring-mounted body, introducing eqs. (3.30) and (3.31) in eq. (3.3), yields

$$-i\omega y = z, \tag{3.35}$$

$$-i\omega z = -\frac{4\pi\gamma_c}{U^*} z - \left(\frac{2\pi}{U^*}\right)^2 y + \frac{4}{\pi m^*}\left(\boldsymbol{F}_f \boldsymbol{q}_f + \boldsymbol{F}_e \boldsymbol{\xi}_e\right). \tag{3.36}$$

Similarly as in equations 2.26 and 2.27 the stress tensor expressed in the steady-deformed ALE reference domain gives the two components of the lift force acting on the body

$$\boldsymbol{F}_f \boldsymbol{q}_f = \int_{\hat{\Gamma}} \left(-p\boldsymbol{n} + 2\mu \tilde{\boldsymbol{D}}(\boldsymbol{u})\boldsymbol{n}\right) \cdot \boldsymbol{e}_y \, d\hat{\Gamma}, \tag{3.37}$$

and

$$\begin{aligned} \boldsymbol{F}_e \boldsymbol{\xi}_e = &\int_{\hat{\Gamma}} \left(-\hat{p}_0 \mathrm{I} + 2\mu \tilde{\boldsymbol{D}}(\hat{\boldsymbol{u}}_0)\right)\left(\hat{\nabla} \cdot \boldsymbol{\xi}_e \mathrm{I} - \hat{\nabla}\boldsymbol{\xi}_e\right)^T \boldsymbol{n} \cdot \boldsymbol{e}_y \, d\hat{\Gamma} \\ &- \int_{\hat{\Gamma}} \mu\left((\hat{\nabla}\hat{\boldsymbol{u}}_0)(\hat{\nabla}\boldsymbol{\xi}_e) + (\hat{\nabla}\boldsymbol{\xi}_e)^T(\hat{\nabla}\hat{\boldsymbol{u}}_0)^T\right)\boldsymbol{n} \cdot \boldsymbol{e}_y \, d\hat{\Gamma}. \end{aligned} \tag{3.38}$$

The boundary conditions on the cylinder surface are

$$\underbrace{\boldsymbol{u} - z\boldsymbol{e}_y}_{A_{fz}z} = 0 \quad \text{and} \quad \underbrace{\boldsymbol{\xi}_e - y\boldsymbol{e}_y}_{A_{\xi y}y} = 0 \quad \text{on} \quad \hat{\Gamma}. \tag{3.39}$$

Let's now consider the equations on the free-surface boundary. The linearised kinematic boundary condition for the free-surface write as

$$\underbrace{-i\omega\boldsymbol{\eta} \cdot \hat{\boldsymbol{n}}}_{B_{\eta\eta}} = \underbrace{\boldsymbol{u} \cdot \hat{\boldsymbol{n}}}_{\boldsymbol{A}_{\eta f}\boldsymbol{q}_f} + \underbrace{\hat{\boldsymbol{u}}_0 \cdot \left(\frac{\partial \eta_n}{\partial \hat{s}}\hat{\boldsymbol{t}} + \eta_t \frac{\partial \hat{\boldsymbol{n}}}{\partial \hat{s}}\right)}_{\boldsymbol{A}_{\eta\eta}\boldsymbol{\eta}}. \tag{3.40}$$

Note here that the derivative of the extension field is equal to the derivative of the surface displacement on the boundary $\hat{\Gamma}_s$: $\frac{\partial \boldsymbol{\xi}_e}{\partial t}|_{\hat{\Gamma}_s}\hat{\boldsymbol{n}} = \frac{\partial \boldsymbol{\eta}}{\partial t}|_{\hat{\Gamma}_s}\hat{\boldsymbol{n}} = -i\omega\boldsymbol{\eta}e^{-i\omega t}\hat{\boldsymbol{n}}$. The linearised dynamic boundary condition writes as

$$
\begin{aligned}
0 = & \underbrace{-p\hat{\boldsymbol{n}} + 2\mu\tilde{\boldsymbol{D}}(\boldsymbol{u})\hat{\boldsymbol{n}}}_{\boldsymbol{A}_{\kappa f}\boldsymbol{q}_f} \\
& + \underbrace{\Big(-\hat{p}_0\mathrm{I} + 2\mu\tilde{\boldsymbol{D}}(\hat{\boldsymbol{u}}_0)\Big)\big(\hat{\nabla}\cdot\boldsymbol{\xi}\mathrm{I} - \hat{\nabla}\boldsymbol{\xi}\big)^T\hat{\boldsymbol{n}} - \mu\Big((\hat{\nabla}\hat{\boldsymbol{u}}_0)(\hat{\nabla}\boldsymbol{\xi}) + (\hat{\nabla}\boldsymbol{\xi})^T(\hat{\nabla}\hat{\boldsymbol{u}}_0)^T\Big)\hat{\boldsymbol{n}}}_{\boldsymbol{A}_{\kappa\xi}\boldsymbol{\xi}_e} \\
& \underbrace{-\gamma\kappa\hat{\boldsymbol{n}}}_{A_{\kappa\kappa}\kappa} \underbrace{-\hat{\kappa}_0\left(\frac{\partial\eta_n}{\partial\hat{s}}\hat{\boldsymbol{t}} + \eta_t\frac{\partial\hat{\boldsymbol{n}}}{\partial\hat{s}}\right)}_{\boldsymbol{A}_{\kappa\eta}\boldsymbol{\eta}}.
\end{aligned}
\tag{3.41}
$$

Finally, the boundary condition linking the extension field and the free-surface displacement gives

$$
\underbrace{\boldsymbol{\xi}_e - \boldsymbol{\eta}}_{\boldsymbol{A}_{\xi\eta}\boldsymbol{\eta}} = 0. \tag{3.42}
$$

Considering the coupled problem formulated in terms of the state-vector $\boldsymbol{q} = \big[\boldsymbol{q}_f, \boldsymbol{\xi}_e, y, z, \boldsymbol{\eta}, \kappa\big]$, the equations detailed in this section can be written in the following matricial system

$$
-i\omega\begin{bmatrix}
\boldsymbol{B}_{ff} & \boldsymbol{B}_{f\xi} & 0 & 0 & 0 & 0 \\
0 & 0 & 1 & 0 & 0 & 0 \\
0 & 0 & 0 & 1 & 0 & 0 \\
0 & 0 & 0 & 0 & 0 & 0 \\
0 & 0 & 0 & 0 & 0 & 0 \\
0 & 0 & 0 & 0 & \boldsymbol{B}_{\eta\eta} & 0
\end{bmatrix}\boldsymbol{q} = \begin{bmatrix}
\boldsymbol{A}_{ff} & \boldsymbol{A}_{f\xi} & 0 & \boldsymbol{A}_{fz} & 0 & 0 \\
0 & \boldsymbol{A}_{\xi\xi} & \boldsymbol{A}_{\xi y} & 0 & \boldsymbol{A}_{\xi\eta} & 0 \\
\frac{4}{\pi m^*}\boldsymbol{F}_f & \frac{4}{\pi m^*}\boldsymbol{F}_e & 0 & 1 & 0 & 0 \\
0 & 0 & -(\frac{2\pi}{U^*})^2 & -\frac{4\pi\gamma_c}{U^*} & 0 & 0 \\
\boldsymbol{A}_{\eta f} & 0 & 0 & 0 & \boldsymbol{A}_{\eta\eta} & 0 \\
\boldsymbol{A}_{\kappa f} & \boldsymbol{A}_{\kappa\xi} & 0 & 0 & \boldsymbol{A}_{\kappa\eta} & A_{\kappa\kappa}
\end{bmatrix}\boldsymbol{q}.
\tag{3.43}
$$

3.2.4 Structural sensitivity

Alternatively, we will use the concept of structural sensitivity as introduced by Giannetti & Luchini (2007). For hydrodynamic oscillators, structural sensitivity analysis of unstable global modes identifies the wavemaker region where the instability develops. This is done by computing the sensitivity tensor defined as

$$
\boldsymbol{S}(x,y) = \frac{\boldsymbol{q}^+(x,y)\boldsymbol{q}(x,y)}{\int_\Omega \boldsymbol{q}^+\cdot\boldsymbol{q}\;d\Omega}.
$$

The tensor is constructed from the product of the direct ($\boldsymbol{q}$) and adjoint ($\boldsymbol{q}^+$) modes that are solutions of the linearized and adjoint equations. Further details can be found in Giannetti & Luchini (2007); Luchini & Bottaro (2014).

3.3 Numerical implementation

3.3.1 General considerations

The equations are rewritten in a variational formulation. The weak formulation of the fluid equations is the same as Pfister *et al.* (2019). For the free-surface equations, the alternative unknown σ_n was chosen instead of κ as described in Achour (2022). As done in the previously cited work, Lagrange multipliers were added to the weak problem in order to enforce the inlet and outlet boundary conditions. Additionally, to avoid tangential displacement of the free-surface, we applied the conditions $\frac{\partial^2 \eta_t}{\partial s^2} = 0$ in the whole domain as well as $\eta_t = 0$ at the inlet and outlet. The equations are spatially discretised and solved with the FreeFem++ open-source software (Hecht, 2012). The steady state is computed using a Newton method. Note that, for the calculation of the steady-state, the reference domain $\hat{\Omega}$ can either remain undeformed or we can apply the deformation $\hat{\boldsymbol{\xi}}_{e_0}$ and produce a new deformed reference domain. The second option has been chosen for the current problem. In other words, the equations lead to a determination of the Newton increment (correction) which can be solved iteratively. At each step of the Newton iteration, the algorithm proceeds in three steps : first compute the increment, secondly, update the flow field and finally deform the domain by applying the mapping $\tilde{\boldsymbol{x}} = \hat{\boldsymbol{x}} + \hat{\boldsymbol{\xi}}_{e_0}$ to deform $\hat{\Omega}$ into the new reference domain. The eigenproblems are solved using a shift-invert method as implemented in the SLEPc library. The domain is 150 diameters in length and 80 diameters in width, and the cylinder is placed at one third of the domain length in the middle of its width. Monitoring of all computations and post-processing is done thanks to the StabFem interface (Fabre *et al.*, 2018).

3.3.2 Mesh adaptation

Adaptive mesh refinement is systematically used and different refinement procedures were applied. First a mask was applied to create a constant grid spacing in the vicinity of the free surface. Secondly, a curvature-dependent mask that enforces mesh refinement in the regions where the curvature is important was implemented. An example of the mesh produced is given figure 3.2 for $Re = 60$, $H = 2$, $Fr = 0.927$ and $\gamma \to 0$ ($Ca \to \infty$).

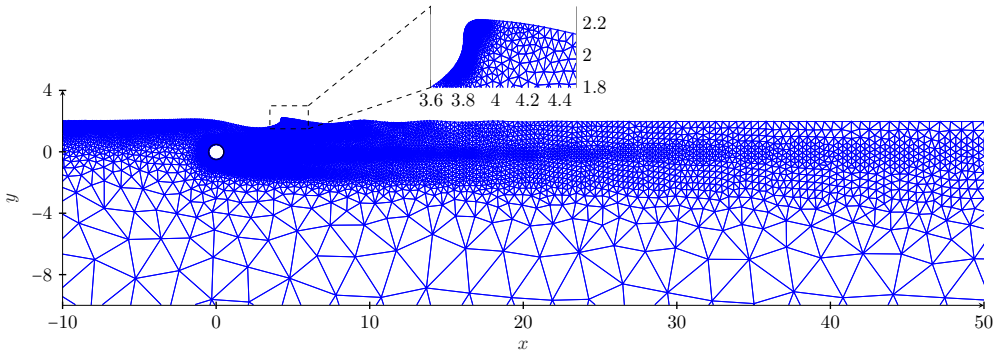

Figure 3.2: Refined mesh for $Re = 60$, $Fr = 0.927$, $H = 2$, $\gamma \to 0$.

3.3.3 Sponges

Sponges are implemented in an attempt to avoid reflection effects with the inlet and outlet boundary conditions. First, both for the steady-state and linear perturbation problems, a localized penalization on the tangential gradient of the normal free-surface displacement is implemented. By penalizing this term near the inlet and outlet, the curvature is damped. Secondly, for the linear perturbation problem, the viscosity is artificially increased at the inlet and outlet in order to dissipate perturbations that might be reflected from those boundaries. The viscosity is kept equal to its physical value in the central part of the domain and is smoothly increased toward the inlet and outlet using a hyperbolic tangent profile.

3.3.4 Direct numerical simulations with Basilisk

Additionally, the Basilisk finite volume open-source software (Popinet, 2015) is used for direct numerical simulations of the flow in the wake of a fixed cylinder submerged close to a free-surface. The incompressible Navier–Stokes equations are solved on an adaptive Cartesian grid using a second-order accurate, centred spatial discretisation. The two-phase flow is modelled using a volume-of-fluid formulation with large density and viscosity contrasts. The fixed cylinder is represented using a cut-cell embedded boundary method. Adaptive mesh refinement is applied dynamically using a wavelet-based error estimator on the volume fraction, velocity, and solid fraction fields, ensuring adequate resolution of the free surface, the immersed boundary, and the

near-wake region. We consider a square domain of size $60D$.

3.4 Validation

First, the validity of the steady-state formulation is investigated by examining the ALE treatment of the free surface. Steady-state solutions for a fixed cylinder are computed at a Reynolds number of $Re = 40$ for different values of the Froude number and immersion depth. Corresponding direct numerical simulations are also performed for comparison. Figure 3.3 shows the resulting deformation of the free surface. For both configurations considered, an excellent agreement is observed with results obtained using the Basilisk solver. In addition, for the case $H = 1.05$ and $Fr = 0.5$ (figure 3.3(a)), the predicted free-surface shape is in close agreement with that reported by González-Gutierrez *et al.* (2019).

Secondly, we assess the validity of the linear stability solver for a spring-mounted cylinder. The generalized eigenvalue problem 3.43 is solved using the steady-state solution described in section 3.2.2 for $H = 2$, $Re = 60$, $m^* = 20$, and $Fr = 0.001$. As a reference, we consider the configuration of a spring-mounted cylinder with a slip boundary condition in place of the free surface. In the limit $Fr \to 0$, the free surface remains undeformed and is therefore equivalent to a wall with a slip boundary condition. The reference results are obtained using the stability solver described in section 2.3.1, with the base flow computed via the Newton method of Fabre *et al.* (2018). The growth rates and frequencies of the leading eigenmodes are reported in figure 3.4. An excellent agreement is observed between the two approaches. Note however that this only validates the implementation of the linear ALE formulation in the bulk, not the linearised free-surface boundary conditions themselves. Finally, we can note that these results were obtained using two independent codes for the base-flow computation and two distinct linear stability solvers.

3.5 Limitations

The Newton algorithm used to compute the steady-state solutions fails to converge beyond a critical Froude number, whose value depends on both the immersion depth H and the Reynolds number Re. This loss of convergence could reflect the absence of a steady solution, possibly due to the onset of wave breaking at the free surface. Indeed, González-Gutierrez *et al.* (2019)

(a)

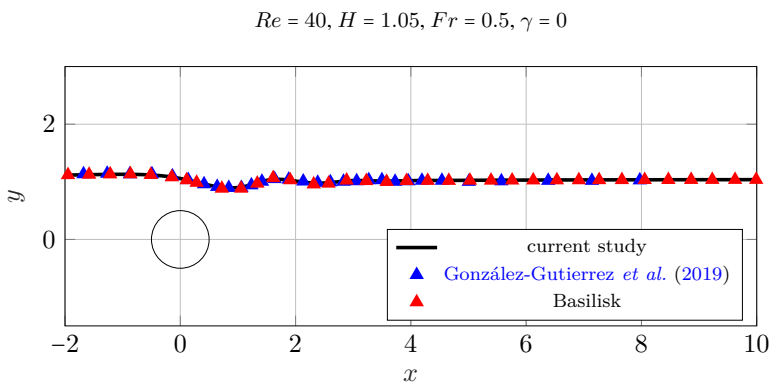

(b)

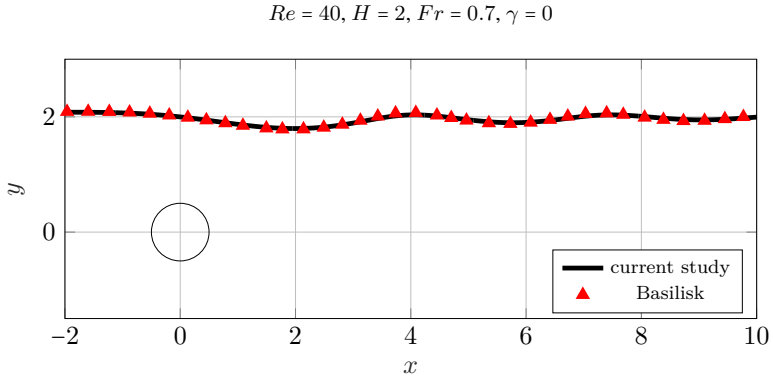

Figure 3.3: Steady-state computations of the shape of the deformed free-surface with a fixed cylinder.

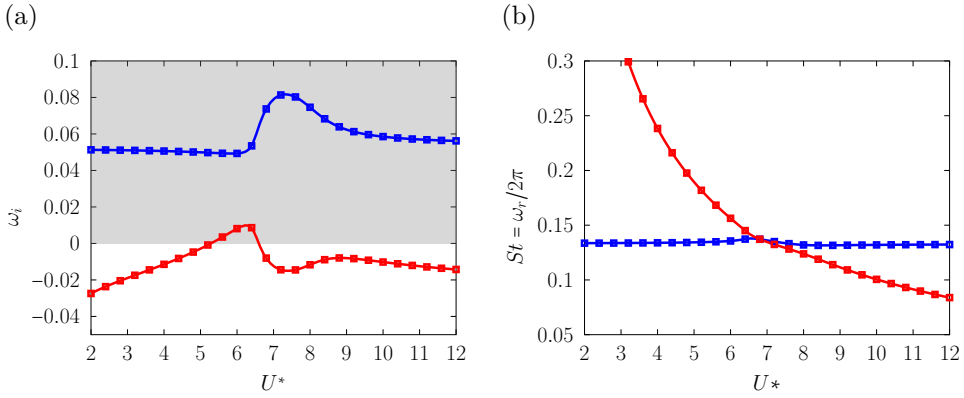

Figure 3.4: Real and imaginary parts of the leading eigenvalues with respect to U^* at $Re = 60$ for $m^* = 20$ and $H = 2$. — and — show the eigenvalues computed solving the flat free surface ($Fr = 0.001$). □ and □ show the eigenvalues computed solving the "slip-wall" problem.

were able to compute base flows at much larger Froude numbers by applying a stabilization procedure. In the present work, we restrict the study of vortex-induced vibrations to the range of Froude numbers for which steady solutions can be robustly computed. This parameter range leaves substantial scope for investigating the influence of a deformable free surface on VIV mechanisms.

Additional insight into the loss of convergence is provided in figure 3.2, which shows the mesh immediately before the Newton algorithm fails. The appearance of a sharp cusp in the free-surface profile (see zoomed inset) strongly suggests the development of wave breaking, for which a stationary solution is unlikely. Additional evidence of the onset of wave breaking is given in section 6.2.1. The ALE framework assumes a smooth and bijective mapping of the computational mesh and therefore cannot accommodate singularities such as self-intersections or topological changes of the free surface.

A natural continuation of the present work would be to investigate the bifurcation responsible for the disappearance of steady solutions. To that end, the implementation of an arc-length continuation method for steady-state computations is promising. Complementary insight could also be gained from fully nonlinear direct numerical simulations using the Basilisk solver, which is well suited to capture wave breaking.

Part III

Results

Chapter 4

Two bodies

This chapter is divided in two parts. In the first one (section 4.1), we present results for the tandem configuration of spring mounted bodies. First, results from the linear framework are presented in sections 4.1.1.1 and 4.1.1.2. This includes classical stability analysis as well as impedance-based predictions of the stability thresholds. Then, non-linear dynamics of the fixed and spring mounted cases are discussed in sections 4.1.2.1 and 4.1.2.2 respectively. A short section is dedicated to the effect of damping (4.1.2.3). In the second part (section 4.2), we discuss the linear dynamics of the side-by-side configuration.

4.1 Tandem configuration

4.1.1 Linear analysis

4.1.1.1 Paper: Stability prediction of vortex induced vibrations of multiple freely oscillating bodies

The following paper was published in the Journal of Fluid Mechanics (vol. 1032, A70, DOI: 10.1017/jfm.2026.11365). It details the development of the linear ALE framework described section 2.3. Therefore, there is a redundancy with parts of chapter 2. On the other hand, the derivation of the impedance-based criterion shortly mentioned in section 2.4 is thouroughly detailed in the paper. The methods are then applied to a tandem of spring-mounted cylinders and the parameter space is extensively explored.

Stability prediction of vortex induced vibrations of multiple freely oscillating bodies

Théo Mouyen [1,2], Javier Sierra[3], David Fabre[1] † and Flavio Giannetti[2]

[1]IMFT, Institut de Mécanique des fluides de Toulouse, CNRS, Toulouse 31400, France

[2]Università degli Studi di Salerno - Via Giovanni Paolo II, 132, 84084 Fisciano, Italia

[3]ONERA Toulouse BP74025, F-31055, Toulouse, France

(Received xx; revised xx; accepted xx)

The vortex-induced vibration of multiple spring-mounted bodies free to move in the orthogonal direction of the flow is investigated. In a first step, we derive a Linear Arbitrary Lagrangian Eulerian (L-ALE) method to solve the fluid-structure linear problem as well as a forced problem where a harmonic motion of the bodies is imposed. We then propose a low computational-cost impedance-based criterion to predict the instability thresholds. A global stability analysis of the fluid-structure system is then performed for a tandem of cylinders and the instability thresholds obtained are found to be in perfect agreement with the predictions of the impedance-based criterion. An extensive parametric study is then performed for a tandem of cylinders and the effects of mass, damping and spacing between the bodies are investigated. Finally we also apply the impedance-based method to a three-body system to show its validity to a higher number of bodies.

Key words: vortex shedding, parametric instability, flow–structure interactions, impedance-based stability criterion

1. Introduction

Fluid-induced vibrations (FIV) are of great interest to many fields of engineering. They are generally classified either as vortex-induced vibrations (VIV), wake-induced vibrations (WIV) or galloping. In the field of engineering, we find two main design philosophies. On the one hand, the design of structures that prevent such vibrations to avoid damage is an obvious example. Griffin & Ramberg (1982) reviewed studies on vortex-induced vibrations of marine risers and listed means to suppress such oscillations. On the other hand, we find the design of oscillating/deformable structures that are conceived to harvest energy. Here, one aims to optimise the motion of the submerged rigid body or deformation of the flexible structure in order to harvest the most energy. Some examples include submerged oscillating/deformable structures that are able to convert energy from marine currents and waves (Bernitsas 2016, see review from). The Wave Carpet project developed by Alam (2012) aims to extract energy

† Email address for correspondence: david.fabre@imft.fr

from waves using a deformable carpet. In contrast, the VIVACE concept from Bernitsas *et al.* (2008) proposes to convert kinetic energy from marine currents to electricity using vortex-induced vibrations of multiple oscillating cylinders. Energy harvesting strategies also find applications in microfluidics: for instance, Lee *et al.* (2019) proposed a MEMS energy harvester based on the oscillation of a cylinder mounted on a piezoelectric chip. In this context, at low Reynolds numbers, they found that the efficiency of the device was greater when placed in a dense field of oscillating cylinders.

The canonical case of a single freely-oscillating cylinder has been extensively studied with heavy focus on the lock-in phenomenon (Williamson *et al.* 2004). It is defined as a synchronisation between the frequency associated to transverse oscillations of the rigid body and that of the vortex shedding in the wake of the cylinder. Outside of the lock-in regime, however, the frequency tends to the vortex shedding frequency of a fixed cylinder. Navrose & Mittal (2016) found that the lock-in phenomenon induces high amplitude vibrations of the cylinder. It has also been shown that a decrease in the reduced mass ratio between the density of the body and the fluid leads to a wider synchronisation regime. Note that most studies with a single cylinder considered a single degree of freedom (1DOF) corresponding to transverse motion. According to Williamson *et al.* (2004), in-line motion, if structurally allowed (2DOF), does not change much the dynamics, and mostly turns the transverse oscillation into a figure-eight trajectory where the streamwise motion is induced by a nonlinear effect. On the other hand, pure in-line oscillations seem not to have been observed for a single cylinder. Such motion would be linked to symmetric vortex shedding, which is likely not observed.

A number of configurations involving multiple freely oscillating bodies have been explored. Authors have first focused on wake-induced vibrations (WIV). King & Johns (1976) first explored WIV of flexible cylinders (two-degree of freedom i.e. 2DOF) in tandem traversing a free surface, either rigidly connected or not, for spacings of $L/D = [1.25 - 7]$, where D is the diameter of the cylinders and L is the distance between the centres, at Reynolds numbers $Re = \frac{U_\infty D}{\nu} = [10^3 - 2 \times 10^4]$, where U_∞ is the inlet velocity and ν the fluid's viscosity. They observed both transverse oscillations and in-line oscillations, but the latter were only reported at much larger values of the Reynolds number, in the range $[10^3 - 2 \cdot 10^4]$.

Bokaian & Geoola (1984) focused on the transversal WIV (1DOF) of the rear body by fixing the front one. In the interval $Re = [2900, 5900]$, they found that the vortex shedding behind the front cylinder is suppressed for spacings of $L/D \leqslant 2$. Later studies explored in detail the WIV of a rear oscillating body in the 2DOF (Brika & Laneville 1999) and 1DOF configurations (Assi *et al.* 2006, 2010). Assi *et al.* (2010) found that for high separation between bodies, the amplitude of the rear body is decreased and resembles a VIV amplitude. Assi *et al.* (2013) (1DOF) developed the concept of wake stiffness in the galloping of cylinders placed in tandem. The steady lift across the wake is defined as a restoring force towards the center line, acting as a fluid dynamic spring. The Strouhal number associated with the wake stiffness was found to be constant with the Reynolds number. Mittal & Kumar (2001) numerically studied the tandem and staggered configurations with a 2DOF configuration for low Reynolds number ($Re = 100$) in the wake interference regime ($L/D = 5.5$). For this large spacing, the front body behaves like an isolated cylinder with trajectories resembling an eight shape. Soft lock-in was observed and the vortex-shedding frequency of the bodies is detuned from the natural frequency. The rear body displays trajectories in the shape of an eight or a tilted ovoid, whether it is placed in tandem or in staggered configuration. Papaioannou *et al.* (2008) used an Arbitrary Lagrangian-Eulerian (ALE) method to further explore the effect of spacing on the 2DOF tandem. For a $Re = 160$ and reduced mass $m^* = 10$, they explored spacings ($L/D = [2.5, 3.5, 5.0]$) corresponding to different flow regimes in the fixed tandem case (Zdravkovich 1987). Small values of the spacing lead to stronger oscillations of the

upstream cylinder over a wider reduced velocity range and shift the response curves to higher reduced velocities. Borazjani & Sotiropoulos (2009) directly simulated a tandem of cylinders with 1DOF for a low reduced mass, $L/D = 1.5$ and $Re = 200$. For low values of the reduced velocity ($U^* = 2\pi U_\infty \sqrt{m_c/k}/D$, k and m_c being the stiffness and cylinder's mass respectively), they found that the oscillation amplitudes are small and therefore outside of the lock-in region. The front cylinder exhibits larger oscillation amplitudes than the rear one. The effect of an increase of the reduced velocity is to bring the cylinders' oscillations out of phase, thus increasing their amplitudes of motion. At a critical reduced velocity, the cylinders continue to oscillate out of phase but the rear cylinder's amplitude becomes greater than the front one. In particular, the authors found a wider lock-in region than for an isolated cylinder. Besides, a structure that would be outside of the lock-in region can be brought into it by placing it in tandem with a similar structure.

Kim *et al.* (2009*b*) experimentally studied the VIV of the tandem configuration with 1DOF transversal to the fluid flow for several spacings ($L/D = 1.1-4.2$) at $Re = 4365-74200$. Five distinct regimes were identified. Regime I ($1.1 < L/D < 1.2$) features negligible vibrations due to minimal fluctuating lift forces, while Regime II ($1.2 < L/D < 1.6$) exhibits strong vibrations, particularly in the upstream cylinder, for higher reduced velocities. Regime III ($1.6 < L/D < 3.0$) shows significant vibrations of both bodies, with the upstream cylinder's response being influenced by the downstream cylinder. In Regime IV ($3.0 < L/D < 3.7$), vibrations are again minimal; the downstream cylinder stabilises the wake. Finally, Regime V ($L/D > 3.7$) displays higher vibrations in the downstream cylinder, attributed to periodic Karman vortex shedding. In a subsequent study, Kim *et al.* (2009*a*) used tripping wires to suppress vortex-induced vibrations. They found that placing the wires at an optimal position effectively suppressed vibrations in flow regimes I–IV by altering the shear layer behaviour and preventing vortex formation.

Prasanth & Mittal (2009*b*,*a*) numerically examined the free vibrations of two cylinders in the staggered and tandem configurations with 2DOF at $Re = 100$ for $m^* = 10$, $L/D = 5.5$ and compared the dynamic responses to those of a single cylinder. In the staggered configuration, the upstream cylinder behaves similarly to a single cylinder but with slightly higher oscillation amplitudes, while the downstream cylinder exhibits significantly larger transverse oscillations. Lock-in occurs over a range wider than for a single cylinder, with shared vortex shedding frequencies. The downstream cylinder in the staggered case displays both an eight-shape and orbital motions, influenced by complex vortex interactions and asymmetrical flow patterns. For the tandem configuration, the upstream cylinder shows early lock-in and significant influence from the downstream cylinder, despite having a qualitatively similar transverse response to an isolated one. The downstream cylinder experiences much larger oscillations that are twice that of a single cylinder in the laminar regime. Its behaviour mimics high Reynolds number responses, including the presence of an upper branch in vibration response. Both cylinders undergo synchronisation, with frequency and phase shifts tied to vortex shedding and lift forces. Phase differences and hysteresis effects are observed, and the flow regime is divided into different regions based on flow-structure interactions.

Griffith *et al.* (2017) investigated the dynamic response of staggered cylinders at $Re = 200$ with 1DOF, for a fixed stream-wise spacing ($L/D = 1.5$). They found that gap flow, which reverses direction as the cylinders oscillate, plays a critical role. A regime map was developed, categorising major vortex shedding modes and temporal behaviours. Unlike a single cylinder, matched natural and shedding frequencies do not produce synchronised oscillations; instead, quasi-periodic and chaotic responses emerge. For rigid cylinders, three base modes were observed: no gap flow, gap pair dominated, and wake pair dominated—shifting with cross-stream offset. Near the gap/wake pair transition, more complex flow states appear. When

cylinders are free to oscillate, low reduced velocities yield minimal motion and rear-cylinder vortex shedding. At intermediate velocities, out-of-phase oscillations enlarge the gap and produce an irregular vortex street. At higher velocities, the rear cylinder chases the front, with joint vortex shedding. As the spacing increases, vortex pairs dominate and the system approaches single-cylinder behaviour. Huera-Huarte & Gharib (2011) conducted an experimental study of VIV and WIV of a tandem of flexible cylinders (2DOF) in the wake interference regime. They found that both flexible cylinders in a tandem arrangement exhibit classical VIV near lock-in reduced velocities, regardless of the gap distance. At higher reduced velocities, their dynamic responses diverge depending on the spacing between the bodies. The upstream cylinder shows stronger VIV for smaller gaps, while the downstream cylinder may experience WIV at larger gaps, from the presence of vortex shedding in the gap region. Zhang *et al.* (2024*a*) investigated fluid-induced vibrations (1DOF) of two square cylinders in tandem through simulations and reduced-order modelling. Multiple vibration branches, such as VIV, biased oscillation, and galloping, are identified depending on reduced velocity and spacing ratio and their link to wake and structural modes is analysed. Tirri *et al.* (2023) and Zhang *et al.* (2024*b*) conducted a Linear Stability Analysis (LSA) at low Reynolds number of the tandem configuration with 1DOF over a very limited range of structural parameters. They both found two leading unstable eigenmodes, one being associated to the classical vortex shedding behaviour in the wake of a tandem of fixed bodies and the other being of structural nature since they don't have a counterpart in the case of fixed bodies.

Some other authors explored configurations with more bodies and outlined the complexity of such systems. Hosseini *et al.* (2021) have investigated the tandem configuration of both two and three fixed cylinders at $Re = 200$. They found that when the distance between the two bodies is large, the wake exhibits a two-row vortex structure. Adding a third body in that wake has no impact in the majority of cases. However, a region was identified where the placement of an additional body suppresses the vortex shedding in the gap between the two upstream bodies. The tandem of three cylinders oscillating transversely at low Reynolds number was also investigated by Chen *et al.* (2018); Zhu *et al.* (2024).

Note that, in most of the cited bibliography, configurations in which the cylinders are allowed to move in two directions (2DOF) essentially lead to the same dynamics as those in which the cylinder are only allowed to vibrate transversely (1DOF), driven by the transverse force due to antisymmetric vortex shedding. Pure in-line oscillation, which would be linked to symmetric vortex shedding, have not been reported, with the notable exception of King & Johns (1976). However, such behaviour was only observed for $Re > 10^3$, away from the range considered here. Likewise, no known study seem to have reported coupling with the third degree of freedom corresponding to rotational motion of the cylinder. Such motion would be linked to a torque, which is not expected to be significant for a cylinder, as it would be exerted by viscous stress only and not pressure, unlike for more elongated bodies where this kind of motion, known as flutter, is an important subject of research (Chai *et al.* 2021).

The consequent number of parameters in a multi-body system renders exhaustive parametric studies time-consuming, which justifies the search for new methodologies that enable a systematic scanning of the problem's parameters. A strategy for analysing fluid-structure interactions has been to project the fluid forces onto the structural degrees of freedom and treat the problem as a harmonically forced structural oscillator, using generalized aerodynamic forces (GAF) to represent the fluid loading. This line of thought was formalised early on by Hassig (1971), who introduced the $p - k$ method later also referred as Schur complement formulation. In the original formulation, the unsteady aerodynamic forces are available for harmonic oscillations at discrete reduced frequencies. In practical implementations, the use of simplified aerodynamic models (analytical or semi-empirical), frequency interpolation for the approximation of the GAFs (Houtman & Timme 2023), Kriging interpolation (Timme

et al. 2011) or POD-based (Bekemeyer & Timme 2019) has historically been a pragmatic way to reduce computational cost.

The idea of exploiting the unsteady forces exerted on a body undergoing prescribed oscillatory motion to predict instability was also pursued by Sabino *et al.* (2020). In that work, the unsteady forces were obtained by the exact resolution of the linearized Navier–Stokes equations, rather than from aerodynamic models or frequency interpolation. Subsequently, they defined a mechanical impedance as the ratio between the lift force and the velocity of the cylinders. This allowed to treat the problem by exploiting an analogy with electric systems (Conciauro & Puglisi 1981) for which an impedance of negative real part is a necessary condition for instability. Note that a similar concept of impedance can be applied to acoustic systems, as was done by Fabre *et al.* (2019) for an oscillating flow through a thin circular aperture. It was then applied for the stability prediction of the flow through a circular aperture in a thick plate (see Fabre *et al.* 2020; Sierra-Ausin *et al.* 2022)

The objective of this study is to extensively explore the stability of the flow past a tandem of oscillating cylinders, exploiting the impedance method just outlined. As the coupling with the other degrees of freedom is not expected to be significant, we restrict to a single degree of freedom (1DOF) for each cylinder corresponding to transverse motion. The instability of the tandem is first investigated through the fluid-structure problem in an Arbitrary Lagrangian-Eulerian frame and a Linear Stability Analysis is performed for several (Re, m^*, U^*). Secondly, we derive an impedance-based criterion from calculations of the forced case, i.e., where the cylinders are forced to oscillate sinusoidally in the transverse direction of the flow. The results of the coupled case and the impedance-based predictions are compared and we then use the impedance-based method to explore the stability of the tandem for a vast range of parameters.

2. Problem formulation

We consider N spring-mounted cylinders immersed in a Newtonian, incompressible fluid. Let $\tilde{\Omega}(t)$ denote the (deformable) fluid domain and $\tilde{\Gamma}_i(t)$ its interface with the cylinders. The flow is physically parametrized by dynamic viscosity ν, density ρ, incoming velocity U_∞, diameter D and spacing L between the cylinders, yielding two dimensionless parameters, the Reynolds number $Re = \frac{U_\infty D}{\nu}$ and the spacing ratio L/D. The fluid flow is described by the velocity and pressure fields $\tilde{\boldsymbol{u}}, \tilde{p}$, which are governed, in non-dimensional form, by the following set of equations and boundary conditions at the cylinder walls:

$$\left.\frac{\partial \tilde{\boldsymbol{u}}}{\partial t}\right|_{\tilde{\boldsymbol{x}}} + (\tilde{\boldsymbol{\nabla}}\tilde{\boldsymbol{u}}) \cdot \tilde{\boldsymbol{u}} - \tilde{\boldsymbol{\nabla}} \cdot \tilde{\boldsymbol{\sigma}}(\tilde{\boldsymbol{u}}, \tilde{p}) = \boldsymbol{0} \qquad \text{in} \quad \tilde{\Omega}(t), \tag{2.1}$$

$$\tilde{\boldsymbol{\nabla}} \cdot \tilde{\boldsymbol{u}} = 0 \qquad \text{in} \quad \tilde{\Omega}(t), \tag{2.2}$$

$$\tilde{\mathbf{u}} = \dot{Y}_i \mathbf{e}_y \qquad \text{on} \quad \tilde{\Gamma}_i(t). \tag{2.3}$$

The symbol $(\tilde{\ })$ is used for time-dependent quantities as well as time and spacial derivatives evaluated in the time-dependent domain. $(\dot{\ })$ refers to time derivatives. The stress tensor is defined as $\tilde{\boldsymbol{\sigma}}(\tilde{\boldsymbol{u}}, \tilde{p}) = -\tilde{p}\mathrm{I} + 2\mu\tilde{\boldsymbol{D}}(\tilde{\boldsymbol{u}})$ with $\tilde{\boldsymbol{D}}(\tilde{\boldsymbol{u}}) = \left(\tilde{\boldsymbol{\nabla}}\tilde{\boldsymbol{u}} + \tilde{\boldsymbol{\nabla}}\tilde{\boldsymbol{u}}^T\right)$. The notation $(|_{\tilde{\boldsymbol{x}}})$ refers to the time derivative in the deformed domain. This term contains the coupling with the motion of the body through the deformation of the domain, handled by the ALE framework as will be explained below. The coupling is also contained in the boundary condition 2.3. In the latter, $Y_i(t)$ is the instantaneous displacement of the i-th cylinder in the transverse direction.

The cylinders are physically parametrized by their masses m_{c_i}, spring stiffnesses k_i and damping parameters g_i. In a nondimensional way, this yields three nondimensional

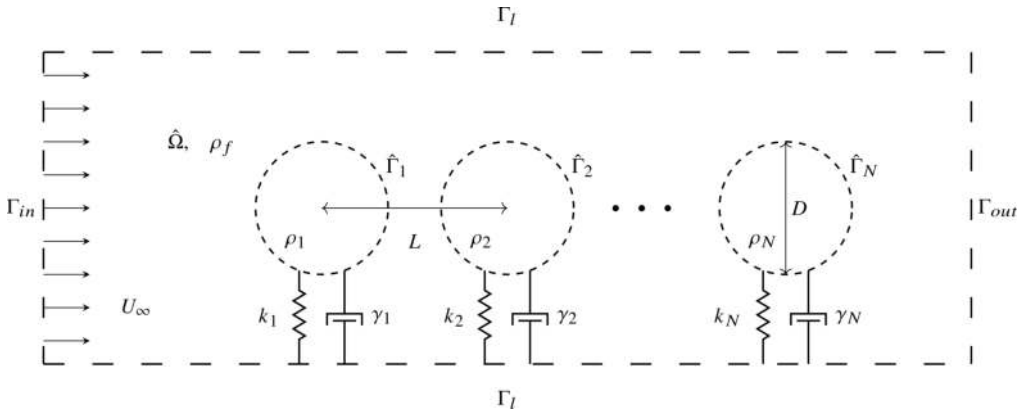

Figure 1: Array of N spring mounted cylinders with densities, spring stiffness and damping parameters: ρ_i, k_i and γ_i. The cylinders are immersed in a fluid domain $\hat{\Omega}$ of density ρ_f. The domain is delimited by inlet and outlet boundaries, Γ_{in} and Γ_{out} as well as lateral boundaries Γ_l.

parameters for each cylinder, namely a mass ratio $m_i^* = \frac{4m_{c_i}}{\pi D^2 \rho_f}$, a reduced velocity $U_i^* = 2\pi U_\infty \sqrt{m_{c_i}/k_i}/D$, and a damping coefficient $\gamma_i = g_i/(2\sqrt{m_{c_i} k_i})$. The equation governing the motion of the i-th cylinder is, in a non-dimensional form:

$$\ddot{Y}_i + \frac{4\pi\gamma_i}{U_i^*}\dot{Y}_i + \left(\frac{2\pi}{U_i^*}\right)^2 Y_i = \frac{4F_{y_i}(t)}{\pi m_i^*}, \qquad \text{for } i = 1, \ldots, N, \tag{2.4}$$

$$\text{with } F_{y_i} = \int_{\tilde{\Gamma}_i} \boldsymbol{e}_y \cdot \tilde{\boldsymbol{\sigma}} \cdot \boldsymbol{n}\, d\tilde{\Gamma}_i. \tag{2.5}$$

2.1. *Arbitrary Lagrangian Eulerian formulation*

2.1.1. *General formalism*

The Arbitrary Lagrangian Eulerian method is a conforming method that allows to treat interfaces in a Lagrangian frame of reference while the fluid is treated in an Eulerian frame of reference. We consider a fixed reference domain $\hat{\Omega}$ where unknowns are evaluated in an Eulerian frame of reference. Lagrangian variables on the other hand are evaluated on the actual physical domain $\tilde{\Omega}(t)$, which is time-dependent. Let us define the diffeomorphism $\mathcal{A}$ that allows us to express the position $\tilde{\boldsymbol{x}}(t)$ of the actual domain with respect to the position $\hat{\boldsymbol{x}}$ of the reference domain:

$$\begin{aligned} \mathcal{A} : \hat{\Omega} \times \mathbb{R}^+ &\longrightarrow \tilde{\Omega} \times \mathbb{R}^+, \\ (\hat{\boldsymbol{x}}, t) &\longmapsto (\tilde{\boldsymbol{x}}(t), t)\,. \end{aligned} \tag{2.6}$$

This diffeomorphism allows a mapping of the actual domain through the position

$$\tilde{\boldsymbol{x}} = \hat{\boldsymbol{x}} + \hat{\boldsymbol{\xi}}_e(\hat{\boldsymbol{x}}, t), \tag{2.7}$$

where $\hat{\boldsymbol{\xi}}_e$ is an extension displacement field that propagates the Lagrangian interface deformation to the fluid domain (as schematised in figure 2). This field is arbitrary and it is determined as a solution of an elliptic equation, $-\hat{\nabla} \cdot \boldsymbol{\mathcal{E}}\left(\hat{\boldsymbol{\xi}}_e\right) = \boldsymbol{0}$, which ensures a smooth distribution over the whole domain. Following the methodology employed by Pfister *et al.* (2019), we apply the diffeomorphism to the Lagrangian variables and we substitute them into

eqs. (2.1) and (2.2) which yields the ALE formulation of the incompressible Navier-Stokes equation in a stress-free configuration:

$$\hat{J}\left(\hat{\boldsymbol{\xi}}_e\right)\frac{\partial \hat{\boldsymbol{u}}}{\partial t}+\left((\hat{\boldsymbol{\nabla}}\hat{\boldsymbol{u}})\hat{\boldsymbol{\Phi}}\left(\hat{\boldsymbol{\xi}}_e\right)\right)\left(\hat{\boldsymbol{u}}-\frac{\partial \hat{\boldsymbol{\xi}}_e}{\partial t}\right)-\hat{\boldsymbol{\nabla}}\cdot\hat{\boldsymbol{\Sigma}}\left(\hat{\boldsymbol{u}},\hat{p},\hat{\boldsymbol{\xi}}_e\right)=\mathbf{0}\quad\text{in}\quad\hat{\Omega}, \tag{2.8}$$

$$-\hat{\boldsymbol{\nabla}}\cdot\boldsymbol{\mathcal{E}}\left(\hat{\boldsymbol{\xi}}_e\right)=\mathbf{0}\quad\text{in}\quad\hat{\Omega}, \tag{2.9}$$

$$-\hat{\boldsymbol{\nabla}}\cdot\left(\hat{\boldsymbol{\Phi}}\left(\hat{\boldsymbol{\xi}}_e\right)\hat{\boldsymbol{u}}\right)=0\quad\text{in}\quad\hat{\Omega}. \tag{2.10}$$

In the previous expressions, $\hat{\boldsymbol{\nabla}}$ is the gradient in the reference coordinates. $\hat{\boldsymbol{\Phi}}\left(\hat{\boldsymbol{\xi}}_e\right)=\hat{J}\left(\hat{\boldsymbol{\xi}}_e\right)\hat{\boldsymbol{F}}\left(\hat{\boldsymbol{\xi}}_e\right)^{-1}$ denotes the deformation operator introduced by the change of variables, with $\hat{J}\left(\hat{\boldsymbol{\xi}}_e\right)=\det\left(\hat{\boldsymbol{F}}\left(\hat{\boldsymbol{\xi}}_e\right)\right)$ the Jacobian of the deformation gradient $\hat{\boldsymbol{F}}\left(\hat{\boldsymbol{\xi}}_e\right)=\mathrm{I}+\hat{\boldsymbol{\nabla}}\hat{\boldsymbol{\xi}}_e$. The ALE fluid stress tensor expressed in the reference configuration writes as

$$\hat{\boldsymbol{\Sigma}}\left(\hat{\boldsymbol{u}},\hat{p},\hat{\boldsymbol{\xi}}_e\right)=\hat{\boldsymbol{\sigma}}\left(\hat{\boldsymbol{u}},\hat{p},\hat{\boldsymbol{\xi}}_e\right)\hat{\boldsymbol{\Phi}}\left(\hat{\boldsymbol{\xi}}_e\right)^T, \tag{2.11}$$

where $\hat{\boldsymbol{\sigma}}=-\hat{p}\mathrm{I}+\frac{1}{Re}\hat{\boldsymbol{D}}$, with the viscous dissipation tensor defined as

$$\hat{\boldsymbol{D}}\left(\hat{\boldsymbol{u}},\hat{\boldsymbol{\xi}}_e\right)=\frac{1}{2}\frac{1}{\hat{J}\left(\hat{\boldsymbol{\xi}}_e\right)}\left((\hat{\boldsymbol{\nabla}}\hat{\boldsymbol{u}})\hat{\boldsymbol{\Phi}}\left(\hat{\boldsymbol{\xi}}_e\right)+\hat{\boldsymbol{\Phi}}\left(\hat{\boldsymbol{\xi}}_e\right)^T(\hat{\boldsymbol{\nabla}}\hat{\boldsymbol{u}})^T\right). \tag{2.12}$$

Hereinafter, we particularize the elliptic operator $\boldsymbol{\mathcal{E}}=\nabla$, that is, the extension displacement field is determined by solving a Laplace equation. The complete formulation used to determine the extension field is as follows,

$$\begin{cases}\Delta\hat{\boldsymbol{\xi}}_e=\mathbf{0}, & (2.13)\\ \hat{\boldsymbol{\xi}}_e=Y_i\mathbf{e}_y\quad\text{on}\quad\hat{\Gamma}_i. & (2.14)\end{cases}$$

2.1.2. *The discrete-ALE ansatz*

Equation 2.13 is linear, and the number of cylinders is finite; thus, according to the superposition principle, we can look for a solution of the extension field as a function of the cylinders' vertical displacement:

$$\hat{\boldsymbol{\xi}}_e=\sum_{i=1}^{N}Y_i(t)\boldsymbol{\xi}_{e_i}, \tag{2.15}$$

where $\boldsymbol{\xi}_{e_i}$ is an elementary field associated to the displacement of the i-th cylinder, namely the solution of the elementary problem

$$\begin{cases}\Delta\boldsymbol{\xi}_{e_i}=\mathbf{0}, & (2.16)\\ \boldsymbol{\xi}_{e_i}=\mathbf{e}_y\quad\text{on}\quad\hat{\Gamma}_i, & (2.17)\\ \boldsymbol{\xi}_{e_i}=\mathbf{0}\quad\text{on}\quad\hat{\Gamma}_{j,i\neq j}. & (2.18)\end{cases}$$

We call (2.15) the *discrete-ALE ansatz*. The main advantage of this expression is that it is sufficient to solve N elementary problems once to reconstruct the deformation field for all possible values of Y_i, allowing for a reduction of the computational time required to solve the entire system.

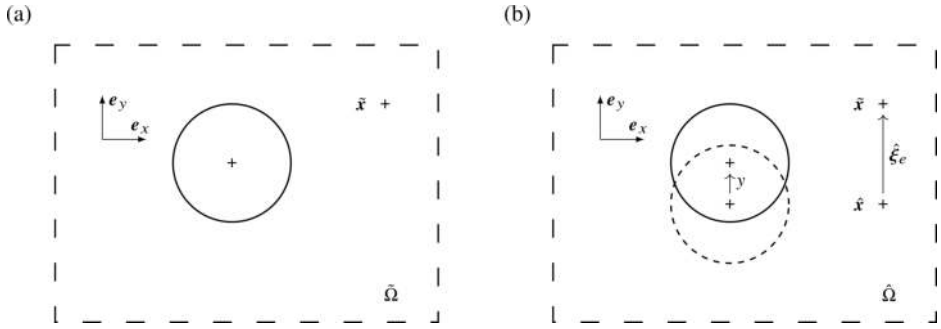

Figure 2: Sketch of the geometrical transformations involved in the ALE approach: (a) Actual time-dependent domain and (b) reference domain.

2.2. *Linearized VIV problem*

Following the usual approach, both the fluid and structural variables are decomposed into a steady component and a small-amplitude perturbation which is searched under a modal form. Namely, for the fluid part of the problem, we start with the expansion

$$\hat{\boldsymbol{q}}_f(\hat{\boldsymbol{x}}, t) = \boldsymbol{q}_{f,0}(\hat{\boldsymbol{x}}) + \varepsilon \boldsymbol{q}_f(\hat{\boldsymbol{x}}) e^{-i\omega t} \tag{2.19}$$

were $\boldsymbol{q}_{f,0}$ is the so-called *base flow*, corresponding to the steady solution of the Navier-Stokes equations in the reference domain, $\varepsilon \ll 1$, $\boldsymbol{q}_f$ is the fluid part of the eigenmode, and ω is an a-priori complex eigenvalue. Unlike in other conventions, the perturbation are chosen to be written without caret symbol. They remain however quantities that are evaluated on the reference domain.

Similarly, for the structural part of the problem, we parametrize the displacement of the cylinders by

$$Y_i(t) = \varepsilon y_i e^{-i\omega t}; \qquad \dot{Y}_i(t) = \varepsilon z_i e^{-i\omega t} \quad \text{with } z_i = -i\omega y_i. \tag{2.20}$$

The eigenmode of the fluid-structure problem is thus defined as $\boldsymbol{q} = \left(\boldsymbol{q}_f, y_1, ..., y_N, z_1, ..., z_N\right)$, where $\boldsymbol{q}_f = (\boldsymbol{u}, p)$ denotes its "fluid" part and $[y_1, ..., y_N, z_1, .., z_N]$ its "solid part".

2.2.1. *ALE fluid-structure coupled formulation*

Substituting the ansatz eq. (2.19) into eqs. (2.3), (2.4), (2.8) and (2.10) and writing the equations in the steady deformed configuration (see Pfister *et al.* 2019, for more details) leads to the following formulations:

$$
\begin{aligned}
&-i\omega\left(\underbrace{\boldsymbol{u}}_{\boldsymbol{B}_{ff}\mathfrak{q}_f}+\sum_{i=1}^{N} y_i\underbrace{(-\boldsymbol{\xi}_{e_i}\cdot\hat{\boldsymbol{\nabla}}\boldsymbol{u}_0)}_{\boldsymbol{B}_{ui}y_i}\right)=\underbrace{-\left(\boldsymbol{u}\cdot\hat{\boldsymbol{\nabla}}\boldsymbol{u}_0+\boldsymbol{u}_0\cdot\hat{\boldsymbol{\nabla}}\boldsymbol{u}\right)+2\mu\hat{\boldsymbol{\nabla}}\cdot\hat{\boldsymbol{D}}\,(\boldsymbol{u})}_{\boldsymbol{A}_{uu}\mathfrak{q}_f}\underbrace{-\hat{\boldsymbol{\nabla}}p}_{\boldsymbol{A}_{up}\mathfrak{q}_f}\\
&+\sum_{i=1}^{N}\underbrace{\left[-\boldsymbol{u}_0\cdot\left(\left(\hat{\boldsymbol{\nabla}}\boldsymbol{u}_0\right)\left((\hat{\boldsymbol{\nabla}}\cdot\boldsymbol{\xi}_{e_i})\mathrm{I}-\hat{\boldsymbol{\nabla}}\boldsymbol{\xi}_{e_i}\right)\right)-\hat{\boldsymbol{\nabla}}\cdot\left[p_0\mathrm{I}\left((\hat{\boldsymbol{\nabla}}\cdot\boldsymbol{\xi}_{e_i})\mathrm{I}-\hat{\boldsymbol{\nabla}}\boldsymbol{\xi}_{e_i}\right)^T\right]\right]}_{\boldsymbol{A}^{(1)}_{ui}y_i}y_i\\
&+\sum_{i=1}^{N}\underbrace{\left[-\mu\hat{\boldsymbol{\nabla}}\cdot\left(\left(\hat{\boldsymbol{\nabla}}\boldsymbol{u}_0\right)\left(\hat{\boldsymbol{\nabla}}\boldsymbol{\xi}_{e_i}\right)+\left(\hat{\boldsymbol{\nabla}}\boldsymbol{\xi}_{e_i}\right)^T\left(\hat{\boldsymbol{\nabla}}\boldsymbol{u}_0\right)^T\right)-2\mu\hat{\boldsymbol{\nabla}}\cdot\left(\tilde{\boldsymbol{D}}(\boldsymbol{u}_0)\left((\hat{\boldsymbol{\nabla}}\cdot\boldsymbol{\xi}_{e_i})\mathrm{I}-\hat{\boldsymbol{\nabla}}\boldsymbol{\xi}_{e_i}\right)^T\right)\right]}_{\boldsymbol{A}^{(2)}_{ui}y_i}y_i,
\end{aligned}
\tag{2.21}
$$

$$
0=\underbrace{\hat{\boldsymbol{\nabla}}\cdot\boldsymbol{u}}_{\boldsymbol{A}_{pu}\mathfrak{q}_f}+\sum_{i=1}^{N}\underbrace{\hat{\boldsymbol{\nabla}}\cdot\left((\hat{\boldsymbol{\nabla}}\cdot\boldsymbol{\xi}_{e_i}\mathrm{I}-\hat{\boldsymbol{\nabla}}\boldsymbol{\xi}_{e_i})\boldsymbol{u}_0\right)y_i}_{\boldsymbol{A}_{pi}y_i}. \tag{2.22}
$$

The boundary conditions on the object's surface are

$$
\begin{cases}
\boldsymbol{u}\cdot\boldsymbol{e}_y=z_i & \text{on}\quad \hat{\Gamma}_i, \qquad (2.23)\\
\boldsymbol{u}\cdot\boldsymbol{e}_y=0 & \text{on}\quad \hat{\Gamma}_{j,i\neq j}. \qquad (2.24)
\end{cases}
$$

They are symbolically noted as $-i\omega\sum\boldsymbol{B}^*_{fi}y_i+\boldsymbol{A}^*_{ff}\boldsymbol{q}_f=0$, where $\boldsymbol{B}^*_{fi}$ and $\boldsymbol{A}^*_{ff}$ are restriction operators extracting the degrees of freedom localized along the boundaries of the cylinders.

The linearization of eqs. (2.8) and (2.10) thus introduces the operators $\boldsymbol{A}_{ff}=\boldsymbol{A}_{uu}+\boldsymbol{A}_{up}+\boldsymbol{A}_{pu}+\boldsymbol{A}^*_{ff}$ and $\boldsymbol{B}_{ff}$ that are purely driven by fluid variables, and the operators $\boldsymbol{A}_{fi}=\boldsymbol{A}^{(1)}_{ui}+\boldsymbol{A}^{(2)}_{ui}+\boldsymbol{A}_{pi}$ and $\boldsymbol{B}_{fi}=\boldsymbol{B}_{ui}+\boldsymbol{B}^*_{fi}$ that arise from the interaction of fluid and ALE variables. In this way, eqs. (2.8) and (2.10) can be symbolically written with the previously defined operators as

$$
-i\omega\left(\boldsymbol{B}_{ff}\boldsymbol{q}_f+\sum_{i=1}^{N}\boldsymbol{B}_{fi}y_i\right)=\boldsymbol{A}_{ff}\boldsymbol{q}_f+\sum_{i=1}^{N}\boldsymbol{A}_{fi}y_i,\qquad\text{in }\hat{\Omega}_f. \tag{2.25}
$$

2.2.2. *Cylinder's equations*

The lift force F_{y_i} acting on the i-th cylinder was defined previously in primitive coordinates by 2.5. Using the ALE ansatz and the definition 2.11 of the stress tensor, one is led to an expression of the form

$$
F_{y_i}=\boldsymbol{F}_{if}\boldsymbol{q}_f+\sum_{j=1}^{N}F^*_{ij}y_j \tag{2.26}
$$

This expression is composed of two terms. The first is found by integrating on the boundary the stress which is purely linked to the fluid motion:

$$
\boldsymbol{F}_{if}\boldsymbol{q}_f=\int_{\hat{\Gamma}_i}\left(-p\boldsymbol{n}+2\mu\tilde{\boldsymbol{D}}(\boldsymbol{u})\boldsymbol{n}\right)\cdot\boldsymbol{e}_y\,d\hat{\Gamma}_i. \tag{2.27}
$$

The second component contains the effect of the deformation of the domain associated with the ALE method, and thanks to the discrete-ALE ansatz, it depends only upon the elementary extension fields $\boldsymbol{\xi}_j$ associated with each of the cylinders:

$$F^*_{ij} = \int_{\hat{\Gamma}_i} \left(-p_0 \mathrm{I} + 2\mu \tilde{\boldsymbol{D}}(\boldsymbol{u}_0) \right) \left(\hat{\boldsymbol{\nabla}} \cdot \boldsymbol{\xi}_{e_j} \mathrm{I} - \hat{\boldsymbol{\nabla}} \boldsymbol{\xi}_{e_j} \right)^T \boldsymbol{n} \cdot \boldsymbol{e}_y \, d\hat{\Gamma}_i$$
$$- \int_{\hat{\Gamma}_i} \mu \left((\hat{\boldsymbol{\nabla}} \boldsymbol{u}_0)(\hat{\boldsymbol{\nabla}} \boldsymbol{\xi}_{e_j}) + (\hat{\boldsymbol{\nabla}} \boldsymbol{\xi}_{e_j})^T (\hat{\boldsymbol{\nabla}} \boldsymbol{u}_0)^T \right) \boldsymbol{n} \cdot \boldsymbol{e}_y \, d\hat{\Gamma}_i. \tag{2.28}$$

Introducing eq. (2.19) in eq. (2.4), we obtain the following system for $i = 1, \ldots, N$

$$-i\omega y_i = z_i, \tag{2.29}$$

$$-i\omega z_i = -\frac{4\pi\gamma_i}{U_i^*} z_i - \left(\frac{2\pi}{U_i^*}\right)^2 y_i + \frac{4}{\pi m_i^*} \left(\boldsymbol{F}_{i,f} \boldsymbol{q}_f + \sum_{j=1}^{N} F^*_{i,j} y_j \right). \tag{2.30}$$

2.2.3. *Eigenvalue formulation for the coupled problem*

Considering the coupled problem formulated in terms of the state-vector $\boldsymbol{q}$ containing both the fluid part $\boldsymbol{q}_f$ and the solid part $[y_1, \ldots y_N, z_1, .., z_N]$, the equations detailed in the two previous subsections can be written in the following matricial system

$$-i\omega \boldsymbol{B} \boldsymbol{q} = \boldsymbol{A} \boldsymbol{q}, \tag{2.31}$$

with matrices

$$\boldsymbol{B} = \begin{bmatrix} \boldsymbol{B}_{ff} & \boldsymbol{B}_{f1} & \cdots & \boldsymbol{B}_{fN} & 0 & \cdots & 0 \\ & 1 & & & & & \\ & & \ddots & & & (0) & \\ & & & 1 & & & \\ & & & & 1 & & \\ & (0) & & & & \ddots & \\ & & & & & & 1 \end{bmatrix}, \tag{2.32}$$

and

$$\boldsymbol{A} = \begin{bmatrix} \boldsymbol{A}_{ff} & \boldsymbol{A}_{f1} & \cdots & \boldsymbol{A}_{fN} & 0 & \cdots & 0 \\ & & & & 1 & & \\ & & (0) & & & \ddots & \\ & & & & & & 1 \\ \frac{4}{\pi m^*} \boldsymbol{F}_{1f} & \frac{4}{\pi m^*} F^*_{11} - \left(\frac{2\pi}{U_1^*}\right)^2 & & \frac{4}{\pi m^*} F^*_{1N} & -\frac{4\pi\gamma_1}{U_1^*} & & \\ \vdots & \vdots & \ddots & \vdots & & \ddots & \\ \frac{4}{\pi m^*} \boldsymbol{F}_{1N} & \frac{4}{\pi m^*} F^*_{N1} & & \frac{4}{\pi m^*} F^*_{NN} - \left(\frac{2\pi}{U_N^*}\right)^2 & & & -\frac{4\pi\gamma_N}{U_N^*} \end{bmatrix}. \tag{2.33}$$

2.3. *Forced problem & Impedance*

Besides the resolution of the coupled problem as an eigenvalue problem as just described, we will also make use of an alternative method which consists of first considering the *forced problem* in which the motion of the cylinders are imposed to behave harmonically, i.e. $Y_i(t) = y_i e^{-i\omega t}$ with imposed amplitudes y_i and real frequency ω. Thanks to the linearity of the problem 2.25, we can express its solution in compact form as

$$\boldsymbol{q}_f = \sum_{j=1}^{N} \boldsymbol{q}_{fj} y_j, \quad \text{with} \quad \boldsymbol{q}_{fj} = -\left[\boldsymbol{A}_{ff} + i\omega \boldsymbol{B}_{ff}\right]^{-1} \left[\boldsymbol{A}_{fj} + i\omega \boldsymbol{B}_{fj}\right]. \tag{2.34}$$

In practice, each $\mathbf{q}_{fj}$ is the solution of the forced problem 2.21 considering a unitary displacement of the j-th cylinder, namely

$$y_j = 1; \qquad z_j = -i\omega; \quad y_{i\neq j} = z_{i\neq j} = 0. \tag{2.35}$$

One can now introduce the decomposition 2.34 into the definition 2.26, of the lift forces acting on the i-th body. Using the operators defined in 2.27 and 2.28, this leads to

$$F_{y_i} = \sum F_{ij} y_j \quad \text{where} \quad F_{ij} = \boldsymbol{F}_{if} \boldsymbol{q}_{fj} + F^*_{ij} \tag{2.36}$$

Each of the terms F_{ij} can be considered as a *transfer function* , corresponding to the ratio of the force exerted on the body i to the displacement of the body j. Note that each term F_{ij} depends only upon the elementary displacement field ξ_{e_j} and the elementary solution $\mathbf{q}_{fj}$ of the forced problem, both calculated by imposing $y_j = 1$, $z_j = -i\omega$, $y_{i\neq j} = 0$ and $z_{i\neq j} = 0$. In other words, we impose the movement of the j-th cylinder and fix all others in order to calculate F_{ij}.

Rather than this definition as a transfer function, it turns out to be more physically significant to define an *impedance* Z_{ij} relating the force on body i to the opposite of the velocity of body j, hence the definition

$$Z_{ij} = -\frac{F_{ij}}{z_j} \equiv \frac{F_{ij}}{i\omega}. \tag{2.37}$$

Note that this definition is equivalent to the one used in Sabino *et al.* (2020), except for a factor 2 due to the fact that they founded their definition upon the lift coefficient C_y instead of the dimensionless force $F_y = C_y/2$.

In a compact form, the impedance Z_{ij} can also be expressed in terms of the previously introduced operators as

$$Z_{ij} = (i\omega)^{-1} \left\{ \boldsymbol{F}_{if} \left[\boldsymbol{A}_{ff} + i\omega \boldsymbol{B}_{ff}\right]^{-1} \left[\boldsymbol{A}_{fj} + i\omega \boldsymbol{B}_{fj}\right] + F^*_{ij} \right\}. \tag{2.38}$$

2.4. *Generalised impedance criterion for a tandem of cylinders*

We will now focus on the case of a tandem of cylinders ($N = 2$). Solving the forced problem for the front and rear cylinder will respectively give the impedances Z_{11}, Z_{21} and Z_{12}, Z_{22}. We can plug equation 2.28 along with the definition of the impedances into the harmonic oscillator equations 2.29 of the fluid-structure problem, which yields:

$$\begin{cases} \left(-\omega^2 - \dfrac{4\pi\gamma_1}{U_1^*} i\omega + \left(\dfrac{2\pi}{U_1^*}\right)^2\right) y_1 = \dfrac{i\omega}{\pi m_1^*} 4 \left(Z_{11} y_1 + Z_{21} y_2\right), \\ \left(-\omega^2 - \dfrac{4\pi\gamma_2}{U_2^*} i\omega + \left(\dfrac{2\pi}{U_2^*}\right)^2\right) y_2 = \dfrac{i\omega}{\pi m_2^*} 4 \left(Z_{12} y_1 + Z_{22} y_2\right). \end{cases} \tag{2.39}$$

Building the matrix

$$Z_T = \begin{bmatrix} -\omega^2 - \dfrac{4\pi\gamma_1}{U_1^*} i\omega + \left(\dfrac{2\pi}{U_1^*}\right)^2 - \dfrac{i\omega 4 Z_{11}}{\pi m_1^*} & -\dfrac{i\omega 4 Z_{21}}{\pi m_1^*} \\ -\dfrac{i\omega 4 Z_{12}}{\pi m_2^*} & -\omega^2 - \dfrac{4\pi\gamma_2}{U_2^*} i\omega + \left(\dfrac{2\pi}{U_2^*}\right)^2 - \dfrac{i\omega 4 Z_{22}}{\pi m_2^*} \end{bmatrix}, \quad (2.40)$$

the equations 2.39 can be condensed as the following system

$$Z_T \cdot \begin{pmatrix} y_1 \\ y_2 \end{pmatrix} = 0, \quad (2.41)$$

Finally, we define a generalised impedance function as

$$H(\omega) = \det(Z_T). \quad (2.42)$$

It is an analytical function of the complex frequency $\omega = \omega_r + i\omega_i$.

At this point, we can remark that complex roots of 2.42, corresponding to nontrivial solutions of the two-dimensional system 2.41, also correspond to solutions of the fluid-structure eigenvalue problem 2.31. We thus have replaced the resolution of a matricial eigenvalue problem of large dimension by the sole inspection of a 2×2 matrix. This is however a non-linear eigenvalue problem since ω appears quadratically in Z_T and most importantly because Z_{ij} depends on ω. In practice, the computation of all physically relevant eigenvalues requires the knowledge of the functions Z_{ij} in the whole complex ω-plane. However, if one is only interested in localizing the marginally stable states, it is only required to know the values of these functions along the real ω axis. This property is at the origin of a very efficient method which will be explained and validated in section 3, and subsequently used to perform parametric studies in section 4.

The impedance-based method developed in the present work is an exact realisation of the classical $p - k$ method (Hassig 1971), as it provides a fully coupled description of the linear fluid–structure interaction. Instead of relying on approximate aerodynamic transfer functions, the fluid response is obtained directly by solving a series of forced problems, in which the bodies are imposed to oscillate harmonically at prescribed real frequencies. This procedure yields frequency-dependent impedance functions that rigorously encapsulate the hydrodynamic feedback of the flow on the moving structures. The resulting impedance matrix, combined with the structural parameters, defines a compact stability criterion from which the onset of instability can be predicted without explicitly solving the coupled eigenvalue problem. The approach thus retains the interpretability of classical generalised aerodynamic forcing (GAF) based methods while extending the concept to the exact hydrodynamic coupling derived from the full linearised Navier–Stokes equations, enabling accurate and efficient parametric stability analyses across a wide range of configurations.

The advantage of the criterion described here is that a limited number of calculations is required in order to get the stability prediction of a vast number of different cases. Once a set of forced problems are calculated for a fixed set of $\{Re \text{ and } L\}$, the stability of systems for any set of $\{U_1^*, U_2^*, m_1^*, m_2^*, \gamma_1^*, \gamma_2^*\}$ is acquired by the simple inspection of the determinant of 2×2 matrices.

2.5. *Numerical implementation*

The equations are rewritten in a variational formulation, spatially discretised and solved with the FreeFem++ open-source software (Hecht 2012). The problem is necessarily formulated along a truncated domain of sufficient dimension (see figure 1), and thus the equations are complemented with suitable boundary conditions for the external boundaries ($\Gamma_{in}, \Gamma_l, \Gamma_{out}$).

For the fluid variables, a Dirichlet boundary condition is imposed at the inflow boundary Γ_{in}: $\boldsymbol{u}_0|_{\Gamma_{in}} = U_\infty \mathbf{e}_x$ with $U_\infty \equiv 1$, and a stress-free condition is imposed on the lateral and outflow boundaries. For the ALE variables, homogeneous Dirichlet boundary conditions are imposed on all outer boundaries. Following the classical procedure, the base-flow is computed using a Newton method, and the eigenproblems are solved using a shift-invert method as implemented in the SLEPc library.

Two additional tricks are employed to lighten the resolution and/or improve the precision. First, mesh adaptation is intensively used to increase the mesh density in regions of strong gradients while decreasing it in other regions. Secondly, for the linearised problem, we employ the complex mapping method (Sierra *et al.* 2020) to characterise the stability properties of the problem and to suppress artificial unstable modes arising due to the strongly convective nature of the wake. Such a method has been successfully employed in the past in other fluid configurations, for instance, the jet flow past a circular aperture (Sierra-Ausin *et al.* 2022), a flow of two coaxial jets (Corrochano *et al.* 2023) or the wake flow past a rotating particle (Sierra-Ausín *et al.* 2022). When using the complex mapping method, the spatial structure of the global mode near the boundary becomes evanescent and does not have an influence on the stability properties of the problem.

Monitoring of all computations and post-processing is done thanks to the StabFem interface (Fabre *et al.* 2018). Following to the philosophy of this project, sample codes reproducing key results of the present paper are available on the website of the project †.

Regarding the method for threshold detection in terms of the impedance concept explained in Sec. 2.4, the numerical resolution procedure consists, in a first step, in generating a tabulation of the impedance functions Z_{ij} as function of ω and Re. Then, zeros of the generalised impedance 2.42 are computed by considering it as two functions (real and imaginary parts of $H(\omega)$ as function of the two variables ω, U^*, and a Levenberg-Marquardt method is used to solve it, using interpolation along the range of tabulated ω to evaluate the impedances Z_{ij} and their ω-derivatives.

If one looks at the computational cost of traditional Linear Stability Analysis (Arnoldi method) on a standard desktop computer on a single core, solving for 20 eigenvalues in our configuration takes approximatively 20 seconds. Let's assume that one needs a total of 10 computations in order to find the thresholds, which brings a total of 200 seconds to find the thresholds for a selected set of parameters $\{Re,\ L,\ U_1^*,\ U_2^*,\ m_1^*,\ m_2^*,\ \gamma_1^*$ and $\gamma_2^*\ \}$. The impedance-based method on the other hand, requires the computation of a set of forced problems, one of them taking approximately 5 seconds. Considering that one needs tabulated values of $\omega = [0.4 : 0.01 : 1.2]$, that brings the computational cost to 405 seconds. These calculations however, are only needed for a set of $\{Re$ and $L\}$. From there, finding the zeros of the impedance fonction for any set of $\{U_1^*, U_2^*, m_1^*, m_2^*, \gamma_1^*$ and $\gamma_2^*\}$ is instantaneous.

3. Validation

Throughout this article, we will consider a tandem of spring-mounted cylinders (with the exception of appendix B). The Reynolds numbers investigated range up to $Re = 100$ and the damping parameters of the cylinders are considered to be the same and noted $\gamma = \gamma_1 = \gamma_2$. The damping ratios are set to 0, except for section 4.2.3. The reduced velocity and reduced mass of both cylinders will be considered to be the same and will be noted as $U^* = U_1^* = U_2^*$ and $m^* = m_1^* = m_2^*$, except for part of section 4.2.5.

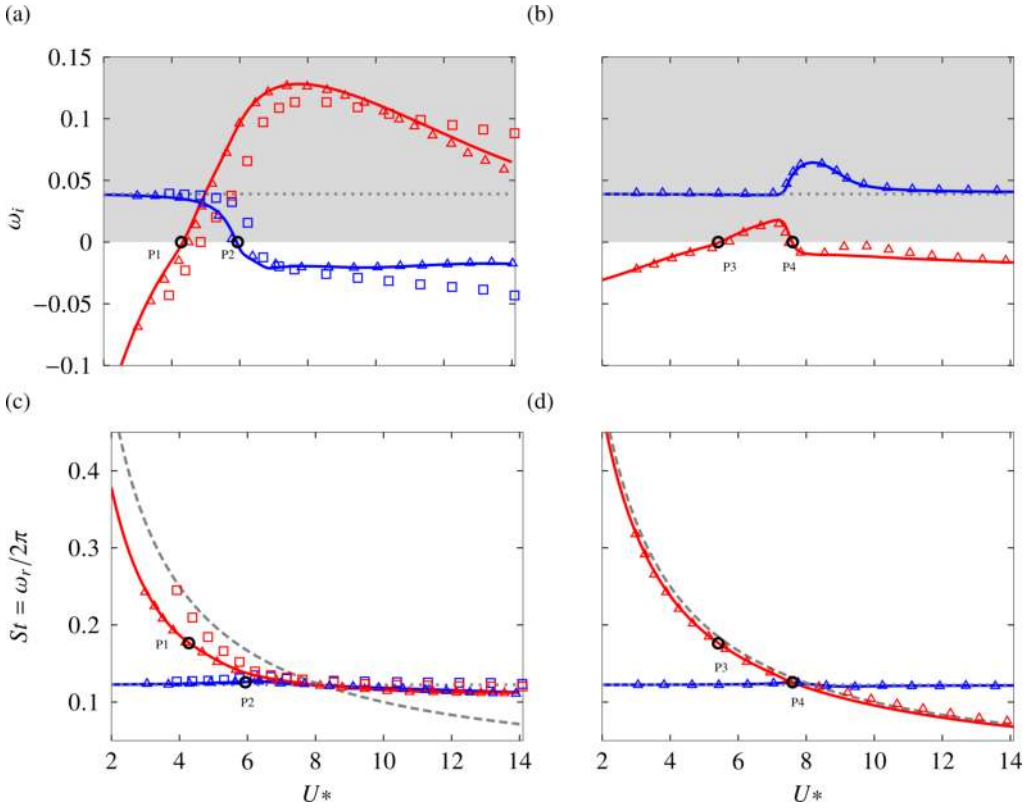

Figure 3: Real and imaginary parts of the leading eigenvalues (LSA) with respect to U^* at $Re = 100$ and $L = 1.5$ for $m^* = 2.546$ (a,c) and $m^* = 20$ (b,d). Plain lines are the results of the current study. Results from Tirri *et al.* (2023) are shown by □ and □. Results from Zhang *et al.* (2024*b*) are shown by △ and △. The unstable region is depicted as the grey zone. The natural frequency of a spring-mounted cylinder in vacuum $\omega_n = \frac{2\pi}{U_n^*}$ is shown as – –. The growth rate and frequency of the fluid mode behind two fixed cylinders are displayed as · · ·. The predictions from the impedance criterion are shown as ○.

3.1. *Linear coupled problem*

Figure 3 shows the real and imaginary parts of the leading eigenvalues against U^* for $L = 1.5$ at a Reynolds number of $Re = 100$ and for $m^* = 2.546$ and $m^* = 20$. Two leading unstable modes are found and the evolution of their growth rate and frequency is in very good agreement with Zhang *et al.* (2024*b*). For $m^* = 2.546$, we observe a slight discrepancy with results from Tirri *et al.* (2023). These authors used an immersed boundary method which was shown to yield incorrect results when the added-mass effect is not properly taken into account (Suzuki & Inamuro 2011).

3.2. *Impedance-based stability predictions*

The generalised impedance provides a criterion of instability: the system is unstable if there exists a non-trivial solution of eq. (2.41), for which $\omega_i > 0$, as described in Fabre *et al.* (2020). The link between impedance and instability can be formulated using Nyquist

† https://stabfem.gitlab.io/StabFem/

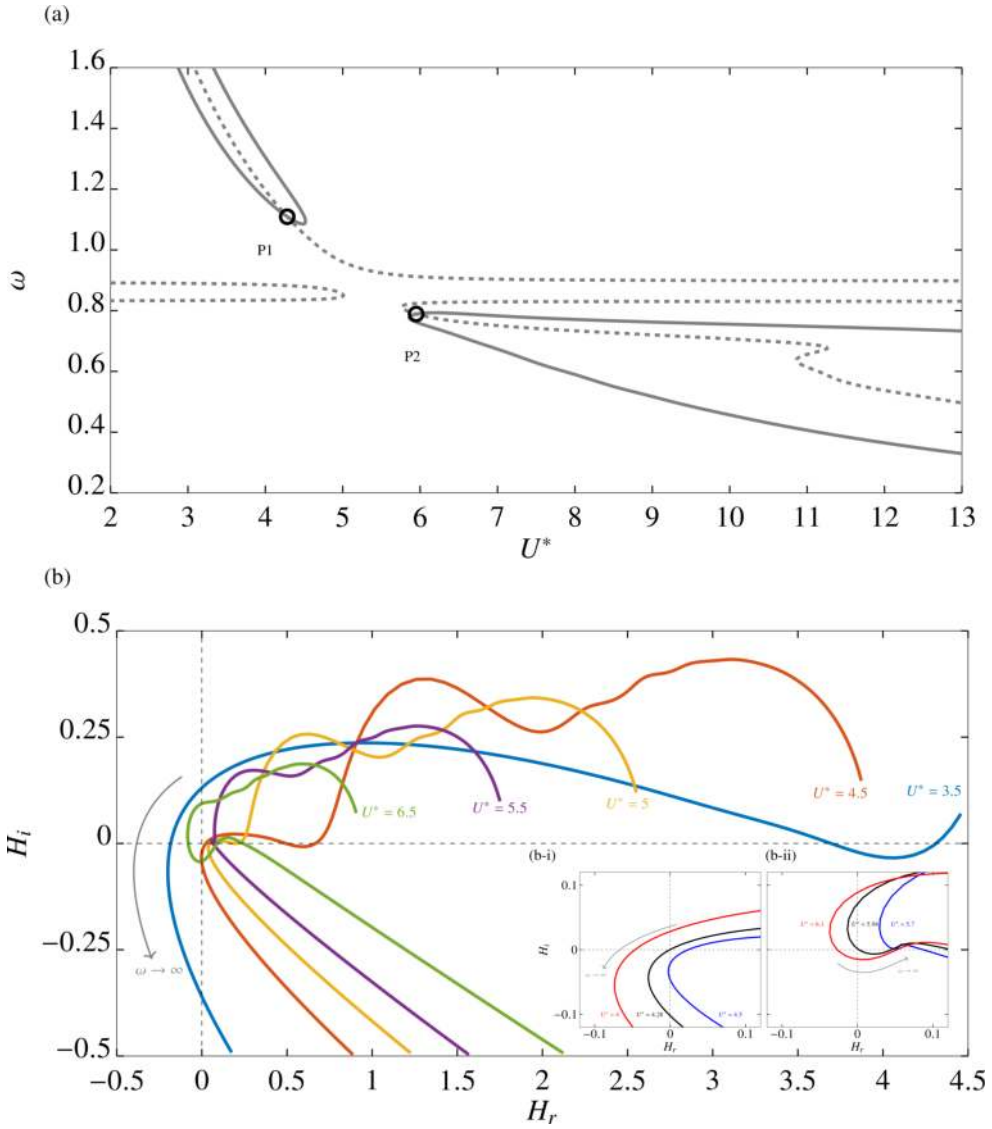

Figure 4: Illustration of the threshold detection based on the impedance criterion. (a) Zero isolines of the real (——) and imaginary (– –) parts of the impedance function H in the $\omega - U^*$ plane. The symbols ○ show the zeros of H. (b) Plot of the imaginary part of the impedance function H with respect to its real part (Nyquist curve) for several values of U^*. Nyquist curves around the points of neutral stability at $U^* = 4.28$ (b-i) and $U^* = 5.94$ (b-ii).

diagrams. Figure 4 shows an example of the threshold detection based on impedance criterion for $L = 1.5$, $Re = 100$ and $m^* = 2.546$. Figure 4(a) shows the zero isolines of both the real and imaginary parts of the function H in the $\omega - U^*$ plane. The intersection of these lines gives the predictions of U^* and ω at which the system is neutrally stable (noted as ○). These predictions are reported in figure 3(a) and 3(c) as points P1 and P2, and are in perfect agreement with the results from linear stability. Figure 4(b) shows the Nyquist diagrams, i.e., the imaginary part of the function H against its real part for different values of U^*.

For the first point of neutral stability (at $U^* = 4.38$), one eigenvalue switches from stable to unstable when increasing the reduced velocity U^*, as the Nyquist curve transitions from encircling the origin to having the origin lying at the right of the curve's trajectory, relative to its parametrization from $\omega = 0$ to $\omega \to \infty$ (see figure 4(b-i)). However, for the second point of neutral stability (at $U^* = 5.94$), one eigenvalue goes from unstable to stable when increasing the reduced velocity U^*, and the Nyquist curve transitions from having the origin lying to the right of the curve's trajectory to the curve encircling the origin (see figure 4(b-ii)). The impedance-based detection for $m^* = 20$ is also in perfect agreement with LSA results as shown in figure 3(b) and 3(d) by the points P3 and P4.

4. Results and discussion

4.1. *Description of the modes*

Let us first come back to the cases $\{L = 1.5; Re = 100; m^* = 2.546\}$ and $\{L = 1.5; Re = 100; m^* = 20\}$ which were previously used for validation and plotted in figure 3, and comment on them from a physical point of view. To explain the physical significance of these results, we will also plot figure 5 the structure of the modes for selected sets of parameters. Each eigenmode has been normalised by setting the highest velocity z_i to 1. The transversal fluid velocity u_y and the vertical velocities of each cylinder z_1 and z_2 are shown figure 5 for $Re = 100$ and for $m^* = 2.546$. The real and imaginary part of the velocities z_i are respectively plotted as an arrow with a triangle (—▷) and a circle head (—○). For the sake of readability, these amplitudes have been doubled when plotted on the following figures. With this choice of normalisation, large values of the transversal velocity u_y in the bulk (indicated by the colour ranges of the subplots) imply that the transversal motion of the cylinder associated with the mode is much weaker than the transversal fluid motion. On the other hand, a low maximum in the transversal fluid velocity implies a strong transversal motion of the cylinder.

As reported in Tirri *et al.* (2023) and Zhang *et al.* (2024*b*), the results of linear stability analysis for $m^* = 2.546$ introduces two leading eigenmodes classified as A (—) and B (—).

The A mode is unstable at low reduced velocities with its growth rate matching that of the leading mode behind the fixed tandem of cylinders $\omega_{f_i} = 0.039$ (· · · in figure 3). It becomes stable at a reduced velocity of $U^* = 5.94$ and its frequency varies little and matches the frequency of the fixed tandem mode $\omega_{f_r} = 0.76$ (· · ·), with a small decrease towards the highest values of the reduced velocity. This mode has been classified as a "fluidic" mode in the literature. Mode B has a more complex structure arising from the fluid-structure interaction. The mode becomes unstable at $U^* = 4.28$ with a maximum growth rate at $U^* = 7$. For low reduced velocities, the frequency of the mode matches the natural frequency of a structure-only system ($\omega_n = \frac{2\pi}{U_n^*}$, shown as – – in figure 3). For higher reduced velocities, its frequency tends to that of the fixed tandem mode. Both cylinders display transverse motion throughout the whole range of reduced velocities, confirming the structural nature of the mode. In accordance with the results of Tirri *et al.* (2023), the flow field of the A mode resembles that of the wake of two fixed cylinders, as can be seen in figures 5(d), 5(e) and 5(f). The large values of the transversal velocity (as seen for the colour ranges used in the subfigure) confirm the fluid-dominated nature of this mode. The region of high transversal velocity is shifted downstream with increasing reduced velocities. On the other hand, the wake of the B mode includes a high transversal velocity region localised around the bodies, especially at low reduced velocities (as seen in figure 5(a)). At higher reduced velocity, however, the high transversal velocity region is shifted downstream, resembling the structure behind a fixed tandem of cylinders. Correspondingly, for low reduced velocity, the low values of the

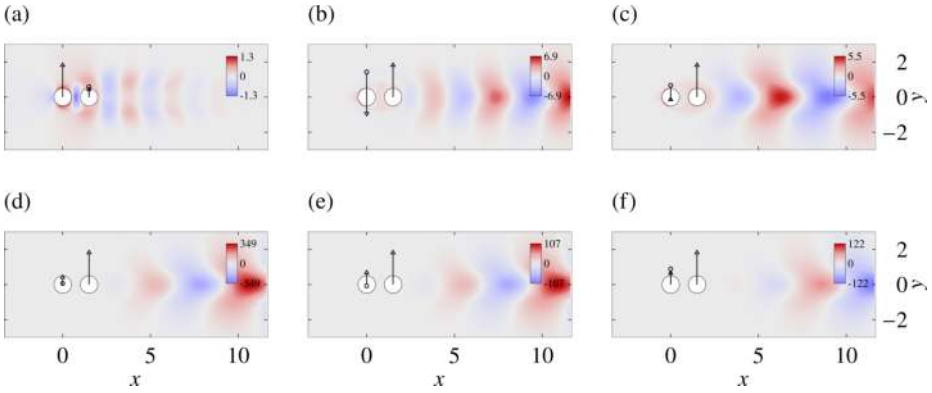

Figure 5: Transversal velocity u_y fields of the flow past a tandem of cylinder spaced of $L = 1.5$ for $Re = 100$ and $m^* = 2.546$: mode B (a,b,c) and A (d,e,f) at reduced velocities $U^* = 3$ (a,d), $U^* = 5$ (b,e) and $U^* = 8$ (d,f). See explanations in text for significance of the colour maps and representations of the cylinder's displacement.

transversal velocity show that the transversal motion of the cylinder is dominant compared to the fluid's motion (figure 5(a)). Increasing the reduced velocity, the value of the transversal velocity increases slightly as the mode transitions to a more fluid-dominated nature (figures 5(b) and 5(c)). We can also note that generally, the motion of the rear cylinder is greater than of the front, except at low reduced velocity (figure 5(a)). Navrose & Mittal (2016) found, for a single oscillating cylinder, that the high frequency of the fluid-elastic modes at low U^* was linked to a high vorticity region close to the body. On the other hand, a low frequency induced a shift of the high vorticity region downstream of the body. We observe the same link between frequency and structure of the wake for the tandem system.

For $m^* = 20$ at $Re = 100$ (see figures 3(b) and 3(d)), the A mode remains unstable for all reduced velocities investigated. Its growth rate matches that of the fixed tandem mode only to depart from it around $7 < U^* < 10$ with a maximum at $U^* = 8.2$. Its frequency is the same as that of the fixed tandem mode ω_{f_r} and the displacement of both cylinders is null. Concerning B, the mode is unstable for $5.425 < U^* < 7.6$ with a maximum in growth rate at 7.15. At $Re = 100$, its frequency follows very closely that of the natural structural-only system ω_n, as shown in figure 3. The structure of the transversal velocity of the different modes is very similar to that at a lower mass ratio. As the Reynolds number decreases, some exchanges of stability between the modes are observed, as reported in section 4.2.

4.2. *Parametric study*

4.2.1. *Neutral curves for* $m* = 2.5$ *and* 20*;* $L = 1.5$ *and* 3.

Figure 6 details the neutral stability curves in the $Re - U^*$ plane, obtained for two values of m^* and two values of L. Note that the figure displays both results obtained through the resolution of the eigenvalue problem, i.e. LSA, (●, ● and ●), and results obtained with the impedance-based method (—, — and —). The excellent agreement of the two methods gives a further validation of the impedance-based method, which will be mostly used in the subsequent section for further parametric studies in a larger range of parameters. Indeed, as already explained, once the impedance functions have been previously calculated and tabulated, one is able to generate results for all values of the structural parameters with no additional cost than simply solving a 2×2 linear system.

Consider, first, the situation for $\{L = 1.5; m^* = 2.5\}$ (figure 6(a)). At this spacing and for

a low reduced mass of $m^* = 2.5$, the A mode (●) is stable for all U^* below $Re = 75$. Above that Reynolds number, the mode is unstable for values of the reduced velocity below $U^* = 6$. Concerning B (●), it is unstable for Reynolds numbers above $Re = 18$, spanning a broad range of reduced velocities from $U^* \approx 4$ to $U^* \approx 18$. For Reynolds numbers above $Re = 80$, B is unstable for all reduced velocities above $U^* \approx 4$. Above $Re \approx 78$, the two unstable modes coexist in a region which is indicated by darker gray shading in figure 6(a).

Consider, now, the case $\{L = 1.5, m^* = 20\}$ (figure 6(b)). For this set of parameters, the mapping of the instability regions is more complex to describe, since an exchange occurs between the two leading branches. Namely, for the largest values of Re considered in the figure, an A mode exists for the whole range of U^* and a B mode exists in a range of U^* centred around the value $U^* = 7$. This is consistent with the results previously shown in figure 3(b) for $Re = 100$ where the threshold of the A branch is displayed in blue while the one of the B branch is displayed in red. When decreasing the Reynolds number, a topological transition occurs, leading to a situation where the A branch for small U^* becomes connected with what was previously the B branch and vice-versa, leading to a situation similar to what was displayed in figure 3(a) . This transition occurs for $Re \approx 84$, at which value one finds a double root of the eigenvalue problem. This exceptional point occurs at $U^* \approx 6.8$ and is identified by a marker in the figure 6(b). It is codimension-2 but does not correspond to a bifurcation point, since the coincidence occurs in the unstable region. Due to this exchange of branches, it becomes difficult to distinguish the two modes in the whole range of parameters. When decreasing further the Reynolds number, an other peculiar feature appears in the stability map. Namely, the right part of the neutral curve displays a small loop, between the values $Re = 80$ and $Re = 75$. Within this loop, two unstable modes exist. A detailed inspection shows that in this region there exists a codimension-2 point where a topological transition occurs. Both exceptional points are represented as ⊙ in figure 6(b). This complex behaviour is detailed in a supplemental material (see appendix A).

Similarly, neutral cuves for $\{L = 3; m^* = 2.5\}$ and $\{L = 3; m^* = 20\}$ are respectively plotted in figures 6(c) and 6(d). Three leading eigenmodes are found: A (●), B (●) and C (●). Figure 7 shows the transversal velocity field of the leading eigenmodes at $m^* = 2.5$ and $Re = 100$ at different reduced velocities, following the normalisation explained previously. For $m^* = 2.5$, A is unstable for $Re > 80$ in the low reduced velocity range. At $Re = 100$, the frequency of the mode is that of the fixed tandem configuration and the shape of the mode also resembles the wake mode behind the fixed tandem configuration (see figures 7(a) to 7(c)). Moreover, the displacement of both of the cylinders is negligible, as can be seen from the values of the transversal velocity. Mode B, on the other hand, is unstable over a wide range of reduced velocities (above $U^* \approx 4$), for $Re > 18$. At $Re = 100$ and for low reduced velocities, the high transversal velocity region is localised around the front body. Both cylinders exhibit high displacement as seen in figure 7(d). At the same time, the frequency of the mode follows that of the natural frequency of the structure-only spring-mounted system. Increasing the reduced velocities, the displacement of the rear cylinder becomes greater than the front one and the high transversal velocity region is shifted downstream (see figures 7(b) and 7(c)). The frequency of the mode then tends to that of the fixed tandem configuration. Mode C is unstable for $Re > 48$, over a limited range of reduced velocities, between $6 < U^* < 11$. At $Re = 100$, its frequency is that of the fixed tandem configuration. For low reduced velocities, the shape of the mode also resembles the wake mode behind the fixed tandem configuration (see figure 7(g)). However, towards higher reduced velocities, the rear cylinder exhibits large vertical displacement as can be seen from the low values of the transversal velocity in figures 7(h) and 7(i). For $m^* = 20$, the branch of neutral stability of A is shifted towards higher reduced velocities and the ranges of reduced velocities over which B and C are unstable are reduced.

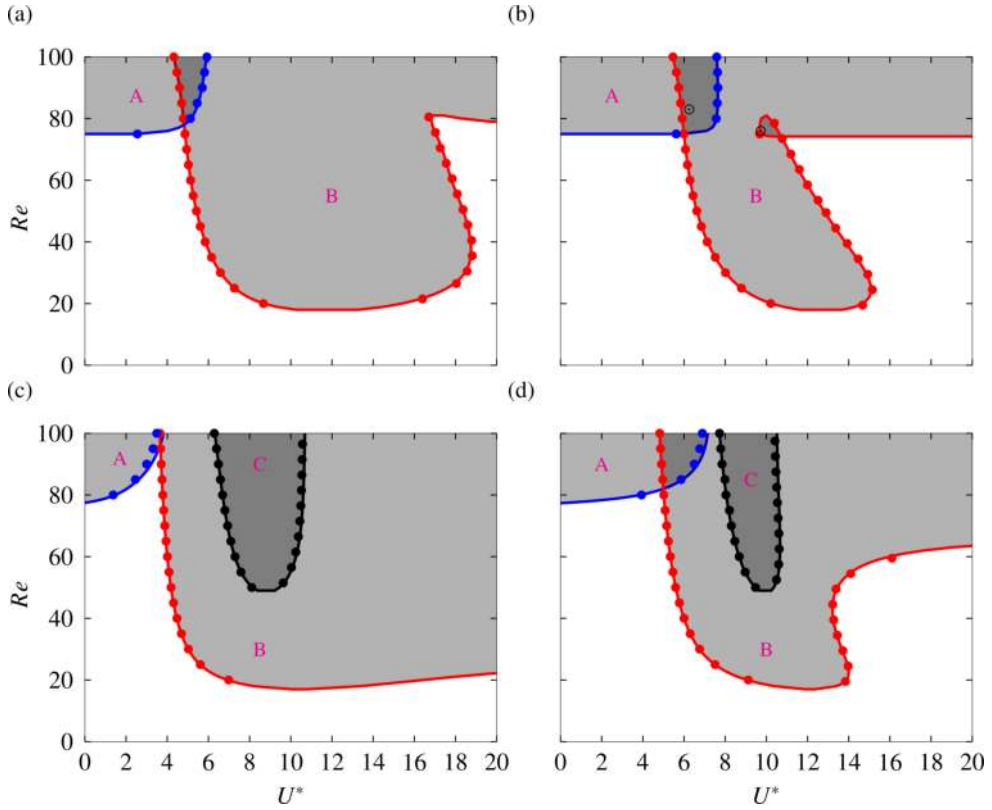

Figure 6: Regions of instability (shaded colors) in the $Re - U^*$ plane for (a,b) $L = 1.5$ and (c,d) $L = 3$; and for (a,c) $m^* = 2.5$ and (b,d) $m^* = 20$. Full lines are the results from the impedance-based predictions and markers are results from LSA. Light gray indicates regions where one unstable mode exists and dark gray regions where two unstable modes exist.

4.2.2. *Effect of the mass*

After having computed the forced problem for $L = 1.5$ and $L = 3$ over a range of Reynolds number $Re = [5 - 100]$ (by steps of $Re = 1$), we apply the impedance-based criterion for a range of reduced masses going from $m^* = 0.01$ to $m^* = 100$. The damping parameter of both cylinders is set to zero. Figure 8 shows the neutral curves in the $Re - U^*$ plane predicted by the impedance-based criterion. For $L = 1.5$ (see figure 8(a)), increasing the reduced mass of the bodies decreases the range of reduced velocities over witch B is unstable. The stability threshold of mode A is shifted towards higher reduced velocities when increasing the reduced mass, extending the range over which the mode is unstable. The exchange of stability observed at $Re \approx 84$ for $m^* = 20$ described in section 4.2.1 is also observed for higher masses. For $L = 3$ (see figure 8(b)), the stability threshold of mode A is also shifted towards higher reduced velocities and the range over which B is unstable is decreased. Concerning mode C, increasing the reduced mass also restricts the range of reduced velocities over which the mode is unstable. Generally speaking, increasing the mass has a stabilising effect on modes B and C and a destabilising effect on mode A.

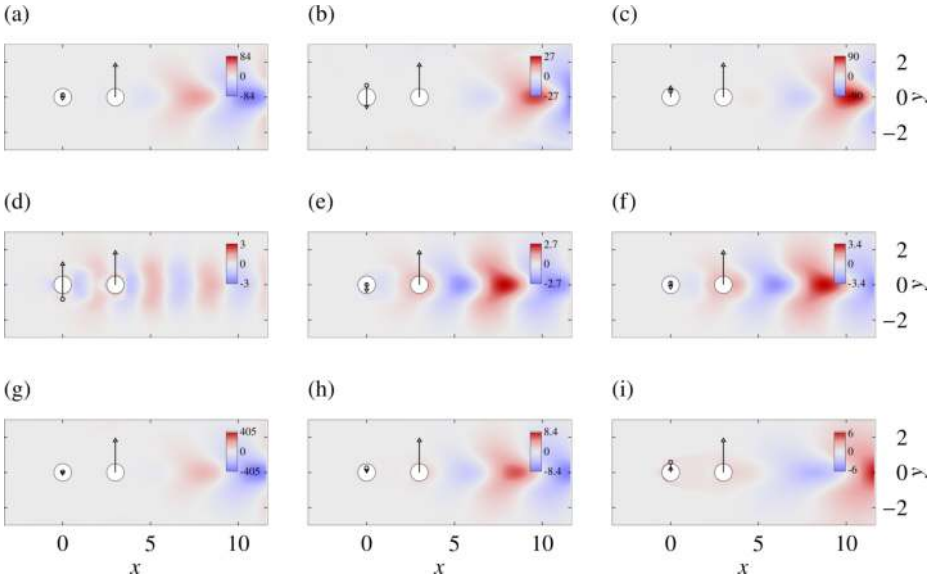

Figure 7: Transversal velocity u_y fields of the flow past a tandem of cylinder spaced of $L = 3$ for $Re = 100$ and $m^* = 2.5$: mode A (a,b,c), mode B (d,e,f) and C (g,h,i) at reduced velocities $U^* = 4$ (a,d,g), $U^* = 8$ (b,e,h) and $U^* = 12$ (d,f,i). See explanations in text for the significance of the colour maps and representations of the cylinder's displacement.

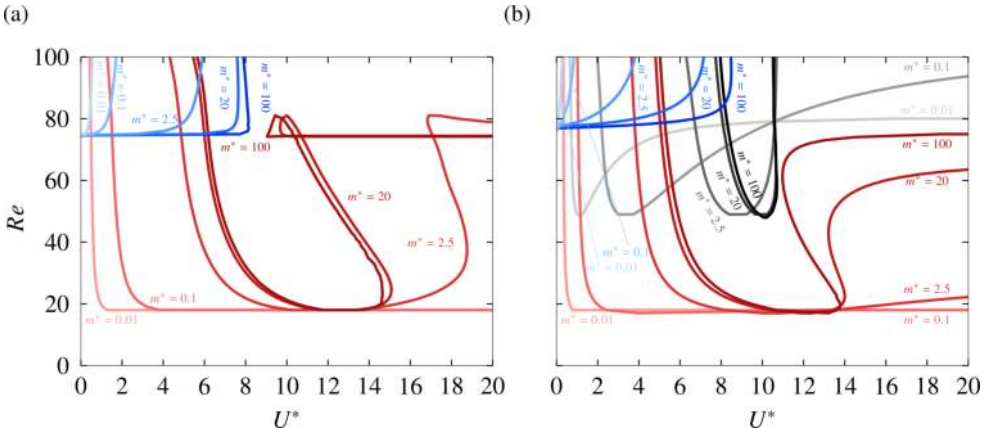

Figure 8: Curves of neutral stability in the $Re - U^*$ plane for (a) $L = 1.5$ and (b) $L = 3$, computed from the impedance-based method. The colour codes for the different modes are similar to figure 6. The colour intensity is going from light to dark for increasing masses whose values are reported in corresponding colours.

4.2.3. *Effect of the damping ratio*

From the same calculations of the forced problem, the impedance-based criterion is used for a range of damping ratios going from $\gamma = 0$ to $\gamma = 1$, keeping the reduced mass fixed to $m^* = 2.5$. Figure 9 shows the neutral curves in the $Re - U^*$ plane predicted by the impedance-based criterion. For $L = 1.5$ (see figure 9(a)), the A mode remains largely unaffected by light damping ($\gamma = 0.1$). On the other hand, the range of reduced velocities over which B is

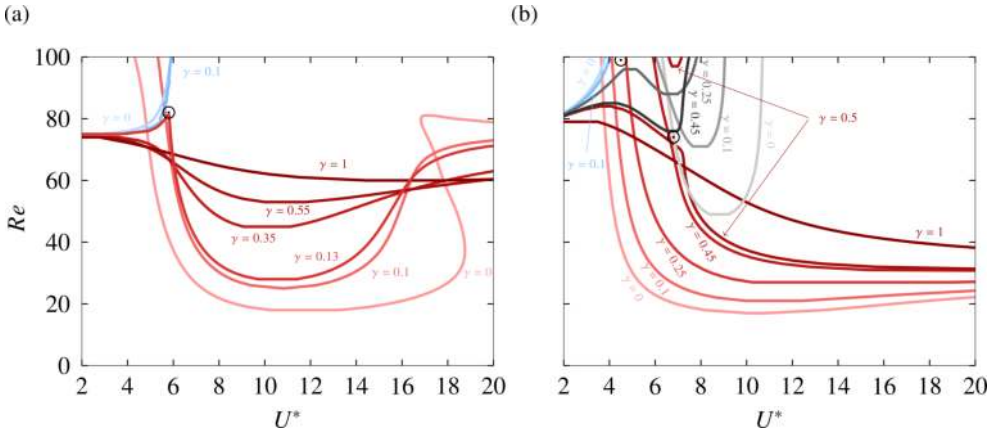

Figure 9: Curves of neutral stability in the $Re - U^*$ plane for a low reduced mass of $m^* = 2.5$ and for (a) $L = 1.5$ and (b) $L = 3$, computed from the impedance-based method. The colour codes for the different modes are similar to figure 6. The colour intensity is going from light to dark for increasing damping ratios, whose values are reported in corresponding colours.

unstable gets narrower with increasing damping. The onset of instability of B is also shifted towards higher Reynolds numbers, going from $Re = 18$ for $\gamma = 0$ to $Re = 60$ for $\gamma = 1$. The system exhibits a critical transition at between $\gamma = 0.1$ and $\gamma = 0.13$ at around $U^* \approx 6$ and $Re \approx 81$, where the branches coalesce. Figures 10(a) and 10(b) respectively show the growth rates and frequencies of the modes before and after the higher codimension point, for a fixed Re number. The frequency of the coalescing modes being the same at the exceptional point, the latter corresponds to a codimension-3 point (double Hopf with strong resonance) and is plotted as ⊙ in figure 9(a).

For $L = 3$ (figure 9(b)), the threshold of A mode is slightly shifted towards higher reduced velocities by light damping and the ranges over which B and C are unstable are reduced by increasing the damping. Two transitions are observed, which are similar to the one observed for $L = 1.5$. Between $\gamma = 0.1$ and $\gamma = 0.25$, around $Re \approx 95$ and $U^* \approx 5$, mode A and the low-U^* branch of C coalesce. Similarly, between $\gamma = 0.45$ and $\gamma = 0.5$, around $Re \approx 75$ and $U^* \approx 7$, we observe the coalescence of mode B with the low-U^* branch of the previously merged A-C modes. These exceptional points are also of codimension-3 and are plotted as ⊙ in figure 9(b).

4.2.4. *Effect of the spacing*

Figure 11 maps the stability of the tandem of cylinders in the $L - U^*$ plane for $Re = 80$ and $m^* = 2.5$. Increasing the distance between the bodies shows dynamics similar to what has been noticed for the fixed-tandem configuration by Zdravkovich (1987) or by Papaioannou *et al.* (2008) for the 2DOF tandem configuration. Mainly, the evolution of mode A, which is foremost a fluid mode, seems to follow different wake interference regimes. For $1.5 < L < 1.8$, mode A is unstable in the low U^* range, as described in section 4.2.1. This coincides with the "slender body" regime of the fixed tandem, where the free shear layer of the upstream body does not reattach to the downstream one. The vortex shedding comes from the detachment of the upstream body shear layers. For $1.8 < L < 3$, mode A is stable and mode C becomes unstable. For the fixed tandem, the shear layers of the front body reattach to the rear one. The vortex street is only formed in the wake of the rear body. In the $3 < L < 4.5$ region, A is unstable. This region could correspond to the "intermittent-regime" where the vortex street

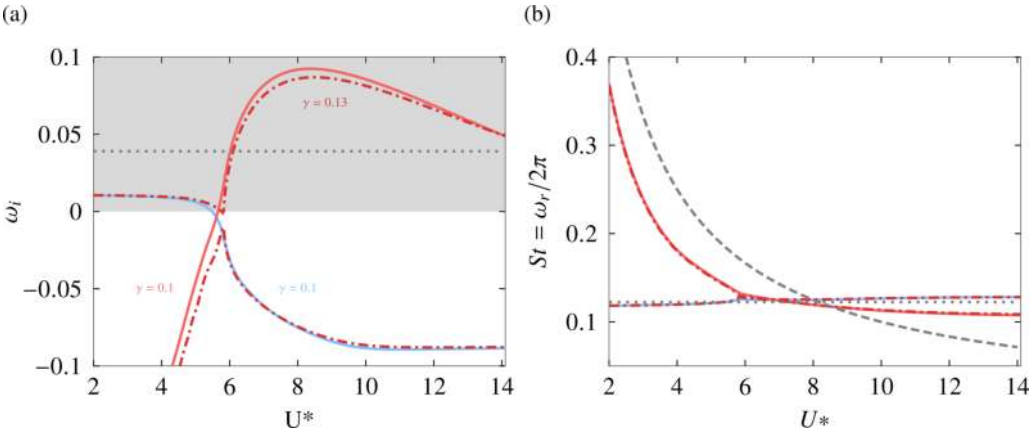

Figure 10: Growth rates (c) and frequencies (d) of the leading eigenmodes (LSA) for $L = 1.5$ and $m^* = 2.5$ at $Re = 81$. The modes for $\gamma = 0.1$ are plotted with (——) and (——) and the coalesced mode for $\gamma = 0.13$ is plotted with (– · –). The unstable region is depicted as the grey zone. The natural frequency of a spring-mounted cylinder in vacuum $\omega_n = \frac{2\pi}{U_n^*}$ is shown as – –. The growth rate and frequency of the fluid mode behind two fixed cylinders are displayed as · · ·.

of the upstream body intermittently reattaches to the rear one. In this region, the eigenmodes were found to be highly sensitive to variations in the base flow within the gap. Since the computational mesh had to be adapted for each value of the length L in order to solve the forced problem, the resulting neutral curve exhibited some oscillations. To address this, a quadratic fit was applied to smooth the curve. As of $L > 4.5$, the dynamics correspond to the binary vortex street regime where vortex streets are being shed in the wake of both bodies. Up to $L = 4.5$, the modes behave in the same way described for $L = 3$ and $Re = 100$ in section 3.2. Mainly, mode A induces no displacement of the bodies and modes B and C induce the displacement of both bodies, depending on U^*. For spacings above $L = 4.5$, however, a change of dynamics is observed. For mode A, both cylinders display motions that are of comparable amplitudes. Mode B induces higher displacement of the front cylinder than of the rear. Finally, C induces higher displacement of the rear cylinder than of the front. Mode B and C start to exhibit a decoupling of the body's motion, whereas mode A arises from the coupling of both cylinders' motion. This phenomenon is confirmed for higher distances, as is explained in the next subsection.

A possible explanation for the disappearance of mode A in the range $1.8 < L < 2.8$ might be that for this range of spacing, the second cylinder lies in the recirculation region of the first one, which corresponds to the region of absolute instability responsible for the instability. A similar explanation was given by Hosseini *et al.* (2021) in their investigation of the fixed tandem and three fixed-cylinder configurations for $Re = 200$. Accordingly, vortex shedding from the first cylinder is suppressed and the global flow reorganises. In the present case, which involves elastically mounted cylinders, the nature of mode A below $L = 4.5$ is dominated by the fluid, so one might expect this scenario to remain essentially valid.

4.2.5. *Mode decoupling at high spacing*

Figure 12 shows results from LSA and from the impedance-based method for $Re = 60$ and $m^* = 2.5$ at $L = 10$. Figures 12(a) and 12(b) respectively show the growth rate and frequency with respect to U^* for different configurations. Calculations where both bodies are

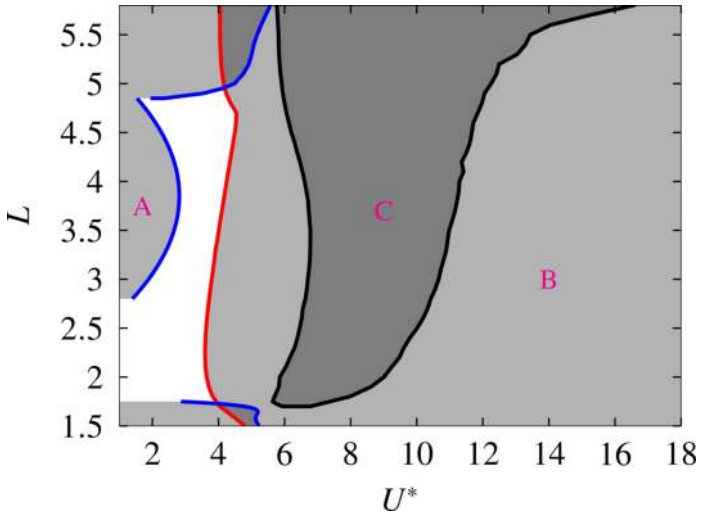

Figure 11: Curves of neutral stability in the $L - U^*$ plane for a low reduced mass of $m^* = 2.5$ at $Re = 80$, computed with the impedance-criterion. The colour codes for the different modes are similar to figure 6. Light gray indicates regions where one unstable mode exists and dark gray regions where two unstable modes exist.

spring-mounted are represented with plain lines. Calculations where either the front or rear cylinder was fixed are respectively shown with circles and rectangles. As can be seen, mode B (—) of the full problem (both cylinders free to oscillate) is identical to the mode arising from the configuration where the rear cylinder is fixed (○). On the other hand, mode C (—) is almost identical to the mode arising from the configuration where the front cylinder is fixed (□). Finally, mode A (—) only follows the mode of the rear-fixed cylinder case (○) for low U^*. For $U^* > 5.5$, neither mode □ nor ○ accounts for mode A's dynamics.

The coupled and decoupled nature of the different modes can also be seen by examination of the terms present in the impedance matrix. Let us define the diagonal terms of Z_T (equation 2.40) as

$$\begin{cases} H_1 = -\omega^2 - \dfrac{4\pi\gamma_1}{U_1^*} i\omega + \left(\dfrac{2\pi}{U_1^*}\right)^2 - \dfrac{i\omega 4 Z_{1,1}}{\pi m_1^*}, \\ H_2 = -\omega^2 - \dfrac{4\pi\gamma_2}{U_2^*} i\omega + \left(\dfrac{2\pi}{U_2^*}\right)^2 - \dfrac{i\omega 4 Z_{2,2}}{\pi m_2^*}. \end{cases} \tag{4.1}$$

Figure 12(c) shows the zero isolines of the real and imaginary parts of H_1 (respectively — and – –) and H_2 (respectively — and – –) in the $\omega - U^*$ plane. The points of neutral stability of the full linear problem (LSA) are reported in figure 12(c) as dashed circles. One can note that the zeros of H_1 approximate relatively well points P1 and P2. As shown from the LSA results, modes B and A are linked to the rear-fixed configuration at these reduced velocities. Similarly, P5 and P6 are relatively well approximated by the zeros of H_2. Correspondingly, mode C is linked to the front-fixed configuration at these reduced velocities. On the other hand, the neutral points P3 and P4 are not detected by the sole zeros of H_1 or H_2, showing there the coupled nature of mode A. Accordingly, the LSA results show that in that range of reduced velocities, A cannot be described from the front-fixed or rear-fixed configurations solely.

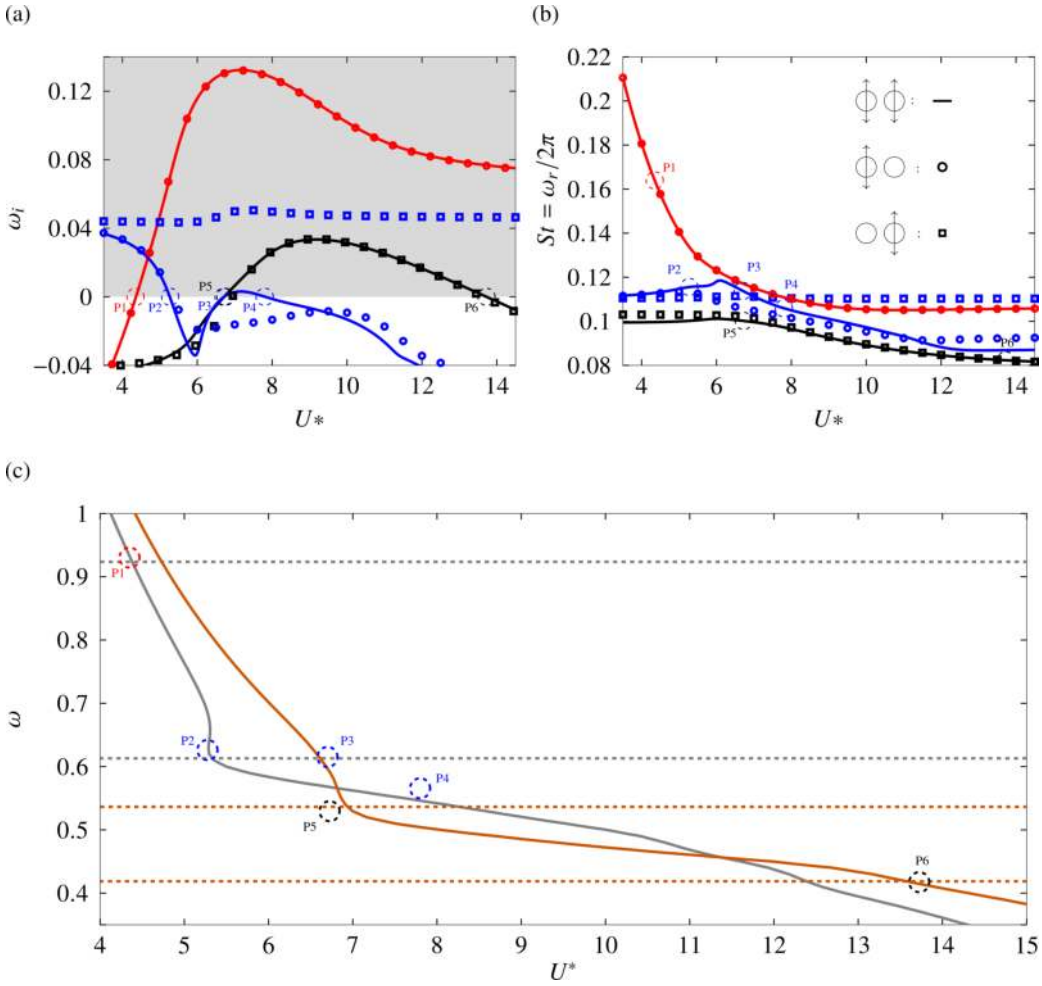

Figure 12: Results from LSA of cases with both freely oscillating cylinders (—, — and —), front cylinder fixed (□, □ and ■) and rear cylinder fixed (○, ○ and ●). Real and imaginary parts of the leading eigenvalues with respect to U^* at $Re = 60$ and $L = 10$ for $m^* = 2.5$ (a,b). Correspondingly, zero isolines of the real and imaginary parts of H_1 (respectively — and – –) and H_2 (respectively — and – –) in the $\omega - U^*$ plane (c). The points of neutral stability of the different modes for both cylinders freely oscillating are reported in both figures as ◌, ◌ and ◌.

5. Conclusion and perspectives

The purpose of this paper was to give a thorough description of the linear stability properties of the flow past a tandem of elastically-mounted cylinders, involving both a parametric analysis in a large range of parameters and a physical description of the unstable eigenmodes.

Due to the large number of parameters involved in the problem, one was led to design an efficient method to perform parametric analyses. For this sake, we designed a generic method which consists of solving in a first step a series of *forced problems* in which the cylinders are imposed to harmonically oscillate at a given real frequency ω. This allows us to define *impedance functions* $Z_{ij}(\omega)$, condensing in a synthetic way the retroaction of the fluid onto

the oscillating bodies. This allows, in a second step, to predict the instability criteria by the sole inspection of a 2×2 matrix involving the parameters of the structure (reduced mass, velocity and damping) along with these impedance functions.

The impedance-based method was compared to the resolution of the eigenvalue problem for the coupled fluid-body problems, yielding very good agreement. Using the impedance-based stability criterion, an extensive parametric study was then conducted. The effect of increasing the mass and the damping ratio are found to be generally stabilising, except for mode A which is destabilised by the increase of the mass. The stability analysis in the $L - U^*$ plane for $Re = 80$ and $m^* = 2.5$ reveals that the tandem cylinder dynamics evolve with spacing, showing similarities to previously observed wake interference regimes. Mode A dominates in certain regions and aligns with fluid instabilities, while transitions between regimes reflect changes in wake interactions, from slender body behaviour to binary vortex shedding. For $L > 4.5$, a shift in dynamics occurs, with modes B and C showing decoupled motions of the cylinders, while A remains a coupled mode. This is confirmed by further analysis at $Re = 60$ and $L = 10$, where comparison with fixed-body configurations shows that modes B and C align with the rear-fixed and front-fixed cases, respectively. A, however, cannot be captured by either configuration alone at higher reduced velocities, underscoring its coupled nature, as supported by the impedance matrix analysis.

A number of perspectives are opened for the continuation of this study. First, the formalism developed here applies to an arbitrary number of rigid bodies, with almost identical computational cost compared to the fluid problem owing to the use of the discrete-ALE ansatz. An illustration for a system of three cylinders is given in the appendix B. Extension to a higher number of bodies is straightforward. A particularly interesting perspective would be to consider periodic configurations, for which one can expect to apply Floquet-Bloch approaches allowing one to predict the large-scale dynamics of such configurations based on the resolution of problems simply formulated into an elementary cell.

Aside from increasing the number of bodies, extending to additional degrees of freedom, including streamwise oscillation and rotational motion, could also be considered. According to the discussion in the introduction, such degrees of freedom are not expected to lead to novel dynamics in the case of tandem bodies for symmetry reasons, as in-line oscillations would be coupled to symmetric vortex shedding which is unlikely to occur. On the other hand, streamwise motions could come into play for configurations such as the side-by-side cylinders or the three-cylinder in pinball configuration investigated in appendix B. In such a case, streamwise oscillations in an antisymmetric manner could happen, especially in configurations where the cylinders are close enough to lead to a global antisymmetric vortex shedding similar to that of a single composite body (Carini *et al.* 2014).

Another perspective would be to investigate the dynamics of a set of oscillating cylinders located below a free surface. Recent studies (Patel *et al.* 2025) have investigated the effect of a free surface on the vortex-shedding instability behind a fixed cylinder. Interesting dynamics can be anticipated by considering spring-mounted objects. This topic is currently the object of ongoing investigations in our team.

Lastly, since the present study was restricted to the linear regime, one should extend the study by considering nonlinear dynamics. Considering the nonlinear dynamics is especially interesting for two main reasons. First, in the course of the parametric study, a number of exceptional points of codimension 2 or 3 have been identified. Rich dynamics can be expected in the vicinity of such points, which could be elucidated thanks to nonlinear simulations or alternative approaches such as weakly nonlinear expansions, Time Spectral Method or Spectral Submanifolds. Secondly, considering the application to energy harvesting which was the original motivation for this work, evaluation of the performances and energy efficiencies necessarily requires investigation of the nonlinear regimes. A key question for

such applications will be to identify the optimal range of parameters, reduced mass and velocity, and most importantly, the parameter γ_i identified here with a damping parameter, but which for an energy harvester would rather be identified as an energy extraction coefficient.

Acknowledgements. Théo Mouyen would like to thank Edouard Boujo for sharing unpublished results and exchanging thoughts during the validation process of the L-ALE method presented in this paper.

Declaration of interests. The authors report no conflict of interest.

Data availability statement. The codes used to produce the results in this paper are available in the StabFEM open source project.

Author ORCIDs. T. Mouyen, https://orcid.org/0000-0001-9590-9126; J. Sierra-Ausin, https://orcid.org/0000-0009-8765-4321; D. Fabre, https://orcid.org/0000-0003-1875-6386; F. Giannetti, https://orcid.org/0000-0002-3744-3978

Appendix A. Exchange of stability between mode branches at $m^* = 20$

In section 4.2 we showed that for $m^* = 20$, multiple exchanges of stability between the modes occur. To clarify the dynamics taking place, we show the growth rates, frequencies as well as root loci from of the different modes from LSA (figure 14) for different relevant Reynolds numbers (plotted as ▬ ▬ figure 13, which is a zoom of figure 6(b)). The points of neutral stability have been plotted firgure 14 as ○ or ○ , according to the colours of the neutral curves in figure 13.

When decreasing the Reynolds number, the first exchange occurs around $Re \approx 84$. The A branch for small U^* becomes connected with what was previously the B branch and vice-versa, as can be seen comparing figure 14(a) for $Re = 100$ and figure 14(d) for $Re = 78$. This exceptional point occurs for $U^* \approx 6.8$ and is identified figure 13 as ⊙.

The second exchange appears in the loop feature of the neutral curve, around $Re \approx 75.5$. For $U^* \approx 9.75$ (second symbol ⊙ in figure 13), the two unstable branches connect and exchange stability behaviour as can be seen comparing figures 14(d) and 14(g). The asymptotic limit for low U^* at $Re = 75$ corresponds to the critical Reynolds number for which the mode of the fixed tandem configuration is neutral (see · · · figure 14(g)).

Note that all neutral points plotted as ○ occur when the modes are structure-dominated, as can be seen by looking at the matching frequency. On the other hand, all neutral points plotted as ○ arise from fluid-dominated modes.

Appendix B. Impedance-based criterion of a 3-body system

The impedance-based stability prediction can be applied to any number n of bodies. We show here the validity of the method for the prediction of the stability of a cluster of three cylinders that are centred on the vertices of an equilateral triangle of side length $3D/2$. The cylinders are free to oscillate in the transverse direction of the flow. For fixed cylinders, Chen *et al.* (2020) showed that the flow dynamics were highly sensitive to the spacing L and Reynolds number Re. This configuration is also known as the fluidic pinball when the cylinders are rotatable. The linear stability analysis at $Re = 60$ for $m^* = 2.5$ introduces five leading eigenmodes, two being fluid-dominated modes while the three others are of structure-dominated nature. Figure 15 shows the real and imaginary parts of the leading eigenvalues against U^* (respectively 15(a) and 15(b)) as well as the vorticity field of the different modes at a reduced velocity of $U^* = 7$ (figures 15(c),15(d),15(e),15(f) and 15(g)). Modes A (——) and B (——) are both unstable over the whole range of reduced velocities investigated and their frequencies

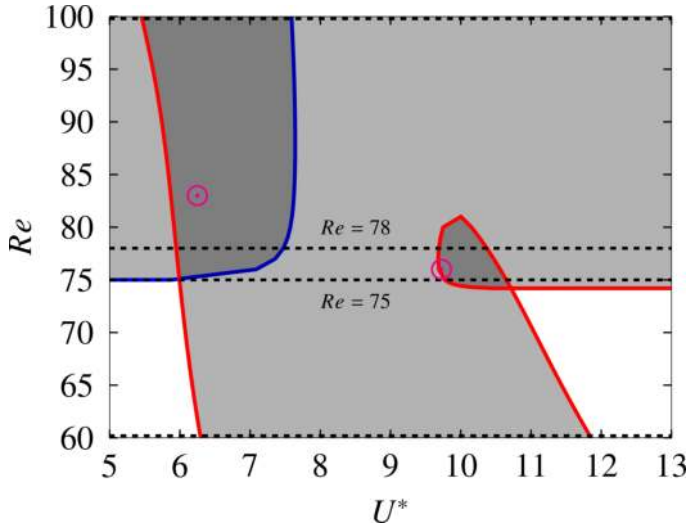

Figure 13: Curves of neutral stability in the $Re - U^*$ plane for $m^* = 2.5$ and $L = 1.5$, from the impedance-based method (zoom of figure 6(b)). The exceptional points are plotted as ⊙.

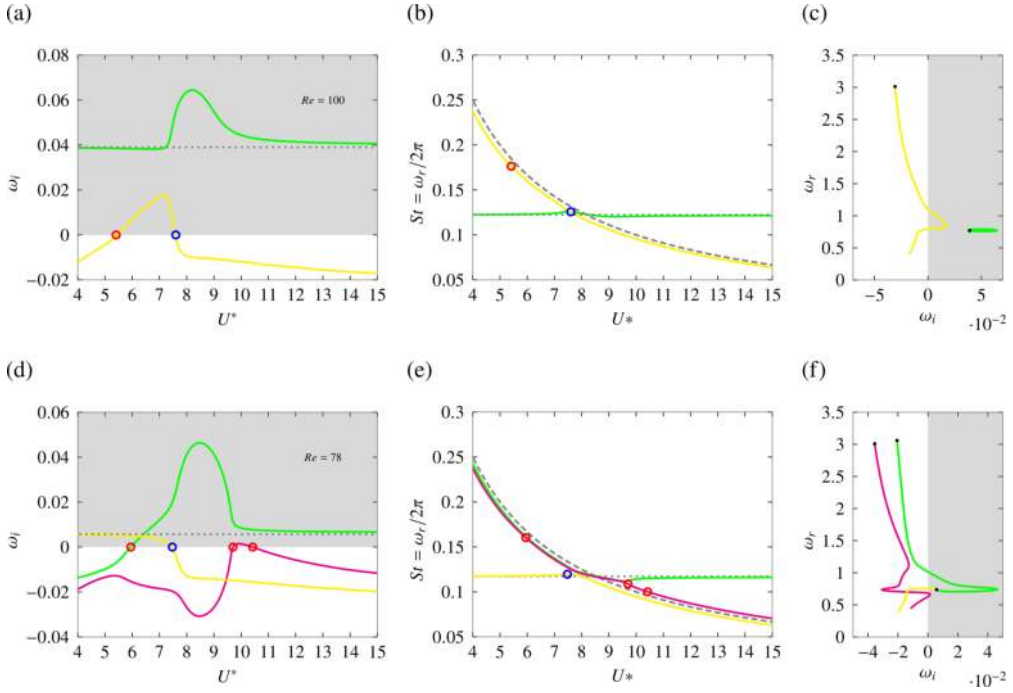

Figure 14: Growth rates (a,d,g,j), frequencies (b,e,h,k) and root loci (c,f,i,l) of the leading eigenmodes (LSA) for $m^* = 20$ and $L = 1.5$: $Re = 100$ (a,b,c), $Re = 78$ (d,e,f), $Re = 75$ (g,h,i) and $Re = 60$ (j,k,l). The natural frequency of a spring-mounted cylinder in vacuum $\omega_n = \frac{2\pi}{U_n^*}$ is shown as – –. The growth rate and frequency of the fluid mode in the wake of the corresponding fixed configuration are displayed as · · ·.

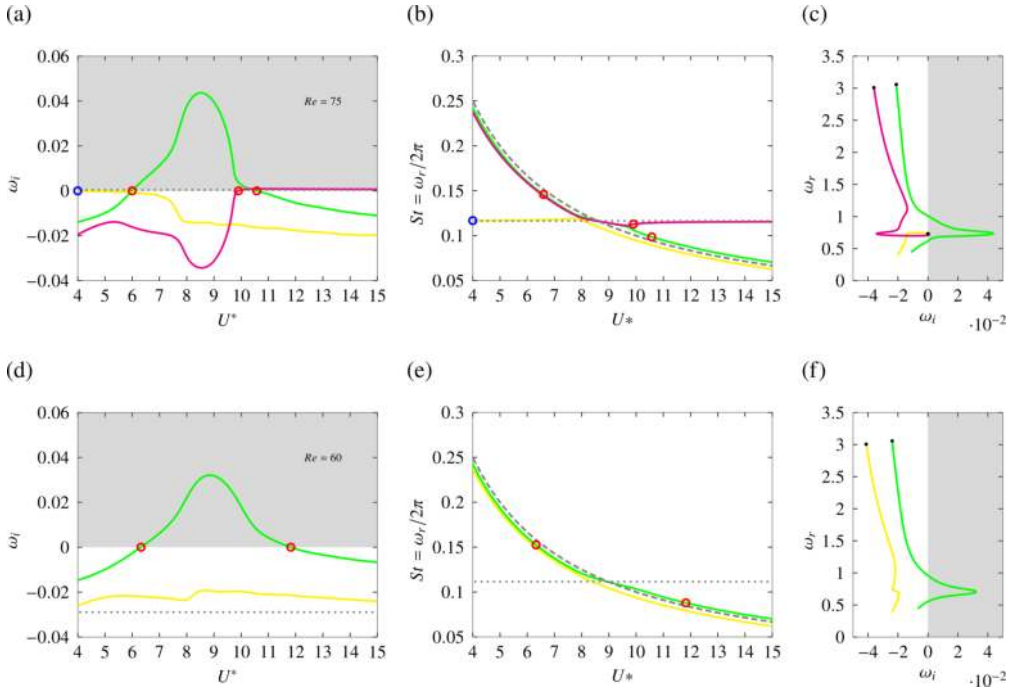

Figure 14: Growth rates (a,d,g,j), frequencies (b,e,h,k) and root loci (c,f,i,l) of the leading eigenmodes (LSA) for $m^* = 20$ and $L = 1.5$: $Re = 100$ (a,b,c), $Re = 78$ (d,e,f), $Re = 75$ (g,h,i) and $Re = 60$ (j,k,l). The natural frequency of a spring-mounted cylinder in vacuum $\omega_n = \frac{2\pi}{U_n^*}$ is shown as – –. The growth rate and frequency of the fluid mode in the wake of the corresponding fixed configuration are displayed as · · ·. (cont.)

respectively match the frequencies of the two unstable modes found in the corresponding fixed case (displayed as · · · and – ·). These modes do not induce displacement of any of the three bodies. Their vorticity fields are respectively plotted in figures 15(d) and 15(f) at reduced velocity $U^* = 7$. Modes C (—), D (—) and E (—) respectively become unstable at reduced velocities $U^* = 5.88$, $U^* = 5.13$ and $U^* = 7.67$. All three modes follow the natural frequency of the structure-only spring-mounted system ($\omega_n = \frac{2\pi}{U_n^*}$, shown as – –). Modes C and E induce the displacement of all cylinders. Both eigenmodes are symmetric and the zone of high vorticity is localised around the bodies as well as in the outer regions of the wake in proximity to the bodies, as seen in figures 15(c) and 15(g). Mode D, on the other hand, induces the displacement of both rear cylinders, leaving the front one stationary. The structure of the mode is similar to that of the other structure-dominated modes but it is antisymmetric, as can be seen in figure 15(e). We computed the forced problem for that configuration and generalised the impedance-based criterion described in section 2.4 to a three-body problem. Practically, the thresholds are found by the inspection of the determinant of a 3×3 matrix. The stability predictions from the impedance-based criterion are plotted as O in figures 15(a) and 15(b). The model correctly predicts the reduced velocities at which the growth rates of the modes become neutral. The prediction of the modes' frequencies is also in very good agreement with the results from LSA.

REFERENCES

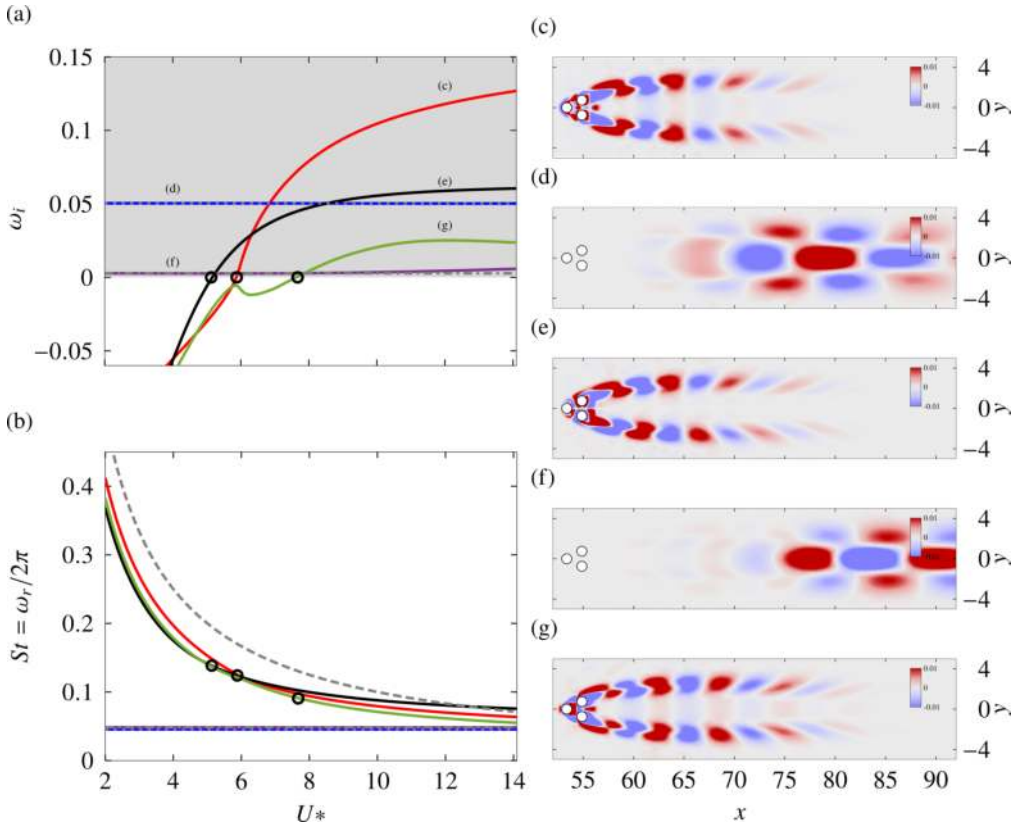

Figure 15: Real part of the leading eigenvalues from LSA (a) and their frequencies (b) with respect to U^* at $Re = 60$ for $m_1^* = m_2^* = m_3^* = 2.5$. The unstable region is depicted as the grey zone. The natural frequency of a spring mounted cylinder in vacuum $\omega_n = \frac{2\pi}{U_n^*}$ is shown as – –. The two leading eigenvalues of the corresponding fixed tandem case are displayed as · · · and – · –. The predictions from the impedance criterion are shown as **O**. Vorticity fields of the eigenmodes (c,d,e,f,g) are showed for $U^* = 7$.

Alam, Mohammad-Reza 2012 Nonlinear analysis of an actuated seafloor-mounted carpet for a high-performance wave energy extraction. *Proceedings of the Royal Society A: Mathematical, Physical and Engineering Sciences* **468** (2146), 3153–3171.

Assi, GR da S, Bearman, Peter W, Carmo, Bruno Souza, Meneghini, Julio Romano, Sherwin, Spencer J & Willden, RHJ 2013 The role of wake stiffness on the wake-induced vibration of the downstream cylinder of a tandem pair. *Journal of Fluid Mechanics* **718**, 210–245.

Assi, GR da S, Meneghini, Julio Romano, Aranha, José Augusto Penteado, Bearman, Peter W & Casaprima, Enrique 2006 Experimental investigation of flow-induced vibration interference between two circular cylinders. *Journal of fluids and structures* **22** (6-7), 819–827.

Assi, Gustavo RS, Bearman, PW & Meneghini, JR 2010 On the wake-induced vibration of tandem circular cylinders: the vortex interaction excitation mechanism. *Journal of Fluid Mechanics* **661**, 365–401.

Bekemeyer, P & Timme, S 2019 Flexible aircraft gust encounter simulation using subspace projection model reduction. *Aerospace Science and Technology* **86**, 805–817.

Bernitsas, Michael M 2016 Harvesting energy by flow included motions. *Springer handbook of ocean engineering* pp. 1163–1244.

Bernitsas, Michael M, Raghavan, Kamaldev, Ben-Simon, Y & Garcia, EMH 2008 Vivace (vortex

induced vibration aquatic clean energy): A new concept in generation of clean and renewable energy from fluid flow. *Journal of offshore mechanics and Arctic engineering* **130** (4).

Bokaian, A & Geoola, F 1984 Wake-induced galloping of two interfering circular cylinders. *Journal of Fluid Mechanics* **146**, 383–415.

Borazjani, Iman & Sotiropoulos, Fotis 2009 Vortex-induced vibrations of two cylinders in tandem arrangement in the proximity–wake interference region. *Journal of fluid mechanics* **621**, 321–364.

Brika, D & Laneville, A 1999 The flow interaction between a stationary cylinder and a downstream flexible cylinder. *Journal of Fluids and Structures* **13** (5), 579–606.

Carini, Marco, Giannetti, Flavio & Auteri, Franco 2014 First instability and structural sensitivity of the flow past two side-by-side cylinders. *Journal of fluid mechanics* **749**, 627–648.

Chai, Yuyang, Gao, Wei, Ankay, Benjamin, Li, Fengming & Zhang, Chuanzeng 2021 Aeroelastic analysis and flutter control of wings and panels: a review. *International Journal of Mechanical System Dynamics* **1** (1), 5–34.

Chen, Weilin, Ji, Chunning, Alam, Md Mahbub, Williams, John & Xu, Dong 2020 Numerical simulations of flow past three circular cylinders in equilateral-triangular arrangements. *Journal of Fluid Mechanics* **891**, A14.

Chen, Weilin, Ji, Chunning, Williams, John, Xu, Dong, Yang, Lihong & Cui, Yuting 2018 Vortex-induced vibrations of three tandem cylinders in laminar cross-flow: Vibration response and galloping mechanism. *Journal of Fluids and Structures* **78**, 215–238.

Conciauro, G & Puglisi, M 1981 Meaning of the negative impedance. *NASA STI/Recon Technical Report N* **82**, 14458.

Corrochano, Adrián, Sierra-Ausín, Javier, Martin, JA, Fabre, David & Le Clainche, Soledad 2023 Mode selection in concentric jets: the steady–steady 1: 2 resonant mode interaction with o (2) symmetry. *Journal of Fluid Mechanics* **971**, A30.

Fabre, David, Citro, Vincenzo, Ferreira Sabino, D, Bonnefis, Paul, Sierra, Javier, Giannetti, Flavio & Pigou, Maxime 2018 A practical review on linear and nonlinear global approaches to flow instabilities. *Applied Mechanics Reviews* **70** (6).

Fabre, David, Longobardi, Raffaele, Bonnefis, Paul & Luchini, Paolo 2019 The acoustic impedance of a laminar viscous jet through a thin circular aperture. *Journal of Fluid Mechanics* **864**, 5–44.

Fabre, David, Longobardi, Raffaele, Citro, Vincenzo & Luchini, Paolo 2020 Acoustic impedance and hydrodynamic instability of the flow through a circular aperture in a thick plate. *Journal of Fluid Mechanics* **885**, A11.

Griffin, OM & Ramberg, SE 1982 Some recent studies of vortex shedding with application to marine tubulars and risers. *Journal of Energy Resources Technology* **104** (1), 2–13.

Griffith, Martin D, Jacono, David Lo, Sheridan, John & Leontini, Justin S 2017 Flow-induced vibration of two cylinders in tandem and staggered arrangements. *Journal of Fluid Mechanics* **833**, 98–130.

Hassig, Hermann J 1971 An approximate true damping solution of the flutter equation by determinant iteration. *Journal of Aircraft* **8** (11), 885–889.

Hecht, Frédéric 2012 New development in freefem++. *Journal of numerical mathematics* **20** (3-4), 251–266.

Hosseini, Negar, Griffith, Martin D & Leontini, Justin S 2021 Flow states and transitions in flows past arrays of tandem cylinders. *Journal of Fluid Mechanics* **910**, A34.

Houtman, Jelle & Timme, Sebastian 2023 Global stability analysis of elastic aircraft in edge-of-the-envelope flow. *Journal of Fluid Mechanics* **967**, A4.

Huera-Huarte, FJ & Gharib, M 2011 Vortex-and wake-induced vibrations of a tandem arrangement of two flexible circular cylinders with far wake interference. *Journal of Fluids and Structures* **27** (5-6), 824–828.

Kim, Sangil, Alam, Md Mahbub, Sakamoto, Hiroshi & Zhou, Yu 2009*a* Flow-induced vibration of two circular cylinders in tandem arrangement. part 2: Suppression of vibrations. *Journal of wind engineering and industrial aerodynamics* **97** (5-6), 312–319.

Kim, Sangil, Alam, Md Mahbub, Sakamoto, Hiroshi & Zhou, Yu 2009*b* Flow-induced vibrations of two circular cylinders in tandem arrangement. part 1: Characteristics of vibration. *Journal of Wind Engineering and Industrial Aerodynamics* **97** (5-6), 304–311.

King, R & Johns, DJ 1976 Wake interaction experiments with two flexible circular cylinders in flowing water. *Journal of Sound and Vibration* **45** (2), 259–283.

Lee, Yin Jen, Qi, Yi, Zhou, Guangya & Lua, Kim Boon 2019 Vortex-induced vibration wind energy harvesting by piezoelectric mems device in formation. *Scientific reports* **9** (1), 20404.

Mittal, S & Kumar, Vinod 2001 Flow-induced oscillations of two cylinders in tandem and staggered arrangements. *Journal of Fluids and Structures* **15** (5), 717–736.

Navrose & Mittal, Sanjay 2016 Lock-in in vortex-induced vibration. *Journal of Fluid Mechanics* **794**, 565–594.

Papaioannou, GV, Yue, DKP, Triantafyllou, MS & Karniadakis, GE 2008 On the effect of spacing on the vortex-induced vibrations of two tandem cylinders. *Journal of Fluids and Structures* **24** (6), 833–854.

Patel, Kuntal, Sun, Jun, Yang, Zixuan & Zhu, Xiaojue 2025 Coupled liquid–gas flow over a submerged cylinder: interface topology, wake structure and hydrodynamic lift. *Journal of Fluid Mechanics* **1008**, A10.

Pfister, Jean-Lou, Marquet, Olivier & Carini, Marco 2019 Linear stability analysis of strongly coupled fluid–structure problems with the arbitrary-lagrangian–eulerian method. *Computer Methods in Applied Mechanics and Engineering* **355**, 663–689.

Prasanth, TK & Mittal, S 2009*a* Flow-induced oscillation of two circular cylinders in tandem arrangement at low re. *Journal of fluids and structures* **25** (6), 1029–1048.

Prasanth, T.K. & Mittal, Sanjay 2009*b* Vortex-induced vibration of two circular cylinders at low reynolds number. *Journal of Fluids and Structures* **25** (4), 731–741.

Sabino, Diogo, Fabre, David, Leontini, JS & Jacono, D Lo 2020 Vortex-induced vibration prediction via an impedance criterion. *Journal of Fluid Mechanics* **890**.

Sierra, Javier, Fabre, David & Citro, Vincenzo 2020 Efficient stability analysis of fluid flows using complex mapping techniques. *Computer Physics Communications* **251**, 107100.

Sierra-Ausin, J, Citro, V & Giannetti, F 2022 Acoustic instability prediction of the flow through a circular aperture in a thick plate via an impedance criterion. *Journal of Fluid Mechanics* **943**, A48.

Sierra-Ausín, J, Lorite-Díez, M, Jiménez-González, JI, Citro, V & Fabre, D 2022 Unveiling the competitive role of global modes in the pattern formation of rotating sphere flows. *Journal of Fluid Mechanics* **942**, A54.

Suzuki, Kosuke & Inamuro, Takaji 2011 Effect of internal mass in the simulation of a moving body by the immersed boundary method. *Computers & Fluids* **49** (1), 173–187.

Timme, S, Marques, Simao & Badcock, KJ 2011 Transonic aeroelastic stability analysis using a kriging-based schur complement formulation. *AIAA journal* **49** (6), 1202–1213.

Tirri, Antonia, Nitti, Alessandro, Sierra-Ausin, Javier, Giannetti, Flavio & de Tullio, Marco D 2023 Linear stability analysis of fluid–structure interaction problems with an immersed boundary method. *Journal of Fluids and Structures* **117**, 103830.

Williamson, Charles HK, Govardhan, R & others 2004 Vortex-induced vibrations. *Annual review of fluid mechanics* **36** (1), 413–455.

Zdravkovich, MM 1987 The effects of interference between circular cylinders in cross flow. *Journal of fluids and structures* **1** (2), 239–261.

Zhang, Cheng, Tang, Guoqiang, Lu, Lin, Jin, Yan, An, Hongwei & Cheng, Liang 2024*a* Flow-induced vibration of two tandem square cylinders at low reynolds number: transitions among vortex-induced vibration, biased oscillation and galloping. *Journal of Fluid Mechanics* **986**, A10.

Zhang, Zhiyu, Lu, Jianfeng & Zhang, Xing 2024*b* Global stability analysis of flow-induced-vibration problems using an immersed boundary method. *Journal of Fluids and Structures* **130**, 104187.

Zhu, Hongjun, Zhong, Jiawen, Shao, Ze, Zhou, Tongming & Alam, Md Mahbub 2024 Fluid-structure interaction among three tandem circular cylinders oscillating transversely at a low reynolds number of 150. *Journal of Fluids and Structures* **130**, 104204.

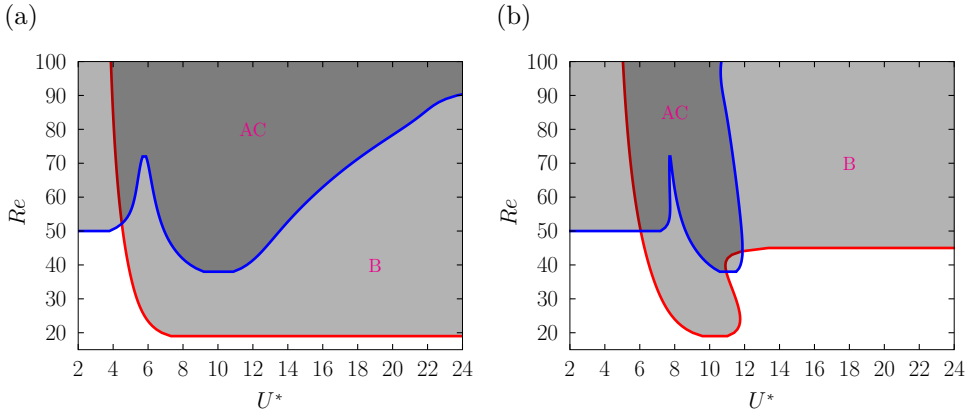

Figure 4.1: Regions of instability (shaded colors) in the Re–U^* plane for $L = 6$ and $m^* = 2.5$ (a) and $m^* = 20$ (b). Results come from the impedance-based predictions. Gray indicates regions where one unstable mode exists while dark gray regions indicate where two unstable modes exist.

4.1.1.2 Complement on linear dynamics at large spacing

To complement the results of the previous section, the impedance-based method was applied to a case with large spacing.

As can be seen in figure 11 of Mouyen, T. et al. (2026) (paper section 4.1), increasing the spacing between the bodies brings the thresholds of mode A and C close to each other in the U^* plane. We find that, for large spacings the two modes are merged. Figure 4.1 shows the neutral curves for $L = 6$ in the $Re - U^*$ plane. The nature of the newly merged mode, conveniently named AC, is fluid-dominated at low U^*, while it is structure-dominated at higher U^* where it mainly involves the motion of the rear cylinder (as was the case for mode C at lower spacings).

4.1.2 Non-linear dynamics

4.1.2.1 Low-U^* limit

The low-U^* limit corresponds to a spring-mounted body with infinite stiffness, and can thus be interpreted as the fixed-body configuration.

As depicted in figure 11 of Mouyen, T. et al. (2026) (paper section 4.1), the fluid-dominated mode A displays different regimes depending on the spacing

between the bodies. This behaviour is confirmed in the non-linear regime. At a low reduced velocity ($U^* = 1$), the cylinders are stationary (see figure 4.2, black crosses mark the initial position of the bodies). The flow regimes tend to be the ones of the fixed tandem configuration and we observe similar behaviour as described in Zdravkovich (1987) and Hosseini *et al.* (2020). For $L = 1.5$, there is vortex shedding in the wake of the bodies which resembles the single "slender body regime" (W-TI in Zdravkovich, 1987) or "short pitch regime" described in previous studies (see figure 4.2(e)). The shear layers of the first body reattach to the second one. The flow sees a unique structure and the periodic vortex shedding is formed in the wake. For $L = 2$, as the shear layers of the first body reattach to the second one, the vortex shedding disappears and the flow is stabilised, as can be seen in figure 4.2(d). This is consistent with the disappearance of mode A observed in the linear regime. Moreover, in the investigation of the fixed tandem and fixed three-cylinder configurations, Hosseini *et al.* (2020) observed a similar behaviour. For a specific range of spacing the rear body lies in the recirculation region of the first one, which is a region of absolute instability likely to induce reorganisation of the flow. For $L = 3$, the flow in the gap remains unfluctuating but it destabilises downstream and vortex shedding is once more observed in the wake (see figure 4.2(c)). Increasing the spacing further to $L = 4$, fluctuations are observed in the gap but the shear layers are still reattaching to the rear body (see figure 4.2(b)). The behaviour at these two spacings resemble the W-TII regime where Zdravkovich (1987) observed intermittent reattachment of the front bodies boundary layer ("medium pitch regime" as described by Hosseini *et al.* (2020)). For $L = 5.25$, we recover the two vortex street regime where there is vortex shedding in the wake of both cylinders (see figure 4.2(a)). Note however that the "two-row" wake structure observed by Hosseini *et al.* (2020) at that spacing is not present here, likely due to the difference in Reynolds number. Hosseini *et al.* (2020) noticed that the behaviour of the tandem of cylinders is similar to that of a cylinder followed by a flat plate positioned in tandem (Hwang *et al.*, 2003). This hints that the shape of the second body has a relatively small influence on the overall flow dynamics, while the distance between the bodies has a predominant one.

4.1.2.2 Non-linear dynamics of the spring-mounted tandem

Figure 4.3 shows the results of direct numerical simulations for the spacings at $Re = 80$ and $m^* = 2.5$ for varying reduced velocity. The frequencies were

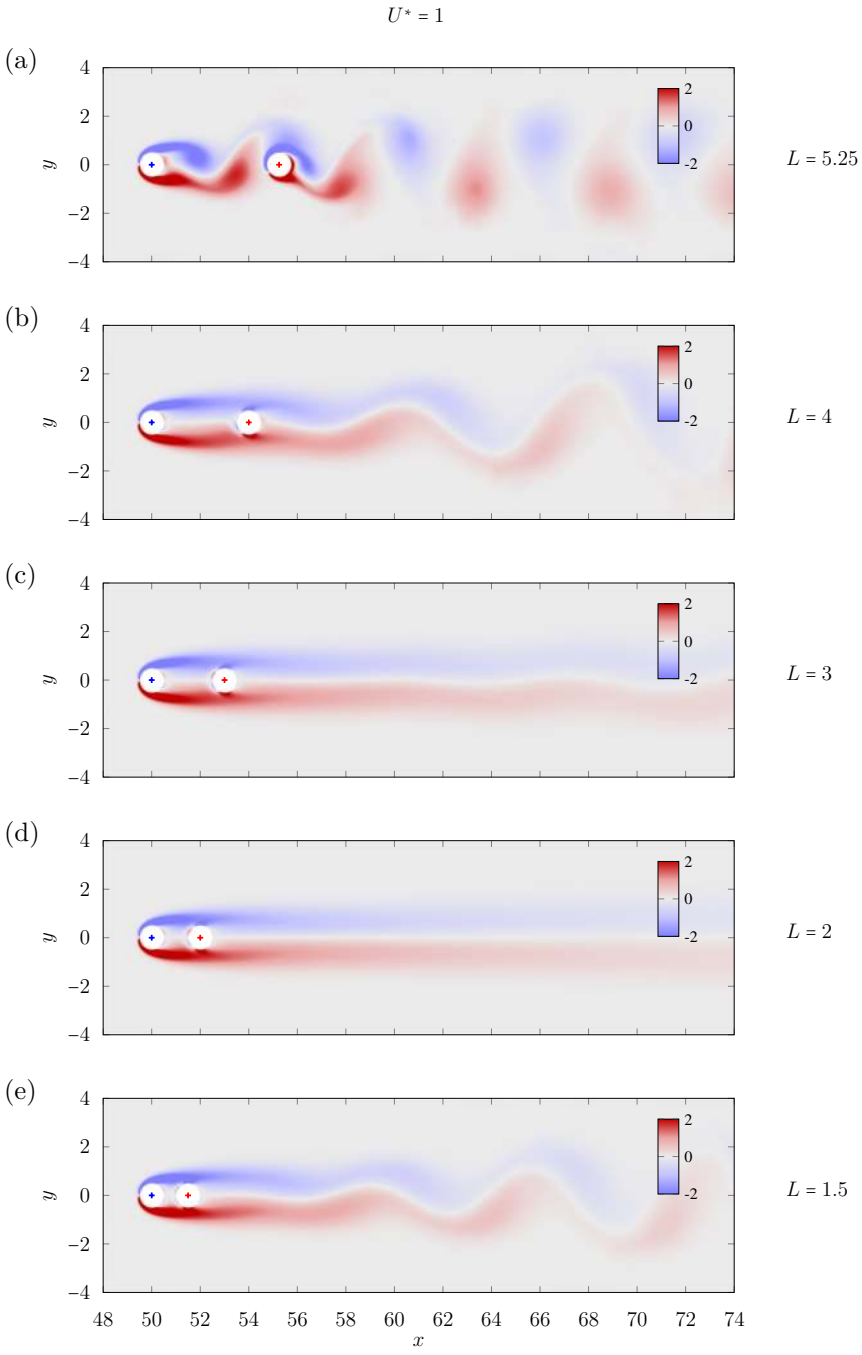

Figure 4.2: Flow visualisation (vorticity field) for the tandem of cylinders at $Re = 80$, $m^* = 2.5$ and $U^* = 1$ for different spacings L. The blue and red crosses represent the initial rest positions of the front an rear cylinders respectively.

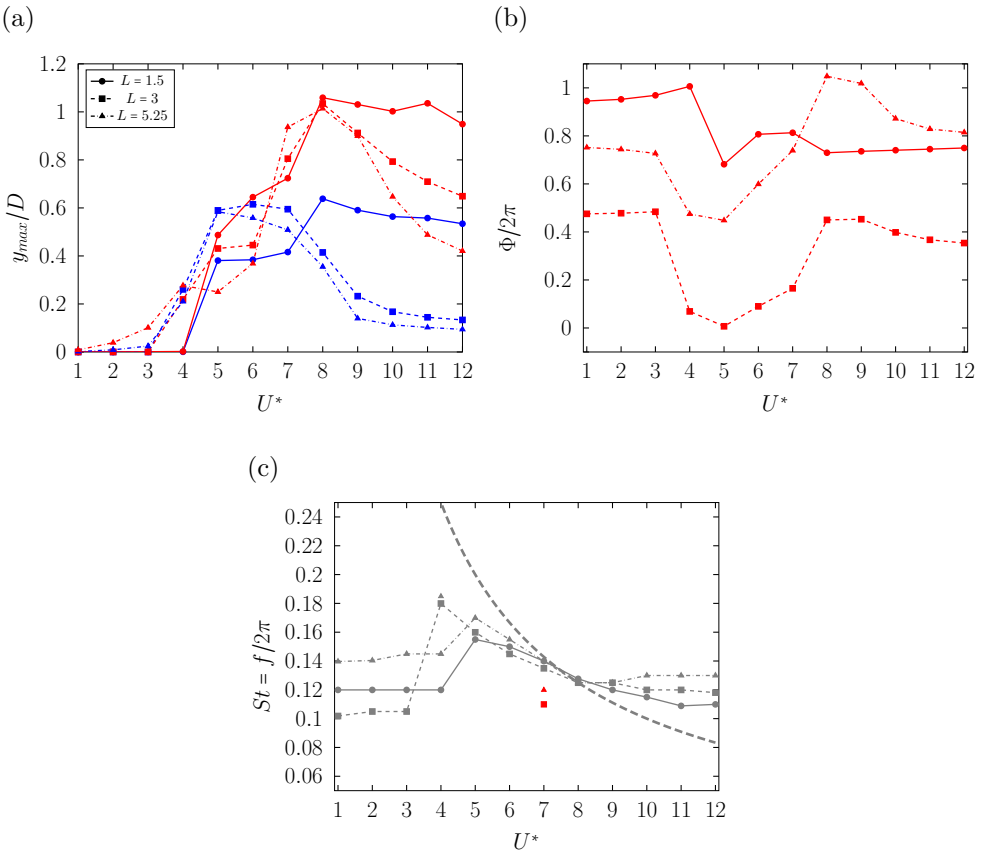

Figure 4.3: Vortex-induced vibrations of $N = 2$ in-line spring-mounted cylinders at $Re = 80$ and $m^* = 2.5$, for different spacings L: (a) maximum oscillation amplitudes, (b) phase differences between the cylinder motions, and (c) dominant frequencies extracted from the Fast Fourier Transform (FFT) of the bodies' displacement. In (a), the (—) and (—) curves correspond to the front and rear cylinders. In (b), the phase difference between the cylinders is shown in red. In (c), the common dominant frequency shared by all bodies is plotted in gray. In cases where an additional dominant frequency is present for a given cylinder, this secondary frequency is shown in blue or red when it corresponds to the front or rear cylinder respectively. If this secondary frequency is present for all bodies, it is shown in gray. In dashed gray is shown the natural frequency of a spring-mounted body.

obtained from the Fast Fourier Transform of the vertical displacement of the bodies. To quantify the phase relationship between the bodies' motion, the instantaneous phase of the displacement signals was computed using the Hilbert transform. The instantaneous phase was obtained from the argument of the analytic signal and the phase difference was defined as the mean of the difference between the two instantaneous phases. A phase difference of $\Phi/2\pi \approx 0$ or $\Phi/2\pi \approx 1$ corresponds to the bodies oscillating in-phase. $\Phi/2\pi \approx 0.5$ corresponds to the bodies oscillating in phase opposition, while $\Phi/2\pi \approx 0.25$ or $\Phi/2\pi \approx 0.75$ corresponds to a quarter phase lag between the bodies' motion.

For $L = 1.5$ and for all reduced velocities investigated, the motion of the rear cylinder dominates with a maximum amplitude of $1.1D$ at $U^* = 8$ (see figure 4.3(a)). At low reduced velocity ($U^* = [1 - 4]$) the cylinders have a negligible amplitude while vortex shedding is observed in the wake of the bodies (see for instance figures 4.4(a) and 4.4(b)). This behaviour is consistent with the linear stability analysis, which predicts that the fluid-dominated A mode is unstable in this region (see figure 11 of Mouyen, T. et al. (2026)). For $U^* = 5$, which corresponds to the onset of mode B, oscillations set in (see figure 4.4(d)). The rear cylinder oscillates with a bigger amplitude than the front one and exhibits a quarter-cycle phase lag relative to it. The dominant frequency extracted from the FFT is common for the rear and front cylinders indicating synchronisation. The behaviour described for $U^* = 5$ continues as the reduced velocity is increased, while the maximum amplitudes of the bodies' motion increase.

For $L = 3$, the motion of the front cylinder dominates at reduced velocities of $U^* = [3 - 6]$ while the rear cylinders' motion dominates for $U^* > 6$. The amplitude of motion of the rear cylinder reaches a maximum of $1D$ at $U^* = 8$. For $U^* = 1$ there is vortex shedding in the wake of the rear cylinder and both cylinders remain stationary (see figure 4.5(a) and 4.5(b)). For $U^* = 3$, there is a stabilisation of the flow. Indeed, at that point in the parameter space, the linear calculations predict no unstable mode as can be seen in figure 11 of Mouyen, T. et al. (2026) (paper section 4.1). At $U^* = 4$ oscillations start to appear. For $U^* = [4 - 6]$ both cylinders oscillate in phase (see figure 4.3(b), as well as figure 4.5(f) for an example at $U^* = 5$), the front one having a slightly greater amplitude of motion. For $U^* = [9 - 12]$, the cylinders are in phase opposition (as can be seen for example figure 4.5(f)). The amplitude of the rear cylinder is much bigger than that of the front one. Note that, for that reduced velocity, the linear calculations predict that mode C, which

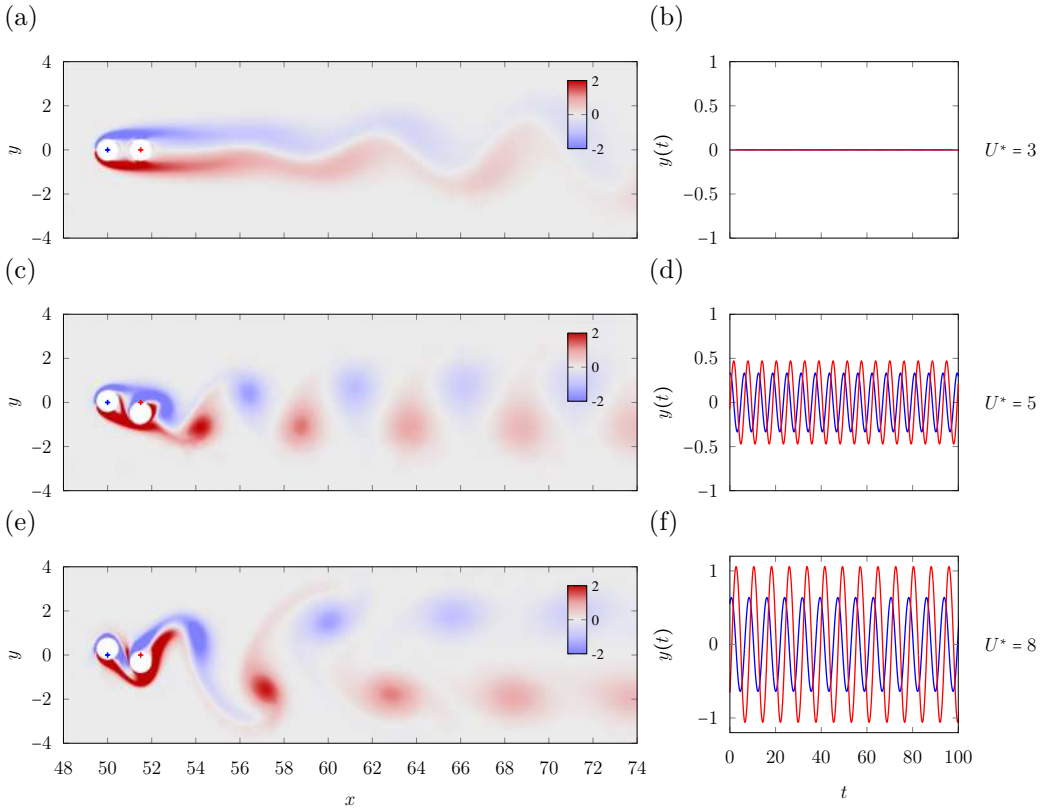

Figure 4.4: Flow visualisation (vorticity field) and amplitude of motion in time for the tandem of cylinders at $Re = 80$, $m^* = 2.5$ and $L = 1.5$ for different reduced velocities U^*. The blue and red crosses represent the initial rest positions of the front and rear cylinders respectively. Similarly, — and — represent their position in time.

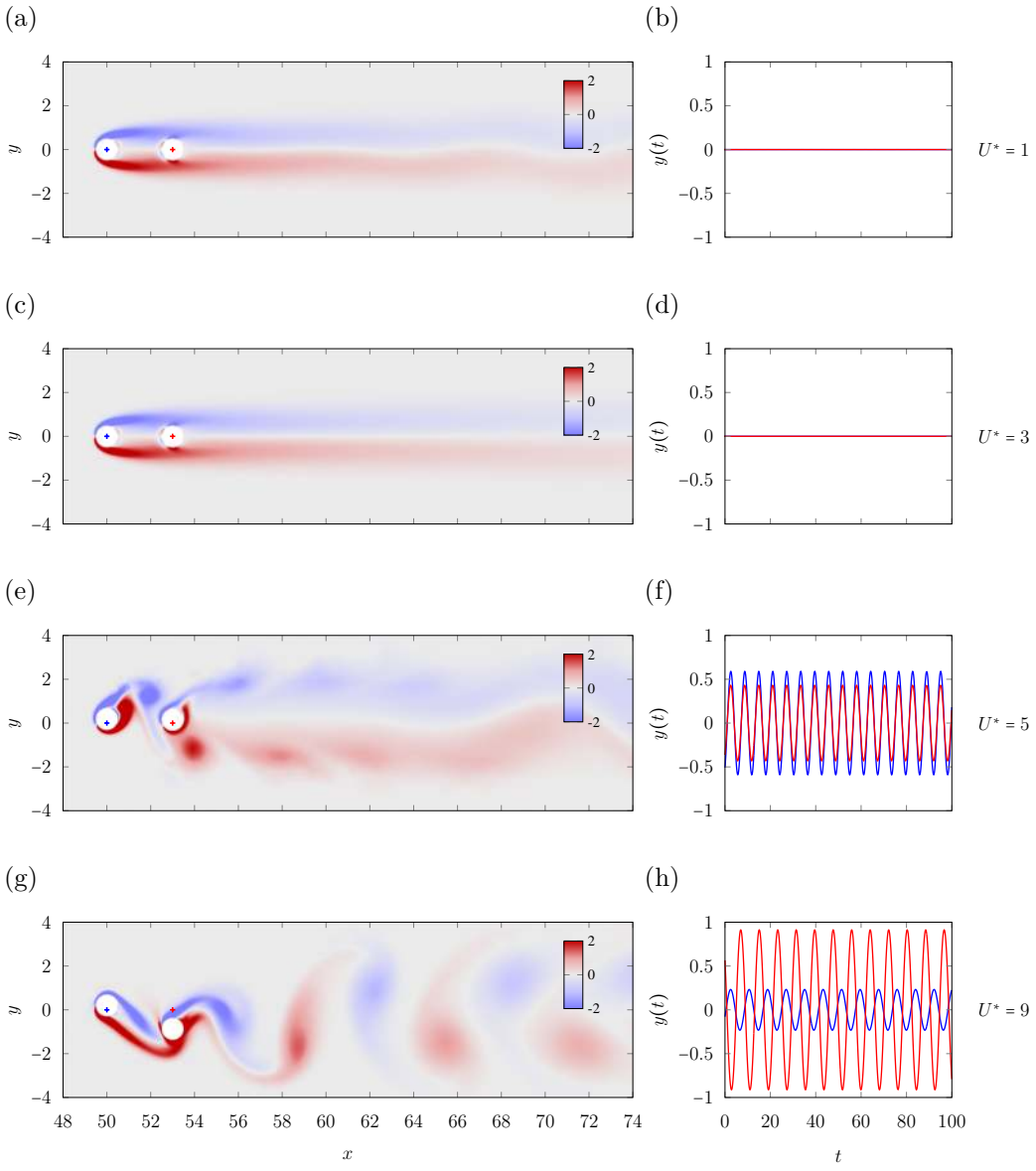

Figure 4.5: Flow visualisation (vorticity field) and amplitude of motion in time for the tandem of cylinders at $Re = 80$, $m^* = 2.5$ and $L = 3$ for different reduced velocities U^*. The blue and red crosses represent the initial rest positions of the front and rear cylinders respectively. Similarly, — and — represent their position in time.

(a)

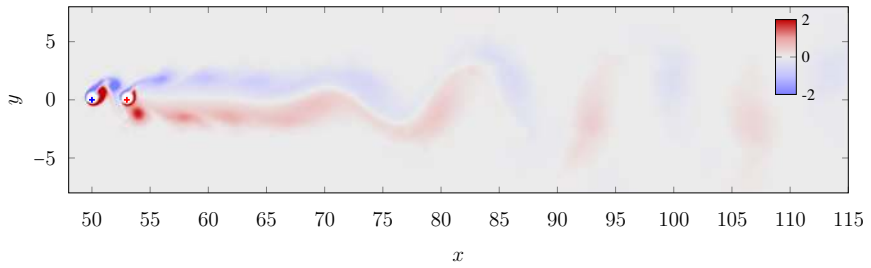

Figure 4.6: Extension of figure 4.5(e): flow visualisation (vorticity field) for the tandem of cylinders at $Re = 80$, $m^* = 2.5$, $L = 3$ and $U^* = 5$.

is associated to the motion of the rear body, is unstable (see figure 11 of Mouyen, T. et al. (2026)). For all U^*, the dominant frequency is the same for the front and rear body: in the non-linear regime, there is a synchronisation of the bodies motion. For $U^* = 7$, we observe quasi-periodic behaviour of the rear cylinder (see motion in time and phase portrait in figures 4.7a and 4.7b) and two frequencies coexist (see FFT in figure 4.7c). One is close to the natural frequency of the spring mounted system and the other one is close to the vortex shedding frequency. In the linear regime, this reduced velocity corresponds to the onset of mode C in the region where mode B is unstable. Finally, for some reduced velocities, we observe the reorganisation of the flow downstream. The vortex shedding in the proximity of the bodies seems to have a different shedding frequency as that which is observed further downstream as can be seen for $U^* = 5$ in figure 4.6(a).

For $L = 5.25$, the motion of the rear cylinder dominates for most reduced velocities investigated. Figure 4.8 shows the flow visualisation and amplitude of motion of the bodies for several reduced velocities. For $U^* = [1 - 3]$ both cylinders exhibit oscillations that are quite limited in amplitude, of the order of $0.1D$. This is to put in contrast with the cases previously described where no oscillations were detectable at such reduced velocities. For the higher spacings, however, mode A will eventually merge with mode C in a new AC mode of hybrid nature, which involves structural motion. At $U^* = 4$, oscillations start to settle in, with maximum amplitudes of motion above $0.1D$. We observe quasi-periodic behaviour for both cylinders as can be seen in the phase portrait of figure 4.9b. The displacement of both cylinders display a second dominant frequency, as reported in figure 4.3(c) by the additional gray marker. For

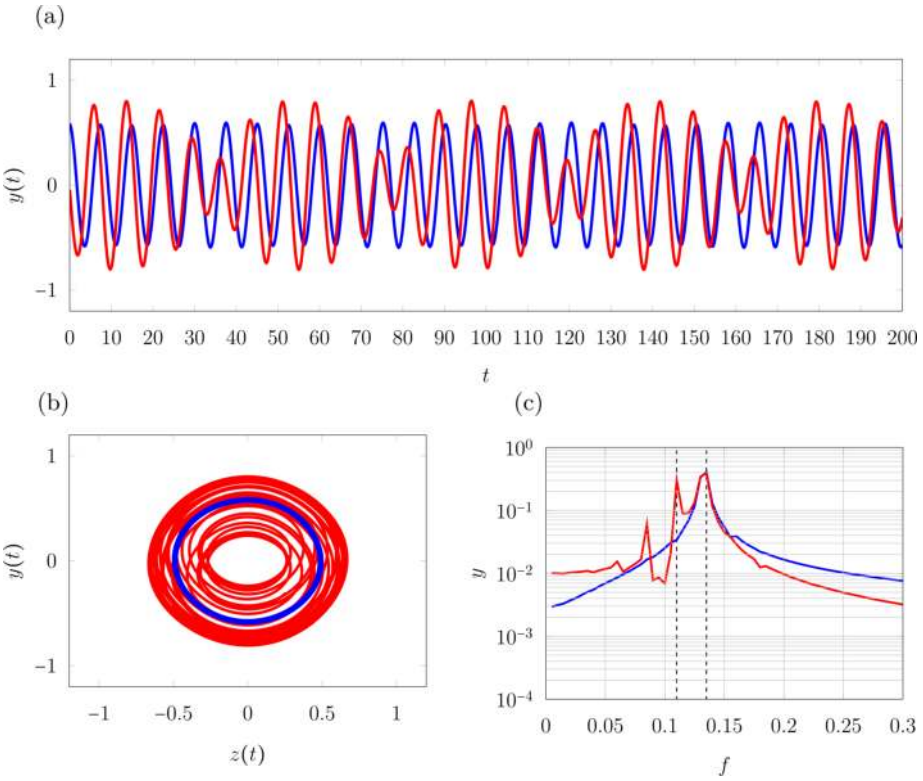

Figure 4.7: (a) Amplitude of motion in time for the $N = 2$ in-line configuration at $Re = 80$, $m^* = 2.5$, $L = 3$ and $U^* = 7$. (b) Phase portrait: velocity of the bodies against their position. (c) Fast Fourier Transform of the position in time of the bodies. — and — are respectively used for the front and rear body.

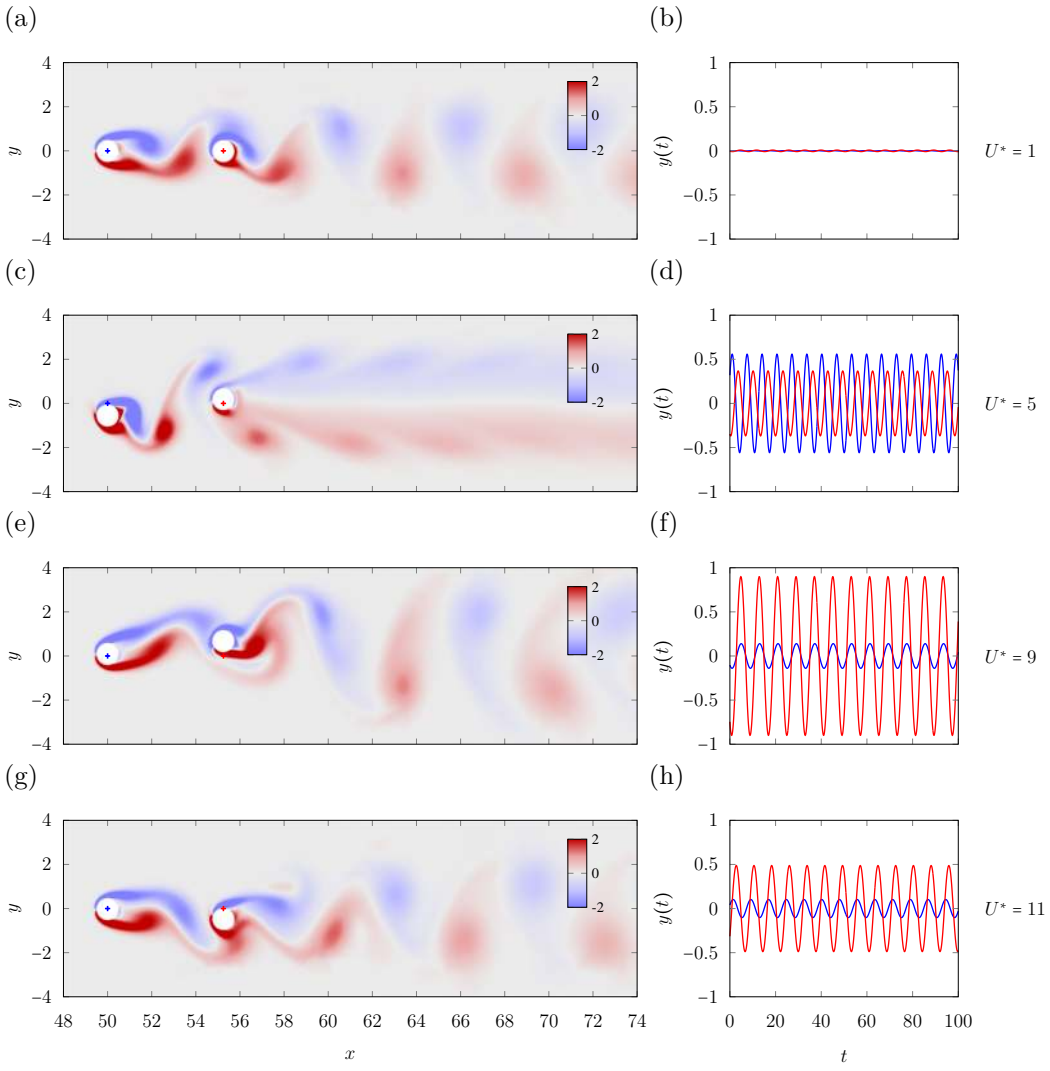

Figure 4.8: Flow visualisation (vorticity field) and amplitude of motion in time for the tandem of cylinders at Re = 80, m^* = 2.5 and L = 5.25 for different reduced velocities U^*. The blue and red crosses represent the initial rest positions of the front and rear cylinders respectively. Similarly, — and — represent their position in time.

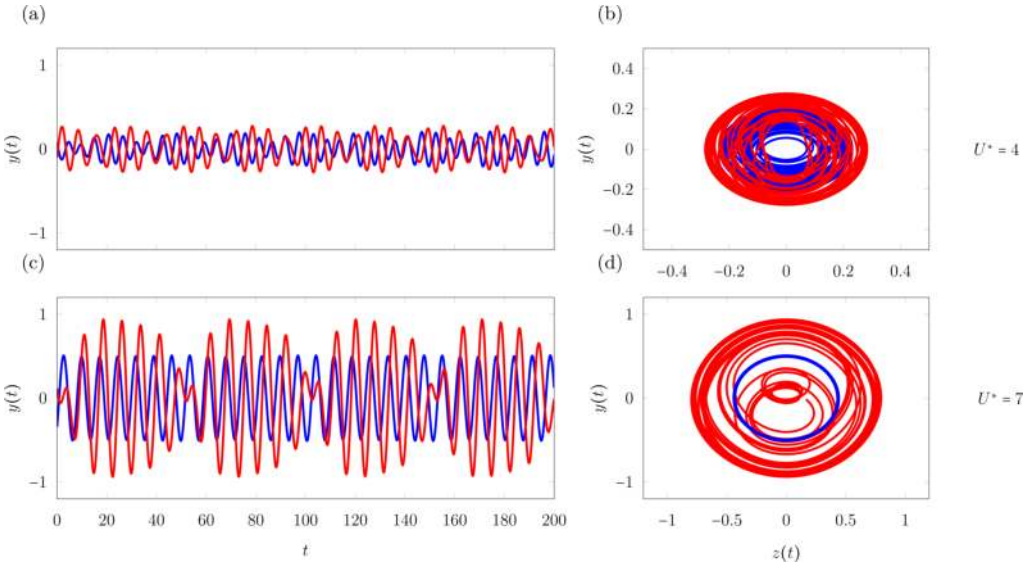

Figure 4.9: (a,c) Amplitude of motion in time for the $N = 2$ in-line configuration at $Re = 80$, $m^* = 2.5$, $L = 5.25$ for $U^* = 4$ and $U^* = 7$. (b,d) Phase portrait for the same values of U^*. — and — are respectively used for the front and rear body.

$U^* = [5 - 6]$, the cylinders are in phase opposition and the front cylinder exhibits slightly higher amplitudes than the rear. At $U^* = 7$, we observe quasi-periodic motion of the rear cylinder only, as shown in figures 4.9c and 4.9d. The second frequency is reported in figure 4.3(c) by the additional red marker. For $U^* = 9$, the cylinders are in phase and the rear cylinder displays maximum amplitude while the amplitudes of the front one are decreased. For $U^* > 9$, the cylinders are in a quarter phase lag and the amplitudes of the rear cylinder decrease with increasing reduced velocity. For that higher spacing, the transition observed at $U^* = 4$ (with a quasi-periodic behaviour of both bodies) corresponds in the linear regime to the onset of mode B (associated with the motion of both bodies) while mode A is unstable (see figure 11 of Mouyen, T. et al. (2026)). On the other hand, for the transition $U^* = 7$, quasi periodic behaviour of the rear cylinder only is observed at a reduced velocity which, in the linear regime, corresponds to the onset of mode C (which is associated to the motion of the rear body) while mode B is unstable.

For most of the cases explored for $N = 2$ (and as will later be shown

for $N = 3$ and $N = 4$), the transitions marked by the appearance of the quasiperiodic regimes match relatively well to the onsets predicted on the neutral curves produced from the linear calculations. However, note that, in the linear regime, if a mode is unstable and another one becomes unstable, the transition should not be expected to be the same in the non-linear regime. Indeed, the transition of the second mode corresponds to a perturbation around the baseflow which is an assumption not valid in the non-linear regime.

4.1.2.3 Damping effect and power output for energy harvesting

In the context of energy harvesting, one is interested in the output power that can be generated from the spring-mass system. That power comes from the damping of the system and one is then faced with the problem of optimising the damping while having the maximum amplitudes possible. The power output is calculated as the product of a velocity and a force. In our case, taking the velocity of the body and the damper force leads to

$$\bar{P} = \frac{1}{T}\int_T 2\pi^2 m^* \gamma \frac{1}{U^*} z^2 dt. \tag{4.1}$$

Soti *et al.* (2017) investigated the effect of the damping on the amplitudes, velocities and power output of a spring-mounted cylinder for $Re = 200$, $m^* = 2$ and $U^* = 5.2$. They found decreasing amplitudes of motion and velocity of the body with increasing damping. The maximum of power output ($\bar{P} = 0.13$) for that set of structural parameters was found for a damping of $\gamma = 0.14$. The authors focused on the reduced velocity $U^* = 5.2$ because it corresponds to the lock-in regime for a single spring-mounted cylinder. Figure 4.10 shows the variation the amplitudes of motion and power output with damping ratio for the tandem configuration spaced of $L = 3$ for $Re = 80$ and $m^* = 2.5$. The reduced velocity was fixed to $U^* = 8$ because it yields the maximum amplitudes of the rear body (as shown in figure 4.3(a)). Increasing the damping ratio results in the decrease of the amplitudes of motion of both cylinders. The power output from the front and rear cylinder ($\bar{P}_1$ and $\bar{P}_2$) respectively reach a maximum at $\gamma = 0.38$ and $\gamma = 0.32$. The resulting total maximum power that can be harnessed out of the tandem configuration for that set of parameters is $\bar{P}_{tot} = 0.367$ found at $\gamma_{opt} = 0.32$.

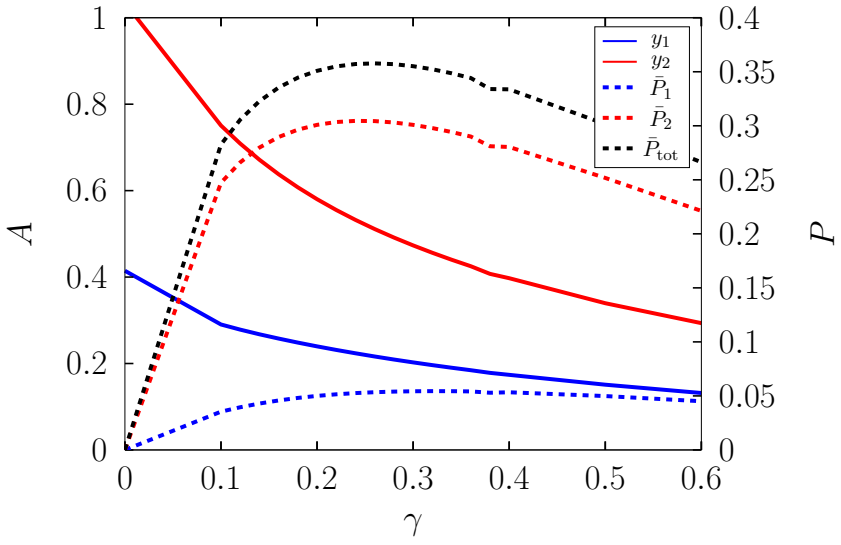

Figure 4.10: Variation of the maximum amplitude of motion and average power output of the front and rear cylinders in tandem configuration at $Re = 80$, $m^* = 2$, $L = 3$ and $U^* = 8$.

4.2 Linear dynamics of the side-by-side configuration

The goal of this section is to provide a linear analysis of the impact of vortex-induced vibrations on the side-by-side configuration. In that case, the cylinders are placed at the same longitudinal position and spaced of T diameters centre to centre.

Carini *et al.* (2014) explored the instability of the flow past two fixed cylinders in side-by-side configuration. For the gaps and Reynolds numbers investigated, they found four unstable leading eigenmodes: three harmonic modes and a steady antisymmetric one. For increasing gaps, they described in turn Hopf bifurcations of a single bluff-body mode (SB), an asymmetric steady flow mode (AS) and an in-phase and antiphase synchronized vortex shedding mode (IP and AP). Note that, in Carini *et al.* (2014), the authors considered the gap between the bodies (named g in their study) while here, we will consider the distance centre to centre T ($T = g + D$).

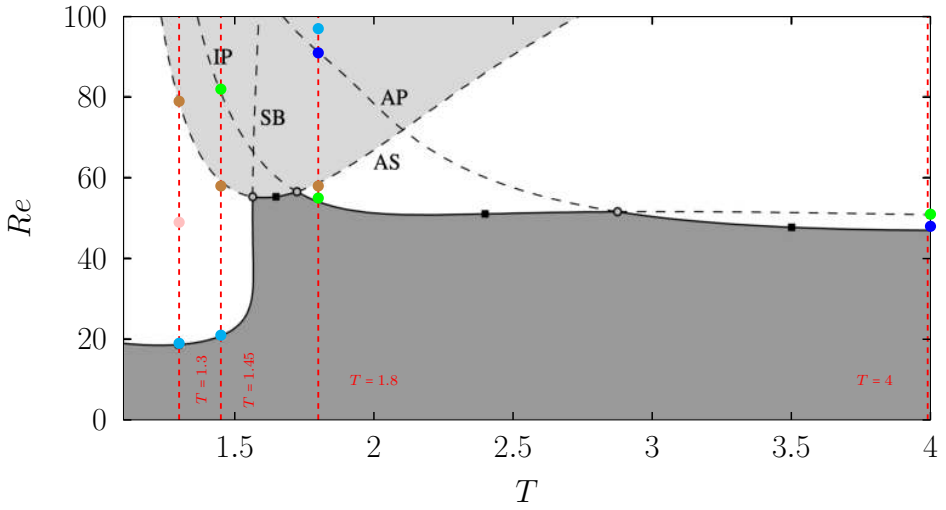

Figure 4.11: Neutral curves adapted from Carini *et al.* (2014). The dark gray zone represents the region of stability. See Carini *et al.* (2014) for further details. The (····) lines represent the gaps investigated in the current study for the spring-mounted case. The points of neutral stability found in the current study in the low-U^* limit are displayed as: ● (IP_A), ● (AP_A), ● (SB), ● (SB_2) and ● (AS).

Let us now consider the case of spring-mounted cylinders free to oscillate vertically. Figure 4.12 shows the neutral curves produced from the impedance-based method for the spacings of $T = 4$, $T = 1.8$, $T = 1.45$ and $T = 1.3$.

At a spacing of $T = 4$ and for $Re = 100$ and $m^* = 2.5$, we find four leading unstable modes. We find in-phase and anti-phase fluid-dominated modes. Following the denomination of Carini *et al.* (2014), they will respectively be denominated as IP_A and AP_A. We then also find in-phase and anti-phase structure-dominated modes, respectively denominated IP_B and AP_B. The growth rates and frequencies of the modes are shown figures 4.13(a) and 4.13(c). The dynamics of the AP_A (—) and AP_B (—) modes roughly follow that of the modes in the case of a single oscillating cylinder as described in Sabino *et al.* (2020). Mainly, mode AP_A is an anti-phase mode (see figures 4.14(g), 4.14(h) and 4.14(i)) which is fluid-dominated in the low-U^* region. Mode AP_B on the other hand is an anti-phase mode (see figure 4.14(a), 4.14(b) and 4.14(c)) which is structure-dominated in the low-U^* region and

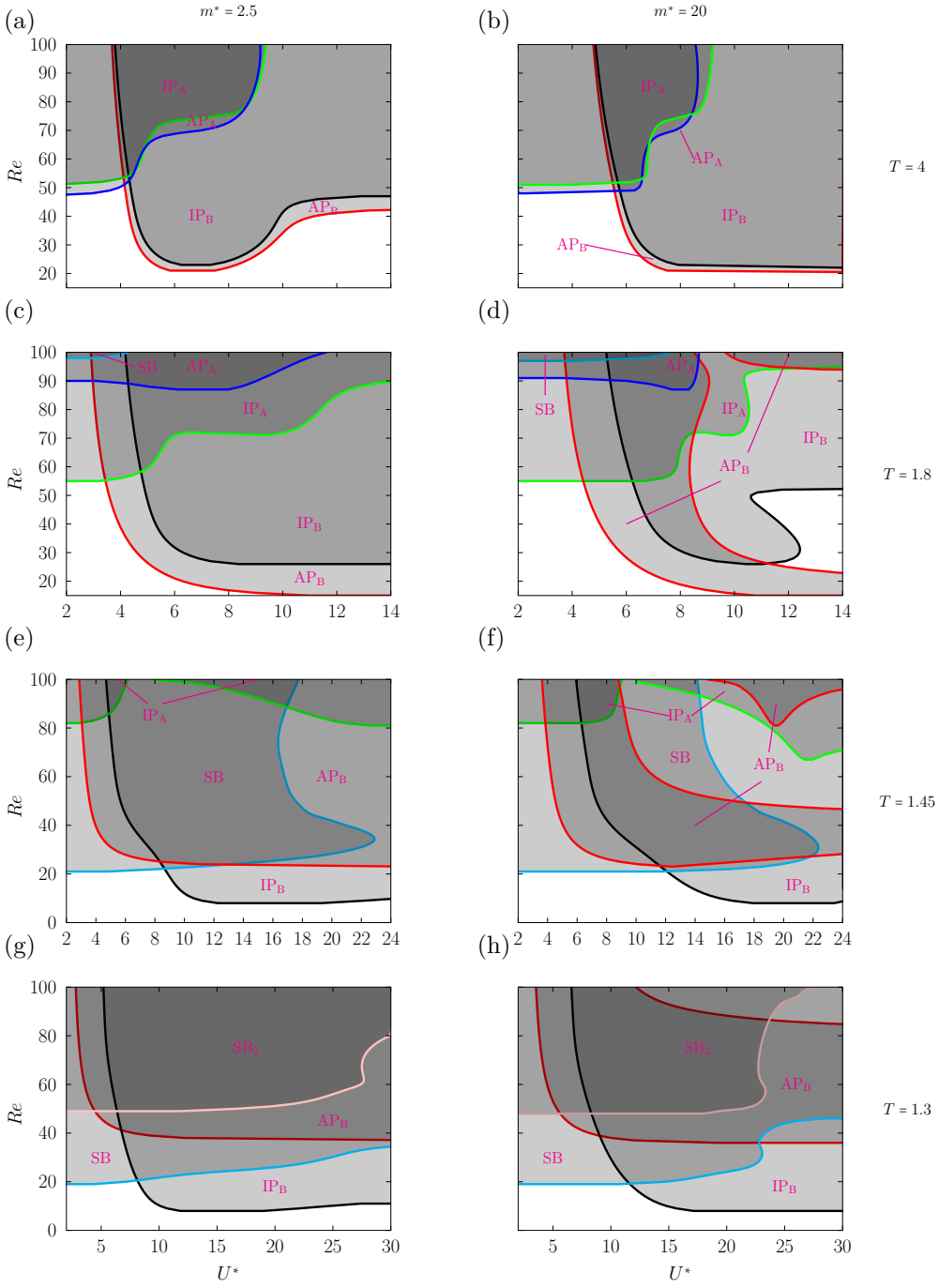

Figure 4.12: Neutral curves in the $Re - U^*$ plane of $N = 2$ cylinders in side-by-side configuration, for $m^* = 2.5$ and $m^* = 20$: $T = 4$ (a,b), $T = 1.8$ (c,d), $T = 1.45$ (e,f) and $T = 1.3$ (g,h). Results come from the impedance-based predictions. Gray indicates regions where one unstable mode exists while darker gray regions indicate where there are more unstable modes.

fluid dominated in the high-U^* region. Then, two corresponding in-phase modes are found. Mode IP_A (—) is the in-phase version of mode AP_A (see figures 4.14(j), 4.14(k) and 4.14(l)) while IP_B (—) is the in-phase version of mode AP_A (see figure 4.14(d), 4.14(e) and 4.14(f)). The in-phase modes follow closely the dynamics of their anti-phase counterpart. Note that, at this spacing, the eigenmode structures reveal two distinct wakes associated with each cylinder, as was observed in Carini *et al.* (2014) for high spacings. At $m^* = 2.5$ (figure 4.12(a)), the IP_A and AP_A modes are stable for all U^* below $Re \approx 50$ and for all Re above $U^* \approx 9$. Concerning IP_B and AP_B, they are unstable for Reynolds numbers above $Re = 20$, spanning a broad range of reduced velocities. Towards the higher U^* region, their instability threshold is shifted towards $Re \approx 45$, and the neutral curve displays a lobe like feature. Increasing the reduced mass to $m^* = 20$ (figure 4.12(b)) increases the range of instability of modes IP_A and AP_A, while the high-U^* threshold of instability of mode IP_B and AP_B is shifted towards $Re \approx 20$.

Let us now consider the spacing $T = 1.8$. For $m^* = 2.5$, the four leading eigenmodes found for the previous spacing are still present. The modes IP_A (—) and AP_A (—) are still fluid-dominated in the low U^* region, while modes IP_B (—) and AP_B (—) still are structure-dominated in the low-U^* region and fluid-dominated in the high-U^* region. An additional mode, mode SB (—), appears. It is a fluid-dominated mode, its frequency follows that of the fixed equivalent configuration (see figures 4.13(b) and 4.13(d)). It is unstable at low reduced velocities and high Reynolds numbers (see figure 4.12(c)). The structure of the mode corresponds to a single large scale wake as described in Carini *et al.* (2014). Increasing the reduced mass to $m^* = 20$ (figure 4.12(d)) reduces the span of reduced velocities over which AP_A is unstable. The span of instability of the left branch ($55 < Re < 70$) of mode IP_A is increased while the one of its right branch ($70 < Re < 90$) is reduced. The region of instability of mode IP_B is reduced and the neutral curve displays a lobe like feature. The span over which mode AP_B is unstable is extensively reduced and a region of global stability appears at high reduced velocities centred around $Re = 40$. However, another unstable region is present at high reduced velocities and Reynolds number. On the other hand, the span over which mode SB is unstable is extended with the increase of the reduced mass. Similarly to what was observed for the previous spacing, the eigenmode structures again indicate that each cylinder generates its own wake, except for mode SB.

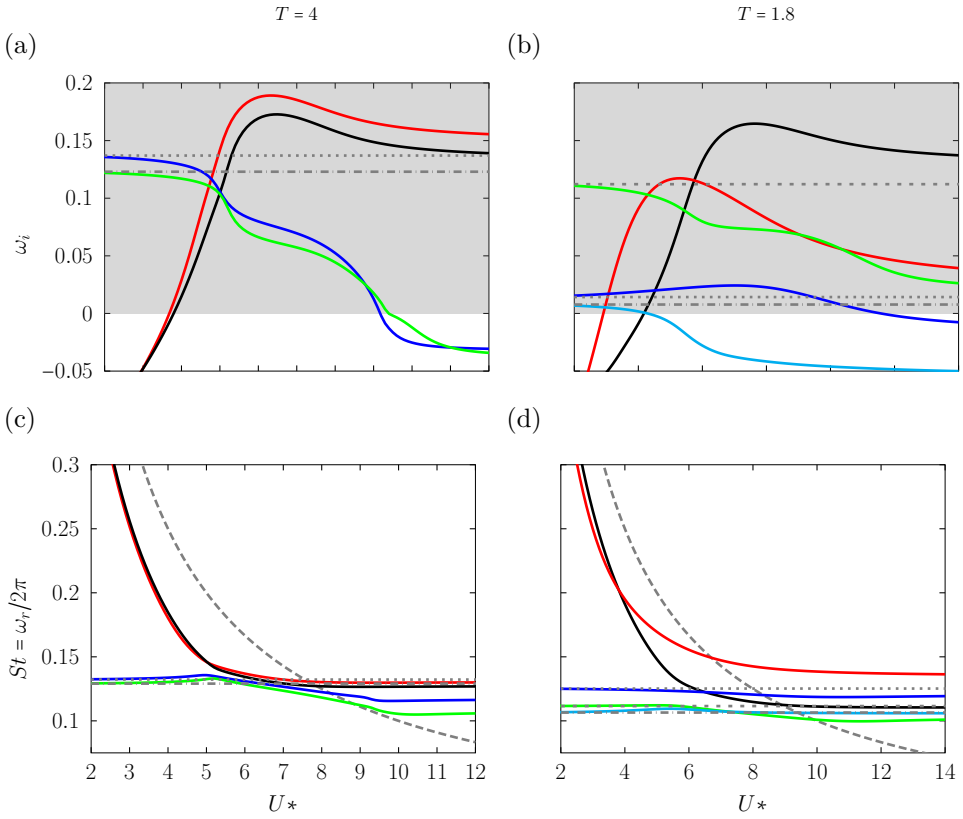

Figure 4.13: Real and imaginary parts of the leading eigenvalues (LSA) with respect to U^* for $N = 2$ in the side-by-side configuration, for $m^* = 2.5$ and $Re = 100$: $T = 4$ (a,c) and $T = 1.8$ (b,d): $\mathrm{IP_A}$ (—), $\mathrm{IP_B}$ (—), $\mathrm{AP_A}$ (—), $\mathrm{AP_B}$ (—) and SB (—).

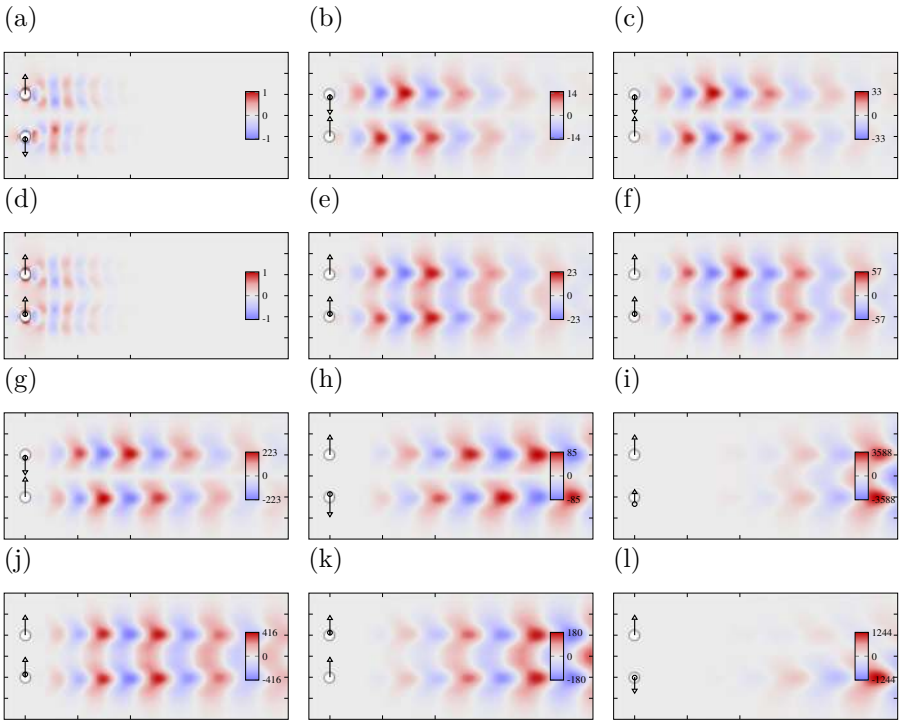

Figure 4.14: Transversal velocity u_y fields of the flow past two cylinders in side-by-side configuration spaced of T = 4 for Re = 100 and m^* = 2.5: mode IP_A (j,k,l), mode AP_A (g,h,i), mode IP_B (d,e,f) and AP_B (a,b,c) at reduced velocities U^* = 3 (a,d,g,j), U^* = 8 (b,e,h,k) and U^* = 12 (d,f,i,l). See explanations in text section 4.1.1.1 for the significance of the colour maps and representations of the cylinder's displacement.

For the case $T = 1.45$, modes IP_B (—), AP_B (—), IP_A (—) and SB (—) are still present while mode AP_A is no longer unstable. For $m^* = 2.5$ (figure 4.12(e)), mode IP_A threshold is shifted towards higher Reynolds numbers. On the other hand, the region of instability of mode SB is extensively increased, with a threshold of $Re \approx 20$ for most U^*. Its growth rate and frequency follow almost exactly those of one of the modes (– –) found in the fixed corresponding case (see figures 4.15(a) and 4.15(c)). Also, for this spacing the mode corresponds to vortex shedding in the wake of a single-body. Increasing the reduced mass to $m^* = 20$ (figure 4.12(f)), reduces the span over which mode IP_B is unstable and the neutral curve displays a lobe like feature. The span over which the AP_B is unstable is extensively reduced as it becomes stable again towards higher reduced velocities. Increasing further the reduced velocity creates again an unstable region at high Reynolds numbers.

For a spacing of $T = 1.3$, modes IP_B (—), AP_B (—) and SB (—) are still present. Mode SB remains purely fluidic as its growth rate and frequency follow almost exactly those of one of the modes (· · ·) found in the fixed corresponding case (see figures 4.15(b) and 4.15(d)). We can also note that mode IP_B seems to be purely structural at this spacing, as its frequency follows closely that of the natural frequency of the spring-mounted system. Strikingly, we observe the appearance of a second single-body mode denominated SB_2 (—). Its frequency is slightly higher than that of the SB mode, and it follows exactly that of the second mode found in the corresponding fixed configuration (– · ·). At $m^* = 2.5$, the range over which mode IP_B is unstable remains essentially similar as the previous case. On the other hand, the threshold of mode AP_B is increased to $Re \approx 37$. Mode SB_2 and SB are unstable over a wide range of reduced velocities. Particularly, the threshold of mode SB is decreased to $Re \approx 20$, for most reduced velocities. Increasing the reduced mass to $m^* = 20$ slightly shifts the neutral curve of modes IP_B and AP_B towards higher reduced velocities. Moreover, as previously observed, mode AP_B becomes stable again towards the higher Reynolds numbers, for $U^* > 12$. Note that the mode SB_2 was not found by Carini *et al.* (2014). This decrepancy could be linked to mesh and domain size differences in the current study. That being said, different meshes and complex mapping regions investigated in this study led to the presence of that mode.

Carini *et al.* (2014) found the existence of a steady antisymmetric mode. This mode was also found in the current study, but it was decided that the production of neutral curves and the description of its behaviour was out of

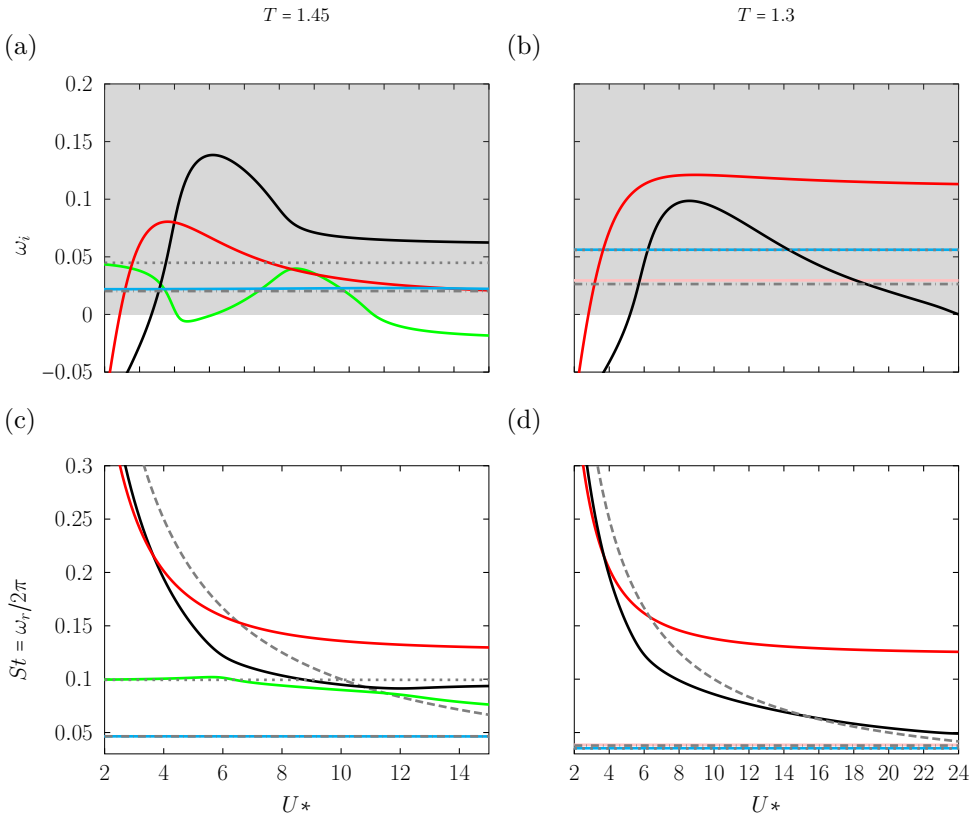

Figure 4.15: Real and imaginary parts of the leading eigenvalues (LSA) with respect to U^* for $N = 2$ in the side-by-side configuration, for $m^* = 2.5$ and $Re = 100$: $T = 1.45$ (a,c) and $T = 1.3$ (b,d): IP_A (—), IP_B (—), AP_B (—), SB (—) and SB_2 (—).

scope. However, the points of neutral stability in the low-U^* limit are reported in figure 4.11 as (●).

Note that, in the low-U^* limit, the modes' behaviour should tend to that of the fixed-configuration. The thresholds found in that limit are reported in figure 4.11 and a good agreement is found with Carini *et al.* (2014) for the fluid-dominated modes.

Finally, it is worth noting that, if one only takes the in-phase modes present in the side-by-side system, the configuration is equivalent to a cylinder beneath a slip-wall. The latter case will be investigated in the beginning of chapter 6 to explore confinement effects in more details.

4.3 Synthesis

In this chapter we have investigated the vortex-induced vibrations of two spring-mounted cylinders arranged in tandem and side-by-side configurations, combining linear stability, impedance-based threshold predictions and direct numerical simulations of the non-linear dynamics. We have found that the impedance-based method provides an efficient and accurate framework to predict instability thresholds and modal interactions over a wide parameter space.

For the tandem configuration, the dynamics are strongly governed by the bodies' spacing. In the linear regime, three main modes (A, B and C) were identified, with mode A remaining intrinsically coupled while modes B and C progressively decouple and recover single-body characteristics at large spacing. Increasing further the spacing, a merging of modes A and C was also observed. In the non-linear regime, these linear predictions translate into distinct vibration patterns, including synchronised, phase-opposed and quasi-periodic responses, with transitions that closely follow the neutral stability curves. The flow physics at low reduced velocity recover classical wake interference regimes of fixed cylinders.

For the side-by-side configuration, the linear analysis revealed a rich modal structure, including in-phase and anti-phase fluid- and structure-dominated modes, as well as single-body wake modes emerging at small gaps. The evolution of these modes with spacing highlights a transition from two independent wakes to a strongly coupled single-wake behaviour.

Chapter 5

Multiple in-line bodies

This chapter presents results for $N = 3$ and $N = 4$ in-line spring-mounted cylinders. It is divided in two parts for each number of bodies investigated. Each part contains both linear results from stability analysis and impedance-based predictions as well as non-linear results.

5.1 Three bodies

5.1.1 Linear analysis

We show in figure 5.1 the neutral curves computed from the impedance-based method in the $Re-U^*$ plane for spacings of $L = 1.5$, $L = 3$ and $L = 6$ and for a reduced mass of $m^* = 2.5$ and $m^* = 20$. The growth rate and frequency of the corresponding modes are shown in figure 5.2 for $m^* = 2.5$ and $Re = 100$.

For $L = 1.5$ and $m^* = 2.5$ (figure 5.1(a)), the neutral curves for the tandem and the $N = 3$ in-line bodies are extensively different. First, the fluid-dominated mode A (—) which was present in the tandem configuration (figure 6(a) of Mouyen, T. et al. (2026), paper section 4.1) is not present here. That is to be expected as, for such short L, the flow sees an elongated bluff body, and adding a third cylinder therefore increases the critical Reynolds number of the vortex-shedding wake instability. Mode B (—), however, remains similar in essence as that of the tandem configuration. It is a structure-dominated mode that involves the motion of all three cylinders. Its frequency follows the natural frequency of a spring-mounted system as can be seen in figure 5.2(c). The threshold for the onset of instability is shifted towards lower Reynolds

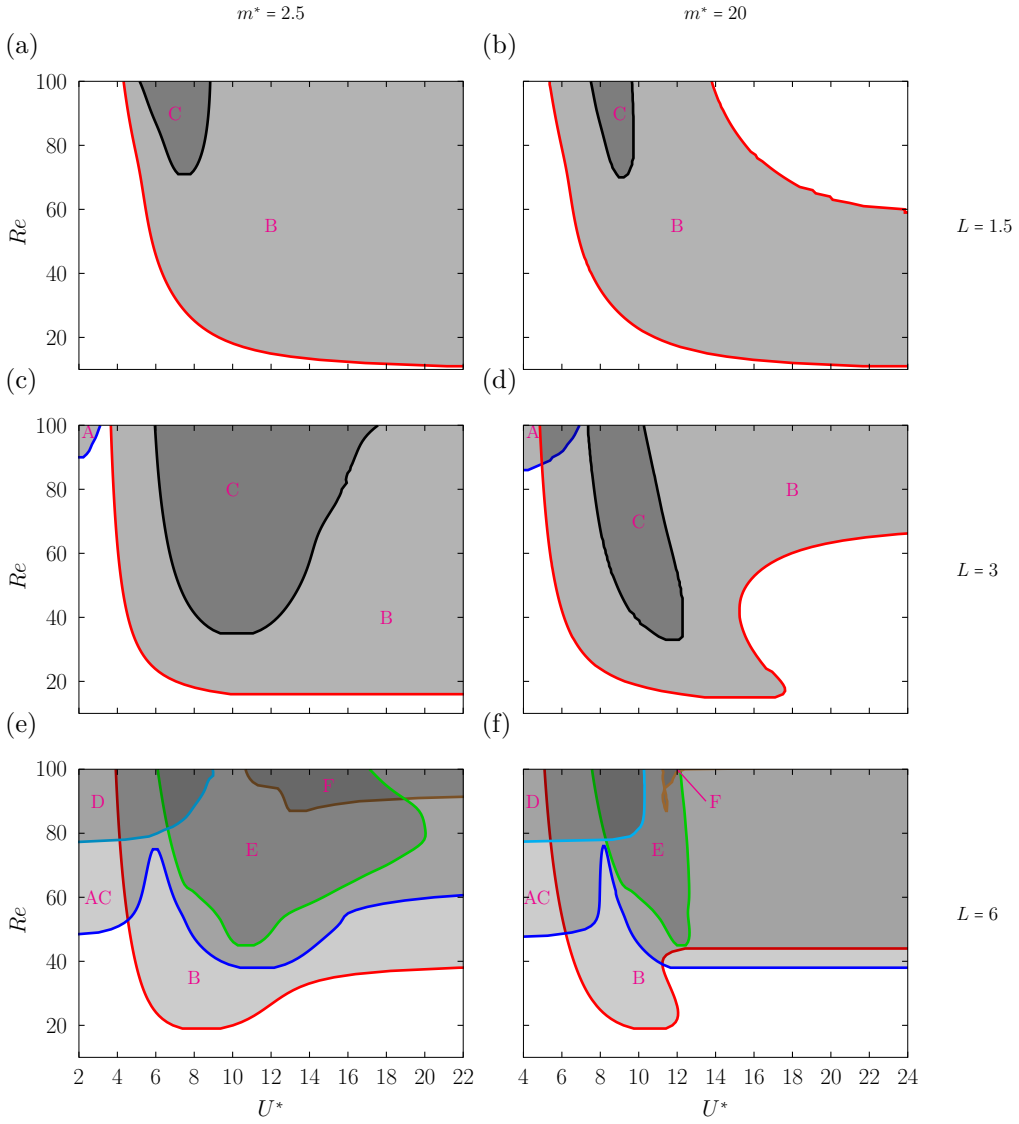

Figure 5.1: Neutral curves in the $Re - U^*$ plane for $N = 3$ in-line cylinders for $m^* = 2.5$ and $m^* = 20$. (a,b) $L = 1.5$, (c,d) $L = 3$ and (e,f) $L = 6$. Results come from the impedance-based predictions. Gray indicates regions where one unstable mode exists while darker gray regions indicate where there are more unstable modes.

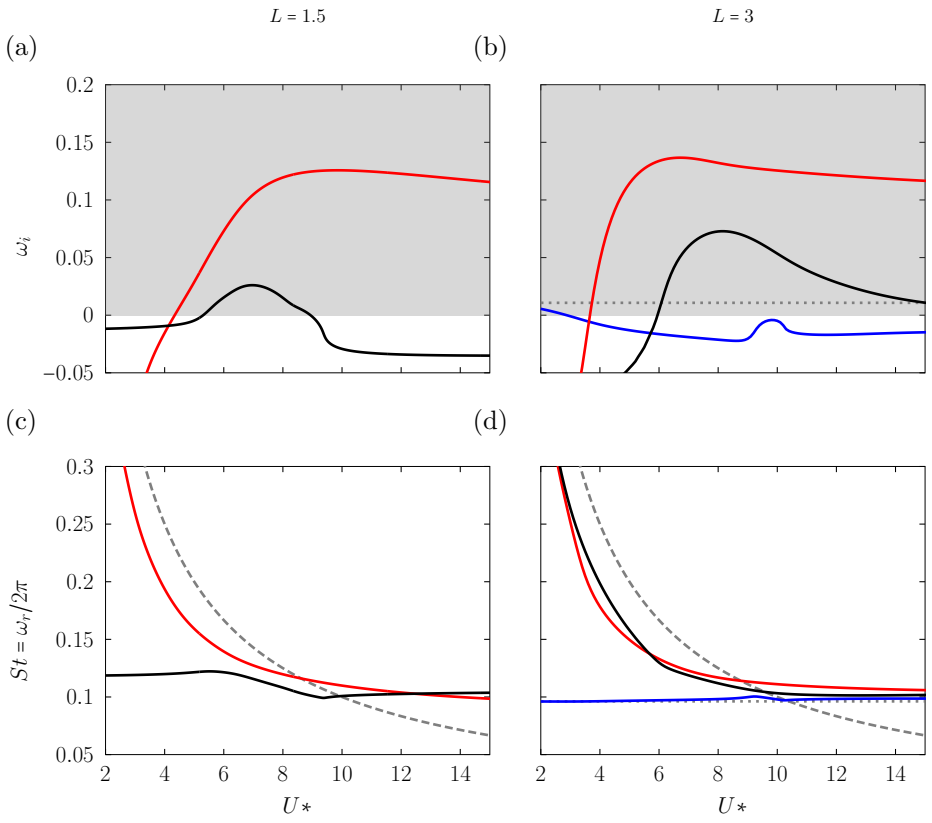

Figure 5.2: Real and imaginary parts of the leading eigenvalues (LSA) with respect to U^* for $N = 3$, $m^* = 2.5$ and $Re = 100$: $L = 1.5$ (a,c) and $L = 3$ (b,d). Modes A, B and C are respectively represented with (—), (—) and (—).

numbers ($Re \approx 11$). Mode C (—), which was not present in the tandem case at this spacing, involves the motion of the third cylinder mainly. However, the frequency of that mode remains mainly constant. Note that, at that spacing, no unstable mode exist for the corresponding fixed configuration. Increasing the reduced mass reduces the span over which the modes are unstable and a region of global stability appears at high reduced velocity and Reynolds number (see figure 5.1(b)).

For $L = 3$, the neutral curves strikingly resemble that of the tandem configuration. The increasing spacing between the bodies removes the "elongated-body" effect therefore allowing for vortex shedding in the wake of the first bodies. Similarly as the tandem case, mode A is a fluid-dominated

mode and its frequency follows that of the fixed configuration, as can be seen in figure 5.2(d). Mode B is a structure-dominated mode that involves the motion of all three cylinders and mode C involves the motion of the third cylinder mainly. Their frequencies follow that of the natural frequency. Interestingly, modes B and C have the same behaviour as in the tandem case, mainly mode B involves the motion of all bodies and mode C involves the motion of the rear-most body. Increasing the reduced mass reduces the span over which the structure-dominated modes are unstable and shifts the region of instability of mode A towards higher reduced velocities.

For $L = 6$ increasing again the spacing between the bodies increases the complexity of the system. As in the corresponding tandem case, the modes A and C are merged in an AC mode (—). It is a fluid-dominated mode at low reduced velocities and a structure-dominated one at higher reduced velocities, involving mainly the motion of the rear-most body. Mode B remains a structure-dominated mode associated to the motion of all bodies. Three additional modes appear at that spacing. Mode D (—) is a fluid-dominated mode. Mode E (—) is structure-dominated and involves the motion of the second and third bodies. On the other hand, mode F (—) is structure-dominated and involves the motion of the third body only. Increasing the reduced mass reduces the span over which the modes E,F and B are unstable. It also shifts the region of instability of mode D and the left branch of mode AC towards higher reduced velocities.

5.1.2 Non-linear dynamics

Figure 5.3 shows the results of direct numerical simulations of the $N = 3$ in-line configuration, for the spacings $L = 1.5$ and $L = 3$ at $Re = 100$.

For $L = 1.5$, in the interval $U^* = [7 - 9]$, the motion of the middle cylinder dominates, while outside of that region, the motion of the rear cylinder dominates. The maximum amplitude reaches approximately $1.2D$ for the rear cylinder at $U^* = 10$. At low reduced velocity ($U^* = [2 - 4]$) the system remains stationary and the flow in the wake of the bodies is stable (see figures 5.4(a) and 5.4(b)). This behaviour is consistent with the linear stability analysis, which predicts no unstable mode in this region. For $U^* = 5$, which corresponds to the onset of mode B, oscillations set in. All cylinders oscillate, and they exhibit similar amplitudes. The second cylinder exhibits a quarter-cycle phase lag relative to the first and the third cylinder is in phase

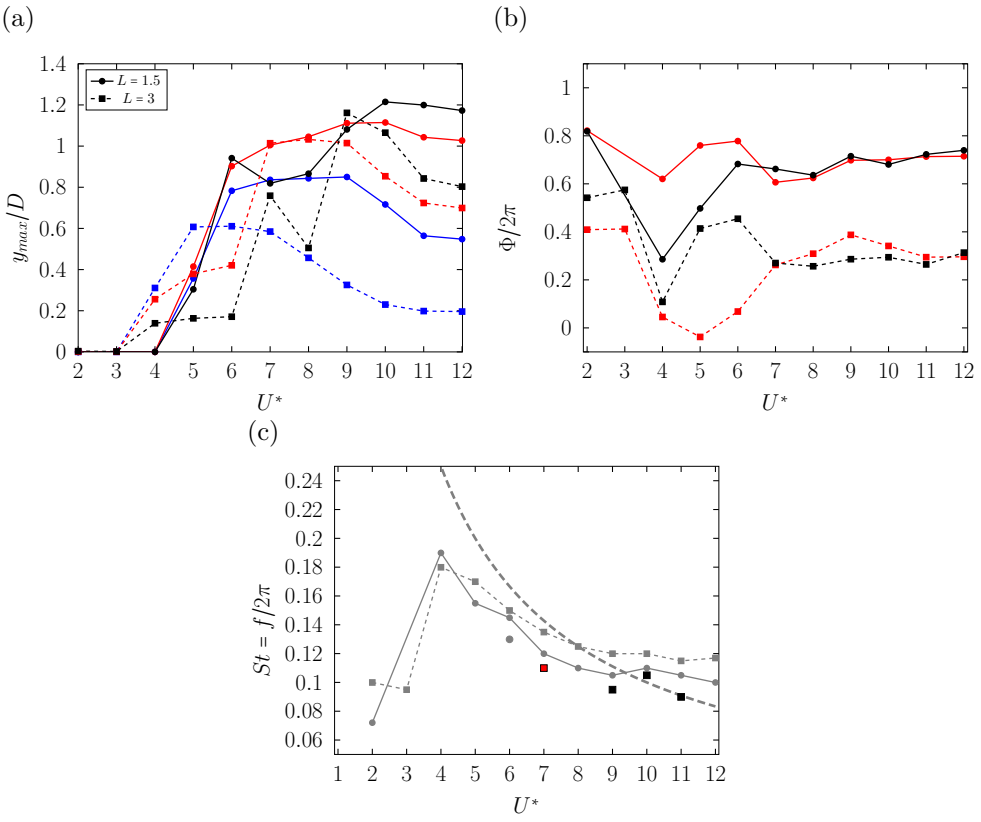

Figure 5.3: Vortex-induced vibrations of $N = 3$ in-line spring-mounted cylinders at $Re = 100$ and $m^* = 2.5$, for different spacings L: (a) maximum oscillation amplitudes, (b) phase differences between the cylinder motions, and (c) dominant frequencies extracted from the Fast Fourier Transform (FFT) of the bodies' displacement. In (a), the (—), (—), and (—) curves correspond to the front, middle, and rear cylinders, respectively. In (b), the phase difference between the middle and front cylinders is shown in red, while that between the rear and middle is shown in black. In (c), the common dominant frequency shared by all bodies is plotted in gray. In cases where an additional dominant frequency is present for a given cylinder, this secondary frequency is shown in blue, red, or black when it corresponds to the front, middle, or rear cylinder respectively. If this secondary frequency is present for all bodies, it is shown in gray. In dashed gray is shown the natural frequency of a spring-mounted body.

opposition with second one. At $U^* = 6$, quasi-periodic behaviour is observed for all cylinders, as shown in figure 5.5. The phase portrait does not collapse on a single closed trajectory, while the FFT reveals the coexistence of two frequencies, close to the natural frequency of the spring–mass system. The middle cylinder lags the first by a quarter of a cycle and the same phase shift is observed between the rear and middle cylinders. This transition coincides with the onset of mode C in the linear regime. At higher reduced velocities, first the motion of the middle cylinder dominates, then the one of the rear. The front and middle cylinders, as well as the middle and rear cylinders, remain in a quarter-cycle phase lag. In the oscillatory regime, the dominant frequency extracted from the FFT is common for the three cylinders, indicating global synchronisation (with the exception of the case described at $U^* = 6$). For certain reduced velocities, a reorganisation of the wake is observed downstream of the array (in a similar manner as what was described for the tandem case in figure 4.6). It is specifically visible for $U^* = 7$, around $x = 68D$, as can be seen in figure 5.4(e).

For the larger spacing $L = 3$, the amplitudes of motion of all three cylinders are weaker compared to the $L = 1.5$ case. Some examples of the flow dynamics and displacement of the bodies in time are shown in figure 5.6. In the interval $U^* = [4 - 6]$, the front cylinder dominates the dynamics. The middle and rear cylinders respectively dominate the dynamics for $U^* = [7 - 8]$ and $U^* > 8$. The maximum amplitude of $1.1D$ is reached by the rear cylinder at $U^* = 9$. At $U^* = [2 - 3]$, all cylinders remain stationary despite the presence of vortex shedding in the wake. This observation is in agreement with the linear analysis, which predicts the unstable fluid-dominated mode A in this region. At $U^* = 4$ the cylinders start to oscillate in phase and for $U^* = [5–6]$, the middle and front cylinders oscillate in phase while the rear and middle cylinders oscillate out of phase. For reduced velocities $U^* > 6$, the front and middle cylinders, as well as the middle and rear cylinders, remain in a quarter-cycle phase lag. At $U^* = 7$, quasi-periodic behaviour is observed for the middle and rear cylinders mainly, as shown in figure 5.7. As can be seen in figure 5.3(c) a second dominant frequency is found in the FFT of the displacement of the middle and rear bodies. For $U^* = [9, 10, 11]$, on the other hand, the quasi-periodic motion is found for the rear body only. Finally, for certain reduced velocities, a marked reorganisation of the wake occurs downstream as described previously.

For a spacing of $L = 6$, the complexity increases as described previously. Additionally, the transitory regime becomes increasingly longer. It was

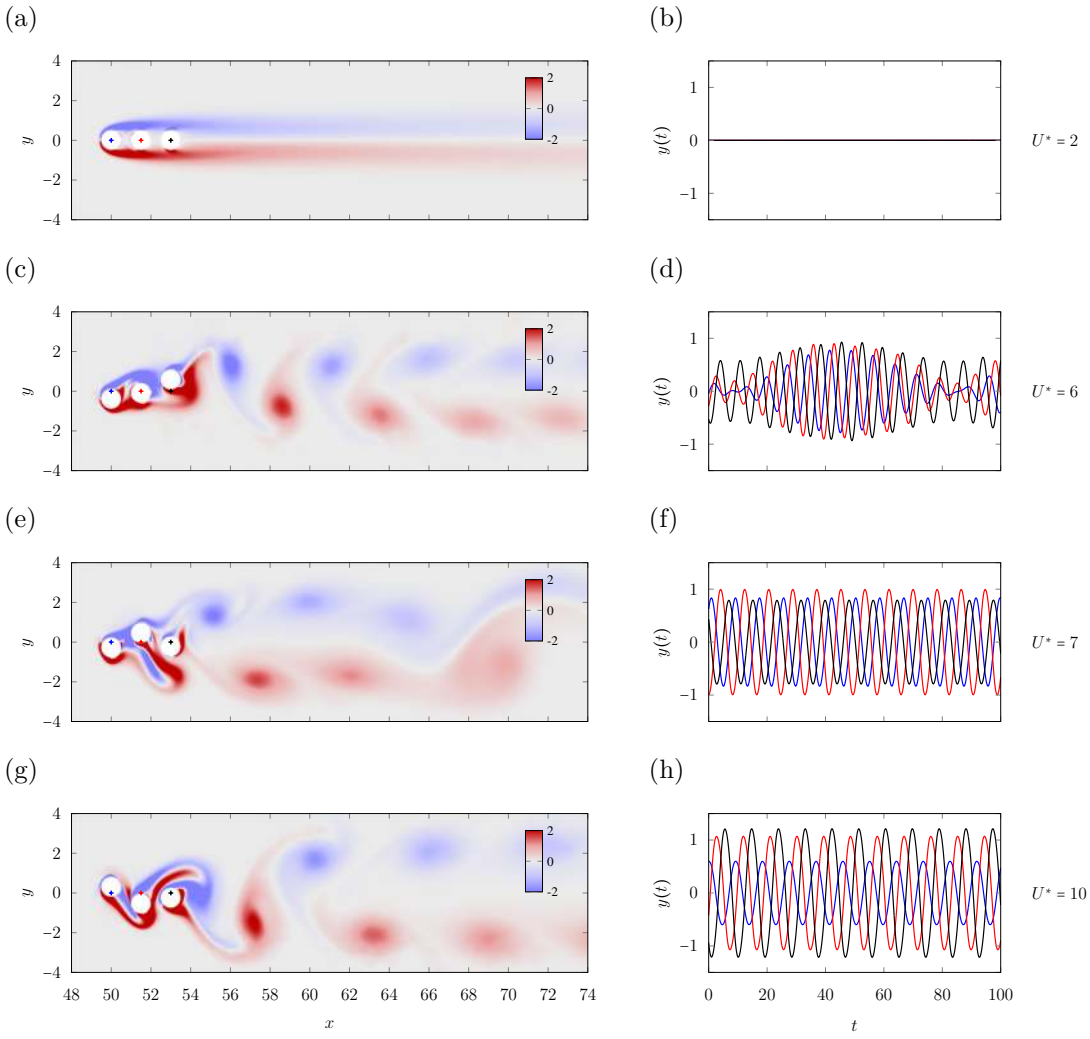

Figure 5.4: Flow visualisation (vorticity field) and amplitude of motion in time for the $N = 3$ in-line configuration at $Re = 100$, $m^* = 2.5$ and $L = 1.5$ for different reduced velocities U^*. The blue, red and black crosses represent the initial rest positions of the front, middle and rear cylinders respectively. Similarly, —— , —— and —— represent their position in time.

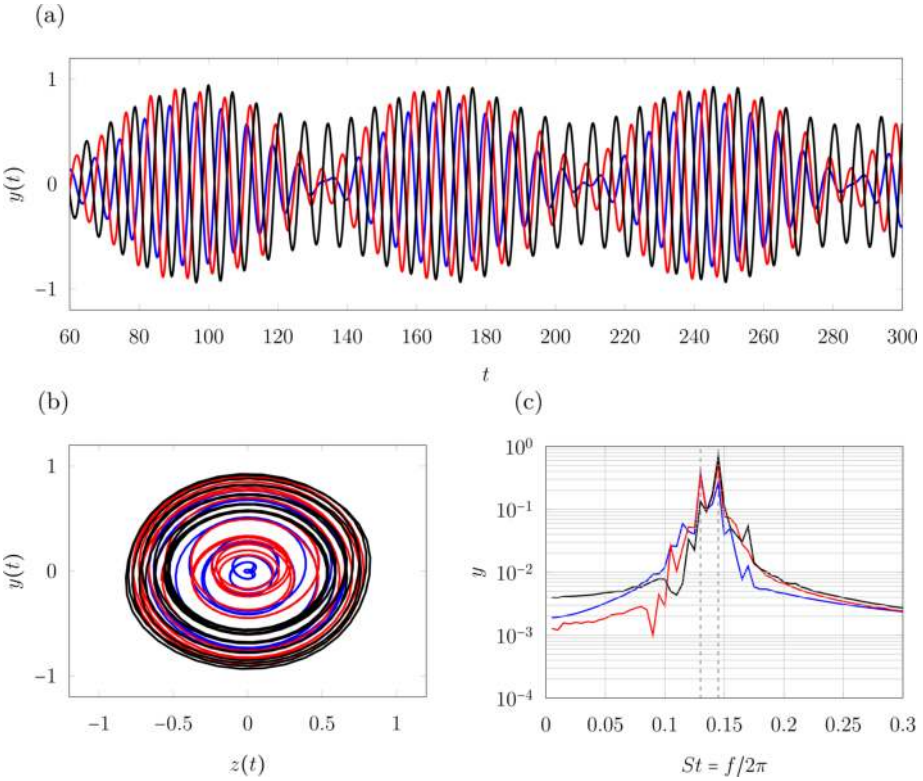

Figure 5.5: (a) Extension of 5.4(d): amplitude of motion in time for the $N = 3$ in-line configuration at $Re = 100$, $m^* = 2.5$, $L = 1.5$ and $U^* = 6$. (b) Phase portrait: velocity of the bodies against their position. (c) Fast Fourier Transform of the position in time of the bodies. —, — and — are respectively used for the front, middle and rear body.

therefore decided that a description of the non-linear dynamics at this spacing was out of scope of the present work.

5.2 Four bodies

5.2.1 Linear analysis

We show in figure 5.8 the neutral curves computed from the impedance-based method in the $Re-U^*$ plane for spacings of $L = 1.5$, $L = 3$ and $L = 6$ and for a reduced mass of $m^* = 2.5$ and $m^* = 20$. The growth rate and frequency of the corresponding modes are shown in figure 5.9 for $m^* = 2.5$ and $Re = 100$.

For $L = 1.5$, mode B (—) is a structure-dominated mode that involves the motion of all four cylinders. Mode C (—) is structure-dominated and mainly involves the motion of the fourth cylinder. One can note that, as is the case for $N = 3$ in-line bodies, this mode is associated with the motion of the rear-most body.

For $L = 3$, mode A (—) is a fluid-dominated mode and its frequency follows that of the equivalent fixed configuration. Mode B remains a structure-dominated mode that involves the motion of all bodies and mode C involves the motion of the fourth cylinder. We note the appearance of mode D (—) which is a structure-dominated mode. Its frequency follows that of the natural frequency of the spring-mounted system as can be seen in figure 5.9(d). It involves the motion of the fourth cylinder and third cylinders mainly. Again, modes A, B and C have a similar behaviour as in the case of the $N = 3$ in-line bodies. At that spacing, it seems that the addition of a body induces the appearance of an additional unstable eigenmode linked to the motion of that body; and that all previously existing eigenmodes retain their behaviour.

For $L = 6$, a substantial number of unstable eigenmodes appear, especially in the range $Re = [100 - 80]$ (curves displayed in gray in figures 5.8(e) and 5.8(f)). At that spacing, all cylinders are allowed their own fluid and structure-dominated mode and the complexity increases drastically as can be seen from the neutral curves. We can note that the modes resemble mode B and AC in the cases discussed above. A rigorous investigation of the linear dynamics at that spacing will not be attempted considering the complexity of that case.

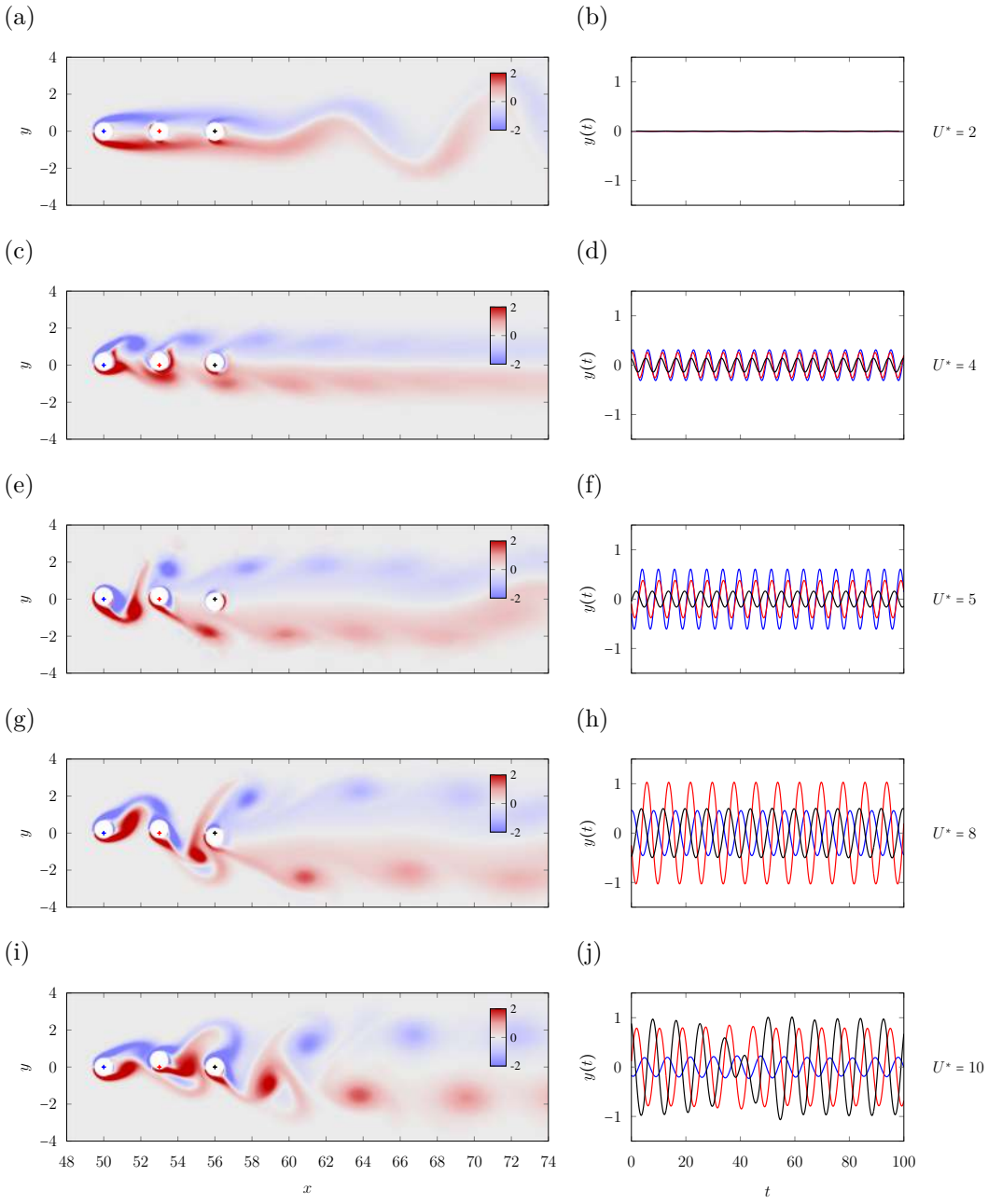

Figure 5.6: Flow visualisation (vorticity field) and amplitude of motion in time for the $N = 3$ in-line configuration at $Re = 100$, $m^* = 2.5$ and $L = 3$ for different reduced velocities U^*. The blue, red and black crosses represent the initial rest positions of the front, middle and rear cylinders respectively. Similarly, —— , —— and —— represent their position in time.

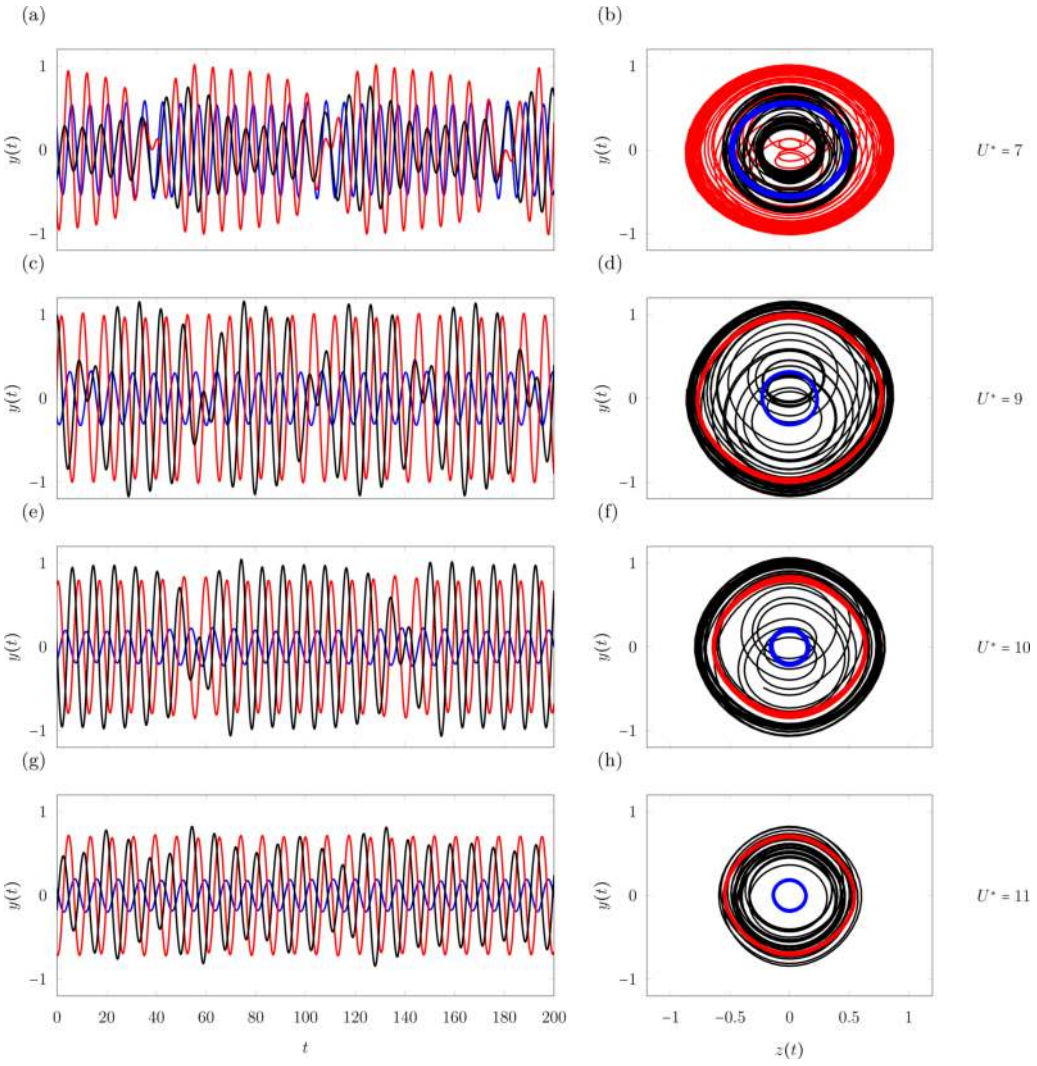

Figure 5.7: (a,c,e,g) Amplitude of motion in time for the $N = 3$ in-line configuration at $Re = 100$, $m^* = 2.5$, $L = 3$ for $U^* = 7$, $U^* = 9$, $U^* = 10$ and $U^* = 11$. (b,d,f,h) Phase portrait for the same values of U^*. The front, middle and rear bodies are respectively represented with —, — and —.

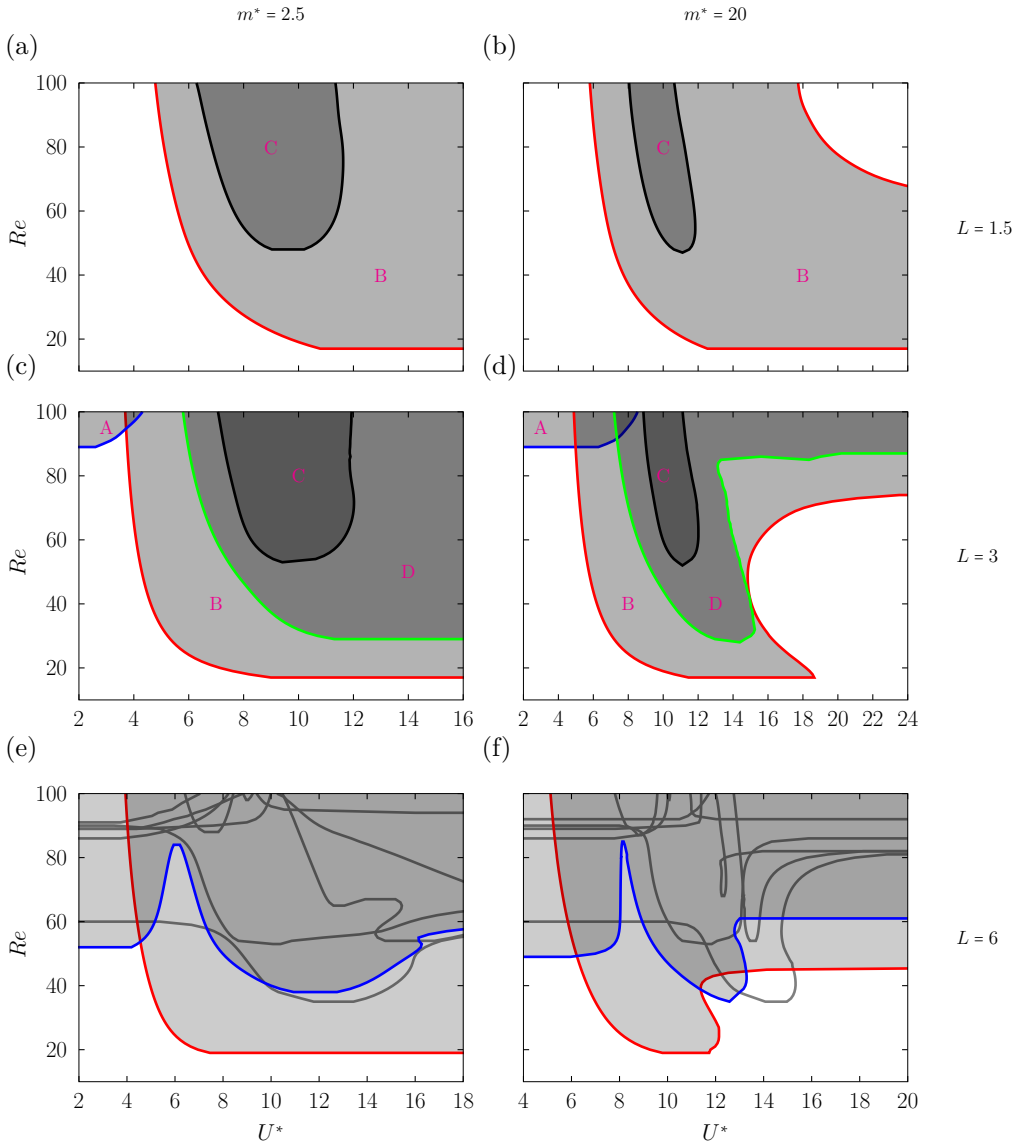

Figure 5.8: Neutral curves in the $Re - U^*$ plane for $N = 4$ in-line cylinders for $m^* = 2.5$ and $m^* = 20$: $L = 1.5$ (a,b), $L = 3$ (c,d) and $L = 6$ (e,f). Results come from the impedance-based predictions. Gray indicates regions where one unstable mode exists while darker gray regions indicate where there are more unstable modes.

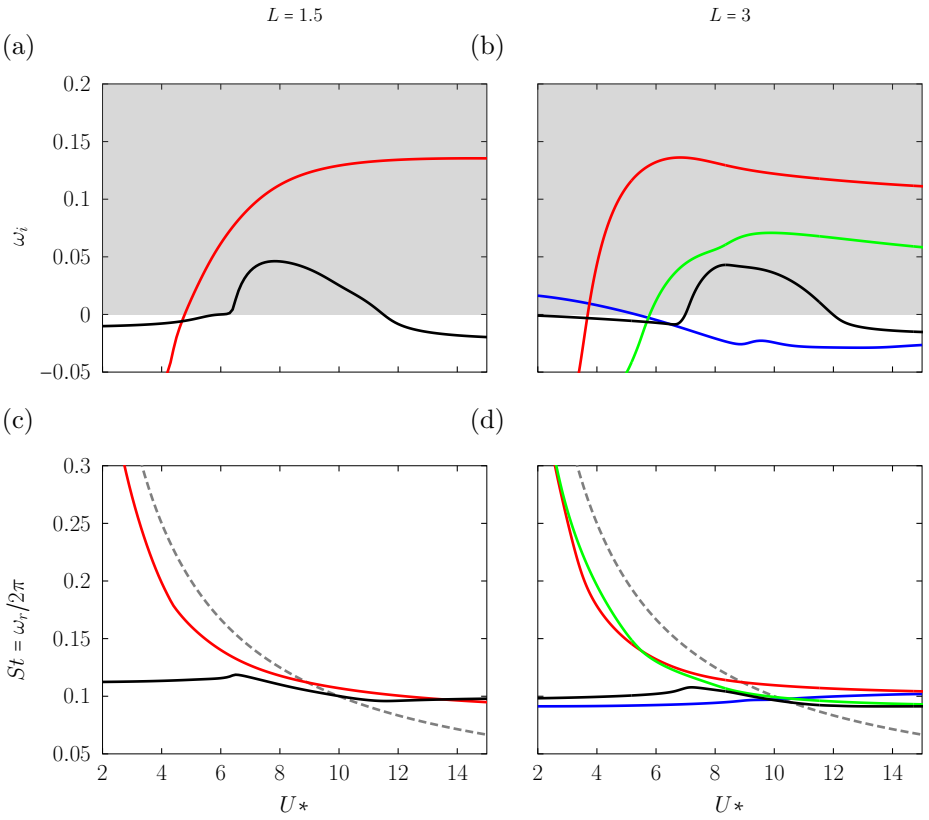

Figure 5.9: Real and imaginary parts of the leading eigenvalues (LSA) with respect to U^* for $N = 4$, $m^* = 2.5$ and $Re = 100$: $L = 1.5$ (a,c) and $L = 3$ (b,d). Modes A, B, C and D are respectively represented with (—), (—), (—) and (—).

5.2.2 Non-linear dynamics

Figure 5.10 shows the results of direct numerical simulations of the $N = 4$ in-line configuration at $Re = 100$ and $m^* = 2.5$, for the spacings $L = 1.5$ and $L = 3$.

For $L = 1.5$, the third cylinder dominates the motion up to $U^* = 8$, after which the fourth one dominates. For $U^* = [2-4]$, the cylinders are stationary and the flow is stable (see figure 5.11(a) and 5.11(b)), as predicted by the linear stability (as can be seen in figure 5.8(a)). At $U^* = 5$, oscillations set in and vortex-shedding appears (see figures 5.11(c) and 5.11(d)). The fourth cylinder is in phase opposition with the third one. The third cylinder is also in phase opposition with the second one and the second cylinder has a quarter phase lag with the first one. At $U^* = 6$, the second and first, as well as the third and second cylinders are in a quarter phase lag. The fourth and third cylinders are in phase opposition. Then, for $U^* > 6$, all cylinders are in the quarter phase lag with the preceding one.

For $L = 3$, the amplitudes of motion of the cylinders are generally smaller than for $L = 1.5$. First the amplitude of motion of the first cylinder dominates then, increasing the reduced velocity, the amplitude of the second one dominates and then finally of the fourth one. For $U^* = [2-3]$, vortex shedding is observed in the wake of the bodies, while their motion is negligible. At $U^* = 4$, oscillations set in and the bodies are mainly in phase. For $U^* = [5-6]$, the second and first bodies are in phase, while the third and second are almost in phase opposition and the fourth and third bodies are in a quarter phase lag. For $U^* = [6, 7]$, quasi-periodic behaviour is observed for the second, third and fourth bodies, as a second dominant frequency is found from the FFT of their motion. For $U^* > 8$, quasi-periodic behaviour is only observed for the third and fourth bodies.

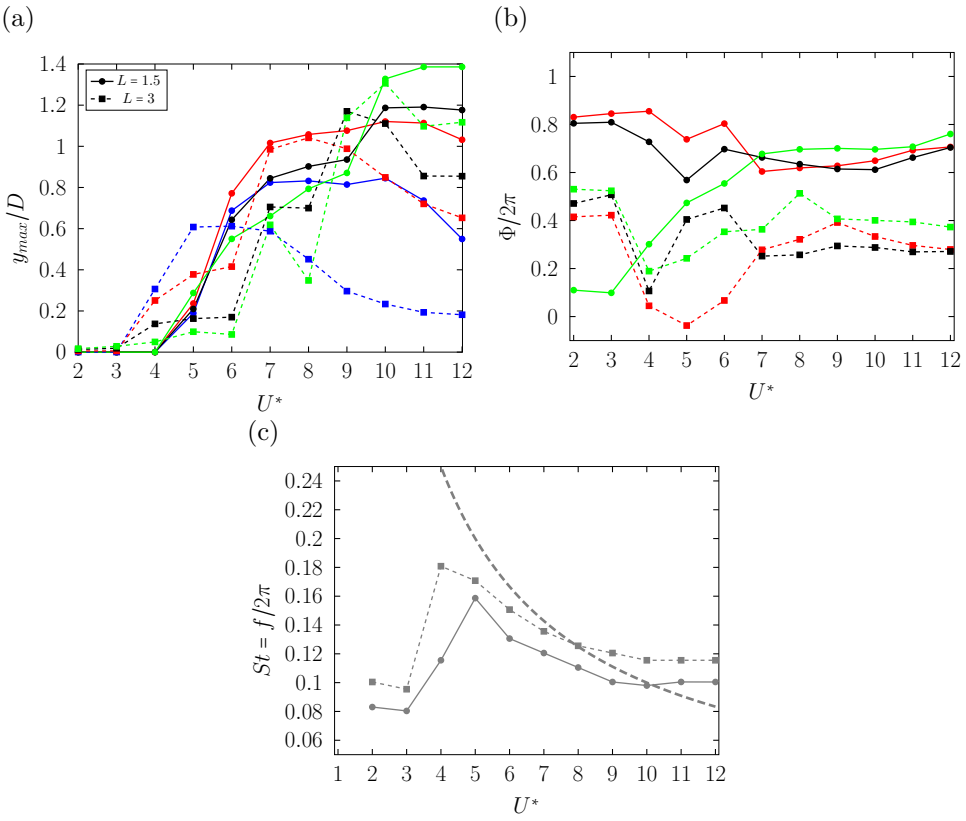

Figure 5.10: Vortex-induced vibrations of $N = 4$ in-line spring-mounted cylinders at $Re = 100$ and $m^* = 2.5$, for different spacings L: (a) maximum oscillation amplitudes, (b) phase differences between the cylinder motions, and (c) dominant frequencies extracted from the Fast Fourier Transform (FFT) of the transverse displacement signals. In (a), the (—), (—), (—) and (—) curves correspond to the front, second, third and rear cylinders, respectively. In (b), the phase difference between the first and second cylinders is shown in red, while that between the second and third and between the third and fourth are shown in black and green respectively. In (c), the common dominant frequency shared by all four cylinders is plotted in gray. In dashed gray is shown the natural frequency of a spring-mounted body.

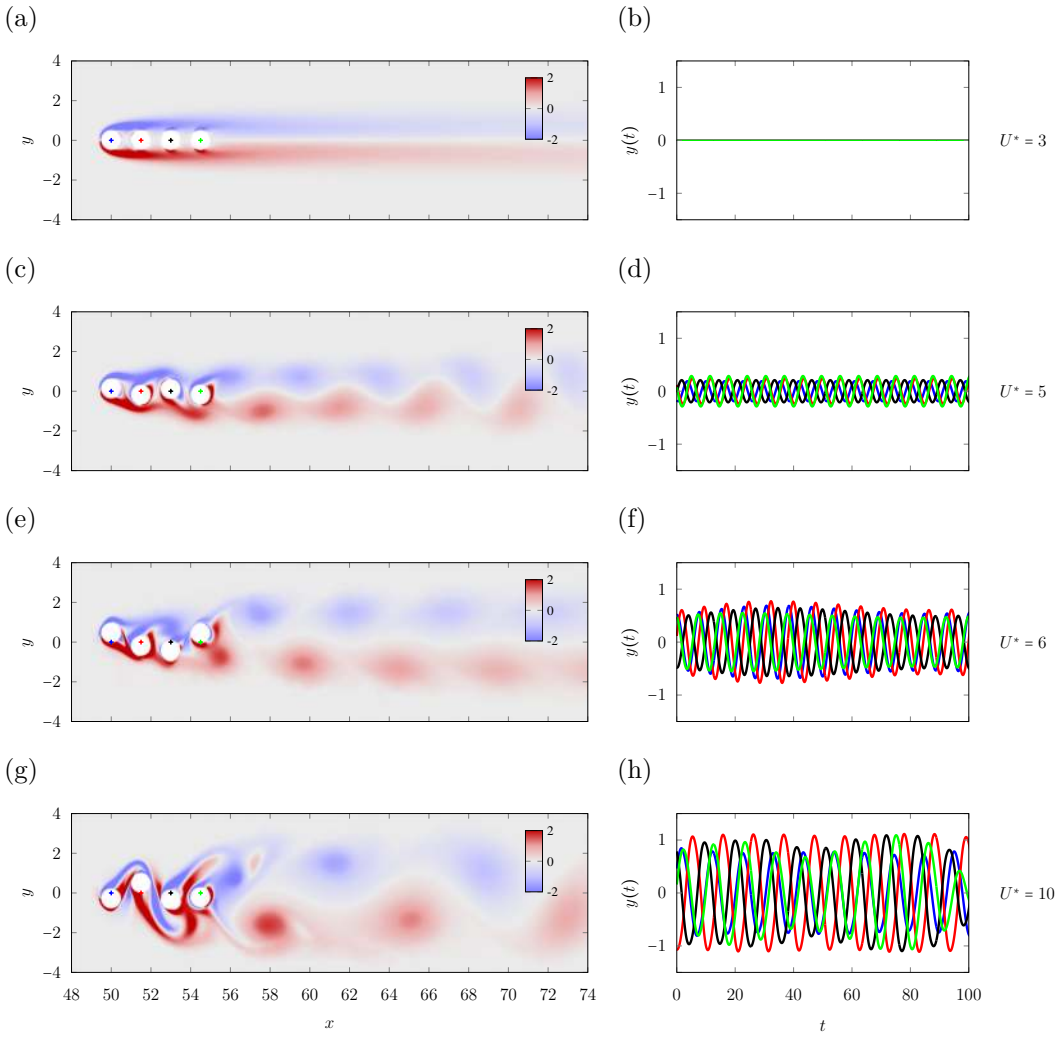

Figure 5.11: Flow visualisation (vorticity field) and amplitude of motion in time for the $N = 4$ in-line configuration at $Re = 100$, $m^* = 2.5$ and $L = 1.5$ for different reduced velocities U^*. The blue, red, black and green crosses represent the initial rest positions of the front, second, third and rear cylinders respectively. Similarly, —— , ——, —— and —— represent their position in time.

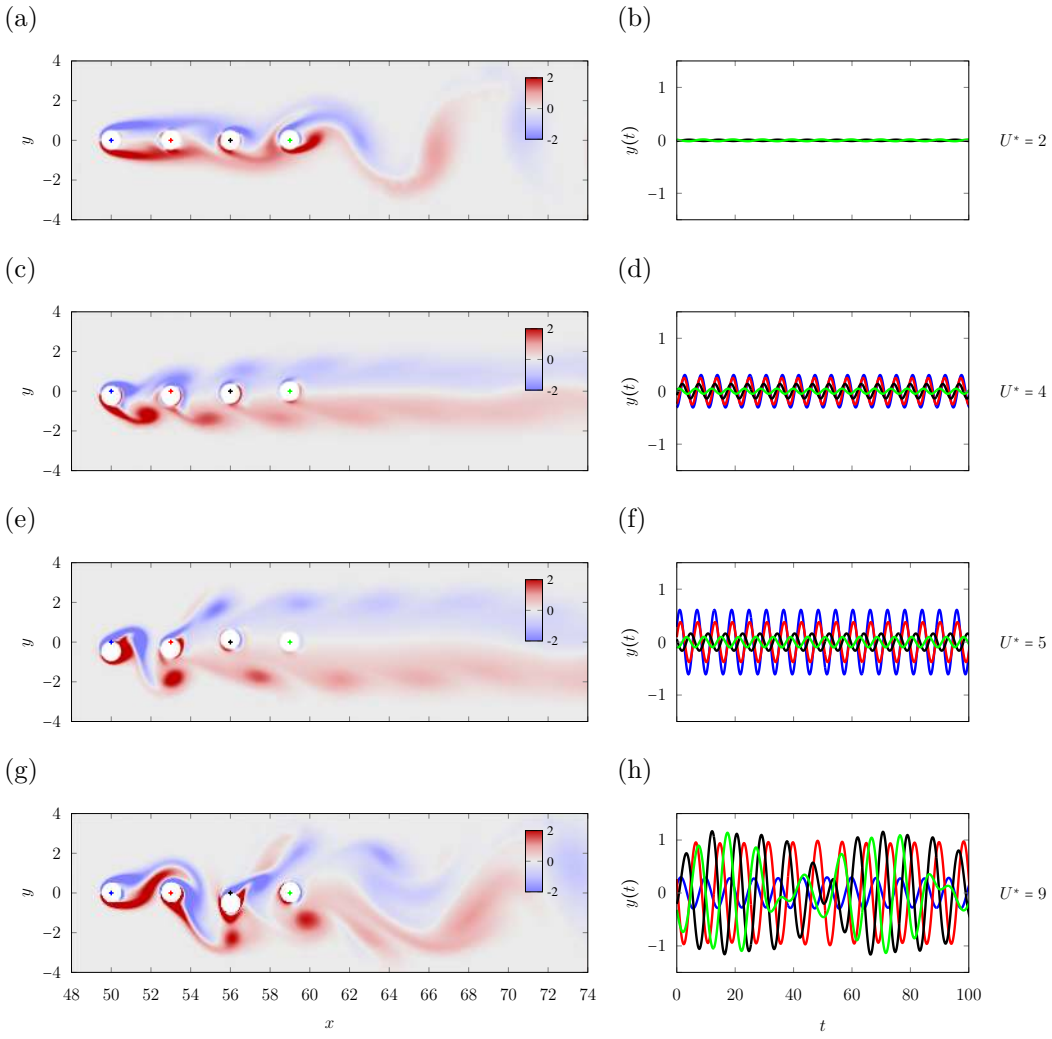

Figure 5.12: Flow visualisation (vorticity field) and amplitude of motion in time for the $N = 4$ in-line configuration at $Re = 100$, $m^* = 2.5$ and $L = 3$ for different reduced velocities U^*. The blue, red, black and green crosses represent the initial rest positions of the front, second, third and rear cylinders respectively. Similarly, —— , ——, —— and —— represent their position in time.

5.3 Synthesis

In this chapter, we extended the analysis to configurations of multiple in-line cylinders ($N = 3$ and $N = 4$), combining linear stability, impedance-based predictions and non-linear simulations to characterise the increasingly complex fluid–structure interactions.

For $N = 3$, the linear analysis showed that the modal structure strongly depends on the spacing. At small spacing ($L = 1.5$), the system behaves as an elongated bluff body, suppressing the classical fluid-dominated mode and favouring structure-dominated modes involving collective or rear-body motion. As the spacing increases ($L = 3$), the dynamics recover features of the tandem configuration, with a clear separation between fluid- and structure-dominated modes. At larger spacing ($L = 6$), the number of unstable modes increases significantly, with mixed fluid–structure modes and additional modes associated with the intermediate and rear cylinders, reflecting a progressive decoupling of the bodies.

The non-linear dynamics for $N = 3$ show the domination of the rear cylinder for small spacings. Transitions to quasi-periodic regimes occur near modal competition regions predicted by the linear analysis. At intermediate spacing, the response weakens and the dominance shifts progressively from upstream to downstream cylinders as the reduced velocity increases. Quasi-periodicity and wake reorganisation are again observed in regimes where multiple modes interact. For large spacing, the dynamics become too complex to be exhaustively characterised within the scope of this work.

For $N = 4$, the linear analysis reveals an extension of the modal structure identified for $N = 3$. At small and intermediate spacings, previously identified modes persist, while additional structure-dominated modes emerge, each primarily associated with the motion of newly added downstream cylinders. At large spacing, the number of unstable modes increases sharply, with each mode supporting its own fluid- and structure-dominated dynamics, leading to a highly complex stability landscape.

The non-linear simulations for $N = 4$ exhibit similar qualitative behaviour to the $N = 3$ case, with an even stronger dominance of downstream cylinders and richer phase dynamics.

Overall, increasing the number of in-line bodies leads to a progressive enrichment of the modal structure and non-linear dynamics. While the fundamental mechanisms identified in simpler configurations remain valid, the system exhibits a rapid growth in complexity, driven by the interaction and coexistence of multiple fluid- and structure-dominated modes, particularly at larger spacings.

Chapter 6

Spring-mounted body beneath a free surface

In this chapter, we will explore the impact of a free-surface on the stability of the flow around a fixed and spring-mounted body. This work extends previous investigations in our team and the reader is referred to Achour (2022) for more details. First, to understand the effect of confinement, the configuration of a body beneath a slip-wall will be investigated (section 6.1). In a second step, the effect of a deformable free-surface is investigated (section 6.2). We remind the reader that, in this chapter, surface tension will be neglected ($Ca \to \infty$).

6.1 Cylinder confined beneath a slip-wall

As a first step in our investigation, we will therefore explore the effect of the confinement with a slip-wall boundary condition. Indeed, the limit $Fr = 0$ corresponds to a non-deformed (or "rigid") free-surface and is equivalent to slip-wall. That configuration is also equivalent to the side-by-side configuration (see section 4.2) if one only takes into account the anti-phase modes. The author stresses on the fact that the results from this section are not computed using the methodology developed for the free-surface but using the methodologies described in chapter 2 and in Fabre *et al.* (2018) with slip-wall boundary conditions.

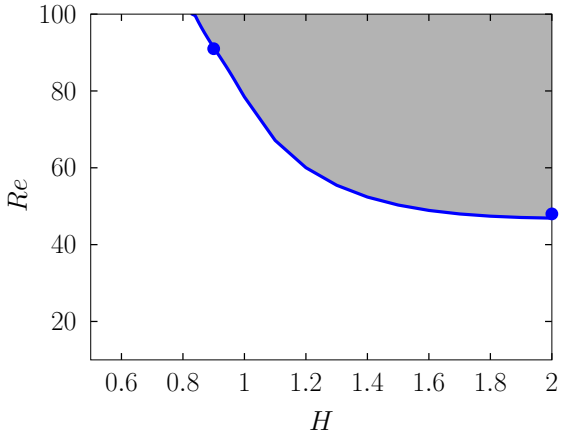

Figure 6.1: Regions of instability (shaded colors) computed from LSA in the $Re - H$ plane for a fixed cylinder. The thresholds of the fluid-dominated anti-phase mode (AP_A) from the side-by-side configuration are reported with ●.

6.1.1 Fixed cylinder

Let us consider the case of a fixed cylinder confined beneath a slip-wall. The base-flow and perturbation equations are solved with appropriate boundary conditions following the classical procedure described in Fabre *et al.* (2018). The linear stability analysis reveals a single unstable eigenmode, and the corresponding neutral curves in the $Re - H$ plane are reported in figure 6.1. Increasing confinement has a stabilising effect: below a critical gap size, $H \lesssim 0.83$, no unstable mode is detected within the investigated Reynolds number range. This observation is consistent with the findings for the confinement with no-slip walls. Bearman & Zdravkovich (1978) and later Lei *et al.* (1999) showed that sufficiently small gaps can suppress vortex shedding by altering the near-wake dynamics. Lei *et al.* (1999) showed that the upper and lower stagnation point respectively move downstream and upstream, therefore breaking the symmetry of the shear layers and modifying the pressure distribution. This results in a stabilisation of the shear layer on the gap side and a marked asymmetry of the flow which prevents the formation of the von Kármán vortex street.

Figure 6.2 shows the base-flow, eigenmode and the structural sensitivity for different confinements, for $Re = 60$.

The base flow exhibits significant modifications as the confinement increases. In the weakly confined configuration (figure 6.2(a)), the flow is symmetric with respect to the wake centerline. As the gap is reduced, this symmetry is progressively broken by the presence of the slip wall (figure 6.2(b)). The streamwise velocity field becomes clearly asymmetric with a marked acceleration of the flow within the gap compared to the unconstrained side (figure 6.2(c)). This induces a downward shift of the wake. In addition, the wake appears elongated in the streamwise direction.

A similar symmetry breaking is observed in the structure of the eigenmode. In the weakly confined case, the mode retains the classical antisymmetric pattern associated with the von Kármán vortex street. As confinement increases, the mode becomes increasingly asymmetric and shifts towards the unconstrained side of the flow. At the same time, the overall amplitude of the eigenmode decreases, indicating a weakening of the global instability.

The structural sensitivity is defined as the product of the adjoint and direct eigenfunctions and quantifies the regions where the instability mechanism acts (feedback leading to self-sustained oscillations, see section 3.2.4 for a formal definition). In the weakly confined case, the structural sensitivity field recovers the classical structure reported by Giannetti & Luchini (2007), as can be seen in figure 6.2(g). Mainly, it is organised into two lobes symmetrically located on either side of the separation bubble, highlighting the region where the wavemaker is maximal. This region extends up to approximately $3D$ downstream and $1.5D$ in the cross-stream direction, while both the near-body region and the far wake contribute only weakly to the instability dynamics. As confinement increases, this symmetry is broken by the presence of the wall as can be seen in figure 6.2(i) for $H = 1.2$. The sensitivity region is shifted towards the lower side of the wake, and the intensity of the lower lobe is significantly reduced. The maximum intensity of the structural sensitivity regions is however increased with the confinement as can be seen from the increasing colormap levels.

6.1.2 Spring-mounted cylinder

We now consider the case of a spring-mounted cylinder beneath a slip-wall. The linear system described in 2.3 is solved for a single spring-mounted cylinder with the appropriate boundary conditions. Figure 6.3 shows the

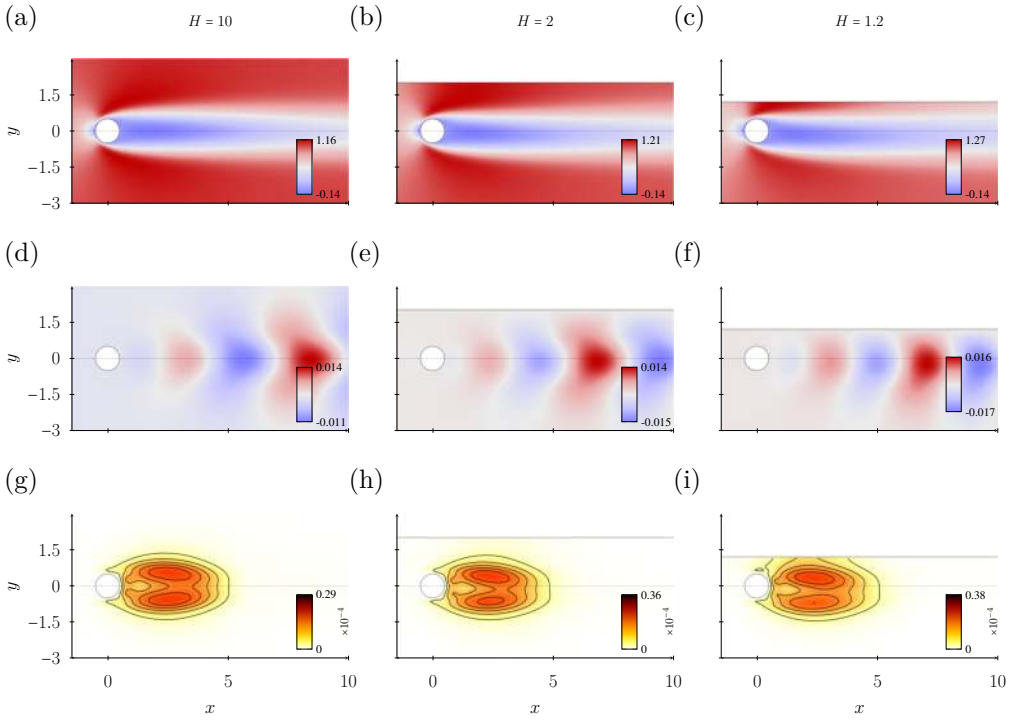

Figure 6.2: Fixed cylinder beneath a slip-wall at Re = 60: (a,b,c) base-flow ($\hat{u}_{0_x}$), (d,e,f) eigenmode (u_y) and (g,h,i) structural sensitivity for different immersions H.

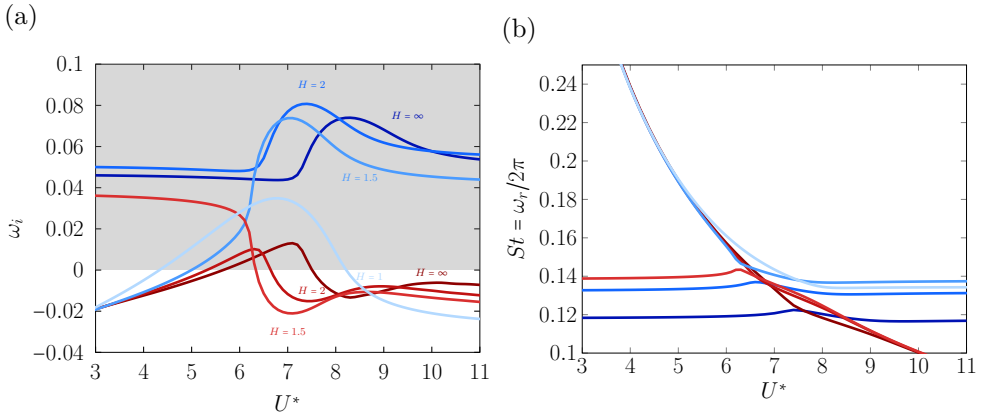

Figure 6.3: Real and imaginary parts of the leading eigenvalues (LSA) with respect to U^* for a single spring-mounted cylinder confined below a slip-wall, for $m^* = 20$ and $Re = 60$: $H = \infty$(—,—), $H = 2$ (—,—), $H = 1.5$ (—,—) and $H = 1$ (—).

growth rates and frequencies of the leading unstable eigenmodes for various confinement levels at $Re = 60$ and $m^* = 20$. At $H = 2$, similarly to what is observed for a single spring-mounted body in an unbounded domain ($H \to \infty$), two unstable eigenmodes are found, corresponding to "fluid-dominated" and "structure-dominated" behaviours. Mode A (—) is "fluid-dominated", it remains unstable over the whole range of reduced velocities and its frequency closely follows that of the corresponding fixed-cylinder configuration. Mode B (—) is "structure-dominated", it is unstable only over a limited range of reduced velocities and its frequency follows that of the natural frequency of the spring-mass system. Compared to the unbounded configuration, the maximum growth rates of both modes are shifted towards lower reduced velocities. Moreover, the range over which the structure-dominated mode is unstable is decreased.

Increasing the confinement further to $H = 1.5$ (—,—), an exchange of stability between the two modes is observed which is characteristic of an exceptional point (similar to the phenomenon observed for the tandem of spring-mounted cylinders described in section 4.1.1.1). In particular, the low-U^* branch of the mode previously identified as fluid-dominated becomes structure-dominated, while the opposite behaviour is observed for

the other mode. Moreover, confinement has a stabilising effect, as shown by the reduction in growth rates in the range of U^* where the modes are of fluid-dominated nature.

For even stronger confinement ($H = 1$), a marked change in the dynamics is observed. The fluid-dominated modes are stabilised and only a single unstable mode remains (—), which is structure-dominated.

Figure 6.4 shows the neutral curves in the $Re - H$ plane for a fixed reduced mass ($m^* = 20$) and reduced velocity ($U^* = 6$). Mode A is unstable for $Re > 48$ for the highest values of H and increasing the confinement stabilises it, as its threshold increases. For confinements of $H < 0.8$ and for the range of Reynolds numbers investigated, mode A is stable. Concerning mode B, it is unstable for $Re > 33$ for the high-H values. Increasing the confinement first destabilises the mode, as was seen figure 6.3 in which the growth rates are shifted towards lower U^* values. Increasing further the confinement sharply stabilises the mode which is found to be stable for $H < 0.58$.

Finally, note that Semin *et al.* (2012) reported the existence of a confinement-induced vibration (CIV) instability for a cylinder confined in a Hele–Shaw cell with no-slip walls (from either side of the body). Such an instability is not observed here in the case of a unilateral confinement with a slip-wall.

6.2 Cylinder beneath a free-surface

After having characterised the effect of the confinement with a single slip-wall, we move to the problem involving a deformable free-surface. As stated section 3.1, a free-surface introduces additional non-dimensional parameters to the system: the Froude number ($Fr = \frac{U_\infty}{\sqrt{gD}}$) and the Capillary number ($Ca = \frac{\mu U}{\gamma}$). The system of equations for the base-flow and perturbations of sections 3.2.2 and 3.2.3 are solved for different immersions, Reynolds numbers and Froude numbers. As was said earlier, we confine our current investigation to the limit where surface tension can be neglected ($Ca \to \infty$).

6.2.1 Steady state

Steady states for immersions of $H = 2$ and $H = 1.05$ and different Froude numbers are plotted figure 6.5 for $Re = 60$. First, in the limit $Fr \to 0$, the

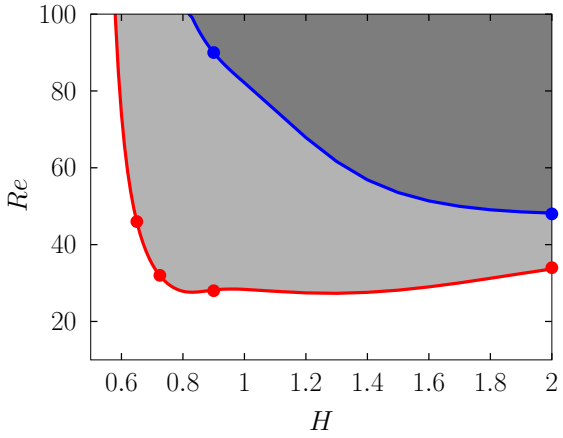

Figure 6.4: Regions of instability (shaded colors) computed from LSA in the $Re - H$ plane for a spring-mounted cylinder with $U^* = 6$ and $m^* = 20$. The thresholds of the fluid- and structure-dominated anti-phase mode (AP_A and AP_B) from the side-by-side configuration are respectively reported with ● and ●.

surface is flat (figures 6.5(a) and 6.5(d)) and we recover the behaviour from a slip-wall boundary condition. Increasing the Froude number induces a deformation of the free-surface as stationnary waves settle in (figures 6.5(b) and 6.5(e)). Increasing further the Froude number leads to a pronounced steepening of the first wave crest. The initially smooth bump sharpens progressively and develops a cusp-like feature, with a marked asymmetry skewed in the upstream direction (figures 6.5(c) and 6.5(f)). We can note that the free-surface profiles obtained at the two immersions display similar shapes, despite different Froude numbers. In particular, the strongly deformed configuration at lower immersion ($H = 1.05$) resembles that observed at larger immersion ($H = 2$) for higher Froude numbers, but with a shorter wavelength. This suggests that decreasing the immersion effectively shifts the response towards lower Froude numbers while reducing the characteristic spatial scale of the surface deformation.

Figure 6.6(a) shows the minimum and maximum amplitudes of deformation of the free-surface in the x-direction and in the y-direction (inset (a-i)), for $H = 2$. These points respectively correspond to the position of the first depression (or trough) and first crest of the wave, represented in

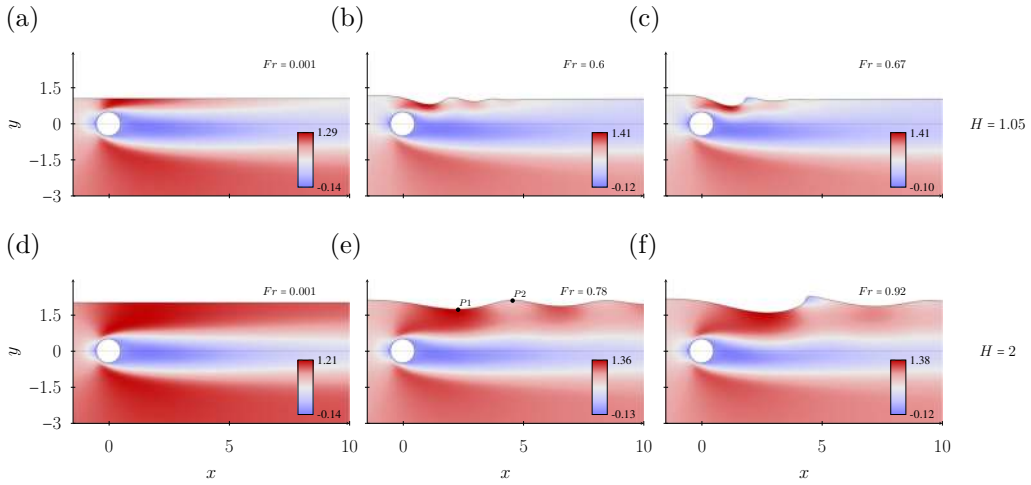

Figure 6.5: Streamwise velocity ($\hat{u}_{0_x}$) profiles for $Re = 60$ and for immersions of $H = 2$ and $H = 1.05$ at different Froude numbers.

figure 6.12(d) by the points $P1$ and $P2$.

Increasing the Froude number decreases the y-position of $P1$ while it's x-position remains roughly around $2.5D$. In other words, the first depression deepens as the Froude number increases. Concerning point $P2$, its position initially increases in both directions, corresponding to the crest of the wave becomes higher and shifts downstream. However, beyond a critical value around $Fr \approx 0.92$ (vertical dotted line), the y-position of $P2$ starts to decrease, shortly followed by a reduction in its x-position. This behaviour corresponds to a pronounced steepening of the first wave crest, which develops a cusp-like shape and begins to fold upstream and downward. As the Froude number is further increased, and before the steady solution ceases to converge (dashed region), the base flow thus evolves towards a configuration characteristic of wave breaking.

Figure 6.6(b) shows the lift and drag forces on the cylinder for $H = 2$. We can note that the lift force is negative and slightly decreases with increasing Froude. On the other hand, the drag force increases slightly.

Note that the critical Froude number beyond which no stationary solution is found depends on the immersion depth, the Reynolds number, and the

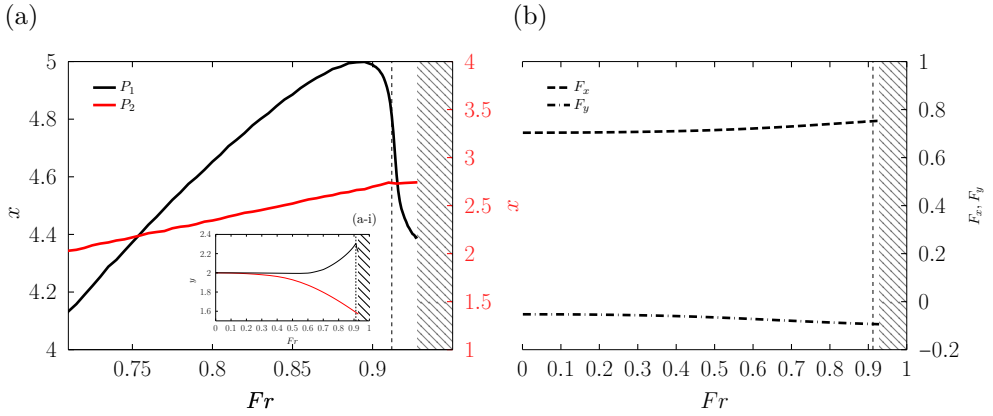

Figure 6.6: $Re = 60$ and $H = 2$: (a) positions of P1 and P2 in the x-direction and in the y-direction (inset (a-i)) with respect to Fr, (b) lift and drag forces acting on the cylinder.

capillary number.

6.2.2 Stability analysis

6.2.2.1 Fixed cylinder at $H = 2$

Let us first investigate the impact of the deformation of the free-surface on the flow dynamics around a fixed cylinder submerged at $H = 2$. This configuration corresponds to that studied by Achour (2022). An implementation error was found in the linear stability code from that work. Once corrected, the stability analysis was repeated and yielded results that deviate substantially from those previously reported. The linear stability analysis shows one unstable eigenmode and figure 6.7 shows its neutral curve in the $Re - Fr$ plane. The critical Reynolds number for instability increases with increasing Froude. For the range of Reynolds number investigated, the system is stable for $Fr > 0.9$. The increase in the deformation of the free-surface therefore stabilises the flow.

TO DO: add figureThis result might be interpreted as a local confinement effect. As discussed in the previous section, the first trough deepens with increasing Froude and is located approximately at $x = 2.5$. This position coincides with the region where the structural sensitivity is localised in the wake of a fixed cylinder. As the Froude number increases, the free-surface

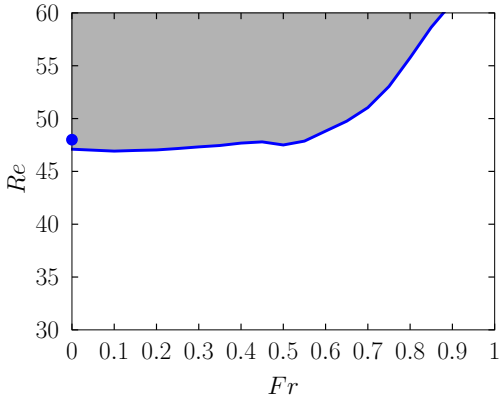

Figure 6.7: Regions of instability (shaded colors) computed from LSA in the $Re - Fr$ plane for $H = 2$ for a fixed cylinder. The thresholds of the fluid-dominated anti-phase mode (AP_A) from the side-by-side configuration (see section 4.2) are reported with ●.

deformation effectively induces a local confinement in this critical region. As previously shown, such confinement has a stabilising effect on the system, which may explain the observed behaviour.

6.2.2.2 Spring-mounted cylinder at $H = 2$

Let's now investigate the impact of the deformation of the free-surface on the vortex-induced vibrations of a spring-mounted cylinder submerged at $H = 2$. We fix the Reynolds number and reduced mass to $Re = 60$ and $m^* = 20$, while varying U^* and Fr. At low Froude number, we recover the behaviour observed when the body is confined with a slip-wall, namely, there exist a "fluid-dominated" (mode A) and a "structure-dominated" mode (mode B). Increasing the Froude number up to $Fr = 0.7$ has a stabilising effect on both modes. First, the growth rate of the fluid-dominated mode is decreased over the whole range of reduced velocities. Secondly, the range of reduced velocities over which the structure-dominated mode is unstable is reduced. The maximum growth rates of both modes are shifted towards lower reduced velocities.

We plot in figure 6.9 the transverse velocity field of the eigenmodes for different reduced velocities for $Fr = 0.7$. For this Froude number, the modes exhibit a structure similar to that observed in the unbounded case. Increasing

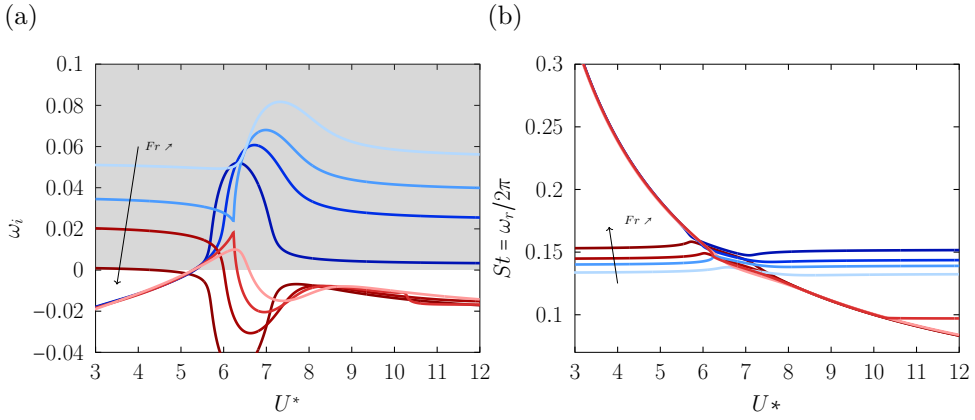

Figure 6.8: Real and imaginary parts of the leading eigenvalues (LSA) with respect to U^* for $N = 1$ spring-mounted cylinder confined below a free-surface, for $H = 2$, $m^* = 20$ and $Re = 60$: $Fr = 0.87$ (—,—), $Fr = 0.78$ (—,—), $Fr = 0.7$ (—,—) and $Fr = 0.001$ (—,—).

the Froude number to $Fr = 0.78$, a topological transition occurs leading to a situation where the A branch for small U^* becomes connected to what was previously the B branch and vice-versa. Similar transitions were observed for the tandem of spring-mounted cylinders as described in section 4.1.1.1. Increasing further the Froude number stabilises the system in the low-U^* branch and no unstable mode is found in that region after a Froude number of $Fr = 0.85$. On the other hand, mode B remains unstable for higher Froude numbers, in a region of reduced velocoties of $5.5 \lesssim U^* \lesssim 7.5$

Figure 6.10 shows the vertical velocity (figure 6.10(a)) and structural sensitivity (figure 6.10(b)) of the mode B for $Fr = 0.92$ and $U^* = 6$. The structural sensitivity region differs from that of the fixed-cylinder case. As shown by Negi *et al.* (2020) for a spring-mounted cylinder in an unbounded domain, the dominant region is shifted towards the cylinder, lying to the top and bottom part of the body. In the present configuration, the confinement induced by the free surface breaks this symmetry and slightly displaces the sensitivity region downward. However, for this immersion, the structural sensitivity remains negligible in the vicinity of the free surface, indicating that the latter has only a limited influence on the instability mechanism.

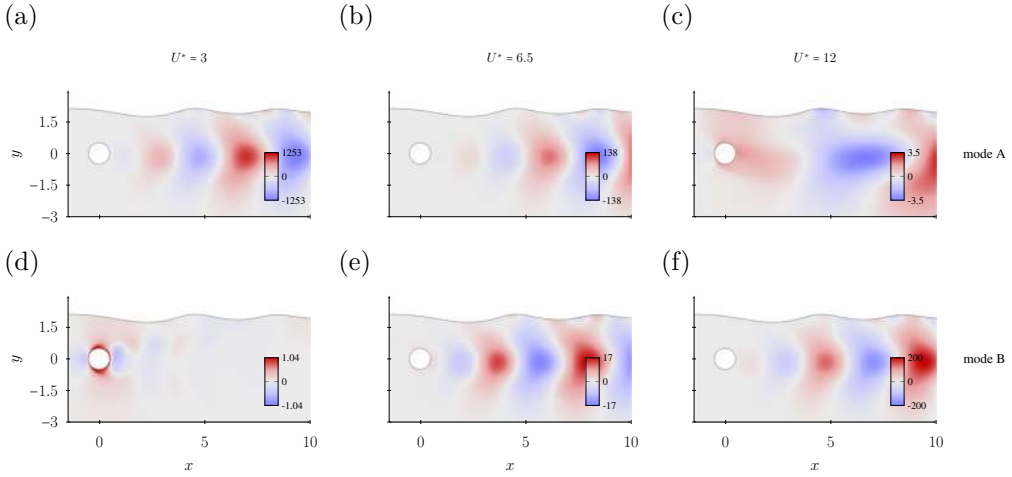

Figure 6.9: Vertical velocity of the eigenmodes for Re = 60, Fr = 0.7 and m^* = 20. The fields were normalised by the body's velocity. See section 4.1.1.1 for details about the meaning of the colormaps' values.

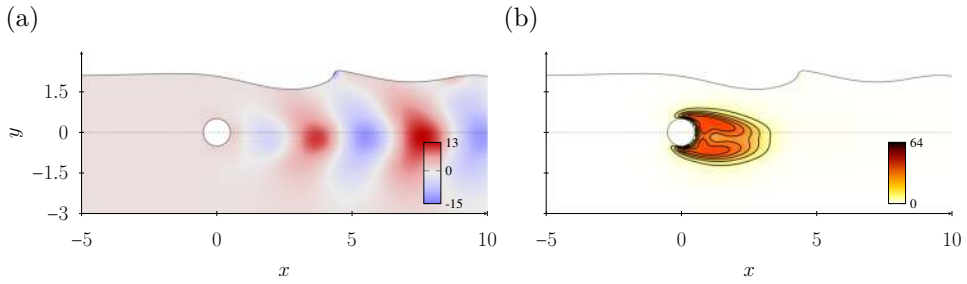

Figure 6.10: (a) Vertical velocity and (b) structural sensitivity of mode B at Fr = 0.92, Re = 60, U^* = 6 and m^* = 20. The fields were normalised by the body's velocity. See section 4.1.1.1 for details about the meaning of the colormaps' values.

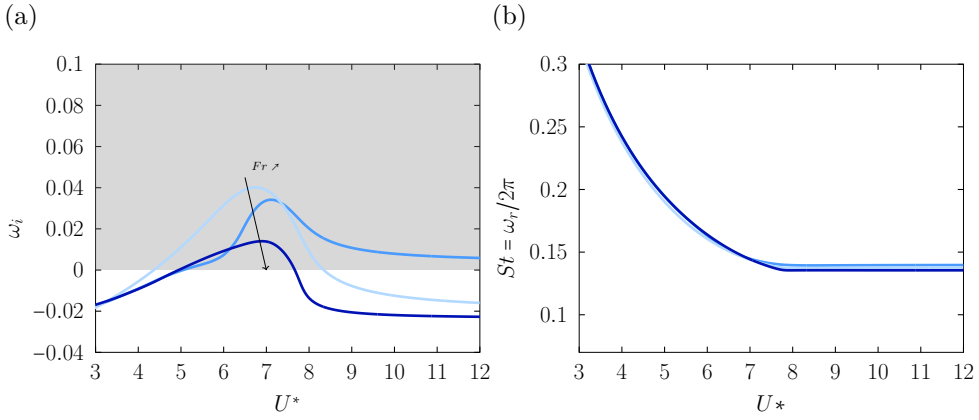

Figure 6.11: Real and imaginary parts of the leading eigenvalues (LSA) with respect to U^* for $N = 1$ spring-mounted cylinder confined below a free-surface, for $H = 1.05$, $m^* = 20$ and $Re = 60$: $Fr = 0.67$ (—), $Fr = 0.6$ (—) and $Fr = 0.001$ (—).

6.2.2.3 Spring-mounted cylinder at $H = 1.05$

Let us now consider the stronger confinement case of $H = 1.05$. The linear stability analysis reveals a single unstable eigenmode. Figure 6.11 shows the growth rate and frequency of this mode for different Froude numbers at $Re = 60$ and $m^* = 20$. Note that in the low-U^* limit which correspond to a fixed body, the system is stable. This is consistent with the findings of Reichl *et al.* (2005) who showed that vortex shedding suppression could occur for small gaps. For low Froude numbers (—), the behaviour is similar to that in the highly confined configuration with a slip-wall: the mode is unstable over a finite range of reduced velocities, approximately $4.5 \lesssim U^* \lesssim 8.5$. The existence of a single eigenmode is here attributed to the strong global confinement. Increasing the Froude number to $Fr = 0.6$ significantly broadens the range of reduced velocities, with the mode becoming unstable for $U^* \gtrsim 5$. However, a further increase in the Froude number ($Fr = 0.67$) reduces this unstable range, indicating a partial restabilisation of the system. Overall, the Froude number seem to have a pronounced influence on the stability characteristics of the mode, for this immersion. Note that a similar behaviour where low and high Froude numbers respectively strengthened and weakened the VIV was observed by Chung (2016) in the 2DOF case.

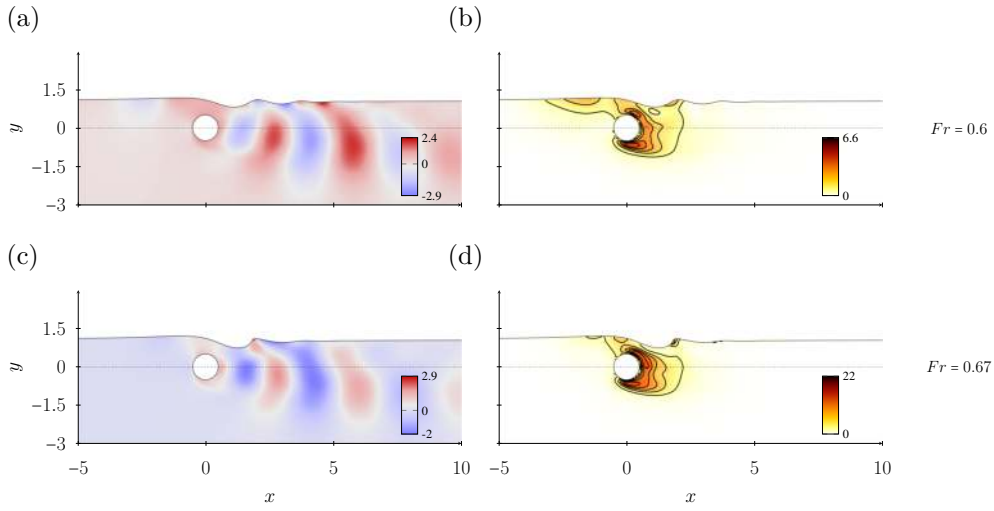

Figure 6.12: Eigenmode at $H = 1.05$, $Re = 60$, $m^* = 20$ and for $U^* = 6$: vertical velocity (a,c) and structural sensitivity (b,d) for different Froude numbers.

Figure 6.12 shows the vertical velocity and structural sensitivity of the eigenmode at $U^* = 6$ for the Froude numbers of $Fr = 0.6$ and $Fr = 0.67$. In contrast to the case $H = 2$ (figure 6.10), the structural sensitivity field confirms that the deformation of the free-surface has a role on the instability mechanism. While the dominant sensitivity regions remain located around the body, additional contributions appear upstream near the free surface and downstream in the vicinity of the wave crest.

For this confinement level ($H = 1.05$), the deformation of the free surface can therefore contribute to a destabilisation of the VIV mechanism.

6.3 Synthesis

Finally, the impact of a free surface on the flow stability and VIV of a single spring-mounted cylinder was investigated. The rigid free-surface limit ($Fr \to 0$), equivalent to a slip-wall, first showed that confinement has an overall stabilising effect on both the fixed-body wake instability and the VIV dynamics. For the fixed cylinder, decreasing the gap progressively suppresses vortex shedding through wake asymmetry and a modification of the wavemaker region. For the spring-mounted case, confinement stabilises the fluid-dominated mode and, for strong confinement, suppresses it entirely so that only a structure-dominated mode remains.

The effect of a deformable free surface was then examined by increasing the Froude number. For moderate immersion ($H = 2$), the deformation of the free surface was found to stabilise both the fixed-body instability and the VIV response. The deepening of the first wave trough occurs near the structural sensitivity region of the wake and acts as a local confinement behind the body, similarly to the stabilising effect observed with a slip-wall. For shallower immersion ($H = 1.05$), however, the free-surface deformation directly participates in the instability mechanism: additional structural sensitivity regions appear near the free surface and around the wave crest, and moderate Froude numbers can destabilise the VIV before a partial restabilisation occurs at higher Fr. This shows that the role of the free surface strongly depends on the immersion depth, acting either as a stabilising confinement effect or as an active source of coupling with the body motion.

Conclusions and outlook

In the first part of this work, we have developed linear and nonlinear methods for the analysis of fluid-structure interaction systems involving spring-mounted bodies and free-surfaces.

First, for spring-mounted bodies in an infinite domain, we have derived a discrete Arbitrary Lagrangian Eulerian formulation to express the domain deformation in terms of a finite set of structural degrees of freedom, thereby reducing the computational complexity of the coupled problem. Due to the large number of parameters to explore, we have also designed a generic linear method based on the calculation of a series of forced problems in which the cylinders are imposed to harmonically oscillate at a given frequency. Then defining transfer functions, we were able to derive an impedance-based criteria that allows the prediction of the instability thresholds.

Secondly, a linear Arbitrary Lagrangian Eulerian formulation was developed to solve the steady states and perturbation equations of a spring-mounted body beneath a free-surface. All methods were validated and found to be in good agreement with the litterature.

In the second part of this work, we have applied these methods to various configurations.

We first considered the case of two spring-mounted bodies in an infinite domain. For the in-line tandem configuration we have used the impedance-based stability criterion to conduct an extensive parametric study. The effect of increasing the mass and the damping ratio are found to be generally stabilising. The stability analysis in the $L-U^*$ plane revealed that the tandem cylinder dynamics evolve with spacing, showing similarities to previously observed wake interference regimes. These regimes were later explored by means of non-linear direct simulations and the maximum amplitudes, frequencies of the oscillations as well as phase lag between the bodies have been identified. Using both linear and non-linear methods, the analysis

was extend to a higher number of in-line bodies. A first exploration of the side-by-side spring-mounted configuration was also done using the linear methods developed. Neutral curves for key spacings were produced and good agreement was found with previous studies on the fixed configuration.

Finally, the influence of a free-surface on the VIV of a single spring-mounted body was explored. For a moderate immersion, increasing the deformation of the free-surface was found to have a stabilizing effect on the VIV and flow dynamics. Since a similar trend is observed for confinement with a slip-wall, this behaviour is attributed to a local confinement effect induced in the wake region by the deformed interface. For a lower immersion, the role of the free-surface was shown to be more complex: it can either stabilize or distabilize the dynamics depending on the Froude number.

A number of perspectives are opened for the continuation of this work.

First, considering spring-mounted bodies in an infinite domain, a particularly interesting perspective would be to consider periodic configurations, for which one can expect to apply Floquet-Bloch approaches allowing one to predict the large-scale dynamics of such configurations based on the resolution of problems simply formulated into an elementary cell. Aside from increasing the number of bodies, extending to additional degrees of freedom, including streamwise oscillation and rotational motion, could also be considered. A number of exceptional points of codimension 2 or 3 have been identified. Rich dynamics can be expected in the vicinity of such points, which could be elucidated thanks to alternative approaches such as weakly nonlinear expansions, Time Spectral Method or Spectral Submanifolds. Considering the application to energy harvesting, the evaluation of the performances and energy efficiencies would require a thourough investigation of the parameter space in the nonlinear regime.

Secondly, the study of the influence of the free-surface on VIV opens a wide range of perspectives. In particular, the investigation of the instability mechanism leading to the loss of convergence observed before wave breaking is of major interest. Implementing an arclength continuation method would enable the solution branch to be followed beyond this limit. In the context of energy harvesting, the development of a non-linear solver would allow the characterisation of amplitudes of oscillation and the associated output power. Finally, the framework could be extended to the study of flexible membranes for which the dynamics are expected to be widely different.

Bibliography

Achour, Nabil 2022 Interactions fluide-structure proche de la surface libre: application à la récupération d'énergie et aux instabilités. PhD thesis, Université Paul Sabatier-Toulouse III.

Aiba, S. & Yamazaki, Y. 1976 An experimental investigation of heat transfer around a tube in a bank. *Journal of Heat Transfer* **98** (3), 503–508.

Alam, Md Mahbub, Zheng, Q, Derakhshandeh, JF, Rehman, S, Ji, C & Zafar, F 2018 On forces and phase lags between vortex sheddings from three tandem cylinders. *International Journal of Heat and Fluid Flow* **69**, 117–135.

Alam, Mohammad-Reza 2012 Nonlinear analysis of an actuated seafloor-mounted carpet for a high-performance wave energy extraction. *Proceedings of the Royal Society A: Mathematical, Physical and Engineering Sciences* **468** (2146), 3153–3171.

Assi, GR da S, Bearman, Peter W, Carmo, Bruno Souza, Meneghini, Julio Romano, Sherwin, Spencer J & Willden, RHJ 2013 The role of wake stiffness on the wake-induced vibration of the downstream cylinder of a tandem pair. *Journal of Fluid Mechanics* **718**, 210–245.

Assi, GR da S, Meneghini, Julio Romano, Aranha, José Augusto Penteado, Bearman, Peter W & Casaprima, Enrique 2006 Experimental investigation of flow-induced vibration interference between two circular cylinders. *Journal of fluids and structures* **22** (6-7), 819–827.

Assi, Gustavo RS, Bearman, PW & Meneghini, JR 2010 On the wake-induced vibration of tandem circular cylinders: the vortex interaction excitation mechanism. *Journal of Fluid Mechanics* **661**, 365–401.

Aurégan, Tristan, Courrech du Pont, Sylvain & Thiria, Benjamin 2024 Shape reconfiguration for underwater propeller efficiency improvement. *Physical Review Fluids* **9** (7), 074402.

Bao, Yan, Zhou, Dai & Tu, Jiahuang 2011 Flow interference between a stationary cylinder and an elastically mounted cylinder arranged in proximity. *Journal of fluids and structures* **27** (8), 1425–1446.

Barbarino, Silvestro, Bilgen, Onur, Ajaj, Rafic M, Friswell, Michael I & Inman, Daniel J 2011 A review of morphing aircraft. *Journal of intelligent material systems and structures* **22** (9), 823–877.

Bearman, PW & Zdravkovich, MM 1978 Flow around a circular cylinder near a plane boundary. *Journal of Fluid Mechanics* **89** (1), 33–47.

Bearman, Peter W 1984 Vortex shedding from oscillating bluff bodies. *Annual review of fluid mechanics* **16** (1), 195–222.

Behara, Suresh, Chandra, Venu & Ravikanth, B 2024 Characterizing vibrations and associated wake structures of tandem square cylinders at different angles of incidence. *Physics of Fluids* **36** (4).

Behara, Suresh, Ravikanth, B & Chandra, Venu 2023 On the galloping cross-flow vibration responses of three in-line square cylinders. *Physics of Fluids* **35** (6).

Bernitsas, Michael M 2016 Harvesting energy by flow included motions. *Springer handbook of ocean engineering* pp. 1163–1244.

Bernitsas, Michael M, Raghavan, Kamaldev, Ben-Simon, Y & Garcia, EMH 2008 Vivace (vortex induced vibration aquatic clean energy): A new concept in generation of clean and renewable energy from fluid flow. *Journal of offshore mechanics and Arctic engineering* **130** (4).

Biermann, David & Herrnstein Jr, William H 1934 The interference between struts in various combinations. *Tech. Rep.*.

Bishop, Richard Evelyn Donohue & Hassan, AY 1964 The lift and drag forces on a circular cylinder oscillating in a flowing fluid. *Proceedings of the Royal Society of London. Series A. Mathematical and Physical Sciences* **277** (1368), 51–75.

Blackburn, HM & Karniadakis, GE 1993 Two-and three-dimensional simulations of vortex-induced vibration of a circular cylinder. In *Proceedings of the Third International Offshore and Polar Engineering Conference, Singapore*, , vol. 3, pp. 715–720.

Bokaian, A & Geoola, F 1984 Wake-induced galloping of two interfering circular cylinders. *Journal of Fluid Mechanics* **146**, 383–415.

Bonnefis, Paul 2019 Etude des instabilités de sillage, de forme et de trajectoire de bulles par une approche de stabilité linéaire globale. PhD thesis, Institut National Polytechnique de Toulouse-INPT.

Borazjani, Iman & Sotiropoulos, Fotis 2009 Vortex-induced vibrations of two cylinders in tandem arrangement in the proximity–wake interference region. *Journal of fluid mechanics* **621**, 321–364.

Boujo, Edouard 2021 Laminar viv of multiple in-line cylinders: linear stability and nonlinear dns. unpublished.

Bourguet, Rémi 2025 Rotation-induced vibrations of a cylinder in quiescent fluid. *Journal of Fluid Mechanics* **1019**, R3.

Brika, D & Laneville, A 1999 The flow interaction between a stationary cylinder and a downstream flexible cylinder. *Journal of Fluids and Structures* **13** (5), 579–606.

Carini, Marco, Giannetti, Flavio & Auteri, Franco 2014 First instability and structural sensitivity of the flow past two side-by-side cylinders. *Journal of fluid mechanics* **749**, 627–648.

Chai, Yuyang, Gao, Wei, Ankay, Benjamin, Li, Fengming & Zhang, Chuanzeng 2021 Aeroelastic analysis and flutter control of wings and panels: a review. *International Journal of Mechanical System Dynamics* **1** (1), 5–34.

Chen, Jingle & Wu, Jie 2024 Numerical investigation of vortex-induced vibration of a porous-coated cylinder at subcritical reynolds number with a combined k-ε model for porous medium. *Ocean Engineering* **304**, 117828.

Chen, Weilin, Ji, Chunning, Williams, John, Xu, Dong, Yang, Lihong & Cui, Yuting 2018 Vortex-induced vibrations of three tandem cylinders in laminar cross-flow: Vibration response and galloping mechanism. *Journal of Fluids and Structures* **78**, 215–238.

Chen, Wen-Li, Huang, Ye-Wei & Meng, Hao 2020 Wake-induced vibration of a suspender cable in the rear of a bridge tower. *Journal of Fluids and Structures* **99**, 103166.

Chung, Meng-Hsuan 2016 Two-degree-of-freedom vortex induced vibration of low-mass horizontal circular cylinder near a free surface at low reynolds number. *International Journal of Heat and Fluid Flow* **57**, 58–78.

Colagrossi, A, Nikolov, G, Durante, D, Marrone, S & Souto-Iglesias, A 2019 Viscous flow past a cylinder close to a free surface: benchmarks with steady, periodic and metastable responses, solved by meshfree and mesh-based schemes. *Computers & Fluids* **181**, 345–363.

Conciauro, G & Puglisi, M 1981 Meaning of the negative impedance. *NASA STI/Recon Technical Report N* **82**, 14458.

Cossu, C. & Morino, L. 2000 On the instability of a spring-mounted cylinder in a viscous flow at low reynolds numbers. *Journal of Fluids and Structures* **14** (2), 183–196.

De Langre, Emmanuel 2006 Frequency lock-in is caused by coupled-mode flutter. *Journal of fluids and structures* **22** (6-7), 783–791.

Fabre, David, Citro, Vincenzo, Ferreira Sabino, D, Bonnefis, Paul, Sierra, Javier, Giannetti, Flavio & Pigou, Maxime 2018 A practical review on linear and nonlinear global approaches to flow instabilities. *Applied Mechanics Reviews* **70** (6), 060802.

Fabre, David, Longobardi, Raffaele, Bonnefis, Paul & Luchini, Paolo 2019 The acoustic impedance of a laminar viscous jet through a thin circular aperture. *Journal of Fluid Mechanics* **864**, 5–44.

Fabre, David, Longobardi, Raffaele, Citro, Vincenzo & Luchini, Paolo 2020 Acoustic impedance and hydrodynamic instability of the flow through a circular aperture in a thick plate. *Journal of Fluid Mechanics* **885**, A11.

Fernández, Miguel Ángel & Le Tallec, Patrick 2003 Linear stability analysis in fluid–structure interaction with transpiration. part i: Formulation and mathematical analysis. *Computer methods in applied mechanics and engineering* **192** (43), 4805–4835.

Fontaine, Emmanuel, Morel, Jean-Pierre, Scolan, Yves-Marie & Rippol, T 2006 Riser interference and viv amplification in tandem configuration. In *ISOPE International Ocean and Polar Engineering Conference*, pp. ISOPE–I. ISOPE.

Ghasemi, A & Kevlahan, NK-R 2017 The role of reynolds number in the fluid-elastic instability of tube arrays. *Journal of Fluids and Structures* **73**, 16–36.

Giannetti, Flavio & Luchini, Paolo 2007 Structural sensitivity of the first instability of the cylinder wake. *Journal of Fluid Mechanics* **581**, 167–197.

González-Gutierrez, Leo M, Gimenez, Juan M & Ferrer, Esteban 2019 Instability onset for submerged cylinders. *Physics of Fluids* **31** (1).

Griffin, OM & Ramberg, SE 1982 Some recent studies of vortex shedding with application to marine tubulars and risers. *Journal of Energy Resources Technology* **104** (1), 2–13.

Griffith, Martin D, Jacono, David Lo, Sheridan, John & Leontini, Justin S 2017 Flow-induced vibration of two cylinders in tandem and staggered arrangements. *Journal of Fluid Mechanics* **833**, 98–130.

Han, Zhaolong, Zhou, Dai, Gui, Xiaolan & Tu, Jiahuang 2013 Numerical study of flow past four square-arranged cylinders using spectral element method. *Computers & Fluids* **84**, 100–112.

Hanke, Wolf, Witte, Matthias, Miersch, Lars, Brede, Martin, Oeffner, Johannes, Michael, Mark, Hanke, Frederike, Leder, Alfred & Dehnhardt, Guido 2010 Harbor seal vibrissa morphology suppresses vortex-induced vibrations. *Journal of Experimental Biology* **213** (15), 2665–2672.

Harimi, Iman & Saghafian, Mohsen 2012 Numerical simulation of fluid flow and forced convection heat transfer from tandem circular cylinders using overset grid method. *Journal of fluids and structures* **28**, 309–327.

He, Fei, Ren, Chengjiao, An, Hongwei & Cheng, Liang 2026 Flow past a line of cylinders at intermediate gap ratio: Three-dimensionality influence. *International Journal of Heat and Fluid Flow* **119**, 110317.

Hecht, Frédéric 2012 New development in freefem++. *Journal of numerical mathematics* **20** (3-4), 251–266.

Hetz, AA, Dhaubhadel, MN & Telionis, DP 1991 Vortex shedding over five in-line cylinders cylinders. *Journal of fluids and structures* **5** (3), 243–257.

Hosseini, Negar 2021 Numerical analysis and investigation of the interaction between fluid and multiple bodies. PhD thesis, Swinburne.

Hosseini, N, Griffith, MD & Leontini, JS 2020 The flow past large numbers of cylinders in tandem. *Journal of Fluids and Structures* **98**, 103103.

Hosseini, N, Griffith, MD & Leontini, JS 2022 Flow-induced vibrations in long rows of cylinders and their links to convective instabilities. *International Journal of Heat and Fluid Flow* **94**, 108922.

Hosseini, Negar, Griffith, Martin D & Leontini, Justin S 2021 Flow states and transitions in flows past arrays of tandem cylinders. *Journal of Fluid Mechanics* **910**, A34.

Huera-Huarte, FJ & Gharib, M 2011 Vortex-and wake-induced vibrations of a tandem arrangement of two flexible circular cylinders with far wake interference. *Journal of Fluids and Structures* **27** (5-6), 824–828.

Hughes, Thomas JR, Liu, Wing Kam & Zimmermann, Thomas K 1981 Lagrangian-eulerian finite element formulation for incompressible viscous flows. *Computer methods in applied mechanics and engineering* **29** (3), 329–349.

Hwang, Jong-Yeon, Yang, Kyung-Soo & Sun, Seung-Han 2003 Reduction of flow-induced forces on a circular cylinder using a detached splitter plate. *Physics of Fluids* **15** (8), 2433–2436.

Igarashi, Tamotsu 1986 Characteristics of the flow around four circular cylinders arranged in line. *Bulletin of JSME* **29** (249), 751–757.

Igarashi, Tamotsu 1993 Aerodynamic forces acting on three circular cylinders having different diameters closely arranged in line. *Journal of Wind Engineering and Industrial Aerodynamics* **49** (1-3), 369–378.

Kevlahan, NK-R 2007 Three-dimensional floquet stability analysis of the wake in cylinder arrays. *Journal of Fluid Mechanics* **592**, 79–88.

Kim, Hoyoung, Lee, Junyoung & Seok, Jongwon 2022 Novel piezoelectric wind energy harvester based on coupled galloping phenomena with characterization and quantification of its dynamic behavior. *Energy Conversion and Management* **266**, 115849.

Kim, Sangil, Alam, Md Mahbub, Sakamoto, Hiroshi & Zhou, Yu 2009*a* Flow-induced vibration of two circular cylinders in tandem arrangement. part 2: Suppression of vibrations. *Journal of wind engineering and industrial aerodynamics* **97** (5-6), 312–319.

Kim, Sangil, Alam, Md Mahbub, Sakamoto, Hiroshi & Zhou, Yu 2009*b* Flow-induced vibrations of two circular cylinders in tandem arrangement. part 1: Characteristics of vibration. *Journal of Wind Engineering and Industrial Aerodynamics* **97** (5-6), 304–311.

Kinaci, Omer Kemal, Demirhan, Alkin Erdal & Duranay, Aytekin 2022 Vortex-induced vibrations of a single-degree-of-freedom circular cylinder in the vicinity of the free surface. *Applied Ocean Research* **124**, 103202.

King, R & Johns, DJ 1976 Wake interaction experiments with two flexible circular cylinders in flowing water. *Journal of Sound and Vibration* **45** (2), 259–283.

Lam, K & Lo, SC 1992 A visualization study of cross-flow around four cylinders in a square configuration. *Journal of fluids and structures* **6** (1), 109–131.

Lee, Yin Jen, Qi, Yi, Zhou, Guangya & Lua, Kim Boon 2019 Vortex-induced vibration wind energy harvesting by piezoelectric mems device in formation. *Scientific reports* **9** (1), 20404.

Lehmann, Marcus, Elandt, Ryan, Pham, Henry, Ghorbani, Reza, Shakeri, Mostafa & Alam, Mohammad-Reza 2013 An artificial seabed carpet for multidirectional and broadband wave energy extraction: Theory

and experiment. In *Proceedings of 10th European Wave and Tidal Energy Conference*.

Lei, Cheng, Cheng, Liang & Kavanagh, Kenneth 1999 Re-examination of the effect of a plane boundary on force and vortex shedding of a circular cylinder. *Journal of Wind Engineering and Industrial Aerodynamics* **80** (3), 263–286.

Li, Xintao, Lyu, Zhen, Kou, Jiaqing & Zhang, Weiwei 2019 Mode competition in galloping of a square cylinder at low reynolds number. *Journal of Fluid Mechanics* **867**, 516–555.

Liang, Chunlei, Papadakis, George & Luo, Xiaoyu 2009 Effect of tube spacing on the vortex shedding characteristics of laminar flow past an inline tube array: a numerical study. *Computers & Fluids* **38** (4), 950–964.

Luchini, Paolo & Bottaro, Alessandro 2014 Adjoint equations in stability analysis. *Annual Review of fluid mechanics* **46** (1), 493–517.

Mehmood, A, Abdelkefi, A, Hajj, MR, Nayfeh, AH, Akhtar, I & Nuhait, AO 2013 Piezoelectric energy harvesting from vortex-induced vibrations of circular cylinder. *Journal of Sound and Vibration* **332** (19), 4656–4667.

Meneghini, Julio R, Saltara, Fábio, Siqueira, Cesareo de La Rosa & Ferrari Jr, JA 2001 Numerical simulation of flow interference between two circular cylinders in tandem and side-by-side arrangements. *Journal of fluids and structures* **15** (2), 327–350.

Mittal, S & Kumar, Vinod 2001 Flow-induced oscillations of two cylinders in tandem and staggered arrangements. *Journal of Fluids and Structures* **15** (5), 717–736.

Mittal, Sanjay & Singh, Saurav 2005 Vortex-induced vibrations at subcritical re. *Journal of Fluid Mechanics* **534**, 185–194.

Mysa, Ravi Chaithanya, Kaboudian, Abouzar & Jaiman, Rajeev Kumar 2016 On the origin of wake-induced vibration in two tandem circular cylinders at low reynolds number. *Journal of Fluids and Structures* **61**, 76–98.

Navrose & Mittal, Sanjay 2016 Lock-in in vortex-induced vibration. *Journal of Fluid Mechanics* **794**, 565–594.

Negi, Prabal S, Hanifi, Ardeshir & Henningson, Dan S 2020 On the linear global stability analysis of rigid-body motion fluid–structure-interaction problems. *Journal of Fluid Mechanics* **903**, A35.

Nicolle, A & Eames, I 2011 Numerical study of flow through and around a circular array of cylinders. *Journal of Fluid Mechanics* **679**, 1–31.

Paidoussis, MP 1981 Fluidelastic vibration of cylinder arrays in axial and cross flow: state of the art. *Journal of Sound and Vibration* **76** (3), 329–360.

Paidoussis, MP 1983 A review of flow-induced vibrations in reactors and reactor components. *Nuclear Engineering and Design* **74** (1), 31–60.

Papaioannou, GV, Yue, DKP, Triantafyllou, MS & Karniadakis, GE 2008 On the effect of spacing on the vortex-induced vibrations of two tandem cylinders. *Journal of Fluids and Structures* **24** (6), 833–854.

Papaioannou, Georgios Vasilios 2006 A numerical study of flow-structure interactions with application to flow past a pair of cylinders. PhD thesis.

Parkinson, Geoffrey 1989 Phenomena and modelling of flow-induced vibrations of bluff bodies. *Progress in Aerospace Sciences* **26** (2), 169–224.

Patel, Kuntal, Sun, Jun, Yang, Zixuan & Zhu, Xiaojue 2025 Coupled liquid–gas flow over a submerged cylinder: interface topology, wake structure and hydrodynamic lift. *Journal of Fluid Mechanics* **1008**, A10.

Peskin, Charles S 1977 Numerical analysis of blood flow in the heart. *Journal of computational physics* **25** (3), 220–252.

Pettigrew, Michel J & Taylor, Colette E 2003 Vibration analysis of shell-and-tube heat exchangers: an overview—part 1: flow, damping, fluidelastic instability. *Journal of fluids and structures* **18** (5), 469–483.

Pfister, Jean-Lou, Marquet, Olivier & Carini, Marco 2019 Linear stability analysis of strongly coupled fluid–structure problems with the arbitrary-lagrangian–eulerian method. *Computer Methods in Applied Mechanics and Engineering* **355**, 663–689.

Popinet, Stéphane 2015 A quadtree-adaptive multigrid solver for the serre–green–naghdi equations. *Journal of Computational Physics* **302**, 336–358.

Prasanth, TK & Mittal, S 2009*a* Flow-induced oscillation of two circular cylinders in tandem arrangement at low re. *Journal of fluids and structures* **25** (6), 1029–1048.

Prasanth, T.K. & Mittal, Sanjay 2009*b* Vortex-induced vibration of two circular cylinders at low reynolds number. *Journal of Fluids and Structures* **25** (4), 731–741.

Price, SJ 1976 The origin and nature of the lift force on the leeward of two bluff bodies. *Aeronautical Quarterly* **27** (2), 154–168.

Rashki, Mohammadreza, Mojtahedi, Alireza, Lotfollahi-Yaghin, Mohammad Ali, Tamimi, Vahid, Dadashzadeh, Mehran, Santos, Paulo Rosa, Bernitsas, Michael M & Srinil, Narakorn 2025 A review of two-degree-of-freedom vortex-induced vibrations with hydrokinetic energy harvesting applications. *Ocean Engineering* **321**, 120376.

Reichl, P, Hourigan, Kerry & Thompson, Mark Christopher 2005 Flow past a cylinder close to a free surface. *Journal of Fluid Mechanics* **533**, 269–296.

Rostami, Ali Bakhshandeh & Armandei, Mohammadmehdi 2017 Renewable energy harvesting by vortex-induced motions: Review and benchmarking of technologies. *Renewable and Sustainable Energy Reviews* **70**, 193–214.

Sabino, Diogo, Fabre, David, Leontini, JS & Jacono, D Lo 2020 Vortex-induced vibration prediction via an impedance criterion. *Journal of Fluid Mechanics* **890**.

Sarpkaya, Turgut 2004 A critical review of the intrinsic nature of vortex-induced vibrations. *Journal of fluids and structures* **19** (4), 389–447.

Sayers, AT 1988 Flow interference between four equispaced cylinders when subjected to a cross flow. *Journal of Wind Engineering and Industrial Aerodynamics* **31** (1), 9–28.

Semin, Benoit, Decoene, Astrid, Hulin, J-P, François, Marc Louis Maurice & Auradou, Harold 2012 New oscillatory instability of a confined cylinder in a flow below the vortex shedding threshold. *Journal of fluid mechanics* **690**, 345–365.

Sheridan, J, Lin, J-C & Rockwell, D 1995 Metastable states of a cylinder wake adjacent to a free surface. *Physics of Fluids* **7** (9), 2099–2101.

Sheridan, John, Lin, J-C & Rockwell, D 1997 Flow past a cylinder close to a free surface. *Journal of Fluid Mechanics* **330**, 1–30.

Sierra, Javier, Fabre, David & Citro, Vincenzo 2020 Efficient stability analysis of fluid flows using complex mapping techniques. *Computer Physics Communications* **251**, 107100.

Sierra-Ausin, Javier, Bonnefis, Paul, Tirri, Antonia, Fabre, David & Magnaudet, Jacques 2022*a* Dynamics of a gas bubble in a straining flow: Deformation, oscillations, self-propulsion. *Physical Review Fluids* **7** (11), 113603.

Sierra-Ausin, J, Fabre, D, Citro, V & Giannetti, F 2022*b* Acoustic instability prediction of the flow through a circular aperture in a thick plate via an impedance criterion. *Journal of Fluid Mechanics* **943**, A48.

Sipp, Denis & Lebedev, Anton 2007 Global stability of base and mean flows: a general approach and its applications to cylinder and open cavity flows. *Journal of Fluid Mechanics* **593**, 333–358.

Soti, Atul Kumar, Thompson, Mark C, Sheridan, John & Bhardwaj, Rajneesh 2017 Harnessing electrical power from vortex-induced vibration of a circular cylinder. *Journal of Fluids and Structures* **70**, 360–373.

Sumner, D 2010 Two circular cylinders in cross-flow: A review. *Journal of fluids and structures* **26** (6), 849–899.

Sumner, D, Price, SJ & Paidoussis, MP 2000 Flow-pattern identification for two staggered circular cylinders in cross-flow. *Journal of Fluid Mechanics* **411**, 263–303.

Sun, Jun, Lu, Min, Patel, Kuntal, Zhu, Xiaojue & Yang, Zixuan 2025 Free-surface flow past a submerged horizontal cylinder: Reynolds-number dependence. *Journal of Fluid Mechanics* **1023**, A39.

Sun, Wan, Guo, Feng & Seok, Jongwon 2019 Development of a novel vibro-wind galloping energy harvester with high power density incorporated with a nested bluff-body structure. *Energy conversion and management* **197**, 111880.

Suzuki, Kosuke & Inamuro, Takaji 2011 Effect of internal mass in the simulation of a moving body by the immersed boundary method. *Computers & Fluids* **49** (1), 173–187.

Tatsuno, Masakazu, Taneda, Sadatoshi & others 1985 Visual studies of wake structure behind two cylinders in tandem arrangement .

Tirri, Antonia, Nitti, Alessandro, Sierra-Ausin, Javier, Giannetti, Flavio & de Tullio, Marco D 2023 Linear stability analysis of fluid–structure interaction problems with an immersed boundary method. *Journal of Fluids and Structures* **117**, 103830.

Träsch, Martin 2019 Caractérisation expérimentale et numérique du comportement hydrodynamique d'une hydrolienne à membrane ondulante. PhD thesis, Lille.

Vickery, Barry J 1981 Across-wind buffeting in a group of four in-line model chimneys. *Journal of Wind Engineering and Industrial Aerodynamics* **8** (1-2), 177–193.

Williamson, Charles HK & Govardhan, R 2008 A brief review of recent results in vortex-induced vibrations. *Journal of Wind engineering and industrial Aerodynamics* **96** (6-7), 713–735.

Williamson, Charles HK, Govardhan, R & others 2004 Vortex-induced vibrations. *Annual review of fluid mechanics* **36** (1), 413–455.

Wu, Ruicong, Liu, Jiabin, Qu, Jinlong & Guo, Anxin 2024 Vortex-induced vibration suppression of cactus-like cylinders. *Ocean Engineering* **299**, 117201.

Xu, Feng, Ou, Jinping & Xiao, Yiqing 2009 Numerical study on vortex induced vibrations of four cylinders in an in-line square configuration. In *Computational Structural Engineering: Proceedings of the International Symposium on Computational Structural Engineering, held in Shanghai, China, June 22–24, 2009*, pp. 553–567. Springer.

Yao, W & Jaiman, RK 2019 Stability analysis of the wake-induced vibration of tandem circular and square cylinders. *Nonlinear Dynamics* **95** (1), 13–28.

Zdravkovich, MM 1987 The effects of interference between circular cylinders in cross flow. *Journal of fluids and structures* **1** (2), 239–261.

Zdravkovich, MM & Pridden, DL 1977 Interference between two circular cylinders; series of unexpected discontinuities. *Journal of wind engineering and industrial aerodynamics* **2** (3), 255–270.

Zhang, Cheng, Tang, Guoqiang, Lu, Lin, Jin, Yan, An, Hongwei & Cheng, Liang 2024*a* Flow-induced vibration of two tandem square cylinders at low reynolds number: transitions among vortex-induced vibration, biased oscillation and galloping. *Journal of Fluid Mechanics* **986**, A10.

Zhang, Zhiyu, Lu, Jianfeng & Zhang, Xing 2024*b* Global stability analysis of flow-induced-vibration problems using an immersed boundary method. *Journal of Fluids and Structures* **130**, 104187.

Zhao, Feng, Wang, Rui, Zhu, Hongbo, Cao, Yong, Bao, Yan, Zhou, Dai, Cheng, Bin & Han, Zhaolong 2024 Free-surface effects on the flow around two circular cylinders in tandem. *Journal of Fluid Mechanics* **1001**, A7.

Zhao, Feng, Wang, Rui, Zhu, Hongbo, Cao, Yong, Bao, Yan, Zhou, Dai & Han, Zhaolong 2022*a* Wake dynamics and hydrodynamic forces of a circular cylinder beneath a free surface. *Ocean Engineering* **265**, 112669.

Zhao, Jisheng, Thompson, Mark C & Hourigan, Kerry 2022*b* Damping effect on transverse flow-induced vibration of a rotating circular cylinder and its implied energy harvesting performance. *Physical Review Fluids* **7** (2), 023905.

Zhao, Ming & Cheng, Liang 2012 Numerical simulation of vortex-induced vibration of four circular cylinders in a square configuration. *Journal of Fluids and Structures* **31**, 125–140.

Zhao, Ming, Cheng, Liang, An, Hongwei & Tong, Feifei 2015 Flow and flow-induced vibration of a square array of cylinders in steady currents. *Fluid Dynamics Research* **47** (4), 045505.

Zhao, Ming, Zhang, Qin & Liu, Yong 2025 Flow-induced vibration and energy harvesting of an elastically mounted circular cylinder with mechanically coupled rotation. *Journal of Fluid Mechanics* **1021**, A26.

Zhou, CY, So, RMC & Lam, K 1999 Vortex-induced vibrations of an elastic circular cylinder. *Journal of Fluids and Structures* **13** (2), 165–189.

Zhou, Yu & Alam, Md Mahbub 2016 Wake of two interacting circular cylinders: A review. *International Journal of Heat and Fluid Flow* **62**, 510–537.

Zhu, Hongjun, Zhong, Jiawen, Shao, Ze, Zhou, Tongming & Alam, Md Mahbub 2024 Fluid-structure interaction among three tandem circular cylinders oscillating transversely at a low reynolds number of 150. *Journal of Fluids and Structures* **130**, 104204.

RÉPUBLIQUE FRANÇAISE
Liberté
Égalité
Fraternité

Université de Toulouse

Titre : Dynamique d'écoulements en interaction avec des structures movibles et des surfaces libres

Mots clés : fluide-structure, surface libre, déformable, VIV, FSI, interaction

Résumé : Dans cette thèse, nous étudions la dynamique des écoulements impliquant des structures mobiles et des surfaces libres.

Un cadre linéaire et non linéaire de type « Arbitrary Lagrangian Eulerian » (ALE) est développé et validé pour des systèmes à plusieurs corps montés sur ressorts. Les formulations obtenues sont ensuite appliquées à un ensemble de configurations, notamment les configurations à deux cylindres en tandem et côte à côte, ainsi qu'aux configurations à plusieurs cylindres en ligne.

Nous proposons ensuite un critère basé sur l'impédance, à faible coût de calcul, pour prédire les seuils d'instabilité. Ce critère s'avère en parfait accord avec l'analyse de stabilité linéaire classique et est utilisé pour détecter les seuils d'instabilité dans l'espace des paramètres. Les effets de la masse, de l'amortissement et de l'espacement entre les corps sont étudiés.

Enfin, un cadre linéaire de type « Arbitrary Lagrangian Eulerian » est développé pour l'interaction d'un corps monté sur ressort avec une surface libre déformable. Nous explorons ensuite l'impact des surfaces libres sur le sillage et les vibrations induites par les tourbillons du corps, pour différentes hauteurs d'immersion.

Title: Flow dynamics involving moving structures and free surfaces

Key words: fluid-structure, free surface, deformable, VIV, FSI

Abstract: In this thesis, we study the flow dynamics involving moving structures and free-surfaces.

A linear and non linear Arbitrary Lagrangian Eulerian framework is developed and validated for multiple spring-mounted bodies. The derived formulations are then applied to a set of configurations including the two-cylinder tandem and side by side configurations as well as the multiple in-line cylinders.

We then propose a low computational-cost impedance-based criterion to predict the instability thresholds. The criterion is found to be in perfect agreement with the classical linear stability analysis and is used to detect instability thresholds in the parameter space. The effects of mass, damping and spacing between the bodies are investigated.

Finally, a linear Arbitrary Lagrangian Eulerian framework is developed for the interaction of a spring-mounted body with a deformable free-surface. We then explore the impact of free-surfaces on the wake and vortex-induced vibrations of the body, for different immersion heights.